KU LEUVEN

ARENBERG DOCTORAL SCHOOL
Faculty of Engineering Science

Selective Laser Sintering and Melting as additive manufacturing methods to produce alumina parts

‘3D printing’ of ceramics

Jan Deckers

Dissertation presented in
fulfillment of the requirements for the
degree of Doctor in Engineering
Science

2013

Selective Laser Sintering and Melting as additive manufacturing methods to produce alumina parts

'3D printing' of ceramics

Jan DECKERS

Supervisory Committee:
Prof. dr. Jean Berlamont, chair
Prof. dr. Jean-Pierre Kruth, supervisor
Prof. dr. Jef Vleugels, supervisor
Prof. dr. Bert Lauwers, secretary
Prof. dr. Jan Van Humbeeck
Prof. dr. Ludwig Cardon
(Ghent University)
Prof. dr. Bert Huis in 't Veld
(University of Twente)

Dissertation presented in
fulfillment of the requirements for
the degree of Doctor
in Engineering Science

2013

D/2013/7515/159
ISBN 978-94-6018-778-0

Dankwoord

> Some years ago - never mind how long precisely - having little or no money in my purse, and nothing particular to interest me on shore, I thought I would sail a little and see the watery part of the world.
>
> Melville, Herman [149]

Voor hun afvaart, moeten de ontdekkingsreizigers zich gevoeld hebben als een beginnende doctoraatsstudent. Ongeduldig door de onwetendheid over wat ze op hun reis zullen tegenkomen, kunnen ze in het begin nog alle richtingen uit. Echter, de richting die ze zullen uitvaren, zal bepalend zijn voor het verloop van de reis. Soms kiezen ze het ruime sop en zal de reis iets langer duren. Soms gaan ze even aan wal om op schattenjacht te gaan. Maar met af en toe de wind in de zeilen, komen ze na verloop van tijd terug veilig en wel aan in de haven.

Deze ontdekkingsreis werd voornamelijk gefinanicieerd door het IWT via het SBO-project DiRaMaP en de KU Leuven. De eerste kapitein op mijn schip was prof. dr. ir. Jean-Pierre Kruth. Zijn vertrouwen en scherpzinnigheid maakten van hem een goede mentor. Bovendien was zijn ervaring als doorwinterde zeeman, die al vele wateren doorvaren had, onontbeerlijk om de reis zonder al te veel zorgen te kunnen voltooien. Al snel kwam kapitein prof. dr. ir. Jef Vleugels aan boord. Hij liet me kennis maken met de wereld van de keramieken. De deur van zijn kajuit stond altijd open en met veel energie kon hij steeds bijsturen waar nodig.

Hierbij zou ik ook de andere leden van de commissie die de opdracht aannam om mijn reisverslag na te lezen, willen danken. Voorgezeten door professor Jean Berlamont wil ik professor Bert Lauwers, professor Jan Van Humbeeck, professor Ludwig Cardon en professor Bert Huis in 't Veld danken voor de tijd

die hiervoor genomen werd.

Deze tocht zou maar eenzaam zijn geweest zonder mijn medereizigers. Tijdens de afvaart heb ik veel gehad aan Tom Craeghs (introductie aan prof. Kruth), Jonas Van Vaerenbergh (introductie tot hersmelten), Peter Mercelis (introductie tot thermische spanningen), Simon Van Bael (herstellen DTM Sinterstation 2000 machine) en Sanjay Kumar ('research is learning by doing'). Tijdens de eerste jaren, toen mijn schip nog in de metallische zee vaarde, heb ik ook veel gehad aan Evren Yasa. *Evren, some nostalgic thoughts come to my mind when I think of the first years of my PhD and the research we did together. Besides, I still have your miracle recipe for making the chocolate cake.*

Eens, na de herstelling van de Sinterstation 2000 machine, de keramische zee bereikt was, startte het échte avontuur. Op drie plaatsen tegelijk (KU Leuven, UGent en VITO) werden er poeders ontwikkeld die getest konden worden in de herstelde machine. Aangezien het ontwikkelen van een poeder telkens veel voeten in de aarde heeft, ben ik volgende personen heel wat verschuldigd: Khuram Shahzad, Bram Neirinck, Ludwig Cardon, An Verberckmoes, Anja Vanbiervliet, Marleen Rombouts en Jan Luyten. *Khuram, after our close collaboration I have to conclude that '1 + 1 = 3' is valid not only in marketing, but also in research.*

Voor hun vakkundige hulp bij het ontwikkelen van de experimentele opstelling voor direct SLS/SLM van keramieken moet ik Joop van Deursen, Kim Vanmeensel, Nick Van Gestel, Dirk Bastiaensen, Eddy Smets, Joachim Van Kriekingen, Tony Debecker en Peter Serverius uitvoerig danken. Ik geef toe dat deze opstelling tijdens de ontwikkeling ervan soms veel weg had van een ruimtetuig dat door één of andere over-het-hoofd-geziene ingenieursfout vlak na de lancering in het water zou belanden. Dankzij jullie nuchtere kijk op de zaken is dit niet gebeurd. Meer details: zie hoofdstuk 7.

De volgende medereizigers die de legendarische status van kajuit 'de gele trap' enkel maar eer aandoen/aandeden verdienen ook niets dan lof: Mohsen Badrossamay (for bringing the persian culture into the office), Stijn Clijsters (voor zijn aanmoedigingen), Karolien Kempen (voor het zorgen voor sfeer op de bureau), Alex Liu (to cheer us up), Sam Buls (voor zijn muzikale intermezzo's), Mathew Speirs (for his well formulated opinions on whatever topic you can think of), Sasan Dadbakhsh (for his enthusiastic advice), Sebastian Meyers (om de vervolg-expeditie te willen leiden), Raya Mertens (girl en brainpower), Filip Bleys (voor het uitleggen van verschillende meetinstrumenten en zijn kritisch luisterend oor), Frank Welkenhuyzen (voor zijn goede raad bij het kleurenwiezen), Bart Boeckmans (voor zijn oprechtheid) en Ye Tan (voor zijn

onbaatzuchtigheid). AM-MTM-ers zoals Lore Thijs en Bey Vrancken en expats, zoals Ruben Wauthlé en Brawley Valkenborgs (LayerWise) verdienen ook het nodige respect. Ze zorgden voor de uitbereiding van de 'gele trap' spirit tot ver buiten de territoriale wateren van ons departement.

Niet minder onmisbaar voor het reilen en zeilen van mijn schip waren alle nog niet genoemde administratief en technisch medewerkers: Lieve Notré, Karin Dewit, Valérie Karlshousen, Regine Vanswijgenhoven, Jean-Pierre Merckx, Bertram Van Soom, Jan Thielemans, Ronny Moreas, Rudy de Vos, Paul Crabbe, Wout Veulemans, Marijke Lauwereyns, José de Krosse, Stephanie Poot, Peter Borry, Carine Coosemans, Pascal Cooremans, Frieda Decoster, en de vele anderen die ik nu allicht vergeet op te sommen.

Als voorlaatste dien ik mijn dichte omgeving te bedanken. Mijn ouders hebben me gemaakt tot wie ik ben en verdienen hier alle credits voor. Zonder de steun van mijn ouders, broers, familie en vrienden had ik allicht de moed niet gevonden om aan dit avontuur te beginnen. Mijn schoonouders en schoonfamilie wil ik ook van harte bedanken voor hun morele steun tijdens dit wedervaren.

Als een schipper verdwaalt is op zee en niet meer weet hoe hij thuis moet geraken, dient hij 's nachts naar de sterren te kijken om zich te kunnen heroriënteren. Helaas wordt deze oriëntatie bemoeilijkt door het tollen van de aarde. Tijdens mijn ontdekkingsreis heb ik gelukkig één sterretje aan de hemel gevonden dat stil bleef staan en me naar huis heeft geleid. Dit sterretje is Lien. Zonder haar was mijn schip allicht nog ergens in de open oceaan aan het ronddobberen, op zoek naar alles en niets, nog niet aan zijn terugtocht begonnen.

De lange schrijfdagen, -weken en -maanden hebben we zij aan zij doorgebracht. Elk aan ons PC'tje werkten we respectievelijk aan een doctoraat over de geschiedenis van de Belgische radio en een doctoraat over 3D printen van keramiek. Binnenkort, na dit avontuur, zullen we ons schip verlaten en beginnen we aan een nieuwe reis, die nog veel groter en avontuurlijker zal zijn. Opnieuw kiezen we, dit keer niet alleen maar met ons tweetjes, voor het ruime sop.

Abstract

Additive manufacturing (AM; aka 3D printing) has the potential to rapidly shape parts, without compromising geometrical properties. Variants of the following powder metallurgy (PM) process, which includes additive manufacturing as a shaping step, were explored to produce ceramic parts: (i) powder synthesis, (ii) additive manufacturing, (iii) binder removal and (iv) furnace sintering. In this study alumina (Al_2O_3) parts were produced, since Al_2O_3 is currently the most commonly used ceramic material for technical applications. Further, two AM methods were investigated as possible shaping steps for the production of alumina parts: indirect Selective Laser Sintering (indirect SLS) and direct Selective Laser Sintering/Melting (direct SLS/SLM).

To explore indirect SLS, different powders, with a particle size of about 10-100 μm and consisting of an alumina and a polymer binder phase (i.e. composite alumina-binder agglomerates), were irradiated by a laser beam. Five different alumina-binder agglomerates were investigated: alumina-polyamide produced through ball milling, alumina-polystyrene produced through dispersion polymerization and alumina-polyamide, alumina-polypropylene and alumina-carnauba_wax-low_density_polyethylene produced through temperature induced phase separation. The laser irradiation, which melted only the binder phase, selectively consolidated the powder agglomerates layer by layer. After subsequent binder removal and furnace sintering, alumina parts, containing inter-agglomerate pores, were obtained. In order to reduce the inter-agglomerate pores, the possibility to include the following steps into the PM process was explored: (i) irradiating the powder layers multiple times instead of only once (i.e. remelting), (ii) cold, quasi and warm isostatic pressing the SLSed parts and (iii) infiltrating the parts obtained at different stages of the PM process. As a result, freeform shaped alumina parts with densities up to approximately 90% could already be obtained. In order to produce higher quality ceramics through indirect SLS, the inter-agglomerate pores should be avoided or completely eliminated.

To explore direct SLS/SLM of alumina parts, an experimental setup was developed. The experimental setup enabled to selectively irradiate densely packed layers of alumina powder, with a particle size of about 0.3 μm and without binder phase, at uniform temperatures up to 800°C. After a subsequent furnace sintering step, alumina samples with a grain size smaller than 5 μm could be obtained. In order to produce high quality ceramics through direct SLS/SLM, the reliability of the of the experimental setup should be improved by homogenizing: (i) the powder deposition process, (ii) the consolidation temperature during selective heating of the powder layers and (iii) the preheating temperature of the powder layers.

Beknopte samenvatting

Materiaal toevoegende productietechnieken (additieve vervaardigingsmethoden; 3D printers) bieden de mogelijkheid om snel voorwerpen te produceren, zonder geometrische beperkingen. Varianten van het volgende poedermetallurgisch (PM) proces, dat gebruik maakt van deze productietechniek als vormgevingsproces, zijn onderzocht om keramische voorwerpen te vervaardigen: (i) poeder productie, (ii) additief vervaardigen, (iii) wegbranden van bindermateriaal en (iv) ovensinteren. In deze studie werd gekozen om alumina (Al_2O_3) voorwerpen te produceren, aangezien dit het meest gebruikte keramische materiaal voor technische toepassingen is. Verder zijn er twee materiaal toevoegende productietechnieken onderzocht als mogelijke vormgevingsprocessen voor het produceren van alumina voorwerpen: indirect Selectief Laser Sintering (indirect SLS) en direct Selectief Laser Sinteren/Smelten (direct SLS/SLM).

Voor het onderzoek naar indirect SLS werden verschillende poeders met een deeltjesgrootte van 10-100 μm en bestaande uit alumina en een polymeer bindermateriaal (ook alumina-binder composiet agglomeraten genoemd), bestraald met een laser. Vijf verschillende alumina-binder agglomeraten zijn onderzocht: alumina-polyamide geproduceerd in een kogelmolen, alumina-polystyreen geproduceerd via dispersie polymerisatie en alumina-polyamide, alumina-polypropyleen en alumina-carnauba_was-lage_dichtheid_polyethyleen geproduceerd via temperatuur geïnduceerd scheiden van fasen. Laagsgewijs versmolten de laserstralen, die enkel de binder smolten, de poeder agglomeraten op selectieve wijze. Na het achtereenvolgens wegbranden van het bindermateriaal en ovensinteren, werden alumina voorwerpen verkregen. Deze voorwerpen bevatten echter poriën tussen de gesinterde poederagglomeraten. Met als doel deze poriën te verminderen, is de mogelijkheid onderzocht om volgende stappen in het PM proces te introduceren: (i) de poederlagen meermaals i.p.v. slechts één maal bestralen met een laser (d.i. hersmelten), (ii) koud, quasi en warm isostatisch persen van de voorwerpen na SLS en (iii) infiltreren van de stukken bekomen in verschillende stadia van het PM proces. Op deze manier werden

reeds alumina voorwerpen met een complexe geometrie en een densiteit van ongeveer 90% verkregen. Om nog hoogwaardigere keramische voorwerpen via indirect SLS te produceren, zouden de poriën tussen de poederagglomeraten ofwel vermeden of wel helemaal weggewerkt moeten worden.

Voor het onderzoek naar direct SLS/SLM werd een experimentele opstelling ontwikkeld. De experimentele opstelling liet toe om laagjes alumina poeder met een deeltjesgrootte van ongeveer 0.3 μm en zonder binder, te verwarmen tot een uniforme temperatuur van 800°C en selectief te bestralen. Na ovensinteren werden op deze manier alumina stukken met een korrelgrootte kleiner dan 5 μm verkregen. Om hoogwaardige keramische voorwerpen te produceren via direct SLS/SLM, zou de betrouwbaarheid van de experimentele opstelling moeten verbeterd worden door de poederlagen: (i) homogeneen te deponeren, (ii) homogeneen te verwarmen tijdens het selectief consolideren en (iii) homogeen voor te verwarmen.

List of abbreviations

3DFD	Three-dimensional Fiber Deposition
3DP	Three-dimensional Printing
A-IJP	Aqueous Inkjet Printing
AJP	Aerosol Jet Printing
AM	Additive Manufacturing
BSE-SEM	Backscattered electron scanning electron microscopy
CAM-LEM	Computer-Aided Manufacturing of Laminated Engineering Materials
carn.	Carnauba wax
CerSLA	Ceramic Stereolithography
CIB	Chemically Induced Binding
CIJ	Continuous Inkjet
CIP	(wet bag) cold isostatic pressing
CLF	Ceramic Laser Fusion
CLG	Ceramic Laser Gelling
CMM	Coordinate measuring machine
$\text{cracks}_{deb+SSS}$	Cracking during debinding and solid state sintering: yes/no
CSL	Ceramic Stereolithography
deb.	Debinding
direct SLS/SLM	Direct Selective Laser Sintering/Melting
disp. polym.	Dispersion polymerization
DLP	Digital Light Processing
DMSO	Dimethyl sulfoxide
DOD	Drop-On-Demand
DP	Direct printing
DSC	Differential scanning calorimetry

DSC-TGA	Thermal analysis: simultaneous application of DSC and TGA
EBM	Electron Beam Melting
EDX	Energy-Dispersive X-ray spectroscopy
EFF	Extrusion Freeforming
ENISE	Ecole Nationale d' Ingénieurs de Saint-Etienne
EP	Electrophotographic printing
EPD	Electrophoretic deposition
FDC	Fused Deposition of Ceramics
FDM	Fused Deposition Modeling
FS	Furnace sintering
FTIR	Fourier transform infrared spectroscopy
gr. inf.	Green infiltration
GRIN	Gradient Index
HAS	Hydrolysis assisted solidification
HIP	Hot isostatic pressing
HVC	High velocity compaction
IC	Investment casting
IJP	(direct) Inkjet Printing
inf.	Infiltration
IP	Isostatic pressing
KU Leuven	Catholic University of Leuven (English); Katholieke Universiteit Leuven (Dutch)
LAMP	Large Area Maskless Photopolymerization
LDPE	Low density polyethylene
LCM	Lithography based Ceramic Manufacturing
LENS	Laser Engineered Net Shaping
LOM	Laminated Object Manufacturing
LPIM	Low pressure powder injection molding
MCR	Material consolidation rate
MFI	Mold flow index
MJS	Multiphase Jet Solidification
NIR	Near Infrared
PA	Polyamide
PA12	Polyamide 12
P-3DP	3DP of dry powder agglomerates
PAA	Polyacrylic Acid
p-inf.	Pressure infiltration
PM	Powder metallurgy
PMMA	Polymethyl Methacrylate
PP	Polypropylene
pre-sint.	Pre-sintering

PS	Polystyrene
PVA	Polyvinyl Alcohol
PVA(BC)	Sub-partially hydrolyzed PVA
PVA(BF)	Fully hydrolyzed PVA
PZT	Lead Zirconium Titanate
QIP	Quasi isostatic pressing
S-3DP	Slurry based 3DP
SEM	Scanning electron microscopy
SE-SEM	Secondary electron scanning electron microscopy
SL(A)	Stereolithography
SLM	Selective Laser Melting
SLPP	Selective Laser Powder Processing
SLPP-SLA	Powder based SLA
SLRS	Selective Laser Reaction Sintering
SLS	Selective Laser Sintering
SSS	Solid state sintering
SSS infiltration	Infiltration after solid state sintering
SSS part	Solid state sintered part
susp.	Suspension
TCP	Tricalcium-Phosphate
TD	Theoretical density
TGA	Thermogravimetrical analysis
TIPS	Temperature induced phase separation, also thermally induced phase separation. $TIPS_1$ and $TIPS_2$ refer to the TIPS powder synthesis processes respectively without and with additional cake formation and ball milling steps.
UV	Ultraviolet
UV-IJP	UV based Inkjet Printing
vac. inf.	Vacuum infiltration
vol%	Volume percentage
vol% binder	The volume binder material in the SLSed part, relative to the 'internal' volume (i.e. not including pores) of the SLSed material.
vol% inf.	The volume (dry) infiltrant material which entered the part during subsequent infiltration steps (after SLS, pre-sintering and/or SSS), relative to the 'internal' volume (i.e. not including pores) of the SLSed material.
vol% shrinkage	The 'external' volume (i.e. including the pores) of the part after solid state sintering, relative to the 'external' volume of the SLSed part.

W-IJP	Wax based Inkjet Printing
WIP	Warm isostatic pressing
wt%	Weight percentage
XRD	X-ray diffraction
YSZ	Yttria-Stabilized Zirconia

List of symbols

Symbol	Unit	Description
$\%vol$	–	volume percentage
$\%wt$	–	weight percentage
δ_c	m	cure depth (i.e. polymerized thickness)
Δweight	–	increase of weight percentage
$\Delta_{x-y}^{e=e*}$	–	% linear shrinkage during debinding and SSS in the scan x and cross-scan y directions, for parts SLSed with an optimized laser energy density
$\Delta_{z}^{e=e*}$	–	% linear shrinkage during debinding and SSS in the z direction, for parts SLSed with an optimized laser energy density
$\dot{\epsilon}$	s^{-1}	strain rate
ϕ	–	the volume fraction of a ceramic powder in a suspension
ϕ_0	–	the volume fraction of a close-packed ceramic powder
ϕ_{1/e^2}	μm	spot size of a Gaussian laser beam: at the focus of the laser, 1-1/e^2% (i.e. 86.5 %) of the laser power is passing through a circle of this diameter
γ_{GB}	J/m^2	surface energy of a grain boundary
γ_{SV}	J/m^2	surface energy of a pore
η	$N/s.m^2$	the viscosity of a suspension
$[\eta]$	–	intrinsic viscosity (i.e. a shape factor)
η_0	$N/s.m^2$	the viscosity of the medium of a suspension
η_r	–	the relative viscosity of a suspension
μ_e	$cm^2/s.V$	electrophoretic mobility
$\rho_{Al_2O_3}$	g/cm^3	theoretical density of alumina = 3.984 g/cm^3
ρ_{binder}	g/cm^3	the absolute density of the binder material

$\rho_{calc.}$	$-$	calculated relative density
ρ_{CIP}	$-$	relative density after CIP
ρ_{FS}	$-$	relative density after debinding and solid state sintering in a furnace; also called final density
ρ_{IP}	$-$	relative density after IP
$\rho_{inf.}$	g/cm^3	the absolute density of the (dry) infiltrant material
$\rho_{meas.}$	$-$	measured relative density
$\rho_{pre-sint.}$	$-$	relative density after pre-sintering
ρ_{SLS}	$-$	relative density after SLS
$\rho_{SLS}^{e=e*}$	$-$	relative density after SLS, for parts produced with optimized laser energy density
$\rho_{SLS,a}$	g/cm^3	absolute density of a part after selective laser sintering
ρ_{SLSmax}	g/cm^3	the maximal possible absolute density of a part after selective laser sintering: i.e. the density of an SLSed part without pores
$\rho_{SSS}^{e=e*}$	$-$	relative density after SSS, for parts produced with optimized laser energy density
$\rho_{SSS,a}$	g/cm^3	absolute density of a part after solid state sintering
A_{GB}	m^2	grain boundary surface
A_{SV}	m^2	vapor-solid surface
D_p	m	penetration sensitivity of a laser beam (i.e. the distance at which the laser intensity is reduced by 1/e)
C_s	g/cm^3	suspension concentration
d	cm	distance between the two EPD electrodes
e	J/mm^3	laser energy density
e^*	J/mm^3	optimized laser energy density
$e_{\rho_{SLS}}^{max}$	J/mm^3	the laser energy density which led to the maximum green density after SLS
E_c	J/m^2	critical energy of photopolymerization (i.e. the minimum energy necessary to trigger the curing process)
E_i	J/m^2	energy density
F	J/m^2	fluence (i.e. the laser energy irradiating the powder surface)
G	m	Gibbs free energy of a system
l	μm	layer thickness
m	g	mass

m_{binder}	g	mass of the binder material present inside an SLSed part
$m_{inf.}$	g	mass of the (dry) infiltrant added during infiltration
m_{SLS}	g	mass of a part after selective laser sintering
m_{SSS}	g	mass of a part after solid state sintering
p	Pa	pressure
p_a	Pa	applied pressure during infiltration
p_c	Pa	capillary pressure during infiltration
p_d	Pa	total driving force for infiltration
p_{ext}	Pa	externally applied pressure
p_i	Pa	internal pressure of compressed air during infiltration
$p_{sintering}$	Pa	sintering pressure
P	W	laser power
s	μm	scan spacing
S	cm^2	size of the deposition surface during EPD
t	s	time
T_{oc}	°C	crystallization onset temperature
T_g	°C	glass transition temperature
T_m	°C	melting temperature
T_{om}	°C	melting onset temperature
U	V	voltage
V	m^3	volume
v	mm/s	scan speed (scan velocity)
$\overline{Z}$	$-$	weight averaged atomic number

Contents

List of Figures

List of Tables

Chapter 1

Literature review: AM techniques to shape ceramic parts

> In January, 1915, Lieut. Col. E.B. Cope, engineer of the commission, was authorized to prepare drawings from previous surveys and to enlarge them into... one large topographical map and with this as a basis to construct a relief map of the cavalry battle field of Gettysburg... The material is pine boards, one sixth inch thick, cut to the shapes of the contours and built up, glued and pinned together, layer upon layer...
>
> a 1915 report by the Gettysburg National Military Park Commission [1, 35]

This chapter gives a general overview of the different additive manufacturing (AM) processes, described in scientific literature, to produce ceramic parts. It will be used as input for chapter 2, to specify the research outline and

concomitant research strategy of the dissertation, which is about the production of ceramic parts through AM.

Williams et al. [224, 225] have created a functional classification framework for the conceptual design of AM technologies. This framework can be used to classify current and future AM technologies. Inspired by the work of Williams et al., figure 1.1 classifies the most common AM technologies which can shape ceramic components not as function of the conceptual design, but as function of the mechanical design. The aim is to gain insight in the process behavior of ceramic powders during additive shaping. The following technologies can be differentiated.

- Direct printing (DP) technologies use AM machines where only the printing head deposits the ceramic powder particles.
- Laminated Object Manufacturing (LOM) technologies use AM machines which consist of a cutting device and a sheet deposition system.
- Three-dimensional Printing (3DP) technologies use AM machines which consist of a printing head and a powder deposition device.
- Selective Laser Powder Processing (SLPP) technologies use AM machines which consist of a laser and a powder deposition system.

DP	LOM	3DP	SLPP
IJP	traditional LOM	P-3DP	SLM
AJP	CAM-LEM	S-3DP	SLS
EPD			SLPP-SLA
EP			
LENS			
FDC			
FDM-LENS			
Robocasting			

Figure 1.1: Classification of AM technologies to shape ceramic components.

1.1 Direct printing (DP)

The AM technologies where only a printing head deposits the ceramic powder particles are the direct-printing or direct-write technologies. The main direct-printing methods which can be used to shape macroscopic ceramic parts are:

1.1.1 (Direct) inkjet printing (IJP)

A suspension containing ceramic powder particles is deposited (directly) from a print nozzle. The print nozzle selectively deposits individual droplets of the suspension onto a substrate. The droplets undergo a phase change upon contact and thus create a solid part. Depending on the nature of the phase change, different sub-technologies can be distinguished: in aqueous IJP (A-IJP) a dilute ceramic suspension evaporates, in hot-melt IJP (W-IJP) a molten droplet (typically paraffin wax based, thus W-IJP) which contains ceramic powder solidifies, in UV-IJP a ceramic containing UV curable polymer droplet (i.e. a photopolymer droplet) hardens under UV light [224]. Two different working principles exist to deliver the droplet during A-IJP, which is the most commonly used IJP system: continuous and drop-on-demand. Continuous inkjet (CIJ, figure 1.2a) technology is based on inducing an electrical charge to the liquid by ejecting a jet of conductive ink from an orifice through an external electric field. After the jet breaks up into isolated droplets, the charge remains on the droplets and can be used to deflect them either toward the substrate or into an ink collection and recirculation system. In the drop-on-demand (DOD, figure 1.2b) inkjet technology, ink droplets are formed only when required. As well piezoelectric as thermal DOD inkjet technology exists. In a piezoelectric DOD inkjet printer, a voltage pulse is applied to a piezoelectric stack or plate, which generates a pressure wave to form the droplet [188]. When using a thermal DOD inkjet printer, a current pulse is passed through a heating element located inside the printing cartridge. This causes a rapid vaporization of the ink to form a bubble, which causes a large pressure increase, propelling a droplet of ink. RWTH Aachen University has been able to produce zirconia parts [67, 162] by using a thermal DOD A-IJP device. Small zirconia specimens (3mm x 4mm x 0.3μm and 2mm x 2mm x 0.3μm) with uniform microstructure as well as a full density have been achieved after sintering. The inkjet printed materials have revealed high mechanical reliability (Weibull modulus = 10 for σ_0=1400MPa) [162].

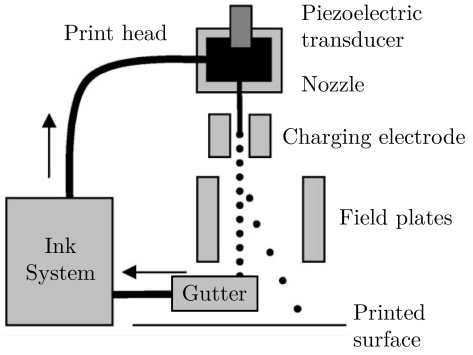

(a) Schematic illustration of the principle of operation of a continuous inkjet system.

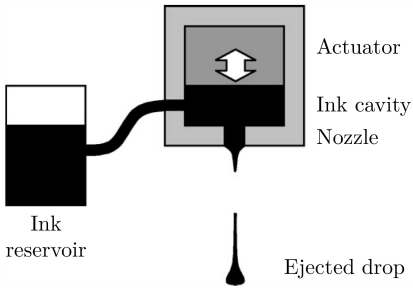

(b) Schematic illustration of the principle of operation of a drop-on-demand printhead.

Figure 1.2: (Direct) inkjet printing [100]

1.1.2 Aerosol jet printing (AJP)

Instead of using individual liquid ink droplets as printing media, an aerosol jet printer uses a focused aerosol, i.e. a suspension of fine ceramic particle containing droplets in a gas. The printing operation consists of three steps (figure 1.3). Firstly, the liquid material is placed into an atomizer, creating a dense aerosol of ceramic particle containing micro-droplets. Secondly, the aerosol is carried by a N_2 gas flow to the deposition head. Finally, within the aerosol head, the aerosol is aerodynamically focused using a flow guidance deposition head, which creates an annular flow of sheath gas to collimate the aerosol [100]. By using ink suspensions of NiO and yttria-stabilized zirconia (YSZ), aerosol jet printers allow to print functionally graded materials which can be used to produce fuel cells [196].

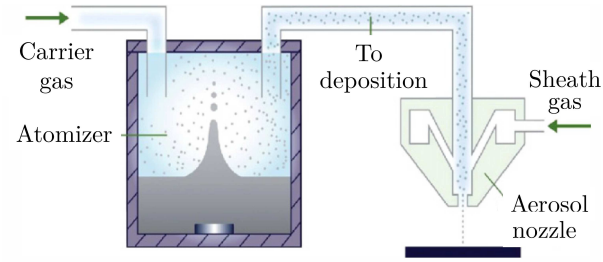

Figure 1.3: Schematic of an aerosol jet printer [100].

1.1.3 Electrophoretic deposition (EPD)

Electrophoretic deposition is a suspension-based process for shaping ceramics. A characteristic feature of this process is that charge carrying colloidal particles suspended in a liquid medium migrate under the influence of an electric field (electrophoresis) and are deposited. By using water as deposition medium, the highest green densities can be achieved and the deposition rate is increased due to the high permittivity of water. If the applied voltage lies above the decomposition voltage of water (typically 1.24 V) [159], problems arise with the formation of gas bubbles (O_2 and H_2) at the electrodes during EPD of aqueous suspensions. In that case, the following chemical reactions occur

Anode: $2\,H_2O \longrightarrow O_2(gas) + 4\,H^+ + 4\,e^-$

Cathode: $4\,H_2O + 4\,e^- \longrightarrow 4\,OH^- + 2\,H_2(gas)$

As gas bubbles are incorporated into the deposited compacts leading to unacceptable holes, they have to be avoided [159]. The membrane method is one possible solution for the gas bubble problem in aqueous suspensions [61]. The cell in which EPD is carried out, is subdivided into 2 chambers by an ion-permeable membrane. The deposition takes place on the membrane so that gas formation and forming of green body are locally separate. At the University of Saarland, Nold et al. [157] adapted the membrane method to enable the production of freeform geometries. Two cathodes and two anodes were mounted whereas the major ones (see figure 1.4) controlled the deposition. Two different setups were demonstrated. In one setup, the two major electrodes were simultaneously controlled by a CAM unit. The second setup was arranging 16 independent electrodes in a 4x4 array in order to parallelize deposition.

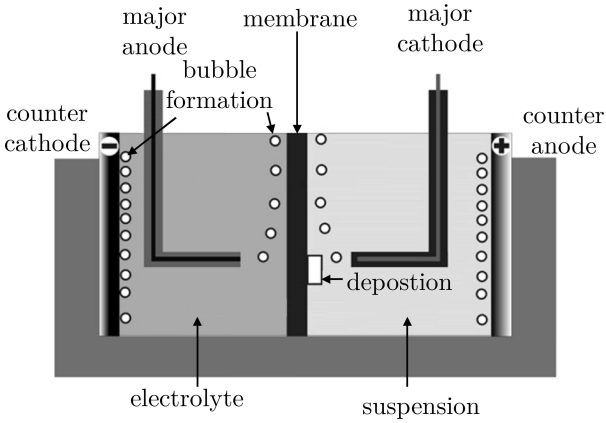

Figure 1.4: EPD cell, major anode and cathode were moved by the CAM unit [157].

1.1.4 Electrophotographic printing (EP)

Electrophotographic printing is an AM process which is capable of patterning 2D powder layers of material at once. The patterning working principle employed by EP is very similar to that seen in photo-copying (figure 1.5). A photoreceptor plate or drum is charged to a specific charge density via a corona device. An electrostatic image of the part layer is created on the photoreceptor by light exposure, using a computer controlled LED printer head. The photoreceptor is aligned over the powder bed where the electrostatic charge causes the powder to be attracted to the plate in the exact shape of the part layer. The layer of powder is then deposited. Overhanging structures are created by the selective deposition of a secondary support powder. The printed layers are then compacted and sintered via an appropriate method (e.g. electric contact sintering, plasma-activated sintering, or microwave sintering). Despite some concerns are formulated which indicate that the production of ceramic parts through the EP process is very difficult, preliminary successes with alumina and silicon nitride have been reported [224].

1.1.5 Laser engineered net shaping (LENS)

In literature, laser engineered net shaping (LENS) is also widely known as laser cladding. The printing head of a LENS system consists of a nozzle which feeds powder particles to the focal point of a laser beam (figure 1.6). The powder melts and solidifies on a substrate. In this way WC-Co hard metal

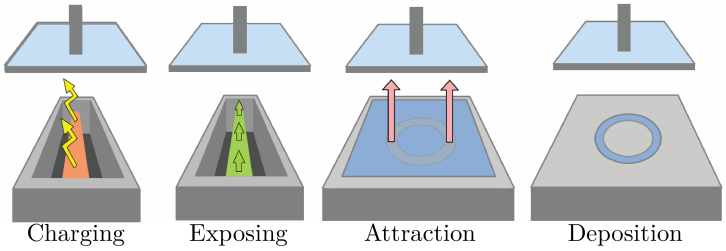

Figure 1.5: Electrophotographic printing: a schematic illustration of the process steps during layer fabrication [213].

parts with a density of 97% could be produced [228]. Also alumina ceramics with a density of 98% could be obtained. However, due to the melting of the alumina powder, grain sizes of about 200 μm were observed, compromising the mechanical properties [20].

1.1.6 Fused deposition of ceramics (FDC)

During the fused deposition modeling (FDM) process, the building material, which is in the form of a flexible filament, is partially melted and extruded from a moving deposition head onto the static worktable. In this way, a three-dimensional part can be produced layer by layer. During fused deposition of ceramics (FDC), also called multiphase jet solidification (MJS) or extrusion freeforming (EFF) [86], the ceramic particles are first densely (up to 60vol%)

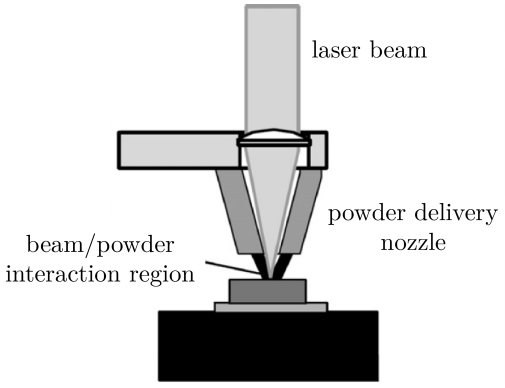

Figure 1.6: Principle of powder deposition during the LENS process [228].

loaded into the thermoplastic (or wax) filament. In this way, the FDM equipment is utilized to produce green parts. Afterwards, binder burnout and sintering processes are needed to obtain the desired part in fully dense form [231]. Amongst others, the following ceramic materials are already reported: alumina, zirconia, lead zirconium titanate (PZT), silicon nitride, graphite [86, 214].

1.1.7 FDM-LENS

At the university of Birmingham, Wang et al. managed to combine the FDM and the LENS process into a hybrid process. Ti-6Al-4V-TiC composite parts could be fabricated by feeding powder (TiC) and wire (Ti-6Al-4V) material into the focus of a CO_2 laser [217].

1.1.8 Robocasting

The robocasting technique, also known as three-dimensional fiber deposition (3DFD, [128]) or Micropen [107], integrates the advantages of colloidal processing of ceramics in an AM process. In robocasting, a concentrated sol is extruded through a nozzle to form a filament that is directly deposited in a controlled pattern to assemble complex, 3-D structures in a layer-by-layer sequence [32]. The process has been demonstrated on a wide variety of ceramic materials, like β-tricalcium phosphate [150], silicon nitride [30] and silicon carbide [32].
Robocasting technologies use various solidification methods. These include coagulation of oppositely charged colloids, coagulation solutions, freezing, or sol-gel transition. More recently, new technologies which employ direct UV illumination for solidification of continuous filaments have emerged [51]. In this way, hydroxyapatite filaments could be produced (figure 1.7).

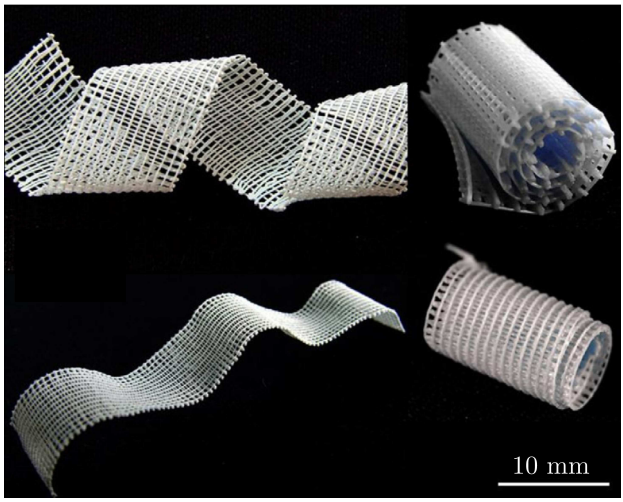

Figure 1.7: Sintered bent and folded/rolled hydroxyapatite structures [51].

1.2 Laminated object manufacturing (LOM)

The main AM technologies which consist of a cutting device and a sheet deposition system are the laminated object manufacturing (LOM) technologies. Basically, two LOM technologies can be differentiated: traditional LOM and Computer-Aided Manufacturing of Laminated Engineering Materials (CAM-LEM).

1.2.1 Traditional LOM

The tradition LOM process consist of a system which deposits green ceramic tape casted layers. These layers are unrolled onto the working bed where a CO_2 laser cuts the outline of each layer of the part. A heated roller is passed over the layer to thermally activate the tape's binder system and to laminate the sheet to the previous layer [224]. The high ceramic powder load in the casted tapes (>40 wt%) requires the use of an adhesive agent, such as double-side adhesive tape or a diluted binder solution, to promote the interconnection between the adjacent tapes. The boundary between the tapes should be undetectable after compression by the roller. After debinding and sintering in a furnace, the final ceramic (e.g. alumina and silica [14], or glass-ceramic [84]) parts are obtained.

1.2.2 CAM-LEM

Another embodiment of this process is the CAM-LEM method. This process is identical to that of LOM, but instead of stacking the layers and then cutting them, each layer is pre-cut and then robotically stacked onto the working part for lamination. This method has some advantages over traditional LOM, e.g. internal voids within each layer can be easily produced [224]. As is the case for the traditional LOM process, also the CAM-LEM process uses ceramic tapes, which have a well-established manufacturing history. Therefore, almost any ceramic material can be processed: e.g. alumina, silicon nitride and graphite [138].

1.3 Three-dimensional printing (3DP)

The AM machines which consist of a printing head and a powder deposition device are called three-dimensional printers. A 3DP device can shape ceramic components by first depositing a layer of ceramic powder and then depositing a binder material to selectively bind the ceramic powder [179]. Generally, two different 3DP methods can be distinguished.

1.3.1 3DP of dry powder agglomerates (P-3DP)

This method is the traditional method to produce ceramic parts through 3D printing. Sequential depositing of powder particles with a roller or scraper system and printing of binder material by ink-jet printing, yields the layers and results in a solid part. After binder burnout and final sintering, the ceramic part is obtained. Some examples of ceramic parts produced by this method can be found on the following website: [4].
At the Massachusetts Institute of Technology, Yoo et al. could produce alumina components with a density greater than 99.2% [243] and average flexural strength of 324 MPa through P-3DP. Prior to printing, a press-rolling system and the addition of moisture (to avoid powder expel during binder deposition) was used to deposit MgO doped alumina agglomerates with a size between 75μm and 150μm. The agglomerates were obtained through sieving as received alumina powder (Reynolds RC172-DBM) with a mean primary particle size of 0.8μm. The binder used for the study was Acrysol WS-24 (Rohm and Haas Company, Philadelphia, PA) wich is an acrylic copolymer dispersion resin.
After the production process, the piston holding the deposited powder and binded material was removed and heated at 125°C for one hour to remove water

from the bed and cure the binder. The printed parts were then separated from the unprinted region. The density of the printed green samples was 33%-36%. In order to increase the green density before debinding and furnace sintering, the green samples were isostatically pressed (both densification through cold isostatic pressing CIP as warm isostatic pressing WIP were investigated). This caused the ceramic powder agglomerates to collapse.

1.3.2 Slurry based three-dimensional printing (S-3DP)

In order to be able to process fine powders ($< 20\ \mu$m) and improve the furnace sintering characteristics of the green part, research of ceramic 3DP shifted away from working with dry powders to working with a slurry-based material (S-3DP, [224]). During S-3DP, each powder bed layer is created by jetting a ceramic slurry onto a substrate. The as-cast layer is then dried and a binder, which cements the ceramic particles, is selectively deposited in the desired pattern. As an example, the S-3DP process has been used to fabricate functional graded materials, such as gradient index (GRIN) lenses, by depositing different concentrations of dopant instead of a binder into each layer at selective positions. In order to do so, aluminum nitrate was dissolved in deionized water and inkjet printed into the silica powder bed as the source of dopant. During heat treatment, aluminum nitride decomposed into alumina (boehmite), which acted as a binder, and ammonia [218] according to the following hydrolyzation reaction.

$$\mathrm{AlN(aluminumnitride)} + 2\,\mathrm{H_2O(water)} \longrightarrow \mathrm{AlOOH(boehmite)} + \mathrm{NH_3(ammonia)}$$

In the domain of colloidal processing, the thermally activated and accelerated hydrolysis of an aluminum nitride, added to a highly concentrated ceramic suspension is known as an example of hydrolysis assisted solidification (HAS).

1.4 Selective laser powder processing (SLPP) techniques to shape ceramic parts

The AM technologies which consist of a laser and a powder deposition system are the selective laser powder processing (SLPP) methods. When a laser irradiates the surface of a solid, the laser energy may be absorbed. The specific mechanisms by which the absorption occurs will depend on the type of material. In general, photons will couple into the available electronic or vibrational states

in the material, depending on the photon energy [195]. For materials containing electrons in the conduction band, the optical absorption is usually dominated by free carrier absorption: electrons in the conduction band absorb photons and gain high energy. In semiconductors, electrons are excited from the occupied valence bands to empty conduction bands, provided that the photon energy exceeds the band gap. In dielectrics with band gaps larger than the photon energy, multiphoton transitions are necessary to promote electrons from the valence band to the conduction band. Multiphoton absorption is a nonlinear process, i.e. the transition probability increases sharply with the laser intensity. After absorption of the laser energy by the electrons, the optical energy is transferred from electrons to phonons [176]. Since phonons can be thought of as lattice vibrations which take discrete energy values in the same way as electrons [103], lattice heating occurs during this energy transfer.
Depending on the material class (i.e. ceramics/glasses, polymers, metals) which is scanned and the wave length of the laser beam, different laser-material interactions occur [103].

- The electrons in ceramics and glasses are ionically or covalently bonded. At room temperature, these materials generally have strong absorption in the infrared region of the energy spectrum, and CO_2 laser radiation is absorbed well. Absorption is generally weak over intermediate wavelengths. E.g.: the absorptivity of alumina at room temperature is 0.90-0.99 % for a wavelength of 10.6 μm (emitted by e.g. a CO_2 laser) and only 0.05-0.1% for a wavelength of 1.06 μm (emitted by e.g. an Nd:YAG laser) [151, 208]. When heating the alumina material, the laser absorptivity for a wavelength of 1.06 μm rises (figure 1.8).

- Absorptivity of far infrared radiation (e.g. a CO_2 laser beam) is high in most polymers. Energy is absorbed at the surface, and transmitted through the polymer by classical heat conduction. Radiation in the range near ultraviolet to near infrared (e.g. Nd:YAG and diode laser wavelengths) is transmitted, unless the polymer contains an absorbing pigment or filler.
  The photon energy of ultraviolet radiation produced by the shorter wavelength excimer lasers is higher than (or similar to) the covalent bond energy of many organic materials. Chemical bonds can therefore be broken.

- The electron cloud in metals and alloys provides a large number of energy levels to which electrons may be promoted when colliding with the photons of a laser beam. In this case, the energy transfer from hot electrons to the initially cold lattice is usually described by the two-temperature model [176]. This model is based on the assumption

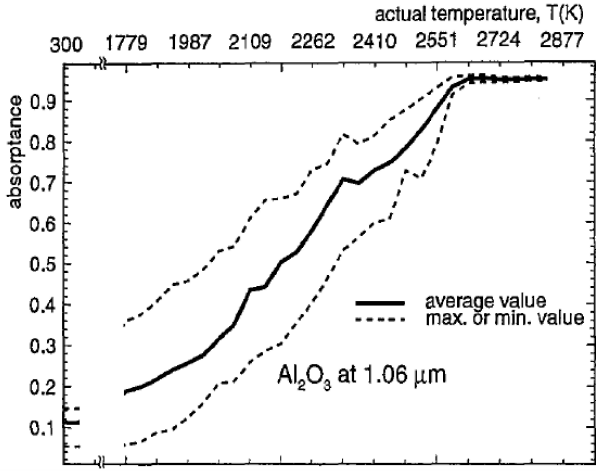

Figure 1.8: Absorptivity of alumina for a 1.05 μm laser beam (Nd:YAG) as function of temperature [222].

that the energy distributions of both electrons and phonons are thermal distributions each characterized by respectively the electron temperature and the lattice temperature.
Processing of metals and alloys is more efficient with short wavelength laser light. Depending on the interaction time and the power density of the laser beam, different laser machining processes can be distinguished (figure 1.9).

It can be concluded that during interaction with the material, the laser beam either causes heating of the material (i.e. a thermal reaction) or causes a chemical reaction[1]. This enables the definition of three SLPP processes which all can be used to produce ceramic shapes.

Selective laser melting (SLM) During selective laser melting (SLM), the laser heats the scanned powder and causes it to fully melt [119].

Selective laser sintering (SLS) During selective laser sintering (SLS), the laser heats the scanned powder but does not cause it to fully melt [119].

[1]In this context, sometimes the terms 'pyrolitic' and 'photolitic' processes are used. In pyrolitic processes, the laser energy is absorbed by heating the material, resulting in a temperature rise, melting or evaporation of the material. Photolitic processes result in photon induced chemical reactions [148].

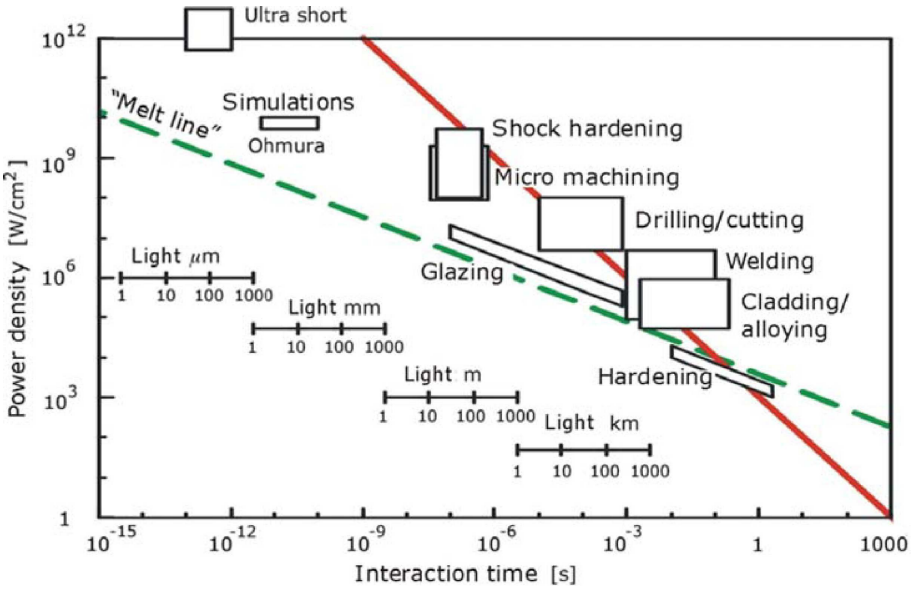

Figure 1.9: Overview of laser machining processes. The 'conventional' laser processes are found around the line of 1 kJ/cm^2. The dotted line indicates the melt boundary of metal [148]. This figure indicates that selective laser sintering (SLS) and melting (SLM) processes can be categorized as welding processes: typical laser-material interaction times and laser power densities (W/cm^2) used during SLS/SLM of metal powders are respectively about 10^{-3}s and 10^6 W/cm^2.

Stereolithography (SLPP-SLA) Stereolithography (SLA, SL) is the AM process where a laser beam causes a chemical reaction which causes the decomposition of photoinitiator molecules. As a result of the decomposition reaction free radicals are created which initiate a polymerization reaction, causing the hardening (i.e. photopolymerization) of liquid monomers and/or oligomers (i.e. a molecular complex that consists of a few monomer units). The liquid medium normally does not contain powder particles. However, if the liquid medium is heavily charged with metal or ceramic powder particles, metal or ceramic parts can be produced after a debinding and furnace sintering step. In this dissertation, the specific SLA process where a UV hardened polymer acts as binder between powder particles, will be denoted as the powder based SLA process (SLPP-SLA).

This section further describes how the SLPP process can be used to shape ceramics. The section is inspired on the work of Kruth et al. [119], who

classified different SLPP processes according to the occurring consolidation mechanism (i.e. binding mechanism). The section also classifies the SLPP processes to produce ceramics by differentiating according to the used powder deposition system.

1.4.1 Selective laser melting (SLM)

During SLM of ceramics, the laser-beam causes the irradiated ceramic powder material to heat and fully melt. In literature, three different layer deposition systems can be distinguished to SLM ceramics: conventional deposition systems, slurry based deposition systems and aerosol assisted spray deposition (figure 1.10).

Conventional deposition system This SLM method is thoroughly investigated at the Fraunhofer Institute of Laser Technology (ILT) in Aachen together with TNO Eindhoven. During initial research, porous silica-tricalcium-phosphate (silica-TCP, [223]) and micro-crack containing zirconia [221, 223] parts were produced by using a CO_2 laser. In order to reduce the micro-cracks which were caused by thermal gradients, a high temperature preheating system was developed. As depicted in figure 1.11a, a CO_2 laser was used to preheat the powder layers (temperature controlled by a pyrometer) prior to scanning with an Nd:YAG laser. As can be seen in figure 1.8, alumina absorbed Nd:YAG laser radiation at higher temperatures.
Although it was not possible to produce yttria stabilized ZrO_2 parts with the developed preheating device, the following ceramic materials could be processed: pure ZrO_2, Al_2O_3 and $MgAl_2O_4$ (spinel). Nevertheless, a large

	SLM		
laser-material interaction	thermal reaction		
binding mechanism	full melting		
powder deposition mechanism	conventional	slurry coater	aerosol assisted spray deposition

Figure 1.10: Classification of different SLM processes to shape ceramic components.

amount of microcracks were present in the parts. It was also concluded that SLM of single phase ceramics, e.g. ZrO_2 and Al_2O_3, resulted in large grained microstructures: as depicted in figure 1.11b, grain sizes of about 100 μm were obtained by SLM of alumina at a preheating temperature of 1850°C, an Yb:YAG laser power of 70 W, scan speed of 200 mm/s, scan spacing (i.e. space between adjacent scan tracks) of 50 μm and layer thickness of 200 μm [222].
In order to SLM ceramics with a fine microstructure (i.e. grain sizes up to 10 μm), an eutectic zirconia-alumina (ZrO_2/Al_2O_3) powder ratio had to be chosen (figure 1.11c). The starting powder was produced through dry mixing of 41.5wt% spherical ZrO_2 powder with 58.5wt% spherical Al_2O_3 powder. The zironia component was partially stabilized by 3 mol% yttria Y_2O_3 (i.e. $Y_{2x}Zr_{1-x}O_{2+x}$ with x=0.03). Both powders, supplied by Innalox bv (Netherlands), had a spherical shape and a monomodalic size distribution of 50μm.
The process parameters for the 41.5wt% ZrO_2 - 58.5wt% Al_2O_3 part produced in figure 1.11d comprised a preheating temperature of 1730°C, a layer thickness of 50 μm, a scanning velocity of 200 mm/s, a laser power of 60 W and a scan spacing of 50 μm. Due to the preheating temperatures close to the melting point of the eutectic powder ratio (1860 °C) a large melt pool evolved, which positively influenced the density of the obtained part. On the other hand, as illustrated in figure 1.11d, a negative influence on the surface quality was examined since the low viscous melt pool exceeded the boundaries of the scanned part and wet the surrounding powder [91, 92, 93].
In order to improve this patented [62, 63] SLM process, the preheating device was modified. As larger specimens with a height > 3 mm could not be processed by the original setup which only heated the powder surface, a bottom up preheating system, using inductive heating technology, was being developed. In addition to the inductive preheating, a selective preheating strategy was being developed. This setup foresaw employment of two laser sources, in which a fiber laser with a focused spot size of $\sim$200 μm was utilized for selective melting while a diode laser-beam was coaxially superpositioned by a dichroidic beam splitter, forming a selective preheating with a focused spot size of $\sim$5 mm [91]. In this way parts with a height up to > 10 mm could be produced [90].

Besides ILT Aachen and TNO Eindhoven, also the AM research group at Ecole Nationale d' Ingénieurs de Saint-Etienne (ENISE) in France attempted to produce ceramic parts through SLM. By using a Phenix PM-100 machine, Shishkovsky et al. [187] reported on SLM of ZrO_2 and alumina-zirconium (Al_2O_3-Zr) parts.

When applying the SLM process, supports need to be generated to anchor

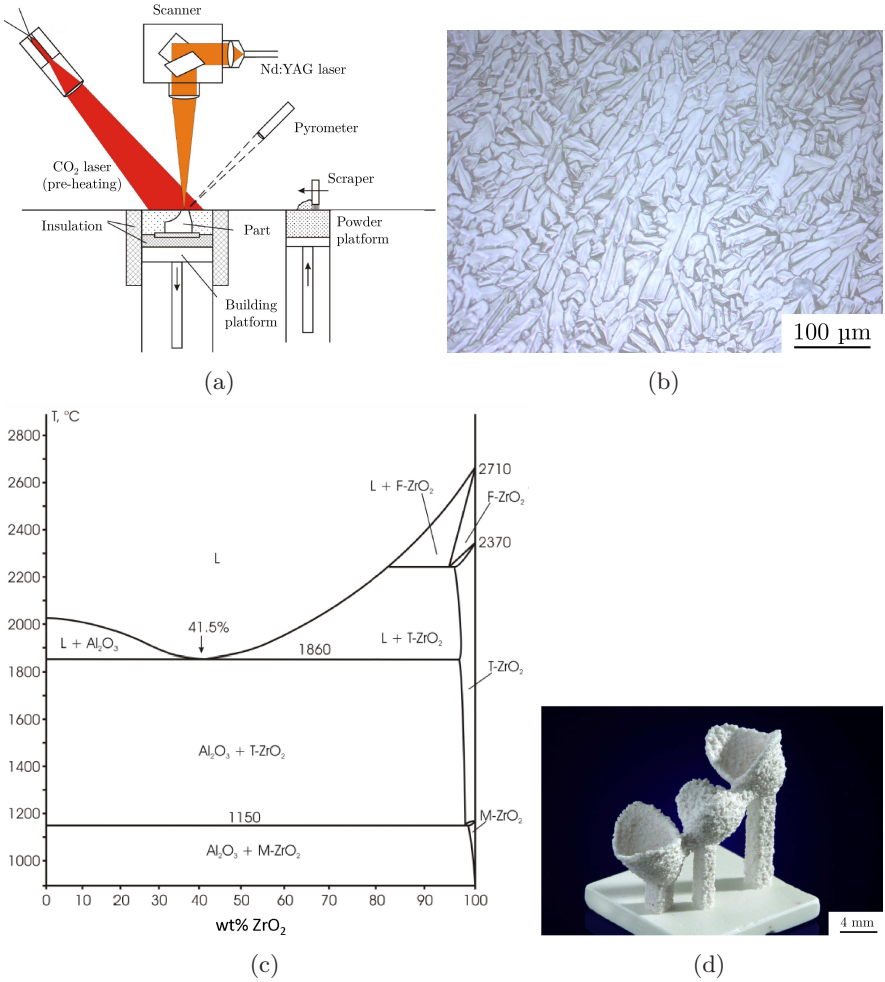

Figure 1.11: SLM by using a preheating system [222]: schematic illustration of an experimental setup for SLM for ceramics using high-temperature CO_2 laser pre-heating (a); light microscope image of molten alumina (b); phase diagram of the system alumina and zirconia (c); dental restoration framework of 41.5wt% ZrO_2 - 58.5wt% Al_2O_3 (d).

the part being produced. In this way, curling of the part due to thermal stresses (caused by laser irradiation) and flowing of the melted material in the underlying powder (i.e. dross formation), can be avoided. Moreover, the SLM process parameters have to be tuned in such a way that a stable melt pool is generated. Instabilities can arise since long thin melt pools are known to break up into balls, called balling. This phenomenon is commonly described as Rayleigh instabilities [119].

Slurry coating At the National Taipei University of Technology in Taiwan, H.H. Tang developed an SLM device which has a slurry coater. In literature the term **ceramic laser fusion (CLF)** is used to depict this technology. SLM in combination with slurry coating is mainly applied to produce silica-clay parts. A slurry of silica and clay is paved by a slurry coater and dried afterwards. The clay is used as an inorganic binder that binds the silica powder during drying. In this way a ceramic green layer substrate is created which can minimize balling and give the part a solid support during building. During laser scanning, the dried layer of silica and clay is fully melted [198, 200, 201, 238].

Aerosol assisted spray deposition Wu et al. [227] applied aerosol assisted spray deposition of a suspension to prepare powder beds for subsequent laser scanning. Alumina suspensions were prepared by adding 5 wt% alumina powder (Alcan Chemicals) to an ethanol solvent (Aldrich, 99.5%) with an optimized content of 0.2wt% of polyacrylic acid (PAA, Aldrich, M_w 2000) as an effective dispersant. During the laser irradiation of the alumina powder beds, the PAA evaporated and the submicrometer sized alumina particles were melted to form a liquid-phase, which facilitated the densification through liquid-phase sintering. With increasing laser energy density, the microstructure of the laser sintered alumina powder beds varied from open/closed pores to a fully densified microstructure (figure 1.12).

1.4.2 Selective laser sintering (SLS)

During SLS of ceramics, the laser beam causes the irradiated ceramic powder material to heat. Instead of fully melting the powder particles, as is the case during SLM, the generated heat can initiate partial melting of the powder particles, solid state sintering of the irradiated powder, a chemical reaction of the powder particles, or a gellation reaction (i.e. the formation of a three-dimensional network that entraps the powder particles). In literature, different layer deposition systems can be distinguished to SLS ceramics (figure 1.13): conventional deposition systems, slurry based deposition systems (i.e. a slurry

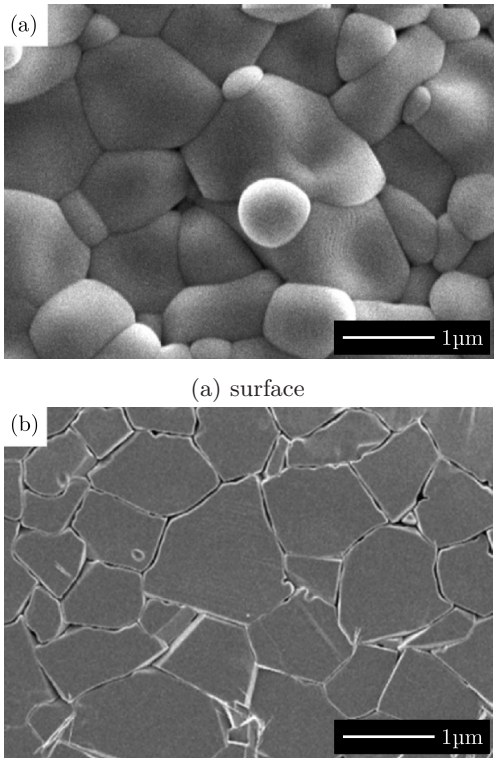

(a) surface

(b) cross-section

Figure 1.12: SEM micrographs of alumina prepared by SLM of aerosol assisted spray deposited layers [227].

coater or sprayer) and a ring blade deposition system (figure 1.14) which can deposit dry submicrometer powder.
SLS of ceramic components can be done directly or indirectly. During indirect SLS, a clear distinction can be made between the binder material and structural material. It involves melting of a sacrificial binder phase, to produce 'green parts', i.e. parts consisting of a binder phase which holds the ceramic particles together. If the binder phase is organic, it is generally removed by thermal debinding in a furnace after the laser sintering step. As a result, a 'brown part[2]' is formed. In a last step, the density and strength of the brown part is improved by furnace sintering and the final part is obtained. Additional post-

[2]In scientific literature, not in this dissertation, the terms green part and brown part are sometimes used interchangeable to denote parts after the shaping process (with or without binder) and after the debinding process.

densification processes like isostatic pressing and/or infiltration can also be used as intermediate steps of the process chain to produce ceramic parts through indirect SLS. Direct SLS comprises no sacrificial binder phase. The ceramic powder mixture is directly melted, solid state sintered, chemically bound or gelled to produce immediately the 'brown' or final parts (see Kruth et al. [119], Dewidar et al. [60]).

	SLS										
laser-material interaction	thermal reaction										
binding mechanism	partial melting						solid state sintering	chemically induced binding			gelling
powder deposition mechanism	conven-tional	slurry coater	slurry sprayer	ring blade	conven-tional	slurry coater	conven-tional	conven-tional	slurry coater	ring blade	slurry coater
indirect/direct	direct				indirect		direct				

Figure 1.13: Classification of different SLS processes to shape ceramic parts.

Figure 1.14: Two ring blades which serve both as powder storage device and a rake to deposit dry submicrometer particles [73].

1.4.2.1 Direct SLS by partial melting

Conventional deposition system At Ecole Nationale d' Ingénieurs de Saint-Etienne (ENISE), Bertrand et al. [24] produced pure zirconia through direct SLS. In order to do so, a Phenix PM-100 machine, equipped with a Nd:YAG laser and a conventional powder deposition system was used. Since the melted powder could not fill all the gaps between the powder particles which were not melted, only low density ceramics could be produced.

At the university of Leeds, Lorrison et al. [140] produced hydroxyapatite - phosphate glass. In this case, the glass acted as structural material as well as binder to glue the hydroxyapatite particles. By using metal as a binder and structural material, Gu and Shen [87] of the Nanjing university of aeronautics and astronautics, produced the ceramic-metal composite WC-10Co/Cu. AM of ceramic containing metal-matrix composites is also investigated through electron beam melting (EBM) [145]. The EBM process is similar to the SLS or SLM process, but an electron beam is used instead of a laser beam during irradiation. EBM of pure ceramic materials is however not thoroughly investigated.

Slurry coating At the Clausthal University of Technology (TU Clausthal) in Germany, a layer-wise slurry deposition (LSD) system has been developed. A powder containing slurry layer is deposited and dried afterwards, as is the case during tape casting. The packing density of the particles, deposited by this system, is much higher compared to the packing density of conventionally deposited particles.
Through SLS of the slurry coated layers, hydroxyapatite [96], porcelain [205, 206, 207] and alumina-silica [80, 97] parts were successfully produced at TU Clausthal (figure 1.15). The produced parts however still contained open porosity. As an example, after the SLS process alumina-silica parts could be obtained with densities of 86-92%. Subsequent thermal post treatment in air in a conventional sintering furnace led to additional phase reactions and caused an increase of density to about 96%.

At the National Taipei University of Technology in Taiwan, Hsiao-Chuan Yen deposited slurry layers which consisted of silica particles, silica sol and polyvinyl alcohol (PVA). During drying, PVA and silica gel could bind silica particles and a uniform gelled layer was formed. During SLS, the PVA degraded and a cristobalite silica part was produced [239].

(a) Parts after SLS

(b) Parts after post-sintering in a furnace.

Figure 1.15: Porcelain parts produced through layer-wise slurry deposition and SLS [206].

Slurry spraying At the Fraunhofer Institute of Production Technology (IPT) in Aken, Klocke et al. [110] produced yttria stabilized zirconia through direct SLS. High density powder layers were formed by spraying (instead of layer deposition) a ceramic suspension before the drying step. As depicted in the right part of figure 1.16, the SLSed layers contained cracks which were caused by contraction during cooling after laser irradiation. The amount of open porosity in the final parts was 24-32%. Despite the high packing density of the deposited layers, the melted powder could not fill all the gaps between the powder particles which were not melted.

Ring blade In 2002, the Laserinstitut der Hochschule Mittweida (LHM) developed the micro SLS process, which is able to produce accurately ceramic parts [75, 164, 170]. The process has been internationally patented in 2004 [68]. It consists of a ring blade (also called 'powder rack'), which is able to deposit dry submicrometer powder particles which are not agglomerated. A compacting system can be used to increase the packing density of the deposited layers and as a result of the fabricated parts [192]. A near-infrared (NIR) laser is used to partially melt the deposited powder particles. In order to control and prevent overheating of the scanned material, the laser is mostly used in a pulsed (q-switched pulses of about 20 ns) instead of continuous mode [173]. Both metal and ceramic parts can be produced through this process. As illustrated in figure 1.17, the powder deposition system enables the production of parts which consist of segments of two different materials (e.g. Cu and Ag).

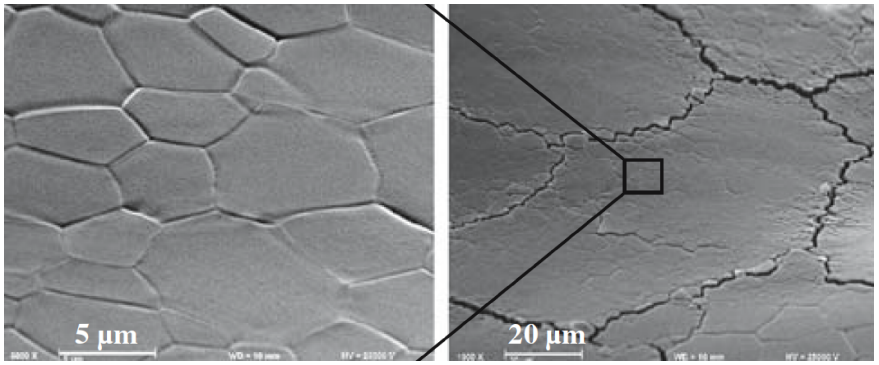

Figure 1.16: Grains (left) of a crack containing (right) zirconia surface after direct laser scanning a slurry sprayed layer after drying [110].

Partial melting submicrometer powders by using the micro SLS device has been applied to the following ceramic materials: alumina (figure 1.18 [11]), alumina-feldspar [74], alumina-silica [171, 173, 174, 175], feldspar [173] and silicon/silicon carbide/carbon (Si-SiC-C, [72, 73, 172, 173, 174, 175, 193]). If no powder compaction device is used and except for powder blends from both, one refractory metal and another metal with a low melting point such as tungsten and aluminum, the resulting sintered bodies have an average density of about 60%. When using the compacting system, relative densities above 95% can be realized [175, 192].

1.4.2.2 Indirect SLS by partial melting

A method for producing high temperature parts by low temperature selective laser sintering was patented in 1993 [21]. Ever since, this method is vastly studied at different universities.

Conventional deposition system A conventional SLS machine is used to selectively sinter composite powders, which consist of ceramic particles and sacrificial binder material. During SLS, the binder phase melts and glues the ceramic particles together. After a furnace cycle, the binder material is usually burned and a ceramic part is obtained. As depicted in figure 1.19, many different ceramics are already produced through this process: a.o. Al_2O_3 [139, 194], Al_2O_3-B_2O_3 [123], Al_2O_3-glass-B_2O_3 [122], Al_2O_3-ZrO_2-TiC [19], apatite-mullite [85], graphite [37], K_2O-Al_2O_3-SiO_2 [136], SiO_2 [14], SiC,

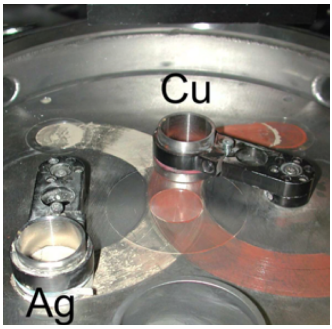

(a) Automatic change of powders during laser micro sintering.

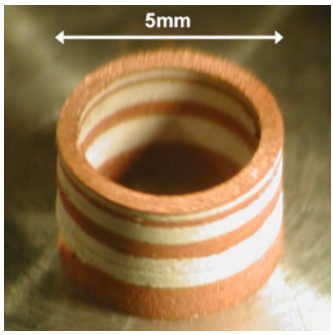

(b) Cylinder with alternating segments of copper and silver (wall thickness: 500 μm).

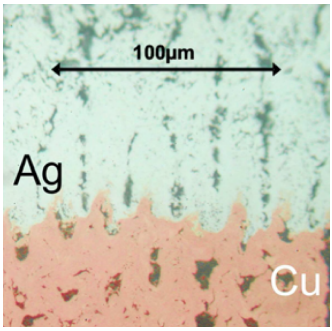

(c) Fusion zone between a sintered copper and the succeeding silver segment.

Figure 1.17: Micro SLS of a part, consisting of two segments of different materials [172].

[70, 190, 191], ZrO_2 [14] and ZrB_2 [125].

Indirect SLS with the use of a sacrificial binder phase allows to produce crack free green parts, but the 'brown' density, i.e. the density of the green part after debinding and before furnace sintering, is generally low and limited to 50%. If the binder is inorganic, it can not be burned. During the thermal treatment, the inorganic binder (e.g. HBO_2) chemically reacts and becomes part of the structural ceramic (e.g. B_2O_3) [122, 123]. Different types of organic binders have been examined to fabricate ceramic parts via SLS: waxes (e.g. stearic acid [125, 139]), thermosets [14, 70, 136, 190, 191] and thermoplastics [85, 194]. Sometimes, a combination of binders is used: e.g. a thermoset in combination

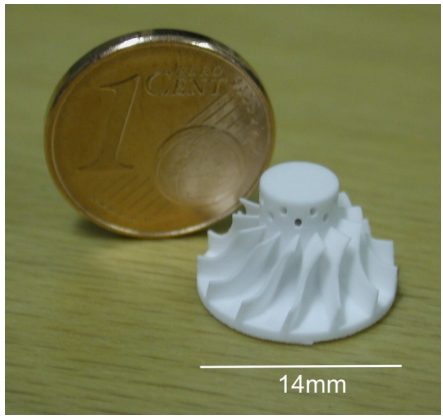

Figure 1.18: Al_2O_3 impeller, produced through micro SLS [11].

		Binder			
		inorganic	organic		
			wax	thermoset	thermoplast
Ceramic	Al_2O_3		stearic		
	Al_2O_3				PMMA
	Al_2O_3-B_2O_3	HBO_2			
	Al_2O_3-glass-B_2O_3	HBO_2			
	Al_2O_3-ZrO_2-TiC		unspecified		PMMA
	Apatite-mullite				unspecified acrylic binder
	Graphite			phenolic resin	nylon 11
	K_2O-Al_2O_3-SiO_2			epoxy resin	
	SiO_2			unspecified	
	SiC			phenolic resin	
	ZrO_2			unspecified	
	ZrB_2		stearic		

Figure 1.19: Sacrificial binders used to produce different ceramic parts using a conventional SLS system.

with semi-crystalline PA-11 (or nylon 11) to produce graphite [37], or a wax in combination with amorphous thermoplast PMMA to produce the composite ceramic Al_2O_3-ZrO_2-TiC [19].

Indirect SLS by partial melting composite agglomerates has been used not only to produce pure ceramics, but also composite ceramics. Gill and Hon [83] investigated SLS of SiC-PA ceramic-polymer composites. Evans et al. [71] infiltrated SiC preforms with molten Si, creating SiC-Si cermets.

Slurry coating At the National Taipei University of Technology in Taiwan, a slurry coating device was used to investigate the indirect production of ceramic parts. Silica parts were produced through the so called ceramic laser sintering (CLS) process [202, 238, 240, 241]. The slurry used in CLS consisted of high melting point silica powder (melting point: ∼1720°C) and silica sol (melting point ∼1700 °C) as a structural material, low melting point clay (melting point: ∼1200°C) as inorganic binder, and water as a solvent. The slurry was deposited and dried. During laser scanning, the clay particles were melted. The melted clay bridged the silica particles to build an interconnective porous structure.
In later experiments, organic polyvinyl alcohol (PVA) was used as binder material to produce alumina parts through slurry-based SLS [203]. Both sub-partially hydrolyzed polyvinyl alcohol PVA(BC) and fully hydrolyzed polyvinyl alcohol PVA(BF) were used as a binder. As depicted in figure 1.20a the submicrometer alumina particles were first coated with the water insoluble PVA(BF). The coated particles and the water soluble PVA(BC) were used to form a water soluble slurry, which was deposited and dried. After laser scanning, the ceramic particles were bound by a PVA(BF)-PVA(BC) mixture that is water insoluble. After thermal debinding and solid state sintering, complex shaped ceramic parts (figure 1.20b) with a homogeneous microstructure, a density of 98% and a mean flexural strength of 363.5 MPa were obtained.

1.4.2.3 Solid state sintering

Conventional deposition system Bertrand et al. [25, 119] of ENISE reported solid state sintering (SSS) as consolidation mechanism during SLS of ceramic materials using the high temperature process chamber of a Phenix PM-100 machine at 900°C. The powder, which was preheated close to the onset temperature of sintering, was sintered due to the extra energy contribution of a Nd:YAG laser source. To obtain the desired characteristics, a post-sintering operation was necessary.

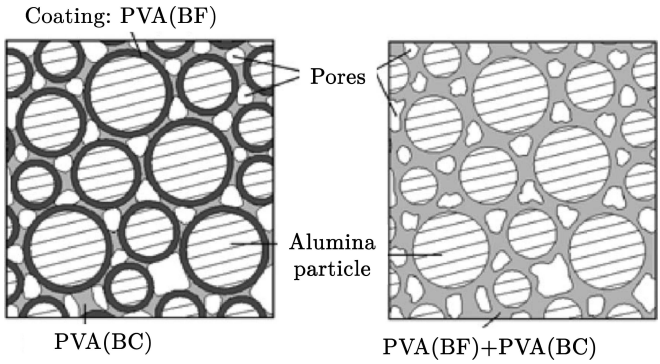

(a) Schematic of the PVA-Al_2O_3 mixture: before (left) and after (right) laser irradiating.

(b) 3D sintered part

Figure 1.20: The slurry based indirect SLS process [203].

1.4.2.4 Chemically induced binding

During chemically induced binding (CIB), the heat of the laser beam is used to initiate a chemical reaction which results in the binding of the powder particles. Different powder deposition systems are used to investigate the production of ceramic parts through this process, which is also known as selective laser reaction sintering (SLRS) [29].

Conventional deposition system Different research groups investigated SLS of ceramic parts through CIB by using a conventional deposition system:

- F. Klocke and H. Wirtz of the Fraunhofer Institute of Production Technology (IPT) SLSed SiC starting powder in argon atmosphere. During laser irradiation, SiC decomposed into Si and C. Despite the inert argon atmosphere, the Si atoms reacted with O_2 and formed SiO_2, which

glued the SiC particles together [111]. Since the melting temperature T_m of Si was about 1420°C, the SiC particles were probably also bound by melted Si.

- B.R. Birmingham and H.L. Marcus of the University of Texas in Austin SLSed Si powder in an NH_3 atmosphere to produce Si_3N_4 [29].

Slurry coating At the National Taipei University of Technology in Taiwan, H.H. Tang deposited slurry layers, consisting of aluminum phosphate and silica [197]. The process, which is also called Ceramic Laser Sintering (CLS), was based on an irreversible chemical reaction of slurry containing aluminum phosphate and silica at a temperature above 250°C.

Ring blade The Laserinstitut der Hochschule Mittweida (LHM) used the patented micro SLS device [68] to produce Si-SiC parts through SLS of SiC. An Nd:YAG laser with a wavelength of 1064 nm was used in a continuous mode to decompose a fraction of the irradiated SiC powder. This yielded elementary silicon, which became the matrix or bridging material for unreacted SiC grains [72, 173, 174, 175, 193].

1.4.2.5 Gellation

At the National Taipei University of Technology in Taiwan, the slurry deposition device was also used to investigate the ceramic laser gelling (CLG) process. During CLG, the heat induced by the laser beam initiates the chemical or physical gelling of a colloidal suspension (i.e. a sol). When a sol is gelled, it first becomes more viscous, then develops rigidity, and finally links, forming three-dimensional networks. For example, when a thin film is deposited by a slurry coater, laser irradiation (CO_2 laser) can be used to dry a portion of the deposited layer, forming a solid network. The portion of slurry film that is not scanned by the laser beam remains in the slurry state.
Yen et al. [242] used a slurry which mainly consisted of Al_2O_3 powder, silica sol and deionized water to fabricate alumina-silica parts. Due to expulsion of water and a part of the ceramic powder during the laser scanning, the density of the final parts (after furnace sintering) was only 75%.
By mixing a silica sol with silica powder, pure silica parts could be obtained through the CLG process (figure 1.21). The maximal green part strength after CLG was 4.7 MPa. After a heat-treatment at 1200°C for 1.5 hours, the flexural strength increased up to 12.5 MPa. No density values were reported [132, 133, 199].

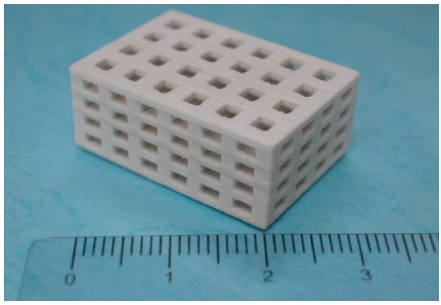

Figure 1.21: A silica part with inner channel structure made by selective laser gelling [133].

1.4.3 Powder based stereolithography (SLPP-SLA)

During stereolithography of ceramics (figure 1.22) different ceramic containing slurry layers are scanned by ultraviolet (UV) radiation. The UV radiation causes a chemical reaction which results in the polymerization (i.e. chemical gelling) of the slurry layers and entrapment of the ceramic particles. After debinding the resulting polymer and sintering the structural material in a furnace, the final ceramic part is obtained. A distinction can be made between the systems which produce macroscopic and microscopic ceramic parts.

(Macro) SLPP-SLA In literature, SLPP-SLA of ceramics is described under different names and abbreviations: e.g. ceramic stereolithography (CerSLA [18], CSL [247]) and lithography based ceramic manufacturing (LCM [129]). Different research teams have investigated the fabrication of ceramics through SLPP-SLA. Although the polymerization reaction is mostly performed by an UV laser, also Large Area Maskless Photopolymerization (LAMP) is sometimes used [95]. During LAMP, each layer is rapidly patterned by UV exposure in the pattern of a bitmap defined by a spatial light modulator.

	SLPP-SLA
laser-material interaction	chemical reaction
binding mechanism	chemical gelling
powder deposition mechanism	slurry coater or lifting mechanism

Figure 1.22: Classification: SLA of ceramics.

Many patents already describe different suspensions or specific applications for SLPP-SLA of ceramics [42, 76, 94, 152, 180, 220]. The suspensions are prepared by inserting different powders in a UV curable medium (also called photopolymer), consisting of monomers and/or oligomers, and photoactive components. In most cases, the medium is a resin-based acrylate or water-based acrylamide medium [27, 247]. It is also possible to use a medium which consists of a UV curable resin as an organic binder and methanol as a solvent and a dispersant [219]. After paving the solvent-based slurry, the solvent is vaporized using a fan. This results in a shrinkage of the slurry volume of the deposited layer. By using this method, alumina parts with a mean density of about 98% and a mean tensile and flexural strength of about 327 and 476 MPa could be achieved. Another route to produce the resin was developed by De Hazan et al. [50]. In this case, surfactants were adsorbed in aqueous media under controlled pH conditions on Al_2O_3, ZnO and Al_2O_3/ZnO particles. After drying, the particles were transferred to an organic medium.

The extend of the photopolymerization reaction during laser irradiation can be described through the following equation which J.P. Jacobs derived, starting from the Beer-Lambert equation [104].

$$\delta_c = D_p \ln\left(\frac{E_i}{E_c}\right)$$

where δ_c is the cured depth (i.e. the polymerized thickness), E_i the energy density delivered at the surface of the resin, E_c the critical energy of photopolymerization which is the minimum input energy necessary to trigger the curing process, D_p the penetration or sensitivity of the laser beam (the distance at which the laser intensity is reduced by 1/e).
Many authors used this equation to describe the hardening of a ceramic suspension under UV radiation [16, 18, 38, 95, 209, 210, 211, 247]. The cured depth δ_c is influenced by extra photoactive components in the light curable medium and the ceramic particles [95]. The photoactive components include: (1) a photoinitiator, which is a dye that decomposes to form free radicals upon absorption of a UV photon, thereby initiating polymerization reactions, (2) inert dyes, which absorb photons without forming free radicals, and (3) inhibitors which react with free radicals to inhibit polymerization.
As depicted in figure 1.23a, the ceramic particles reduce the photopolymerization reaction by diluting the photoactive medium and attenuating the UV light by scattering. The light scattering is essentially the reflection of the UV light by the ceramic particles. Reflection of the UV light will not occur when the refractive index of the ceramic filler is almost equal to the refractive index of the organic matrix, as is the case for SiO_2. On the other hand, the refractive index of the ceramic filler is increasingly higher than the refractive index of the organic medium for respectively Al_2O_3, ZrO_2 and SiC. The higher

the refractive index, the more UV light will be absorbed by the ceramic filler material, reducing the final conversion. This causes SLPP-SLA of SiO_2 [64, 204] or Al_2O_3 [39] to be easier, compared to SLPP-SLA of ZrO_2 or SiC. As depicted in figure 1.23b, smaller particles also reduce the photopolymerization reaction. The deterioration of the final conversion by lowering of the particle size while keeping the vol% of the suspension constant, could be allocated to an increase in scattering centers for a given volume concentration [16].

When the suspensions are highly loaded with ceramic particles and interaction between the particles is not negligible, the viscosity usually has a shear thinning rheological behavior that follows the Krieger-Dougherty equation [38, 95]:

$$\eta_r = \frac{\eta}{\eta_0} = \left(1 - \frac{\phi}{\phi_0}\right)^{-[\eta]\phi_0}$$

where η_r is the relative viscosity of the suspension, η is the viscosity of the suspension, η_0 is the viscosity of the medium, ϕ the volume fraction of ceramic powder, ϕ_0 the volume fraction of the filler for close-packed particles corresponding to an infinite viscosity (no flow) and $[\eta]$ the hydrodynamic shape factor which depends on the shape of the particles ($[\eta]$ is 2.5 for spheres).

The suspensions which are commercially used for SLPP-SLA of ceramics are high viscosity pastes or low viscosity slips. Both kind of suspensions are commercialized through different companies and patents. SLPP-SLA of ceramics through high viscosity paste slurries is commercially exploited by 3DCERAM [2] and Sirris [9]. At Sirris in Belgium, a special coater which can deposit pastes, containing up to 60vol% ceramic (or metal) powder, was developed [41] and patented [42]. The paste-coater is used in combination with an Optoform SLPP-SLA machine to produce ceramic parts.
SLPP-SLA of ceramics through low viscosity slips is commercially exploited by Lithoz GmbH [7], a spin-off from Technische Universität Wien (TU Wien, [10]), in cooperation with Ivoclar Vivadent AG [6, 76, 152]. The CeraFab 7500 machine, sold by Lithoz, uses a lifting mechanism to deposit layers of powder suspension. The part being produced touches a glass support. The layers are deposited through lifting the part from the glass support, so the suspension can flow underneath. The laser or digital light processing (DLP) projector then irradiates the bottom of the part through the glass support. In this way, the CeraFab 7500 machine can produce accurately high-purity alumina parts with densities >3.96 g/cm^3 (i.e. 99.4% of the theoretical density) and 4 point-bending strengths of 430MPa [129] (figure 1.24).
Besides TU Wien, TNO Eindhoven is also well known for its research

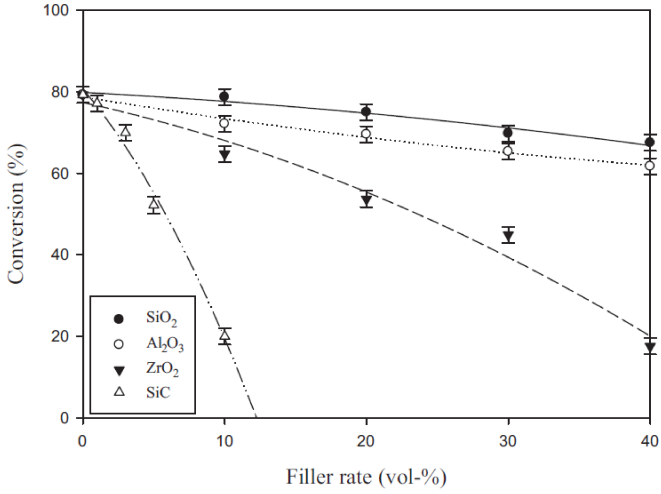

(a) Influence of the refractive index of the ceramic filler and of the concentration ceramic particles. The refractive index is increasingly higher for SiO_2, Al_2O_3, ZrO_2 and SiC.

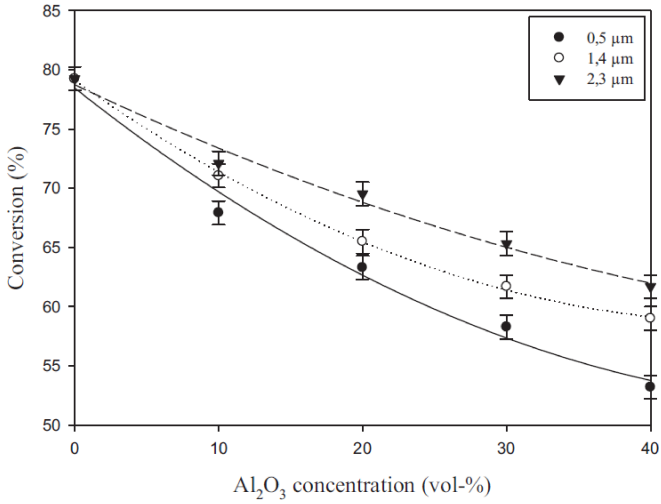

(b) Influence of alumina particle size on photopolymerization.

Figure 1.23: Photopolymerization of a ceramic filler containing acrylate [16].

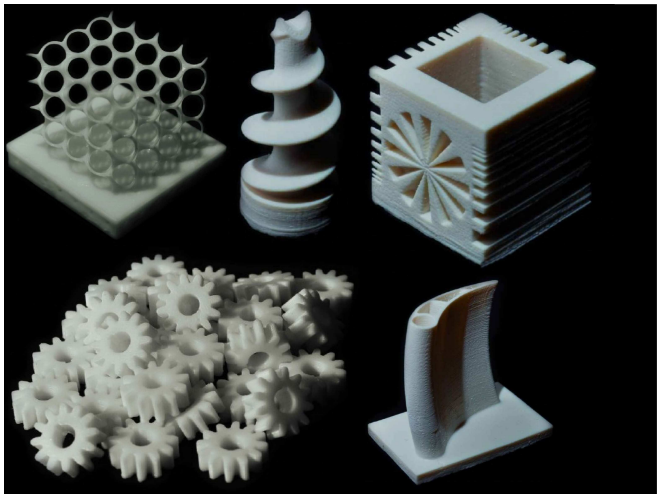

Figure 1.24: Alumina parts produced by the CeraFab 7500 machine of Lithoz GmbH [129].

regarding SLPP-SLA by using a lifting mechanism to deposit layers of powder suspension. Maalderink of TNO Eindhoven [143] illustrated that the green parts produced with such a layer deposition method, contain a small amount of pure photopolymer material (no ceramic particle) between every layer (figure 1.25a). The resulting inhomogeneities can make the parts crack during debinding and solid state sintering (figure 1.25b).

Only relatively thin (maximum 2.5 mm thickness) ceramic parts can be produced through the SLPP-SLA process. Due to the relative large amount of polymer in the produced sample, too thick parts are likely to crack during the debinding process. By choosing low debinding rates, appropriate building parameters [18] and by avoiding the occurrence of uncured monomer material after the SLPP-SLA process [17], the cracking of the parts can be minimized. For these parts, the shrinkage during debinding and furnace sintering is quite uniform and about 10% in all directions (usually somewhat smaller in the z-direction, compared to the x-y direction) [18].

Micro SLPP-SLA Powder based microstereolithography uses the SLPP-SLA process to produce as small as possible complex three-dimensional (3D) components. By starting from suspensions which contain a photopolymerizable medium and ceramic filler material, polymer-ceramic composite parts can be fabricated. After debinding and furnace sintering, ceramic parts can be

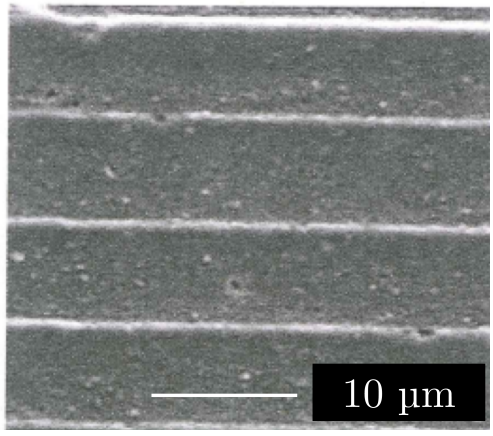

(a) Green part

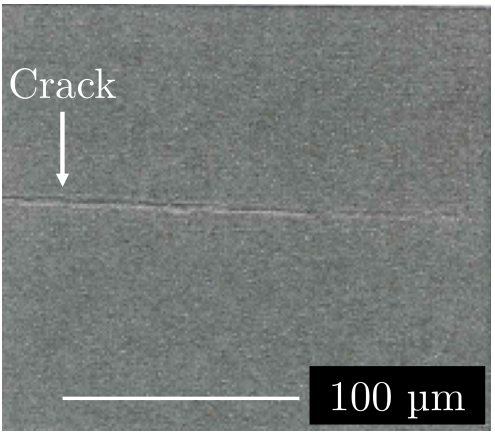

(b) SSS part

Figure 1.25: Cross-section of a green and solid state sintered part produced by the SLPP-SLA process having a lifting mechanism to deposit layers of powder suspension [143].

obtained [26, 27, 167]. As is the case during macro SLPP-SLA, UV radiation can be performed at the top surface or at the bottom surface. Also similar to macro SLPP-SLA, UV radiation can be performed by illuminating deposited layers integrally (e.g. by a DLP projector) or by vector-by-vector scanning by a laser. If pulsed lasers and expensive optics are used, the micro SLPP-SLA technology allows the production of components with a submicrometer resolution as depicted in figure 1.26 [27].

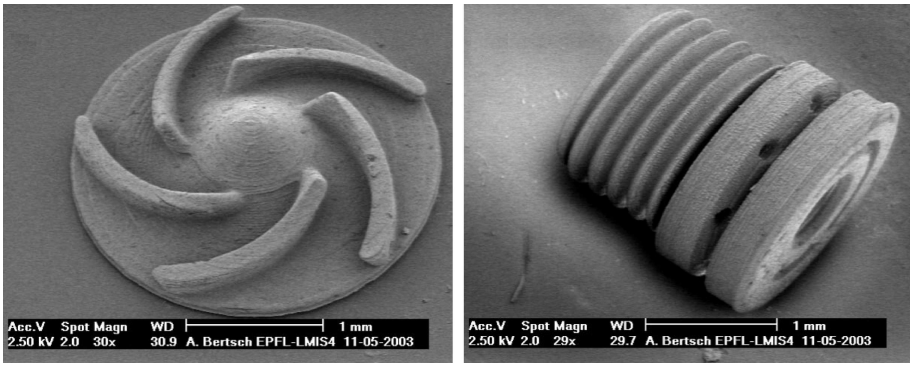

Figure 1.26: Alumina parts produced through micro SLPP-SLA [26].

1.5 Conclusions

As demonstrated in this chapter, different additive manufacturing processes exist to produce ceramic parts. When having a closer look to these AM processes, some trends can be observed. These trends will be used in the next chapter to outline the research of this dissertation:

- The AM processes which currently are most widely investigated to produce ceramics, are laser based processes. For indirect AM, the most convenient processes to produce ceramics are SLS and SLA. For direct AM, the most convenient processes to produce ceramics are SLS and SLM.
- The indirect AM processes, which make use of a binder material, are able to produce different types of ceramics. However, the indirect processes require the time consuming binder removal step. Therefore, indirect AM processes can not produce rapidly ceramic parts.
- The direct AM processes, which do not make use of a binder material, do not require the time consuming binder removal step. Therefore, direct AM processes can produce more rapidly ceramic parts compared to indirect AM processes. However, the direct laser based AM processes (SLS and SLM) are not (yet) able to produce as many different types of ceramics as the indirect AM processes.
- AM processes which incorporate colloidal processing techniques can produce more easily high density ceramic parts than AM processes which do not incorporate colloidal processing techniques.

Chapter 2

Literature review and research outline: AM as primary shaping step of powder metallurgy processes to produce ceramics

After attempting to define ceramics as a material class, this chapter gives a brief overview of the state-of-the-art in ceramic industry and technology. Starting from the current challenge in ceramic industry, the research approach of this dissertation is determined. This research approach combines the advantages of additive manufacturing (AM) and powder metallurgy to produce ceramic parts.

2.1 Definition of ceramic

The most widely accepted definition of a ceramic was given by Kingery et al. in 1976: a ceramic is a nonmetallic, inorganic solid [108]. Unfortunately, this definition is not quite complete in the sense that glass, which behaves at room temperature and below like a solid but has the structure of a liquid, is a very important ceramic [34]. It can also be a misleading approach to define a class

of material through its properties. Nevertheless, ceramics are mainly known through the specific properties associated with them. The specific properties can in many respects not be achieved by other materials (see figure 2.1). To highlight some of the unique properties [78]:

- low density
- high hardness
- high mechanical strength
- dimensional stability (specific stiffness)
- weathering resistance
- high working temperature
- low or high thermal conductivity
- good electrical insulation
- dielectric and ferroelectric properties

The technological developments to process ceramics, together with their specific properties, have led to a wide variety of possible applications and an associated industry.

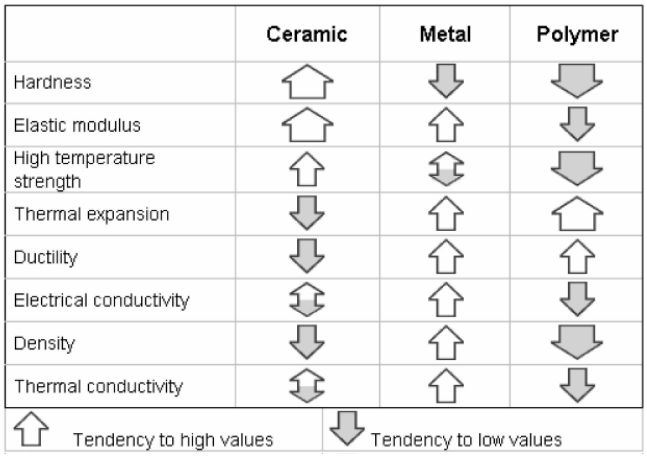

Figure 2.1: Comparison of the properties of ceramics, metals and polymers. (Source: modified from [78])

2.2 Trends in ceramic industry and technology

2.2.1 The ceramic industry

Ceramics are a multibillion dollar industry. Worldwide sales are about 279 billion dollar per year (2012, [8]). In 2007, the general distribution of industry sales was as follows [34]:

- 55% Glass
- 17% Technical ceramics
- 10% Whiteware
- 9% Porcelain enamel
- 7% Refractories
- 2% Structural clay

Financially, the ceramics market is clearly dominated by glass. The major application is windows. Technical ceramics currently form the second largest sector of the industry and is growing fast. Technical ceramics, also called engineering ceramics or advanced ceramics, are ceramic parts which can be used in high demanding engineering applications. Technical ceramics, generally Al_2O_3, ZrO_2, Si_3N_4 or SiC, need to be processed in such a way that the final material properties are superior: homogeneous microstructures, high densities ($> 98\%$), small grain sizes ($< 5\ \mu$m) and low surface roughness ($R_a < 20\ \mu$m) are minimum requirements.
The worldwide market for technical ceramics was forecast to arrive at 40 billion US dollar in 2009 (The Freedonia Group, 2007). Figure 2.2 gives the expected development of the US market up to 2015, indicating that all sectors will exhibit a continuous growth [177].

2.2.2 Powder metallurgy

Ceramics (both technical ceramics as traditional non-technical ceramics) are conventionally processed through powder metallurgical PM processes. As depicted in figure 2.3, a conventional powder metallurgical process can be divided in four (or five) steps: powder production, primary shaping, eventually debinding, furnace sintering[1] and final shaping. During the first step, powder

[1] Reaction sintering processes, where the powder exothermally reacts to become the final part, are not considered.

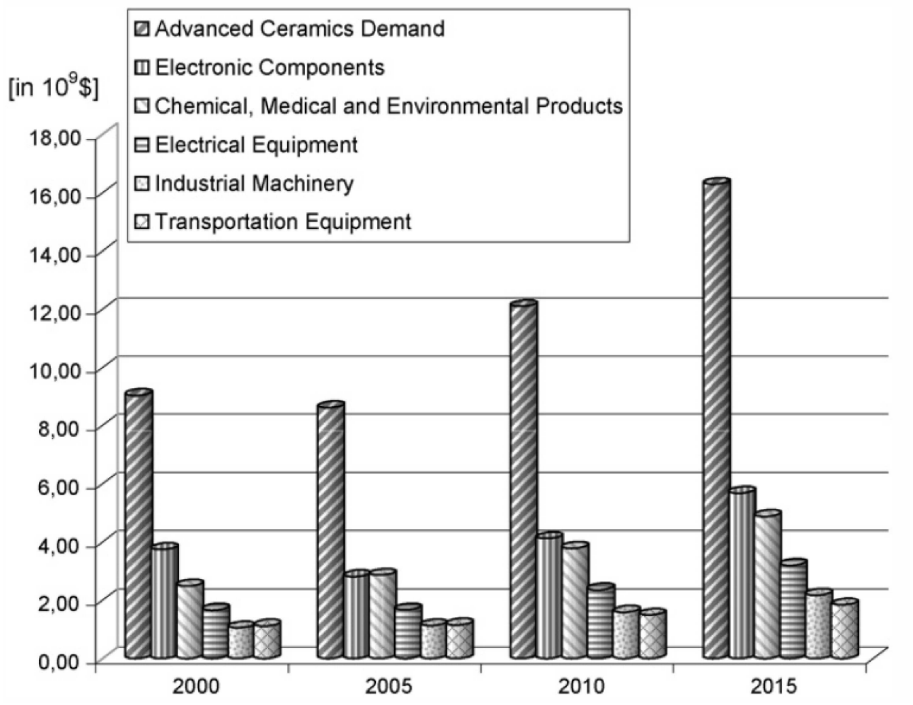

Figure 2.2: Development of the US market for advanced ceramics from 2000 to 2015 [177].

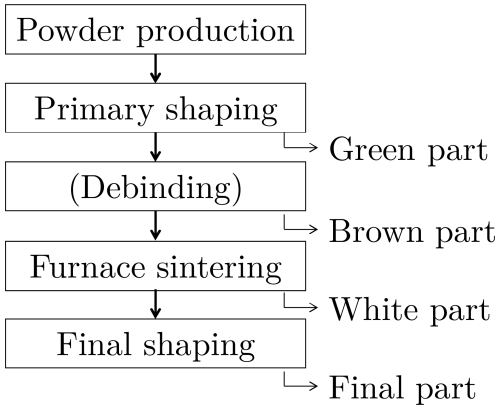

Figure 2.3: Conventional powder metallurgical process to produce ceramic parts.

particles are produced. In the primary shaping step these particles, which eventually contain binder material, are shaped in the desired geometry. The resulting part is called 'green part'. If binder material is used in the primary shaping step, a furnace treatment will remove the binder material (i.e. debinding). The resulting part is called 'brown part' [2]. During the main furnace treatment of the PM process, the ceramic particles are furnace sintered and a so called 'white' ceramic part is obtained. Every 'white' ceramic component has usually (not if reaction-based shaping processes are used [105]) a minimum of 1-2% distortion due to differential shrinkage and gravity effects during sintering. If this distortion can not be tolerated, a last final shaping step (also called finishing) is needed to obtain the 'final' ceramic part. Usually hard machining (e.g. grinding) or non-conventional machining (e.g. electro chemical milling) is used during final shaping to obtain the desired tolerances. In the dissertation, the final shaping step is not investigated. Therefore the terms 'white' and 'final' part will be used as synonyms.

2.2.3 Current challenge of ceramic industry

Regardless of their excellent properties, ceramics are not as widely used in industry as they should and could be. The main reason for the reluctance within industry is the high production cost of ceramic parts. If a company wants to produce a ceramic part for a certain application, a distinction can be made between the associated fixed and variable costs.

Fixed costs: Although many primary shaping processes exist (see figure 2.4), ceramic manufacturing is not (yet) a flexible production process. Most of the primary shaping processes are not able to directly produce complex shaped parts. The conventional processes to primary shape complex ceramics (e.g. conventional slip casting, pressure slip casting or powder injection molding) require molds which have to be optimized according to the part which has to be produced. Also green machining of ceramic powder compacts is restricted to relatively simple geometries and thick walls by the low strength of the powder compacts, even if binders are added in order to increase green strength [105]. Ceramic components should be designed in such a manner as to reduce stress concentrations and to avoid tensile stresses. Therefore, a number of prototypes of the actual component will be required for evaluation in order to introduce a ceramic part into a certain application: e.g. a simple one-to-one substitution of an existing metal part is usually not possible. The ability to deliver ceramic

[2] In scientific literature, not in the dissertation, the terms green part and brown part are sometimes used interchangeable to denote parts after the shaping process (with or without binder) and after the debinding process.

prototypes in a reasonable time and at an acceptable price can be a decisive factor in a competitive market [105].

Variable costs: Final shaping is generally the most energy and cost intensive step of the powder metallurgical process chain. This is especially the case for technical ceramics, which are very difficult to process after furnace sintering, and complex ceramics, which require a lot of finishing. In some cases, hard machining costs account for 80% of the overall manufacturing costs of a ceramic component [105].

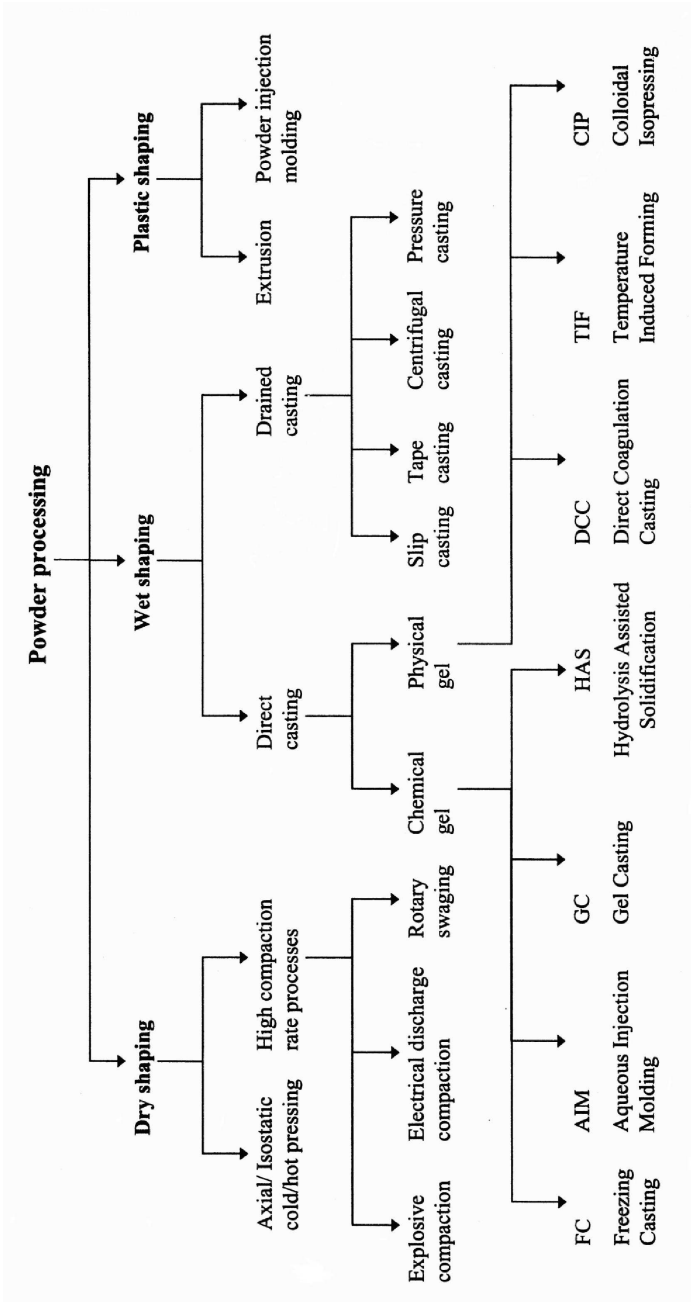

Figure 2.4: Some primary shaping processes [215].

2.3 Mission, strategy and goals of the dissertation

At the beginning of the dissertation, no research on additive manufacturing (AM) of ceramics had been performed at KU Leuven. This section describes how, starting from the observed trends in ceramic industry and technology, direction is given to the research on AM of ceramics.

Mission: In order to start the research on AM of ceramics, first a mission had to be formulated which declared what kind of research we wanted to do and for who we wanted to do the research. It was understood that, since AM has the ability to deliver fast ceramic prototypes, it has the ability to drastically reduce the fixed costs associated with the engineering of a ceramic part for a certain application. In other words: additive manufacturing can act as a catalyst to introduce ceramic parts more easily into a certain application.
It was concluded that the mission of the research is to develop AM of ceramics to a level which enables the fast production of complex and customized ceramic parts with high part quality and accuracy. As KU Leuven is a university with an international character, the stakeholders are not only the Belgian, but also the international industry and society.

Strategy: To fabricate ceramic parts through additive manufacturing, a thorough knowledge of conventional ceramic processing methods is necessary [35]. The overall research strategy followed in the dissertation to enable additive production of ceramics, is combining knowledge of additive manufacturing with knowledge of powder metallurgical (PM) processes. More specifically, AM will be used as primary shaping step to produce ceramic parts. The conceptual idea of incorporating AM in the PM process chain is not new (see e.g. Klocke and Wirtz [111]), but necessary to include the extensive know-how which is currently available in the domain of ceramic processing.

Long term goal: The long term goal of the ceramic research at KU Leuven is the fast production of technical and thus high quality ceramics through additive manufacturing. In this way, the AM research group wants to develop a production process which can rapidly produce parts with equivalent material properties as possible substitute production processes such as ceramic injection molding or slip casting.
In contrast to metal parts, the final quality of ceramic parts is generally not determined by the initial material properties, but by the way it is processed. The quality of the production process determines the largest flaw present in the part, which in turn, determines the strength of the part as described through

Weibull statistics. As a result, the long term goal to produce technical ceramics is equivalent to a long term goal of improving the quality of the AM production process.

Short term goal: Since at the beginning of the dissertation, no research on additive manufacturing (AM) of ceramics had been performed at KU Leuven, the short term goal was to produce ceramic parts and join the international debate. The aim of this pragmatical goal was to gain insight in ceramic processing through AM and in this way objectively optimize the production process.

2.4 Implementation of mission, strategy and goals

The section describes how the research mission, strategy and goals are implemented in the dissertation. The section first reports on which ground alumina (and more specifically α-alumina) has been chosen as a ceramic material to become subject of study. Next, the basic steps which are used to produce ceramic parts through additive manufacturing are described. The final subsections describe how post-AM densification is used to increase the final density of the ceramic parts and how the changes which occur during the PM process are characterized through geometrical assessments, density measurements and microstructural analyses (see figure 2.5).

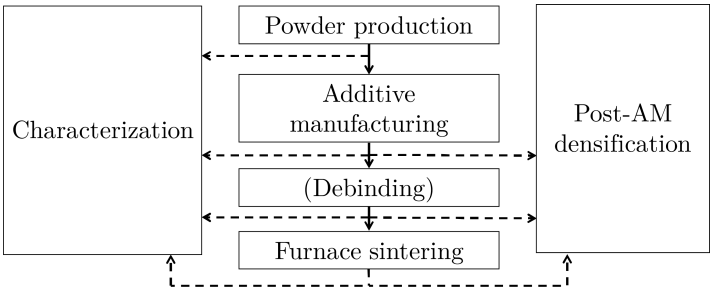

Figure 2.5: Additive manufacturing as a powder metallurgical process step.

2.4.1 Ceramic material

Before starting the research, alumina (aluminum oxide, Al_2O_3) has been chosen as a ceramic material to become subject of the study. Alumina is the most widely used ceramic material for technical applications. According to the Freedonia Group (2007) 39% of the demand for technical ceramics is for alumina. Alumina has the following structures, material properties and applications which make them widely used.

Structure of alumina: Alumina is generally used as a polycrystalline material, which means that the alumina part is comprised of many small crystals or grains. The alumina grains can have different crystal structures (also called polymorphs) at different temperatures or grain sizes (see figure 2.6). The most commonly occurring polymorph is α-alumina (α-Al_2O_3), which has a hexagonal crystal structure stable at room temperature. Emerging metastable aluminas, including γ, δ, η, θ, κ and χ polymorphs, have been growing in importance [163].
Some alumina materials contain atomic impurities. As an example, corundum generally refers to impure α-Al_2O_3. When it is doped with Cr^{3+} the mineral is called ruby. When doped with Ti (or Fe) ions it is called sapphire. The β-aluminas are a family of nonstoichiometric aluminates of which the most important have the approximate formulas $Na_2O.11Al_2O_3$ (β-alumina),

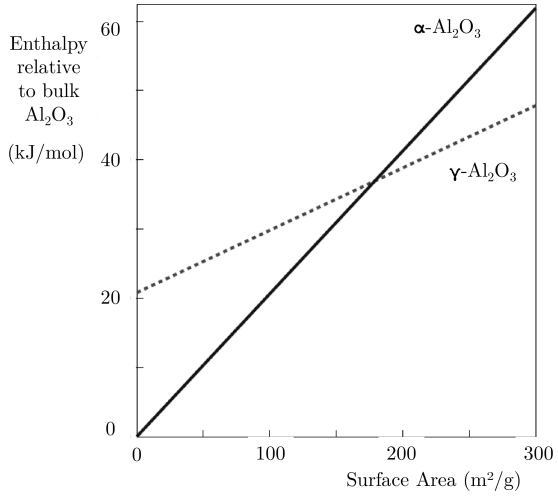

Figure 2.6: Calculated enthalpy of alumina (γ- and α-) polymorphs as it varies with the surface area. A large surface area implies small particles [34].

$Na_2O.8Al_2O_3$ (β'-alumina), and $Na_2O.5Al_2O_3$ (β''-alumina) [34]. Through mixing alumina with other ceramic materials during the first stage of the powder metallurgical process, composite ceramics with improved properties and/or improved processability can be obtained. Some examples are alumina-silica (e.g. mullite) or alumina-yttria (e.g. yttrium aluminum garnet for YAG-lasers) ceramics. Another example is zirconia toughened alumina (ZTA), which typically consists of alumina with 10% to 20% metastable tetragonal zirconia to increase the strength through 'stress induced transformation toughening'. If a sufficient quantity of the metastable tetragonal zirconia is present, then an applied stress, magnified by the stress concentration at a crack tip, can cause the tetragonal phase to convert to monoclinic, with the associated volume expansion. The phase transformation can put the crack into compression, retarding its growth, and enhancing the fracture toughness. Since zirconia, like magnesia, can pin grain boudaries, it also acts as a grain growth inhibitor. This results in a higher strength of the alumina. On the other hand, the addition of zirconia tends to decrease the young's modulus [34].

Properties of alumina: Figure 2.7 depicts the main material properties of high-purity (99.5% or higher) and nearly fully densified (98% of the theoretical density, or higher) sintered polycrystalline α-alumina with a nominal grain size of 5 μm. The theoretical density of alumina is 3.984 g/cm^3 at 20°C. This value is quite high: for example, the ASTM standard for sinter-HIPed alumina for biomaterial applications is 3.92 g/cm^3 (or 98.4%). Nevertheless, 3.984 g/cm^3 will be used in the dissertation as the reference density for reporting relative alumina densities. Densily sintered alumina is well know for the following material characteristics [78]:

- High strength and hardness
- Temperature stability
- High wear resistance and corrosion resistance even at high temperatures[3]

For polycrystalline alumina, the strength is strongly dependent on the porosity and grain size of the material (see figure 2.8).

Alumina applications: The breviary of technical ceramics of the German 'Verband der Keramischen Industrie e.V.' states that synthetically manufactured materials with an alumina content ranging from 80% to more than 99%,

[3] Although wear resistance and corrosion resistance are rather system properties than material properties, they are frequently associated with alumina (and more general with ceramic materials).

Numbers in parentheses denote estimated combined standard uncertainties of the last given digit.
For example, 2050(4) is equivalent to 2050 +/- 4.

Property [unit]	20 °C	500 °C	1000 °C	1200 °C	1400 °C	1500 °C
Bulk Modulus [GPa]	257(50)	247	237	233	229	227
Compressive Strength [GPa]	3.0(5)	1.6	0.7	0.4	0.3	0.28
Creep Rate [10^{-9} s^{-1}] at 150 MPa	0	0	4	280	6600	24600
Density [g/cm^3]	3.984(2)	3.943	3.891	3.868	3.845	3.834
Elastic Modulus [GPa]	416(30)	390	364	354	343	338
Flexural Strength [MPa]	380(50)	375	345	300	210	130
Fracture Toughness [MPa $m^{1/2}$] for crack length of 300 µm	3.5(5)	3.0	2.7	2.6	2.5	2.5
Friction Coefficient [] at 2 GPa	0.40(5)	0.8	0.4			
Hardness (Vickers, 1 kg) [GPa]	15(2)	8.5	4.6	3.7	2.9	2.5
Lattice Parameter a(hexagonal) [Å]	4.761(3)	4.777	4.797	4.806	4.815	4.820
Lattice parameter c(hexagonal) [Å]	12.991(7)	13.040	13.102	13.129	13.156	13.169
Poisson's Ratio []	0.231(1)	0.237	0.244	0.247	0.250	0.252
Shear Modulus [GPa]	169(1)	158	146	142	137	135
Sound Velocity, longitudinal [km/s]	11.00(30)	10.77	10.54	10.44	10.35	10.30
Sound Velocity, shear [km/s]	6.51(20)	6.33	6.14	6.06	5.97	5.93
Specific Heat [J/kg·K]	755(15)	1165	1255	1285	1315	1330
Tensile Strength [MPa]	267(30)	267	243	140	22	13
Thermal Conductivity [W/m·K]	33(2)	11.4	7.22	6.67	6.34	6.23
Thermal Diffusivity [cm^2/s]	0.111(20)	0.0251	0.0150	0.0136	0.0127	0.0124
Thermal Expansion from 0 °C [$10^{-6}K^{-1}$]	4.6(2)	7.1	8.1	8.3	8.5	8.6
Wear Coefficient (Log10) [] at 2 GPa	-6(1)	-4	-6	...	...	...
Weibull Modulus []	11(4)	11	11	11	11	11
Weibull Characteristic Strength,[MPa]	395(25)	390	360	310	210	125

Figure 2.7: Properties of dense polycrystalline α-alumina.
(Source: modified from [5, 154])

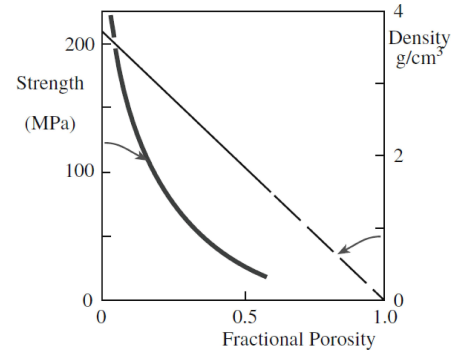

(a) Effect of porosity.

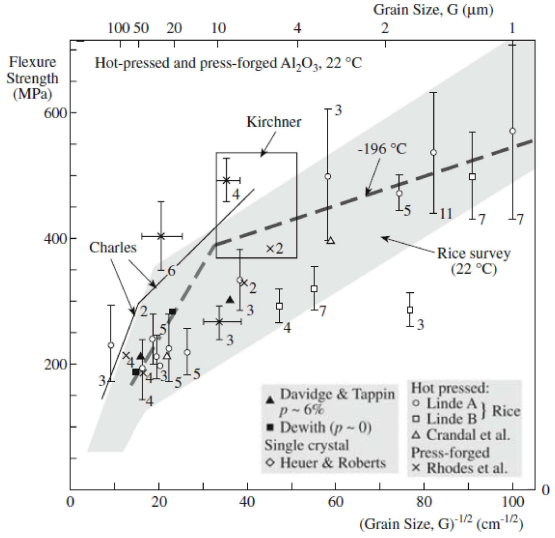

(b) Effect of grain size.

Figure 2.8: Strength of polycrystalline alumina as a function of porosity and grain size [34].

have been proven in practice. The choice of the material is determined by technical and economical criteria. A material with higher alumina content does not necessarily fulfil the needs of an application best. Further, the breviary states that due to their good price/performance ratio and their generally useful properties, alumina ceramics are used in the following industrial applications:

- in the sanitary industry as a sealing element
- in electrical engineering as insulation
- in electronics as a substrate
- in machine and plant construction as wear protection (wear-resistant material)
- in the chemical industry as corrosion protection (corrosion-resistant material, highly resistant to vapors, melting and slag up to high temperatures) and filters
- in instrumentation as a protective tube for thermocouples used for high temperature measurements
- in human medicine as an implant material
- in high temperature applications as a burner nozzle or as a support tube for heat conductors

2.4.2 Powder production

Processing fine, submicrometer ceramic powder is not straightforward but needed in order to get a good final microstructure with small grain sizes (< 5 µm). Submicrometer alumina powder can be produced in different ways. The most commonly known process is the Bayer process. Other alumina powder production processes are the Stöber process (hydrolysis of a metal alkoxide), plasma chemical synthesis and vapor phase deposition. This dissertation mostly uses high purity α-alumina (grade SM8, Baikowski, France [3]) powder with a d_{50} of 0.3 μm as structural starting material. This powder is produced through a modified Bayer loop process.
Interparticle forces make submicrometer powder particles to cluster during primary shaping. As an example, the clustering occurs when submicrometer powder is deposited by a conventional AM deposition system, such as a roller coater or scraper system. The random clustering of the particles decreases the flowability of the powder and the deposited layers are generally inhomogeneous [112]. There are three options to avoid the clustering:

1. Use colloidal processing techniques. As an example, instead of the conventional powder deposition system, colloidal processing based techniques, such as tape casting [80, 110, 203] and spray deposition [227] can be used to deposit high density powder layers of submicrometer particles. Further processing of these high density powder layers lead to dense microstructures. However, since the use of a colloidal suspension requires a drying step before further processing, drying cracks need to be avoided.

2. Cluster the submicrometer ceramic particles into agglomerates (also called granules) before the primary shaping step. The controlled clustering enables the powder particles to gain weight in such a way that during powder deposition the gravitational forces overcome the interparticle forces. This leads to better fluidity during conventional layer deposition. The production of agglomerates can be done in several ways. One option is to spray dry the submicrometer particles.
   The next four chapters and the appendix describe the production of five different powders. These powders are produced by four alternative, in-house developed methods. Each powder contains composite agglomerates which consist of submicrometer alumina particles and a binder phase.

3. Use a dedicated powder deposition system to deposit submicrometer powder particles: e.g. a ring blade (section 1.4.2.1).

2.4.3 Additive manufacturing

The previous chapter was a literature review of additive manufacturing (AM) methods to shape ceramic powders. As a conclusion of this literature review, the following four trends could be distinguished:

- The AM processes which currently are most widely investigated to produce ceramics, are laser based processes. For indirect AM, the most convenient processes to produce ceramics are SLS and SLA. For direct AM, the most convenient processes to produce ceramics are SLS and SLM.

- The indirect AM processes, which make use of a binder material, are able to produce different types of ceramics. However, the indirect processes require the time consuming binder removal step. Therefore, indirect AM processes can not produce rapidly ceramic parts.

- The direct AM processes, which do not make use of a binder material, do not require the time consuming binder removal step. Therefore, direct AM processes can produce more rapidly ceramic parts compared

to indirect AM processes. However, the direct laser based AM processes (SLS and SLM) are not (yet) able to produce as many different types of ceramics as the indirect AM processes.

- AM processes which incorporate colloidal processing techniques can produce more easily high density ceramic parts than AM processes which do not incorporate colloidal processing techniques.

Keeping these trends in mind, the following methods are investigated to AM ceramics, and more specifically α-alumina.

Direct Selective Laser Sintering/Melting Direct Selective Laser Sintering/Melting (direct SLS/SLM) has the potential to drastically shorten the powder metallurgical process to produce ceramics. Since the direct SLS/SLM process does not use a polymer, no time consuming debinding step is required to obtain a white part. On the other hand, it has to be kept in mind that except for glasses, ceramics are conventionally not processed through a melting process. This means that it might be difficult to process different type of ceramics with the same direct SLS/SLM process.
In order to directly fulfill the long term goal of rapidly shaping technical ceramics, an attempt was made to develop a direct SLS/SLM device. As detailed in chapter 7 of the dissertation, for this purpose an experimental setup was designed, constructed and tested.

Indirect Selective Laser Sintering of composite powder agglomerates: In order to meet the short term research goal (i.e. join the international debate, gain insight in ceramic processing through AM and objectively optimize the production process), indirect selective laser sintering of composite powder agglomerates was further explored to produce ceramic parts. For this purpose, the SLS equipment available in the AM lab (i.e. a DTM Sinterstation 2000) could be used. Indirect SLS enabled the production of different types of ceramics. The only drawback of choosing indirect SLS was that a time consuming debinding step was required to obtain the final ceramic part.
Indirect SLS of alumina parts through SLS of composite powder agglomerates became the empirical core of this dissertation. In-house developed powder production methods were used to produce composite powder agglomerates consisting of submicrometer ceramic particles and a polymeric binder. In the four following chapters and the appendix, the production of five different powders is described. These powders are produced by four alternative, in-house developed methods. The four chapters and the appendix also report how densified ceramic parts have been produced, starting from the in-house developed powders.

2.4.4 Debinding

The process of polymer binder removal to obtain a 'brown part' is commonly referred to as debinding. Ideally, the binder system should be removed completely without disrupting the particle packing or producing any new microstructural defects in the green body. Debinding can be a critical step in ceramic processing, especially for forming methods where the binder content in the green body is relatively high (i.e. $>$ 10 vol%). Debinding can be accomplished by three methods [127, 169].

- Extraction by capillary flow, also called wicking: the green body is heated in a packed powder bed or on a porous substrate that absorbs the melted binder.
- Solvent extraction: immersing the component in a liquid that dissolves the binder. If the solvent is a supercritical fluid, this method is called supercritical fluid extraction.
- Thermal decomposition, referred to as thermal debinding: the binder is removed as a vapor/gas by heating at ambient pressure in oxidizing or non oxidizing atmosphere or under vacuum. The process is influenced by both chemical factors (i.e. decomposition temperature and decomposition products) and physical factors (i.e. heat transfer and mass transport).

In the dissertation, only the thermal debinding method was used. In the case of a thermoplastic or a wax binder, thermal debinding can be roughly divided into three stages [169].

1. Stage 1 involves the initial heating of the binder to a point where it softens. This causes the strength of the parts to decrease (figure 2.9a). Chemical decomposition and binder removal are negligible in this stage.
2. In stage 2, typically covering a temperature range of 200-400°C, most of the binder is removed by chemical decomposition and evaporation. The binder removal has features that are similar to those encountered in the drying of a moist granular material. The large pores empty first and the small pores remain full of liquid. After the large pores have been emptied, the small pores start to empty. This process is accompanied by considerable capillary flow, which redistributes the melted binder. As a result, the binder system becomes isolated around the particles, which is called the pendular state. In the pendular state, the liquid binder among the powder particles forms curved surfaces as shown in figure 2.9b. In the pendular state, powder particles mostly tend to move to each other

by capillary forces, which mostly are attractive [147]. As as result, the attractive capillary forces caused by the pendular state can enhance the part strength by limiting the free movement of the binder and powder [137] (figure 2.9a).
In an oxidizing atmosphere, degradation by oxidation occurs during thermal degradation. In this case, decomposition occurs at lower temperatures and leads to an increase in the rate at which the binder is removed.

3. During stage 3, the small amount of binder still remaining in the body is removed by evaporation and decomposition at temperatures above ∼400°C. With the decrease of the binder content, the binder can in some areas of the part no longer provide attractive power for enhancing the compact strength. Instead, only van der Waals forces keep the particles together, which results in a decrease of the strength [137] (figure 2.9a). In this stage, the atmosphere has to be carefully chosen to avoid the retention of an excessive amount of binder residue.

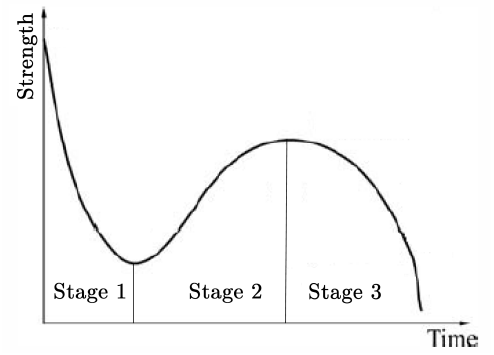

(a) Strength evolution of the parts. [137]

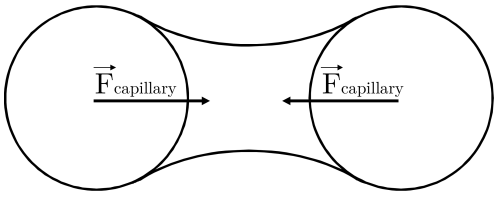

(b) Capillary forces between two powder particles in the pendular stage (i.e. end of stage 2).

Figure 2.9: Different stages of the thermal debinding cycle.

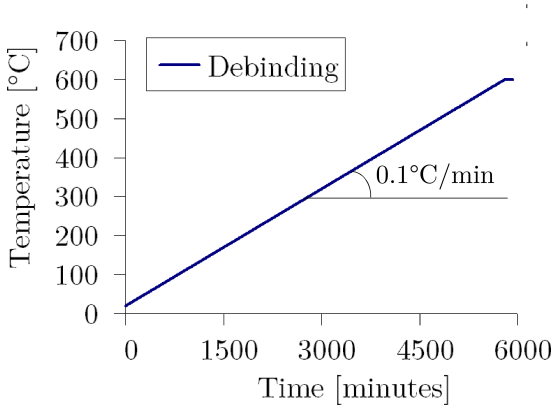

Figure 2.10: Commonly used thermal debinding treatment.

During thermal debinding, several processes such as shrinkage, deformation and bubble formation can seriously affect the ability to control the shape and structural uniformity of the body.

Shrinkage Shrinkage occurs by a rearrangement process as the particles try to achieve a denser packing under the action of the surface tension of the melted binder. The magnitude of shrinkage increases with decreasing particle packing density in the green body.

Deformation Part deformation is enhanced by a lower particle packing density, higher binder content and lower melt viscosity. In order to control the deformation and strength in this stage, the binder system is often designed to be a multi-component system containing low melting point and high melting point components: the high melting component can remain in the solid state to maintain the shape of the parts, when the low component begins to melt [137].

Bubble formation Bubble formation can occur at places in the part where the decomposition products cannot escape. This results in large pores or flaws in the final parts.

Most parts debinded in the dissertation had open porosities and a quite high binder load (up to 70 vol%). Open porosities facilitate the binder removal process since the gases formed during thermal degradation of the polymer can

easily escape from the part. High binder loads make the binder removal process more difficult. Parts having a large amount of binder material, create a large amount of gases during thermal debinding (i.e. bubble formation). If these gases can not escape from the part, e.g. since this is hindered by binder material which is not yet degraded, the part can crack. In this dissertation, mostly a very low heating rate of 0.1°C/min is used to prevent cracking of the parts during debinding. The low heating rate is also believed to favor particle mobility (defined here as the overall behavior of particle movement and rotation), which results in a greater amount of smaller pore sizes [131]. Mostly, the parts are heated up to 600°C, followed by a dwell time of 2 hours and furnace cooling (figure 2.10).

2.4.5 Furnace sintering

As with all other irreversible processes, densification (i.e. sintering) is accompanied by a lowering of the Gibbs free energy of the part (i.e. the thermodynamical system). The sources that give rise to the lowering of the Gibbs free energy are commonly referred to as the driving forces for sintering. Possible driving forces are [169]

1. temperature
2. the curvature of the particle surfaces
3. an externally applied pressure
4. a chemical reaction

This means that parametrical conditions such as temperature, particle size, applied external pressure and gaseous atmosphere are very important during sintering. In this context, also the effect of microstructural inhomogeneities present in the green and brown body (e.g. density, particle size, and compositional variations) is important. It is well recognized that inhomogeneities can seriously hinder the ability to achieve a high density and to adequately control the fabricated microstructure [169]. On the other hand, small levels of impurity can enhance the sintering behavior [79].
From a kinetic point of view, the sintering behavior is determined by processes occurring on the atomic scale [79]. These processes also depend on the properties of the material to be sintered, the externally applied pressure and temperature. As illustrated in figure 2.11, diffusion processes dominate the sintering behavior of non-silicate ceramics (e.g. alumina) if no external pressure is applied. In this case, the predominant mass transport (densification

mechanism) occurs through solid state diffusion, which is also called atomic diffusion (e.g. diffusion of the aluminum and oxygen atoms of alumina). Densification of silicate ceramics or cermets generally occurs through liquid-phase assisted sintering. During liquid-phase assisted sintering a low viscosity liquid (liquid phase sintering) or a viscous flow (viscous sintering) is present at the sintering temperatures [166].

2.4.5.1 Solid State Sintering

During solid state sintering (SSS), the system is heated to a temperature range of 0.5-0.75 of the melting temperature. The powder does not melt. Instead

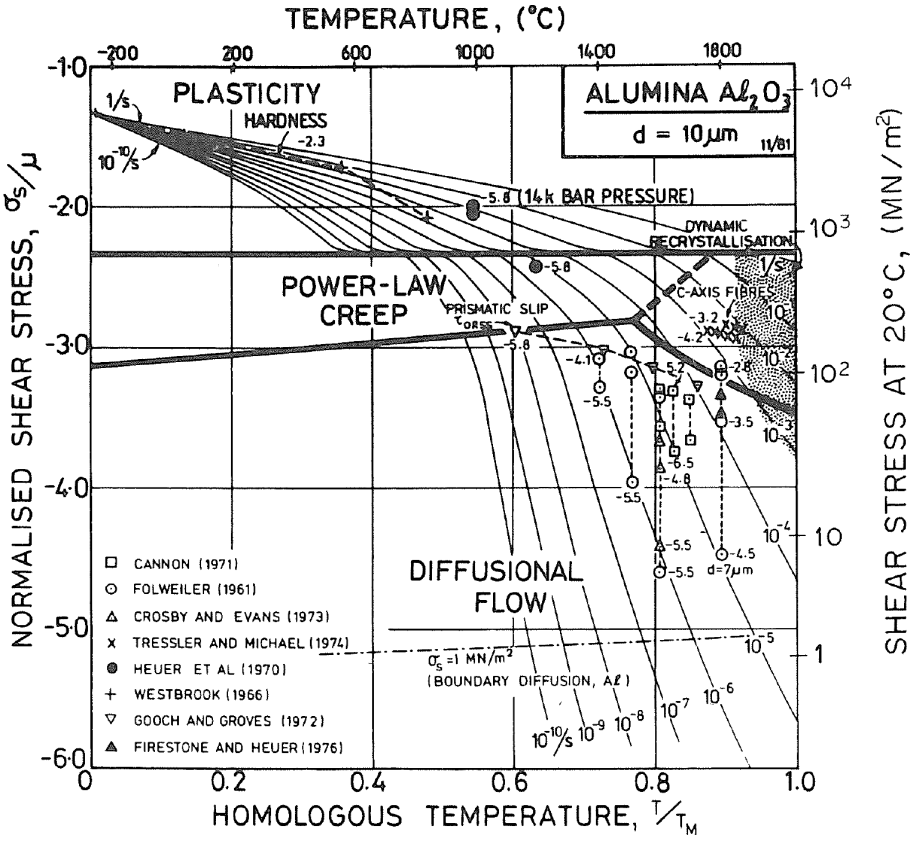

Figure 2.11: A stress/temperature map of Al_2O_3 with a grain size of 10 μm. Data are labeled with $\log_{10}\dot{\epsilon}$ [79]. ($\dot{\epsilon}$ = strain rate)

mainly atomic diffusion in the solid state, but also vapor transport, occurs. The solid state sintering process can be divided into three sequential stages referred to as (1) the initial stage, (2) the intermediate stage, and (3) the final stage. A stage represents an interval of time or density over which the microstructure is considered to be reasonably well defined [169]:

1. During the initial stage, also called pre-sintering, necks are formed between interconnecting particles by removing the large initial differences in surface curvature. As depicted in figure 2.12, the dominant transport mechanisms are surface diffusion (1), lattice diffusion (2) and vapor transport (3) emanating from the particle surface. The pre-sintering stage is assumed to last until the radius of the neck between the particles has reached a value of 40%-50% of the particle radius. This corresponds to a small linear shrinkage of (3% to 5%) and slight increase in density (e.g. from 50%-60% to about 65%).
   In the dissertation, the alumina parts which went only through the initial solid state sintering stage, will be denoted as pre-sintered parts. In order to strengthen the brown parts, only necks are formed between the submicrometer alumina particles. This is done by applying the following furnace cycle in air at atmospheric pressure: a heating rate of 5°C/min

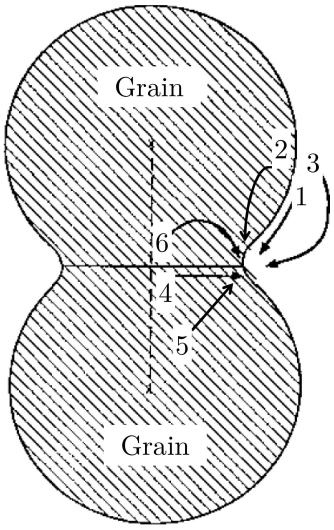

Figure 2.12: Schematic indication of the distinction between densifying (left) and nondensifying (right) microstructural changes resulting from atom transport during the firing of ceramic powders [169].

and dwell time of 2 hours at 1050°C followed by furnace cooling (figure 2.13a).

2. During the intermediate stage, a grain boundary is formed between the crystalline particles. As depicted in figure 2.12, the dominant transport mechanisms are grain boundary diffusion (emanating from the grain boundary, (4)) or lattice diffusion (emanating from the grain boundary (5) or from movement through dislocations (6)). The intermediate stage normally covers the major part of the sintering process, and it is taken to end when the density is 90%-95% of the theoretical density. The intermediate stage ends when the pores start to pinch off, leaving isolated pores.

3. The final stage begins when the pores pinch off and become isolated at the grain corners. In one of the simplest descriptions, the pores are then

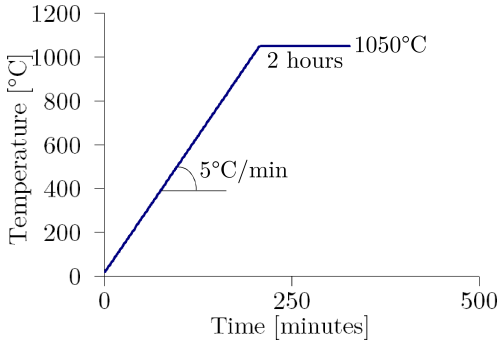

(a) Pre-sintering

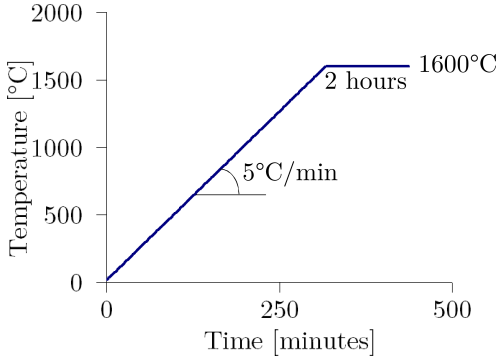

(b) Solid state sintering

Figure 2.13: Commonly used furnace sintering cycles.

assumed to shrink continuously and may disappear altogether.
In reality, the different transport processes lead to either densification and concomitant shrinkage of the body by removing material from the grain boundary region or by moving dislocations (figure 2.12: 4, 5, 6), or to coarsening of the microstructure. Microstructural coarsening is caused either by rearrangement of matter between different parts of the pore surfaces without actually leading to a decrease in the pore volume and concomitant shrinkage (figure 2.12: 1, 2, 3) or by the jumping of atoms over the grain boundaries (not depicted in figure 2.12). A common difficulty in the final stage is that coarsening may dominate the densification process. As a result, high densities are difficult to achieve, restricting the mechanical properties of the final parts. This is mainly the case for highly covalent ceramics (e.g. SiC, which only has a 12% ionic character [34]). Alumina, the material of subject in the dissertation, is a lower covalent ceramic (63% ionic character [34]) with a melting temperature of 2073°C. Therefore, it can be solid state sintered at 1400-1650°C. Possible coarsening of alumina can be reduced by the addition of zirconia or magnesia to 'pin' the grain boundaries.
In the dissertation, the alumina parts which went through the three stages of the solid state sintering process will be denoted as 'solid state sintered parts' (SSS parts). Generally, the submicrometer alumina particles of the brown parts, obtained after indirect SLS and furnace debinding (or direct SLS/SLM), are solid state sintered (SSS) in a furnace in air at atmospheric pressure to form the final part. This means that the brown parts underwent the initial, intermediate and final stage of the SSS process. In order to do so, a heating rate of 5°C/min is applied with a dwell time of 2 hours at 1600°C, followed by furnace cooling (figure 2.13b).

2.4.5.2 Liquid Phase Sintering

As reported in the previous paragraph, highly covalent ceramics have coarsening problems if they are solid state sintered. For these materials, liquid phase sintering is a solution. Liquid-phase sintering is the sintering of a powder in the presence of a liquid [34]. An additive can be used which forms a small amount of liquid phase between the particles at the sintering temperature. The addition of 5-10 wt% of MgO to Si_3N_4 is a classic example favouring liquid-phase sintering in ceramics [169].
During the initial sintering stage, capillary forces rearrange the particles. The liquid phase provides a high diffusivity path for transport of matter, occurring in the second 'solution-reprecipitation' stage (i.e. contacts under pressure/curved surfaces are dissolved, transported in the liquid phase and

reprecipitate on surfaces with smaller curvatures). If no (or a relatively small) external pressure is applied, the last stage of the liquid phase sintering process is generally characterized by the occurrence of 'solid state sintering' and microstructural coarsening (see section 2.4.5.1).

2.4.5.3 Viscous sintering

Viscous sintering occurs when a compact of glassy particles is heated to such a high temperature that the glass becomes a viscous creeping fluid [216]. Liquid present at the sintering temperature flows under the action of the capillary forces of the pores to fill up the porosity of the body [169].

2.4.6 Post-AM densification (post-SLS densification)

Most of the empirical work of the dissertation is about producing ceramic parts through indirect SLS of composite powder agglomerates which contain submicrometer α-alumina powder and a polymeric binder phase. Although this method enables the production of crack-free green parts, the final density after debinding and furnace sintering is generally low since the powder agglomerates do not collapse, which results in a porous microstructure. In order to improve the final density of the parts, additive manufacturing processing strategies (remelting) and powder metallurgy processing techniques (isostatic pressing or infiltration) are investigated. The aim of the post-densification strategies is to eliminate microstructural porosities by rescanning SLSed powder agglomerates (remelting, figure 2.14a), compressing the agglomerates (isostatic pressing, figure 2.14b) or filling up the pores between the agglomerates through impregnation (infiltration, 2.14c).

2.4.6.1 Remelting

Remelting means to laser scan the powder layers multiple times instead of only once. Remelting is vastly studied for Selective Laser Melting (SLM) of metals. It is used to improve the part properties like surface roughness, hardness and density [115, 117, 120, 233, 237]. Through increasing the density of the green parts, remelting during SLS has the possibility to also improve the density of the fabricated final parts.

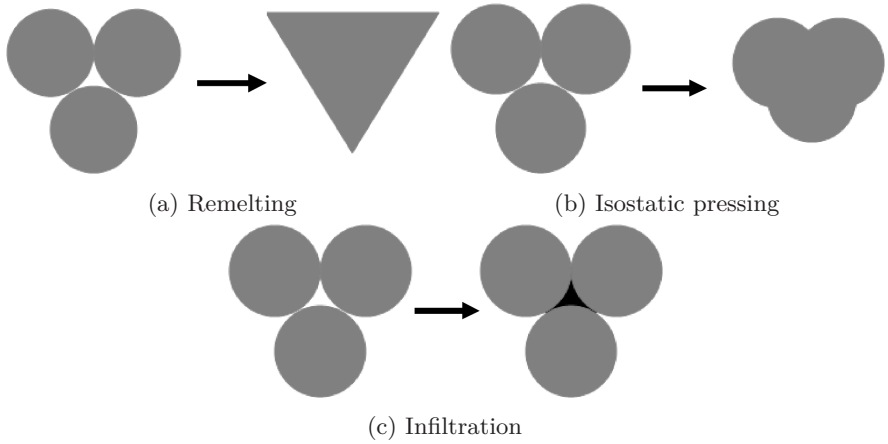

(a) Remelting (b) Isostatic pressing

(c) Infiltration

Figure 2.14: Schematic of the different investigated post-SLS densification strategies.

2.4.6.2 Isostatic pressing

A first strategy to improve the density of parts is to encapsulate and isostatically press (IP) them afterwards. Different IP techniques exist, which all differ in the sense that other pressure transferring media are used: hot isostatic pressing (HIP; a high temperature gas), quasi isostatic pressing (QIP; powder), cold isostatic pressing (CIP; a liquid at room temperature) and warm isostatic pressing (WIP; a heated liquid). CIP, QIP and WIP are generally applied on green parts before debinding and solid state sintering. Prior to the CIP and WIP process, the green parts are encapsulated in a vacuum atmosphere.

Hot isostatic pressing Hot isostatic pressing (HIP) can only be applied on a part that does not contain a polymeric binder. During HIP, the gas is generally heated to very high temperatures (>800 °C). As a result, freeform shapes can not be encapsulated in a rubber sheath or bag (mold): the encapsulating material would degrade at the high temperatures. Nevertheless, HIP is already studied in combination with SLS for the production of metal parts [14, 46, 47, 48, 49, 135, 142, 226]. Different alternatives to combine SLS and HIP can be formulated. They differ in the way the sample is encapsulated prior to the HIP process.

- Ex-situ vacuum encapsulating (i.e. 'canning') of the SLSed parts in a metal container or can. This method is mainly applied together with

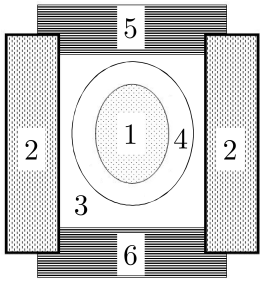

1. Powder or encapsulated porous part
2. Pressure vessel
3. Pressure transferring medium
4. Rubber sheath or bag (mold)
5. Top cover
6. Bottom cover

Figure 2.15: Schematic illustration of different IP techniques: (wet bag) cold isostatic pressing 'CIP', warm isostatic pressing 'WIP', quasi isostatic pressing 'QIP' and hot isostatic pressing 'HIP'. QIP and HIP do not use a rubber sheath or bag to encapsulate the powder/SLSed part. HIP may use 'canning' to encapsulate the sample to be densified.

indirect SLS, since closed porosity of the part is not required before the HIPing step. It is similar to the conventional HIP process, where powder is vacuum encapsulated by a metal can, prior to HIPing. Freeform shapes can be encapsulated ex-situ, if the parts are buried into a powder: e.g. indirectly SLSed AISI304 stainless steel parts could be HIPed after pre-sintering and ex-situ encapsulation in boron nitride powder [135].

- In-situ encapsulating by direct sintering of an integral, dense, gas impermeable skin or 'can' at the part boundaries under vacuum atmosphere. The skin has a density exceeding 92% theoretical density. This is the fractional density at which porosity typically changes from interconnected or surface-connected to closed. The powder in the interior of each layer cross-section is generally laser sintered to an intermediate density of about 80%. [46, 47, 48, 49, 226].

The benefit of ex-situ encapsulation is that the part to be HIPed can have an open porosity. However, adverse container-part interactions can occur and tooling and pre-processing steps are associated with container fabrication and filling.
In-situ encapsulation eliminates the adverse container-powder interactions and post-HIP container removal is not required. Tooling and pre-processing steps associated with container fabrication and filling are also eliminated.

Cold isostatic pressing Cold isostatic pressing (CIP) is commercially used to produce homogeneous and high density (up to 60%) green powder compacts with increased shape complexity by applying pressure from multiple directions.

The CIP technology can be divided into a wet bag or dry bag approach. During wet bag isostatic pressing, the CIPing method used in the dissertation, the powder is encapsulated in a rubber sheath or bag (mould) that is immersed in a liquid that transmits the pressure uniformly to the powder (see figure 2.15). Dry bag presses have a bag as an integral part of the pressure vessel and are used when many parts of simple geometry have to be made.
Since the shape of the parts is maintained during wet bag CIPing, combined indirect SLS and wet bag CIPing can be used as a net shaping technique to produce dense parts. CIPing has been used to produce AISI 304 stainless steel parts by SLS [66, 135, 142]. CIP has also been used to densify ceramic components produced through 3D printing [243] and SLS [136].

Quasi isostatic pressing During quasi isostatic pressing (QIP), a process which is also known as the Ceracon process [142, 161], powder particles are used instead of a liquid as pressure transmitting medium (figure 2.16). It is not needed to encapsulate SLSed samples in a rubber sheath or bag (mold) before isostatically pressing. Moreover, QIPing can be performed at elevated temperatures, which enable the binder to plastically deform during isostatic pressing. On the other hand, since the pressure is only applied in one direction during the QIP process, the concomitant shrinkage is non-uniform. The non-isostatic stress state will in general result in shape distortion in addition to densification [161]. Nevertheless, QIP has been used to fully densify alumina-glass composites fabricated by a selective laser sintering process [122].

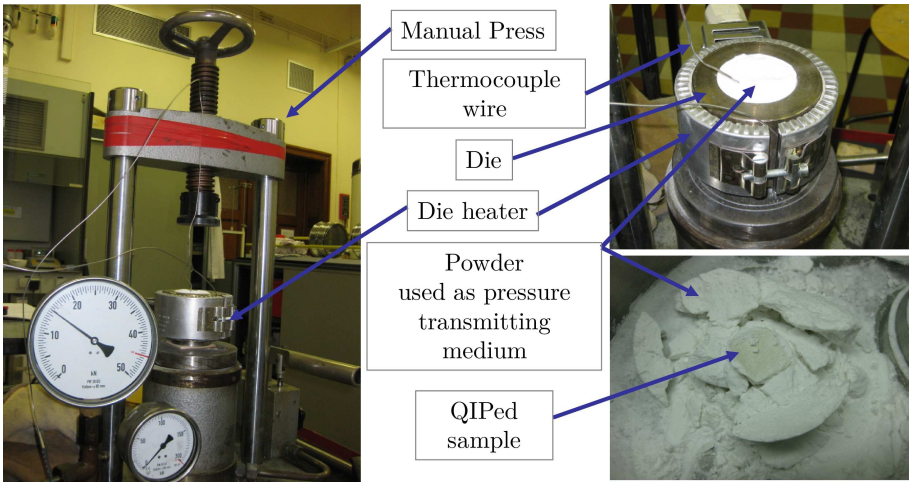

Figure 2.16: Quasi isostatic pressing QIP.

Warm isostatic pressing Although during warm isostatic pressing (WIP, figure 2.15) the SLSed samples need to be encapsulated in a rubber sheath or bag (mold) before isostatically pressing, it combines the benefits of both CIP and QIP. By using a heated liquid as pressure transferring medium, an isostatic pressure can be uniformly applied on the SLSed sample and the binder material can be plastically deformed.
WIPing was already used to produce metal [229] and ceramic [81] parts. WIPing has also been used to densify alumina parts produced through 3D printing [243]. Nevertheless, the combination of WIPing and indirect SLS is new.

Discussion In this dissertation CIP, QIP and WIP were investigated as possible IP techniques to increase the density of the final parts. No experiments which combine SLS and HIP were performed. It would be very difficult to eliminate the adverse container-part interactions if ex-situ HIPing would be applied. The aim was rather to investigate the additive production of closed porosity alumina parts which can be HIPed in future research, without applying the ex-situ 'canning' step.

2.4.6.3 Infiltration

Infiltration methods were successfully used to increase the final density of parts, produced through indirect SLS. As an example, Stevinson et al. [190] infiltrated SiC ceramic preforms with Si. Further, Subramanian et al. [194] reported that green part infiltration with small quantities of alumina colloids largely improved the green part strength during debinding and solid state sintering. In this dissertation, the idea of Subramanian is further explored. Green parts, pre-sintered parts and/or solid state sintered parts (SSS parts) were infiltrated with stable suspensions containing submicrometer α-alumina particles (grade SM8, Baikowski, France [3]). Pressureless infiltration tests, i.e. dipping without external pressure, as well as pressure infiltration and vacuum infiltration tests were performed.

2.4.7 Characterization

This dissertation investigates the quality of the components during the different processing steps through density measurements, geometrical assessments and microscopic and macroscopic imaging. The section first briefly describes the methods and devices which are used to characterize the PM processing steps.

In the second subsection, the performed geometrical assessments are discussed more elaborately.

2.4.7.1 Methods and devices

The following methods and devices were used to characterize the density, geometry and microscopic and macroscopic features of the parts obtained at different steps of the PM process.

Density The density is assessed through measurements with an accurate balance (Analytical Balance, Sartorius, Germany). The following methods are used to measure the density of the parts: the geometrical method, the red lacquer Archimedes method, the Archimedes method without lacquer and the Archimedes method without lacquer but with correction measurement for open porosities. In the latter method, the weight of the part is measured three times: first in air, then immersed in ethanol, and at last again in air in order to know the amount of ethanol that entered the pores of the part during the second measurement.

Geometrical assessments The geometrical assessments are realized with a coordinate measuring machine (CMM, FN905, Mitutoyo, Japan) or a vernier caliper (Mitutoyo, Japan). The reported roughnesses are measured with a Talysurf-120L (Taylor-Hobson, UK).

Microscopic and macroscopic imaging The microscopic images are assessed with a digital camera, 3D microscopy (Discovery.V20, Carl Zeiss Inc., Germany) or scanning electron microscopy (SEM, XL30 FEG, FEI, The Netherlands). The outer shapes of the parts are figured with the digital camera. Internal, cross-sectional images are taken with the 3D microscope or SEM. In order to take the cross-sectional images, the parts were cut with a diamond blade, embedded in an epoxy resin, and ground. Secondary (SE-SEM), and backscattered electron (BSE-SEM) SEM images are taken.

2.4.7.2 Geometrical assessments

As schematically presented in figure 2.17, geometrically assessing different steps of the powder metallurgical process to produce alumina parts through SLS (SLM) can be done qualitatively or quantitatively. Parts produced at different

stages of the powder metallurgical process can be qualitatively analyzed by assessing the trueness of features as sharpness of corners and edges [153]. Quantitatively, these parts can be geometrically characterized by assessing the roughness and dimensional parameters, i.e. the resolution, the repeatability and the accuracy. The minimum resolution of the process is dependent on the particle size and shape [153], and the laser beam diameter. The repeatability of the parts depends on the controllability of the different processing steps. E.g. in order to have a good repeatability, curling of the parts during the SLS (SLM) process should be reduced. This can be done by both increasing the preheating temperature of the SLS (SLM) process and decreasing the laser energy input. The most important geometrical parameter is the accuracy of the parts.
Previous research mainly focused on the accuracy of the SLS process. The accuracy of the SLSed parts can be improved by introducing scale factors, x-y beam offset and z-compensation (figure 2.18).

- Scale factors are introduced to compensate for the dimensional shrinkage which occurs during cooling down the parts, just after production by SLS at elevated temperature. As can be seen in figure 2.19, the shrinkage is material dependent.
- As can be read in the manual of the DTM Sinterstation 2000 machine [13], x-y beam offset adjusts the outline of a part to compensate for the width of the melted region by the laser beam. Sintering is comparable to drawing with a wide-tipped marker. Since the laser beam will trace a path with the center of the beam moving to the intended boundary of the part, the resulting part will be bigger than intended. Figure 2.20a illustrates this. To compensate for the actual boundary being larger than the intended boundary, x-y beam offset moves each vertex of the part inward. This compensated boundary makes the outside edge of the laser beam's footprint touch the intended boundary (figure 2.20b).

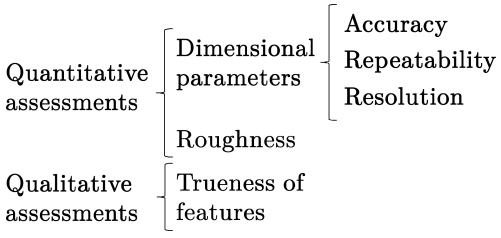

Figure 2.17: Different ways to geometrically assess the powder metallurgical process.

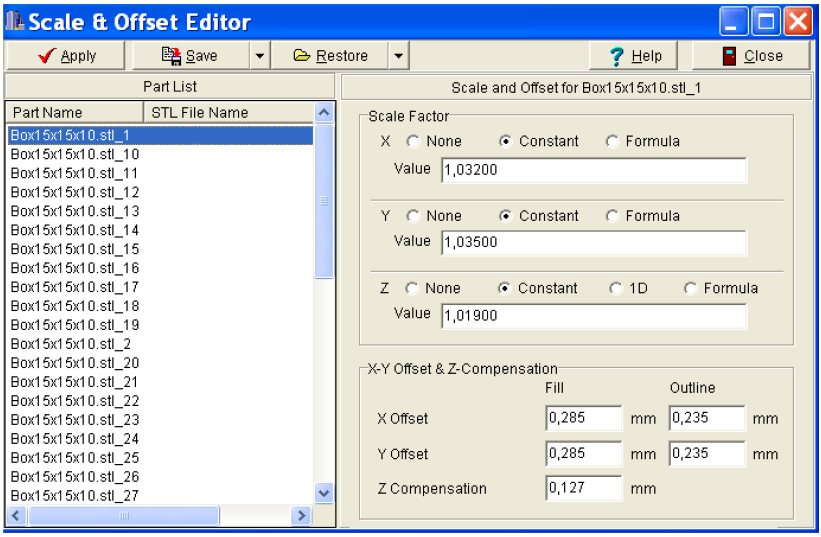

Figure 2.18: Scale and offset editor of a DTM Sinterstation 2000 SLS machine.

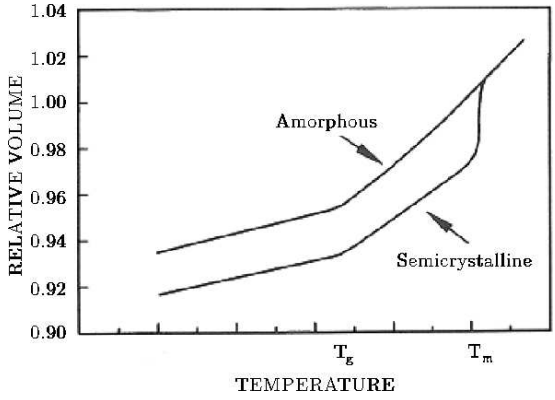

Figure 2.19: Relative volume of an amorphous and a semi-crystalline polymer as function of temperature [22].

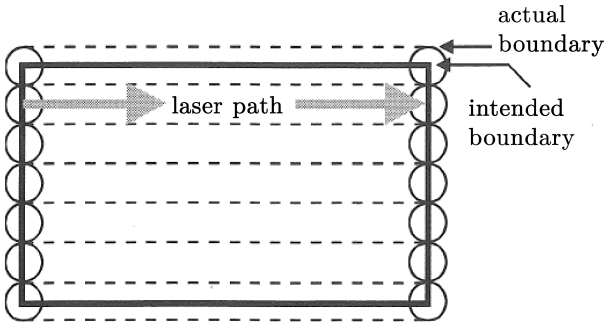

(a) Actual and intended part boundary.

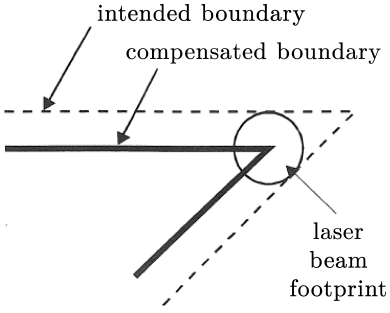

(b) Intended and compensated boundary.

Figure 2.20: x-y offset [13].

- The thermal conductivity of a powder is about 10 times lower compared to the thermal conductivity of a solid of the same material. This makes dissipation of the heat introduced by the laser beam more difficult during the first layers of the SLS process. As a result the first layers of the SLS process are generally thicker as the predefined layer thickness. A 'dross' (also called z-bonus [28]) is formed. Geometrical inaccuracies introduced through dross formation in the build 'z' direction can be eliminated by z-compensation.

Sercombe and Hopkinson [181] have shown that dimensional errors are dependent on the position of the part inside a DTM Sinterstation 2500 machine. The reason for this effect may be explained by the non uniform temperature profile of the part bed during production. They also have shown that the dimensional errors are larger for smaller dimensions and are directional dependent. This means that the software tools of the DTM Sinterstation 2000 (figure 2.18), which is the predecessor of the DTM Sinterstation 2500, are not

sufficient to fully optimize the dimensional accuracy.

The dissertation does not focus on optimizing the geometrical accuracy of the (indirect) SLSed parts. Instead, the trueness of different features of the parts is qualitatively assessed at different stages of the powder metallurgical process. For different starting powders, the change of roughness and percentage shrinkage of the (indirect) SLSed parts during post-processing (i.e. debinding, post-densification and furnace sintering) is investigated (figure 2.21). As illustrated by Stevinson et al. [190], different dimensional changes can take place at different post-processing stages. In this dissertation, the percentage linear shrinkage in the scan (x), cross-scan (y) and build (z) direction is defined as

$$\%linearshrinkage_{x,y,z} = \frac{dimension\,after\,post\text{–}processing\ -\ green\,part\,dimension}{green\,part\,dimension}$$

As can be seen in the formula above, the green part dimensions (i.e. the part dimensions after the SLS process) are taken as a reference to calculate the dimensional change. These dimensions are either measured by a coordinate measuring machine (a CMM) or a vernier caliper.
In the dissertation, the measured shrinkage is caused by

- (mostly) attractive capillary forces during debinding (Rahaman [169]; Megias-Alguacil and Gauckler [147]).
- attractive van der Waals forces after debinding and before solid state sintering
- shrinkage due to atomic diffusion (i.e. diffusion of aluminum and oxygen atoms) during SSS
- sometimes: cracks and curling (deformation) due to inhomogeneous shrinking in the debinding and/or SSS step

The largest amount of shrinkage is caused by atomic diffusion during SSS, which is also called 'sintering shrinkage' or shrinkage due to the sintering pressure. In order to understand this, the basic thermodynamic driving force for sintering has to be considered. The basic thermodynamic driving force for sintering is a decrease in the surface free energy of powdered compacts, by replacing high-energy solid-vapor interfaces (pores with surface energy γ_{SV}) with lower-energy solid-solid interfaces (grain boundaries with surface energy γ_{GB}), thus $\gamma_{GB} < \gamma_{SV}$. The change of system Gibbs free energy dG due to sintering is therefore composed of the increase due to the creation of new grain boundary areas, $dA_{GB}>0$, and due to the annihilation of vapor-solid interfaces, $dA_{SV}<0$.

The necessary global thermodynamic condition for sintering to proceed is:

$$dG = \gamma_{SV} dA_{SV} + \gamma_{GB} dA_{GB} + p_{ext} dV < 0 \tag{2.1}$$

With the total pore surface A_{SV}, the total grain-boundary area A_{GB}, the total volume of the system V and an externally applied pressure p_{ext}. The last term represents the work done against an externally applied pressure (e.g. during HIPing).
The first term of equation 2.1, $\gamma_{SV} dA_{SV}$, is commonly expressed as an equivalent externally applied pressure. This pressure is called the sintering pressure ($p_{sintering}$), sintering stress, the sintering potential or driving force for pore closure. It reflects the effective stress on the atoms under a pore surface and can be calculated by equating the work during compression of a bubble or void with the corresponding decrease in surface energy.

$$p_{sintering} dV = \gamma_{SV} dA_{SV} \tag{2.2}$$

For a surface with two principal curvatures r_1 and r_1, this equation is equivalent to:

$$p_{sintering} = \gamma_{SV} \left(\frac{1}{r_1} + \frac{1}{r_2} \right) \tag{2.3}$$

For ceramics, the surface energy is typically 1 to 2 J/m^2. This means that for submicrometer powder, with an inter particle space of 1 μm, the sintering pressure $p_{sintering}$ equals to 2 to 4 MPa.

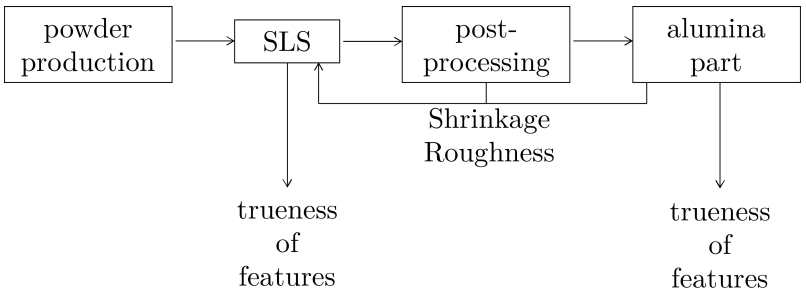

Figure 2.21: Geometrical assessments performed in the dissertation.

2.5 Summary and conclusions

At the beginning of the dissertation, no research on additive manufacturing (AM) of ceramics had been performed at KU Leuven. In order to guide the research on AM of ceramics and the dissertation, the current ceramic industry and technology was investigated. It was found that ceramics are not as widely used in industry as they should and could be. The main reason for the reluctance within industry is the high, both fixed and variable, production costs of ceramic parts. It was understood that, since AM has the ability to deliver fast ceramic functional prototypes, it has the ability to drastically reduce the fixed costs associated with the engineering of a ceramic part for a certain application.

In order to successfully use additive manufacturing to reduce the fixed costs associated with the production of ceramic components, a research mission, research strategy and (both long and short term) research goals were defined. In this context, it was decided that in this dissertation AM will be used as primary shaping step of a powder metallurgical (PM) process to produce ceramic parts. In this way, a PM process consisting of the following main steps will be investigated: powder production, AM, (optionally) debinding and furnace sintering.
The long term research goal was to rapidly produce high quality technical ceramics through AM. The more pragmatic short term goal was to produce ceramic parts and join the international discourse. The aim of the pragmatical goal was to gain insight in ceramic processing through AM and in this way objectively optimize the production process.

At last, this chapter described more specifically how the research mission, strategy and goals were implemented in this dissertation. Since alumina is the most widely used ceramic for technical ceramics, α-alumina was chosen to become the ceramic material to study.
In order to implement the short term research goal, it was decided to further explore indirect Selective Laser Sintering. This process forms the empirical core of the dissertation: as described in the next four chapters and the appendix, indirect SLS of five powders (produced by four alternative, in-house developed methods) was thoroughly investigated in order to produce alumina parts. Furthermore, in order to indirectly SLS alumina parts with increased density, the following post-AM densification techniques were investigated as extra steps of the PM process: remelting, isostatic pressing and infiltration.
As a first attempt to implement the long term research goal, it was decided to process α-alumina through direct Selective Laser Sintering/Melting (direct SLS/SLM). As detailed in chapter 7 of the dissertation, for this purpose an experimental setup was designed, constructed and tested.

Both for the production of alumina parts through indirect SLS and direct SLS/SLM, the different steps of the PM process were assessed through density measurements, microscopic imaging and macroscopic imaging. For the production of alumina parts through indirect SLS, the different steps of the PM process were also assessed through geometrical assessments.

Chapter 3

Production of alumina parts through Laser Sintering of ball milled polyamide-alumina agglomerates

> There is grandeur in this view of life, ... [that] from so simple a beginning endless forms most beautiful and most wonderful have been, and are being evolved.
>
> Darwin, Charles Robert [23, 45]

Reference: *Deckers, J., Shahzad, K., Vleugels, J., Kruth, J. (2012). Isostatic pressing assisted indirect selective laser sintering of alumina components. Rapid Prototyping Journal, 18 (5), 409-419. [58]*

3.1 Structured abstract

Purpose The purpose of this chapter is to assess a new powder metallurgy process to make alumina parts through indirect Selective Laser Sintering (SLS).

Density measurements, some geometrical assessments and scanning electron microscopy (SEM) microstructural analyses were performed after each stage of the process, allowing to provide an objective overview of the challenges and possibilities for the processing of high density technical ceramic parts through SLS of ball milled alumina/polyamide powder agglomerates.

Design/methodology/approach The powder production by ball milling, SLS, cold isostatic pressing (CIP) or quasi isostatic pressing (QIP), debinding and sintering (FS) stages of the powder metallurgy process were sequentially investigated.

Findings Alumina parts with a density up to 92.6% could be produced by a powder metallurgy process containing an SLS step. Microstructural investigation of the sintered ceramics revealed an alumina matrix with a grain size of $\sim$5 μm and two different kind of pore morphologies, i.e. long elongated pores, which originated from the intergranular spacings during SLS, and intermediate pores, which likely originated from polyamide agglomerates in the ball milled powder. Besides, QIPing at elevated temperatures was found to be a good alternative for CIPing at room temperature to increase the final part density.

Research limitations/implications Cracks, long elongated pores and intermediate pores remained in the sintered parts. Homogenizing the microstructure of the parts through optimizing the composite starting powder, the deposition during SLS, the SLS parameters and QIPing parameters is essential to overcome these limitations.

Practical implications Homogenizing the starting powder mixture and the microstructure of the SLS material is the key issue for producing ceramic parts through indirect SLS.

Originality/value Indirect SLS of ceramics has hardly been reported and the combined use of SLS and QIPing is innovative in the field of indirect SLS of ceramics.

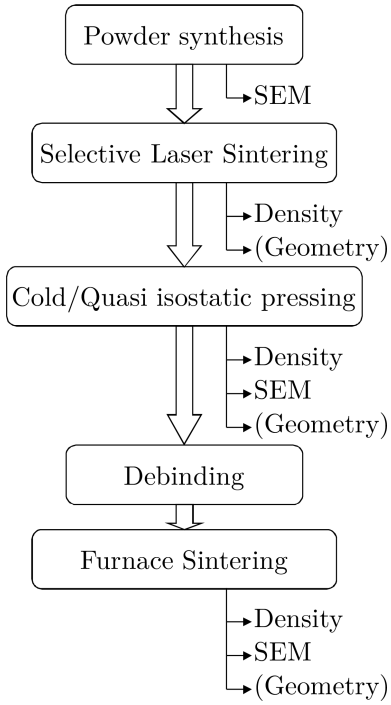

Figure 3.1: Powder metallurgy processing flow chart.

3.2 Powder metallurgy processing flow chart

The ceramic processing flow chart assessed in this chapter is schematically presented in figure 3.1. First a composite alumina/polyamide powder was produced by planetary ball milling. Parts were made from this powder by Selective Laser Sintering in a DTM Sinterstation 2000. During the SLS process, a laser beam melted the polyamide 12 (PA12; $T_m = 179°C$), which glued the ceramic alumina ($T_m = 2072°C$) particles together into a three dimensional green part. In a next step, the green SLS part was additionally densified by isostatic pressing. Cold isostatic pressing (CIP) as well as quasi isostatic pressing (QIP) experiments were performed (see section 2.4.6.2 for more explanation on CIP/QIP). Finally, the polyamide material was removed in a low temperature debinding process and the remaining 'brown' alumina part was densified by a high temperature thermal process in a sintering furnace.

The chapter investigates each of the above processing steps in detail. The quality of the component was assessed by density measurements, some geo-

metrical assessments and scanning electron microscopy (SEM) microstructural analyses after almost every stage of the powder metallurgy process. In this way, the chapter gives an objective view on the feasibility of processing high density technical ceramic parts through SLS of ball milled alumina/polyamide composite powders in a DTM Sinterstation 2000 machine.

3.2.1 Difference with PM processes described in literature

In summary, the PM process described in this chapter differs from the ones described in literature in two ways:

1. The semi-crystalline polyamide 12 is used as polymer binder.
2. The post-densification strategies cold isostatic pressing (CIP) and quasi isostatic pressing (QIP) are tested.

3.3 Production and investigation of the parts

3.3.1 Powder production

To fabricate alumina samples via indirect SLS, high purity α-alumina (figure 3.2a: grade SM8, Baikowski, France) powder with a d_{50}∼0.3 μm was used as structural material and polyamide 12 with a d_{50}∼100 μm (figure 3.2b: grade Duraform PA, 3DSystems, USA) was used as binder phase. Alumina with 22 wt% (= 53 vol%) PA mixtures were prepared by high energy ball milling of both starting powders in a planetary ball mill (PM 400, Retsch, Germany) for 6 hours at 200 rpm. To minimize contamination during ball milling, ZrO_2 containers and 10 mm diameter ZrO_2 balls (grade TZ-3Y, Tosoh, Japan) were used as milling medium. The powder to milling ball weight ratio was 1:2. Before SLS, the milled powder was sieved through a 200 μm sieve. An overview and detail of the milled composite powder are shown in figure 3.2c and 3.2d respectively.

3.3.2 Selective Laser Sintering

Green samples were fabricated using a Sinterstation 2000 (DTM Corporation / 3DSystems, USA) equipped with a 100 W CO_2 laser (f100, Synrad, USA) with a wavelength of 10.6 μm and a laser beam diameter ϕ_{1/e^2} of 400 μm. Powder layers were deposited by a counter rolling roller and irradiated with

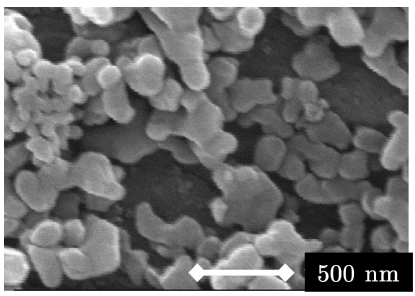

(a) SM8 alumina powder

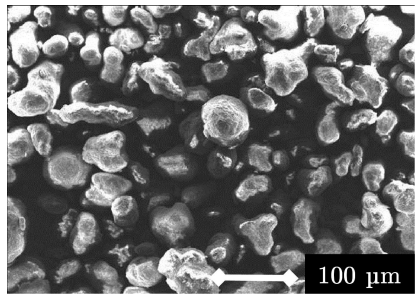

(b) Polyamide 12 powder

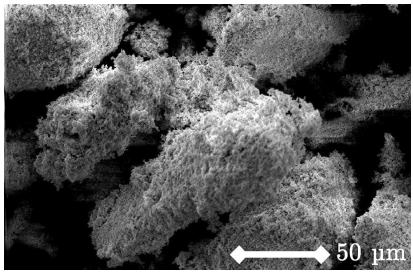

(c) Overview of the milled composite powder

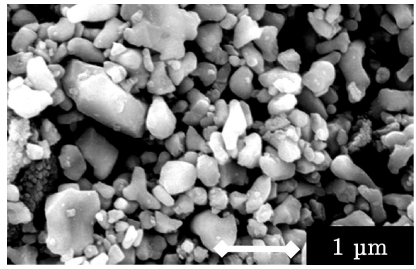

(d) Detail of the milled composite powder

Figure 3.2: Production of composite powder through ball milling.

the laser beam. In order to avoid thermal oxidation, SLS was performed in N_2 atmosphere (Air Liquide, Belgium, $[O_2] < 5$ %). In order to improve the laser sinterability of the powder and to avoid thermal cracks, the parts were produced at elevated temperature. The powder preheating parameters were found to be similar to the standard preheating parameters for SLS of pure Duraform PA powder (without alumina addition). The energy required to melt PA was partly supplied by preheating of the powder bed to a temperature slightly below the melting point of 179°C (distributed cylinder heating and surface IR heating) and by extra laser irradiation which locally raised the temperature above the melting point.

To produce green parts by indirect SLS, the machine and laser scanning parameters had to be tuned in such a way that the binder phase was locally heated between its melting and degradation temperature. In this study the local temperature profile of the powder bed during laser irradiation was controlled by varying the laser power P, the laser beam scan speed v, and the laser beam scan spacing s. For each set of parametrical experiments, the layer thickness l, was kept constant. The laser energy density e, combining

these parameters is an important parameter. It can be defined by dividing the laser energy per unit time which irradiates the powder particles (as an input parameter; P) by the material consolidation rate (as output parameter; MCR).

$$e = \frac{P}{MCR} \tag{3.1}$$

Since the material consolidation rate can be defined as the product of the scan spacing s, scan speed v, and layer thickness l, the laser energy density can be written as:

$$e = \frac{P}{s.v.l} \tag{3.2}$$

This equation shows that the energy density is increased by increasing the laser power and decreasing the scan spacing, scan speed and layer thickness.

In order to produce alumina parts, strong enough for further processing, a parametrical study was executed. In a preliminary set of experiments, which was based on the SLS parameters of pure polyamide, parts of 15x15x10 mm^3 were produced with a laser power, scan speed and scan spacing varying between 3-5 W, 400-1250 mm/s and 150-350 μm respectively. The SLS layer thickness was kept constant at 100 μm. At laser energy densities below 0.2 J/mm^3, the parts were too fragile and could not be taken out of the SLS machine without breaking. At laser energy densities above 0.4 J/mm^3 fumes were formed due to the degradation of PA. Table 3.1 gives some experimental parameters explored in this preliminary set of experiments.

In the main set of experiments, parts with the same geometry (15x15x10mm^3 as x-, y-, z-dimensions) were produced. This time the formation of smoke was not avoided. The scan speed and scan spacing were respectively 300-600-900 mm/s and 150-250-350 μm (figure 3.3). The layer thickness was kept at 80 μm and the laser power was chosen to be 3-5-7 W.
Despite the formation of fumes when the laser energy density was above 0.4 J/mm^3, the green parts produced with 7 W were found to be stronger than those produced with 3 or 5 W. This is due to the viscosity of the PA, which

Parameter combination	laser power, P [W]	scan speed, v [mm/s]	scan spacing, s [µm]	energy density, e [J/mm^3]
P1	3	400	300	0.25
P2	5	500	300	0.33
P3	3	500	250	0.24

Table 3.1: Preliminary set of experiments: parameters of some SLS samples.

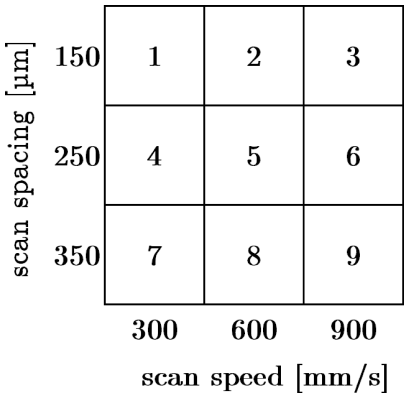

Figure 3.3: Parameters applied in the main set of SLS experiments.

decreases at higher temperatures. When irradiating with higher laser energy densities, the binder material will be heated. Since the viscosity of the binder decreases with increasing temperature, the binder will plastically flow and bind the composite powder agglomerates.
Due to the higher part strength, most parts further discussed in this chapter were produced with 7 W. Since the produced green parts were still too fragile to be covered with a lacquer, the density of the green parts could not be measured by the Archimedes method. Instead, the green density of the parts, scanned with the highest laser energy (parts 1, 2, 3, 4, 5 and 7), were calculated from the measured weight and geometry, as summarized in the second column of table 3.2.

During different stages of the powder metallurgy process, the x-, y- and z-dimensions of the parts were measured by using a Vernier caliper (see table 3.3). The dimensions of the parts after SLS are summarized in columns 2, 3 and 4 of table 3.3. Notice that the nominal dimensions of the SLS green parts were 15x15x10 mm^3. Offset values as defined in figure 2.18 were used.

After depositing the composite agglomerates with the counter-current roller of the DTM Sinterstation 2000, the quality of the deposited layers was not very good. At some places, the deposited powder bed contained small, but visible craters. The occurrence of these craters prior to the laser sintering process and also the fragility of the parts after SLS, made the production of complex shapes impossible.

Laser power: 7 W	Laser energy density [J/mm³]	Density after SLS [g/cm³]	Density after CIP [g/cm³]	Weightloss during debinding [%wt]	Density after furnace sintering: absolute [g/cm³] / relative [% of TD]	vol% Al_2O_3 after SLS	vol% Al_2O_3 after CIP
Sample 1	1.944	0.88	1.96	17	3.60 / 90.4 %	18.3	40.8
Sample 4	1.167	0.92	1.75	19	3.50 / 87.9 %	18.7	35.6
Sample 2	0.972	0.95	1.82	20	3.41 / 85.6 %	19.1	36.5
Sample 7	0.833	0.83	1.73	20.2	3.45 / 86.6 %	16.6	34.7
Sample 3	0.648	0.86	1.86	21.1	3.38 / 84.8 %	17.0	36.8
Sample 5	0.583	0.84	1.68	21.3	3.40 / 85.3 %	16.6	33.2
Sample 8	0.417		1.69	21.5	3.38 / 84.8 %		33.3
Sample 6	0.389		1.81	21.6	3.37 / 84.6 %		35.6
Sample 9	0.278		1.73	22	3.32 / 83.3 %		33.9

Table 3.2: Measured/calculated properties of the parts produced in the main set of experiments, during different stages of the powder metallurgy process.

Laser power: 7 W	Laser energy density [J/mm³]	Dimensions after SLS [mm]			Dimensions after CIP [mm]			Dimensions after furnace sintering [mm]		
		X	Y	Z	X	Y	Z	X	Y	Z
Sample 1	1.944	15.0	15.0	9.0	12.0	12.0	4.5	9.5	9.0	3.5
Sample 4	1.167	15.0	15.0	10.0	12.5	12.5	5.0	9.5	10.0	4.5
Sample 2	0.972	15.0	15.0	10.0	12.0	12.0	6.0	8.5	9.5	5.5
Sample 7	0.833	15.0	14.5	9.5	12.0	12.0	5.5	8.5	9.0	4.5
Sample 3	0.648	14.0	14.0	10.0	10.0	9.0	5.5	8.0	8.0	4.5
Sample 5	0.583	14.5	14.5	10.0	11.0	11.0	5.5	9.0	8.0	4.5
Sample 8	0.417	13.0	12.5	9.5	9.0	8.0	5.5	7.0	6.5	4.0
Sample 6	0.389							8.0	7.0	4.0
Sample 9	0.278							6.5	5.0	3.0

Table 3.3: Overview: geometrical dimensions during different stages of the powder metallurgy process.

In summary:

- The powder preheating parameters to SLS composite alumina-binder agglomerates and pure binder agglomerates, are similar.
- The laser energy density e, which can be defined as the laser energy per unit time divided by the material consolidation rate MCR, is an important parameter to empirically describe the SLS process. When using too low laser energy densities during SLS of alumina-binder agglomerates, the parts are too fragile to take them out of the SLS machine, without breaking. When using too high laser energy densities, the binder material degrades. The strength of the parts after SLS at high laser energy densities, is a compromise between this material degradation and plastic flowing of the binder material to bind the composite powder agglomerates.
- No complex shapes can be produced from the ball milled composite alumina-PA agglomerates. This is due to the occurrence of small craters on the powder bed after layer deposition and due to the fragility of the parts after SLS.

3.3.3 Cold/Quasi Isostatic Pressing

Since the conventional layer deposition systems, such as roller coater and scraper systems, produce low density powder beds [112], the density of the ceramic parts produced by SLS is low. In order to obtain a high sintered density by solid state pressureless sintering in the final stage of the powder metallurgy process, the relative density of the green parts should be $> 50\%$ [131]. To achieve higher green densities, the SLS samples were vacuum packed in a rubber mould and wet bag CIPed for 1 minute at 200 MPa (EPSI, Belgium). The density of the SLS samples was more than doubled, as summarized in the third column of table 3.2. As depicted in columns 5 and 6 of table 3.3, the x- and y-dimensions of the parts were reduced to about $3/4^{th}$ of their values after SLS, for the parts scanned with higher laser energy densities, or $2/3^{th}$ of their values after SLS, for the parts scanned with lower laser energy densities. The z-dimensions of the parts almost halved (column 7 of table 3.3).
After CIPing, a selection of samples of the main set of SLS experiments were put in an epoxy resin, cross-sectioned and investigated by SEM. Representative backscattered electron (BSE) micrographs revealed large isolated elongated pores: black phase in figure 3.4. The elongated shape of the pores and the distance between the pores suggested that these pores were formed due to fusing of the ball milled agglomerates during CIPing of the green SLS samples.

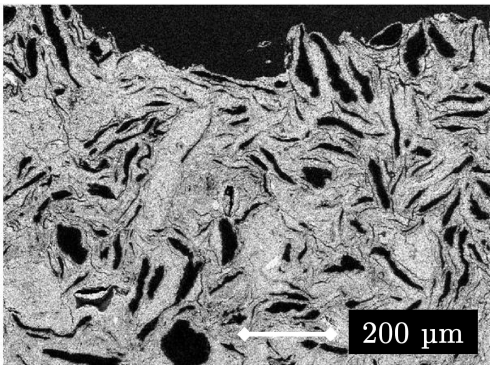

Figure 3.4: Backscattered electron SEM micrographs of an epoxy (black phase) infiltrated CIPed SLS part.

Two samples (denominated as 'Q1' and 'Q2') which were SLSed with a laser power, scan speed, scan spacing and layer thickness of respectively 7 W, 150 mm/s, 300 μm and 80 μm (i.e. laser energy density of 1.944 J/mm^3) were Quasi Isostatically Pressed (QIPed). The difference between QIPing and wet-bag CIPing, is that during QIPing powder particles are used instead of a liquid as pressure transmitting medium. It is also not needed to encapsulate the samples in a rubber sheath or bag (mold) before isostatically pressing. Moreover, QIPing can be performed at elevated temperatures, which enables the PA to plastically deform during isostatic pressing.
As depicted in figure 3.5, for the QIPing process, the SLSed parts were placed in a die of a manual press and surrounded with alumina powder particles ($d_{50}\sim$70 μm). A thermocouple was placed near the parts. After heating the die for approximately one hour to the desired QIPing temperature, the thermocouple was taken out of the powder and a pressure of 20 MPa was applied. If pressures much higher than 20 MPa were applied, the QIPed sample could not be separated from the surrounding powder after pressing. The parts 'Q1' and 'Q2' were QIPed at 165°C for respectively 5 and 15 minutes, but no densities were measured before debinding.

In summary:

- CIP and QIP can be used to increase the density of the SLSed parts.
- During CIP, the part shrinkage is lower in the x- and y- dimensions, than in the z-direction. During CIP, parts SLSed at higher laser energy densities shrink less than parts SLSed at lower laser energy densities.

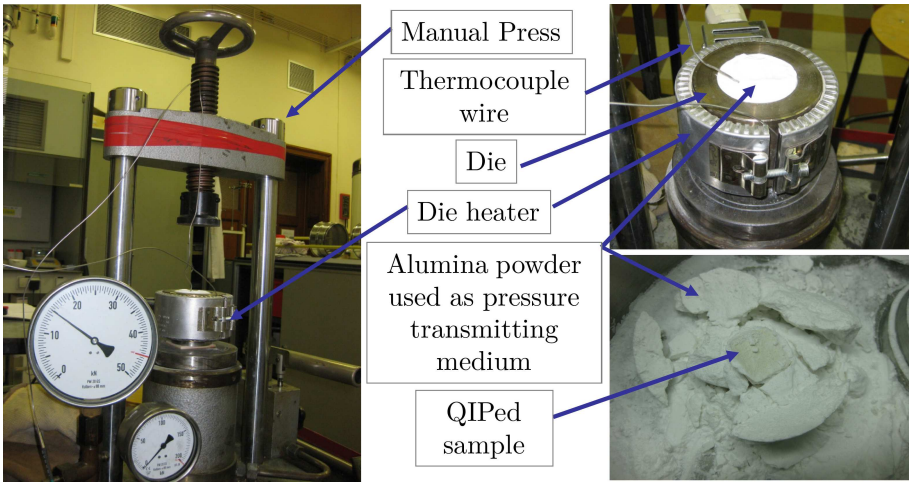

Figure 3.5: Equipment used for the QIPing process.

- The microstructure of CIPed SLSed samples contain large, isolated and elongated pores. These pores are probably formed due to incomplete fusing of the ball milled agglomerates during CIPing.
- If higher pressures than 20 MPa are used during QIPing, it might not be possible to separate the part from the surrounding powder after pressing.

3.3.4 Debinding

The green parts fabricated via indirect SLS contained about 22 wt% PA, which must be removed prior to furnace sintering. Ideally, the binder should be completely removed without disrupting the particle packing or producing any microstructural defects in the green parts. Microstructural flaws like cracks and large voids have an adverse effect on the microstructural evolution during sintering and hence the properties of the fabricated ceramic component [169].

Before debinding the CIPed samples in air, the thermal behavior of the polyamide was studied by thermogravimetrical analysis (TGA) in air at a heating rate of 10°C/min. The TGA curve, shown in figure 3.6, revealed an onset of weight loss around 292°C and a complete burn out of the polyamide at ∼590°C.

The CIPed parts shrunk during the debinding cycle. When the parts made

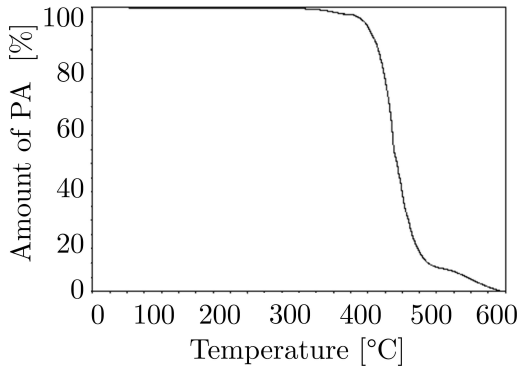

Figure 3.6: TGA analysis of the alumina-22wt%PA mixture.

direct contact to the supporting material during debinding, the parts broke, since friction forces between the part and the supporting surface prohibited the parts to shrink. To avoid this problem, binder removal of the CIPed samples was performed by submerging the parts in an alumina bubble bed (grade IB-100B, Zircar, USA).

The heating rate is a key parameter during debinding and should be adjusted with respect to the size of the part, the amount of polymeric binder and the green density of the material [131]. To optimize the heating rate during the debinding process, two debinding cycles were studied as schematically presented in figure 3.7. In cycle 1, a heating rate of 0.5°C/min was applied with a 2 hours dwell time at 275°C and 600°C, followed by furnace cooling. In cycle 2, a heating rate of 0.15°C/min was applied.
The debinding of the parts according to cycle 1 resulted in swelling of the components and local crack formation, as illustrated in figure 3.8, whereas no visible cracks nor swelling was observed on the samples subjected to debinding cycle 2. Debinding cycle 2 was applied to the parts produced in the main set of SLS experiments (see section 3.3.2). During debinding, the weight loss due to polymer degradation was measured. As summarized in the fourth column of table 3.2, the weight loss of polyamide was lower when higher laser energy densities were used during SLS. This was consistent with the smoke formation due to polymer degradation when applying higher laser energy densities.

In summary:

- Using a heating rate of 0.5°C/min for the debinding step, results in swelling of the components and local crack formation. Debinding at 0.15°C/min does not result in visible swelling or cracking of the parts.

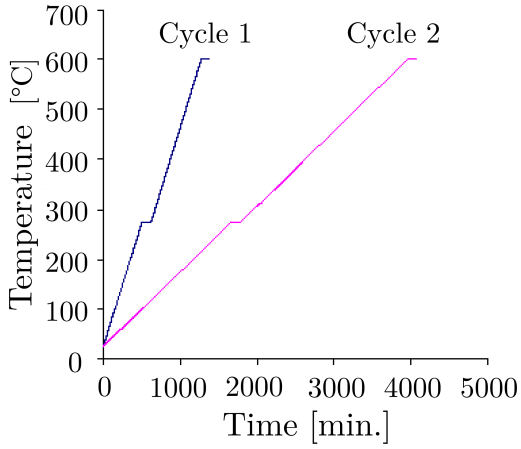

Figure 3.7: Temperature versus time profile for different debinding cycles.

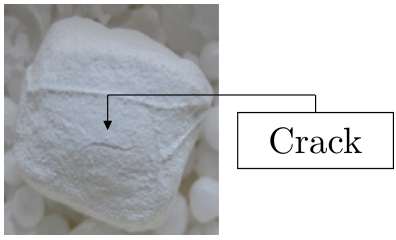

Figure 3.8: Alumina part after SLS, CIP and debinding at a heating rate of 0.5°C/min (cycle 1), showing extensive swelling and crack formation.

3.3.5 Sintering

In conventional powder metallurgy processes, alumina powders are densified by diffusion controlled solid state sintering at temperatures in the 1500-1650°C range. To obtain nearly fully dense parts with a fine microstructure, the particle size of the starting powder, compact green density and structure, packing homogeneity, sintering temperature and sintering time have to be tuned [82]. Samples of the preliminary parametrical SLS study (see section 3.3.2 and table 3.1) were used to study the effect of CIPing at 200 MPa, the furnace sintering temperature and dwell time on the final density and microstructure. Before furnace sintering, the polyamide was removed using debinding cycle 2 (see section 3.3.4).
Based on a literature review on furnace sintering of alumina, three sintering cycles in air were further investigated: 30 min at 1550°C, 60 min at 1600°C

and 120 min at 1600°C. For all these cycles, the heating rate was 20°C/min to 900°C and 10°C/min from 900°C to 1550/1600°C. The first sintering cycle (i.e. 30 min at 1550°C) was also performed on some parts which were not CIPed. To avoid friction between the parts and the furnace crucible, the parts were submerged in an alumina bubble bed (grade IB-100B, Zircar, USA).
As summarized in table 3.4, after the different furnace treatments the density of the alumina parts was measured according to the Archimedes method by weighing the samples in air and subsequently in a fluid (ethanol). In order to accurately measure the densities of the sintered parts which were not CIPed and which had a residual open porosity, an external encapsulating lacquer coating (Red lacquer, Enthone B.V., The Netherlands) was applied to avoid ethanol infiltration into the open porous system (i.e. lacquer method). The relative densities (%) were calculated using the theoretical density (TD) of alumina (i.e. 3.984 g/cm^3, see chapter 2).
The results depicted in table 3.4 show that the sintered density was not substantially influenced by changing the SLS parameters. On the other hand, CIPing at 200 MPa drastically improved the sintered density (for example 56.5 % versus 83.3 - 85.1 % for part 'P1'). The density of the CIPed ceramics sintered at 1550°C for 30 minutes ranged between 83.3 % and 83.8 % depending on the SLS parameters. Sintering the CIPed samples at 1600°C for 60 or 120 minutes slightly increased the final density into the 84.8-86.6% range. A dwell time of 60 minutes at 1600°C resulted in the highest density (86.6% for part 'P2').

As illustrated in table 3.4, the sintered density almost changed 4% when increasing the dwell time and sintering temperature. This difference in density was difficult to observe within the scanning electron micrographs of thermally etched (1350°C for 30 min at a heating rate of 20°C/min) polished cross-sectioned ceramics. The SEM images, depicted in figure 3.9, give an overview and detailed microstructure of alumina parts which were SLSed with P3 parameters (table 3.1), CIPed at 200 MPa, debinded at a heating rate of 0.15°C/min and furnace sintered for 30 min at 1550°C or 60 min at 1600°C.

	absolute density [g/cm^3] / relative density [% of TD]			
	no CIPing	CIPed		
Parameter combination	30 min. 1550°C	30 min. 1550°C	60 min. 1600°C	120 min. 1600°C
P1	2.25 / 56.5 %	3.32 / 83.3%	3.39 / 85.1 %	3.38 / 84.8 %
P2	2.32 / 58.2 %	3.32 / 83.3 %	3.45 / 86.6 %	3.41 / 85.6 %
P3		3.34 / 83.8 %	3.39 / 85.1 %	3.44 / 86.3 %

Table 3.4: Preliminary set of experiments: some densities after sintering.

Homogeneously distributed large isolated elongated pores of about 100 μm are embedded in a dense fine grained alumina matrix. The large pores were introduced during the green shaping (see section 3.3.3 and figure 3.4) and even a prolonged sintering treatment could not eliminate them [141]. They originated from the interparticle space after SLS due to an improper agglomerate packing or insufficient flow of the PA during SLS. During CIP, these inter- or intralayer pores were deformed into elongated pores, but not completely eliminated.
Figure 3.9c shows a detailed SEM image of the microstructure of the P3 ceramic part sintered at 1600°C for 60 minutes. It reveals a fully dense interpore matrix with a grain size of 5 μm. The intermediate 10 μm pores, i.e. the residual pores in the alumina matrix in between the large pores, are substantially smaller than the elongated pores but generally larger than the alumina grain size. This indicates that the applied sintering conditions were appropriate, but the green density and microstructure of the SLS part should be homogenized to improve the final sintered microstructure and density. Most likely, the intermediate pores originated from PA particles which resided in the

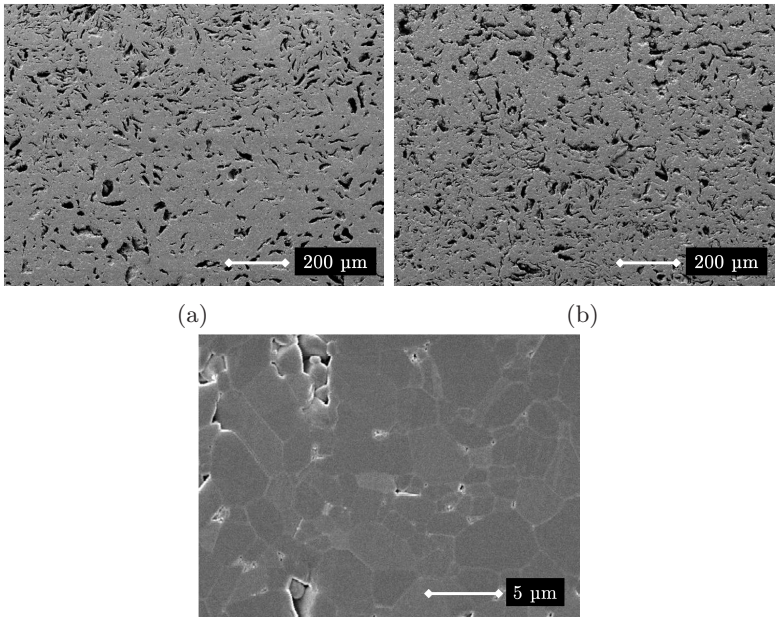

(a) (b)

(c)

Figure 3.9: SEM micrographs of alumina parts obtained after SLS, CIP, debinding and sintering: sintering for 30 min at 1550°C (a); sintering for 60 min at 1600°C (b,c)

alumina/PA agglomerates after ball milling. During debinding, the large PA particles burned away, creating intermediate pores.

The samples of the main parametrical SLS study which were scanned with a higher 7 W laser power (see section 3.3.2), were also sintered at 1600°C for 60 min, after CIP at 200 MPa and debinding with a heating rate of 0.15°C/min. The resulting densities are shown in the fifth column of table 3.2, indicating that the ceramics scanned at higher laser energy densities had higher furnace sintered densities. For example, sample 9, scanned with a laser energy density of 0.278 J/mm^3 had a sintered relative density of 83.3 %, whereas sample 1, scanned with a laser energy density 1.944 J/mm^3, had a substantially higher relative density of 90.4 %. The variation of relative density with laser energy density can also be observed in SEM images taken from the samples of the main parametrical SLS study (see figure 3.10). The images reveal that the amount of long isolated pores, as well as the amount of smaller intermediate pores was reduced when higher laser energy densities were used during the SLS stage.
As depicted in table 3.3, the x- and y-dimensions of the parts were reduced after furnace sintering to about $2/3^{th}$ of their values after SLS, for the parts scanned with higher laser energy densities, or $1/2^{th}$ of their values after SLS, for the parts scanned with lower laser energy densities. The z-dimensions of the parts were reduced to $1/3^{th}$ of their values after SLS.

The parts QIPed at 165°C, were debinded at a heating rate of 0.15°C/min (see section 3.3.4) and furnace sintered at 1600°C for 120 minutes in air. The density of parts 'Q1' and 'Q2', QIPed for respectively 5 and 15 minutes were respectively 3.56 g/cm^3 (89.4 % of TD) and 3.69 g/cm^3 (92.6 % of TD), as summarized in table 3.5. Longer QIPing times, seemed to result in higher furnace sintered densities.
Figure 3.11 shows SEM images of the sample Q1 and Q2 at different magnifications. At lower magnification (figure 3.11a and 3.11b) a relative low amount of long elongated pores was visible. QIPing the SLSed parts at a temperature above the glass transition temperature T_g of the polyamide (T_{qip} = 165°C > $T_{g,PA}$ =156.9°C) caused the agglomerates to deform under

	Laser energy density [J/mm³]	Density after furnace sintering: absolute [g/cm³] / relative [% of TD]
Sample Q1	1.944	3.56 / 89.4 %
Sample Q2	1.944	3.69 / 92.6 %

Table 3.5: Furnace sintering densities of QIPed ceramics.

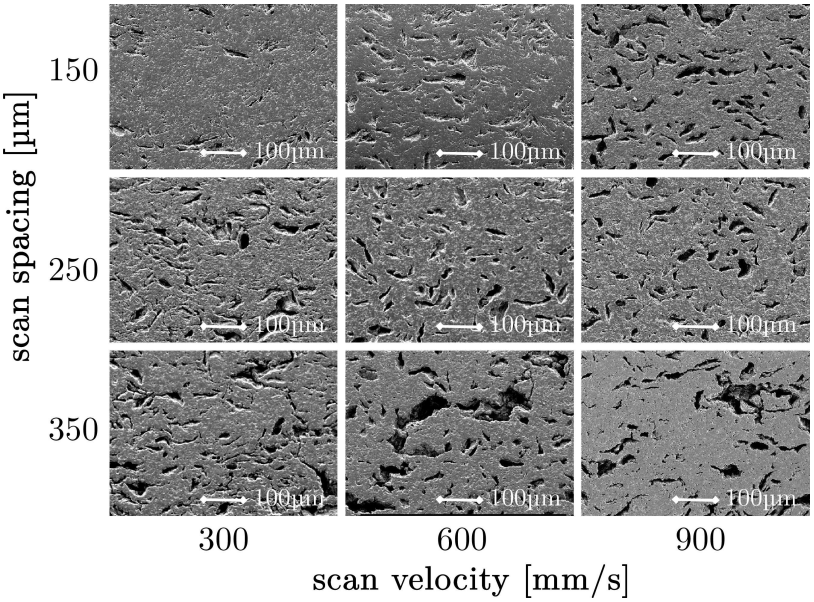

(a) Moderate magnification.

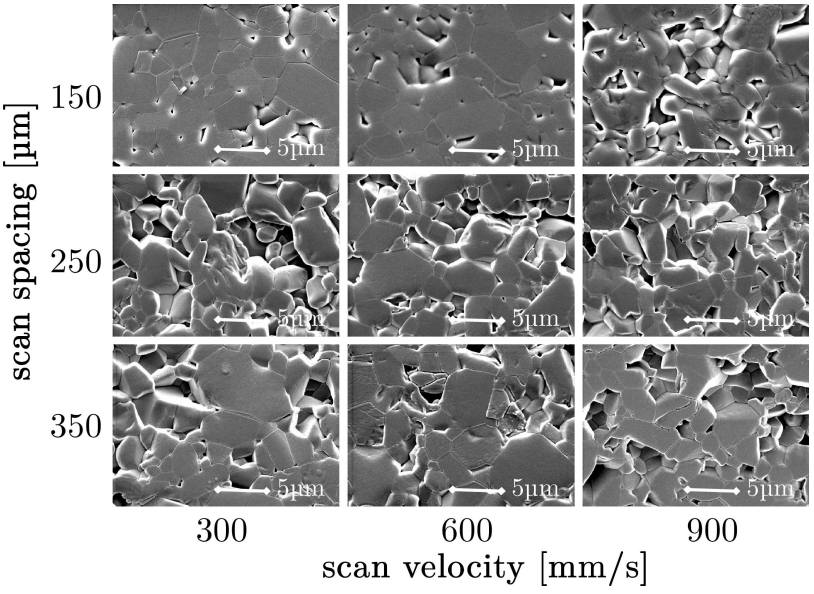

(b) High magnification.

Figure 3.10: Microstructure of the parts produced in the main set of experiments.

lower pressures. This resulted in a denser microstructure after furnace sintering. At a higher magnification (figure 3.11c and 3.11d) smaller intermediate pores could be observed.

In summary:

- Solid state sintering alumina parts in a furnace at 1600°C results in higher densities than at 1550°C.
- The microstructure after furnace sintering consists of homogeneously distributed large isolated elongated pores of about 100 μm and intermediate pores of about 10 μm, embedded in a dense fine grained (grain size of 5 μm) alumina matrix. The amount of pores is reduced when SLSing at higher laser energy densities.
  The large pores originate from the interparticle space after SLS due to an improper agglomerate packing or insufficient flow of the PA during SLS. During CIP these pores are not completely eliminated, but deformed into elongated pores. Most likely, the intermediate pores originate from PA particles which reside in the alumina/PA agglomerates after ball milling.

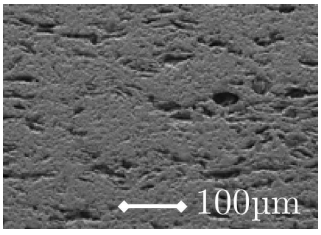

(a) Sample Q1, moderate magnification.

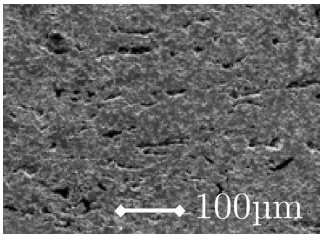

(b) Sample Q2, moderate magnification.

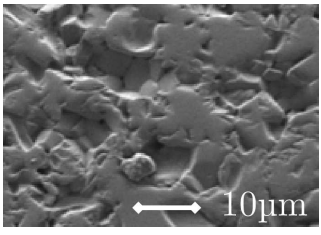

(c) Sample Q1, high magnification.

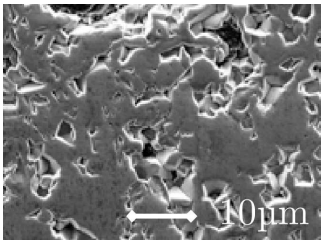

(d) Sample Q2, high magnification.

Figure 3.11: SEM images of the QIPed samples at different magnifications.

During debinding, the large PA particles burn away, creating intermediate pores.

- During the powder metallurgy process, a larger shrinkage of the parts is obtained in the z-direction (SLS build direction) than in the x- and y-direction. Further, less shrinkage is obtained if the parts are laser sintered with higher laser energy densities.
- QIPing the SLSed parts at a temperature above the glass transition temperature of the binder material causes the agglomerates to deform under lower pressures. Longer QIPing times, also seem to result in higher furnace sintered densities.

3.3.6 Discussion

For the samples of the main set of SLS experiments (see section 3.3.2), the vol% of alumina in the component after SLS and CIP can be calculated using the following formulas (see last two columns of table 3.2):

$$\%vol\ after\ SLS = (100\% - \%wtPA).\frac{\rho_{SLS}}{\rho_{Al_2O_3}} \tag{3.3}$$

$$\%vol\ after\ CIP = (100\% - \%wtPA).\frac{\rho_{CIP}}{\rho_{Al_2O_3}} \tag{3.4}$$

with

- $\%wtPA$: the weight percentage of PA after SLS (see table 3.2)
- ρ_{SLS}: density of the samples, after SLS (see table 3.2)
- ρ_{CIP}: density of the samples, after CIP (see table 3.2)
- $\rho_{Al_2O_3}$: theoretical density of alumina: $\rho_{alumina}$= 3.984 g/cm^3

By combining the data of table 3.2 and table 3.5, the laser energy density could be plotted against the vol% of alumina in the component during the different stages of the powder metallurgy process (see figure 3.12). Due to the large amount of PA and residual porosity, the vol% of alumina after SLS was only 16.6-19.1%. CIPing the parts at 200 MPa doubled the volume fraction of alumina to 33.2-40.8%. After debinding at a heating rate of 0.15°C/min and sintering for 60 minutes at 1600°C, the alumina content was again doubled to 83.3-90.4%.
During each stage of the powder metallurgy process, the vol% of alumina

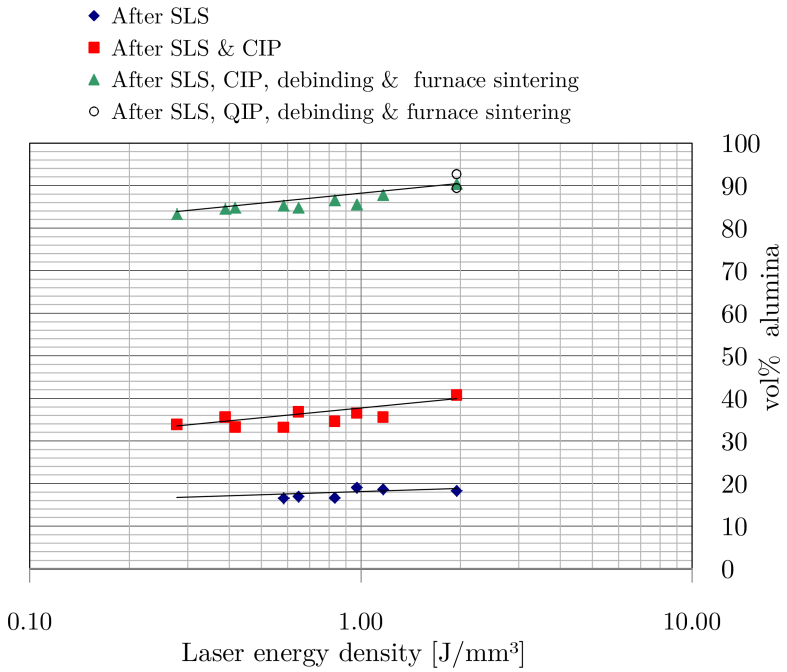

Figure 3.12: Laser energy density versus vol% Al_2O_3 during the different stages of the powder metallurgy process.

slightly increased with increasing laser energy density during SLS. The reason for this phenomenon is twofold. When scanning at higher laser energy densities during SLS (see section 3.3.2), larger melt pools were formed which forced the alumina particles to lie closer to each other by capillary attraction. Moreover, when using higher laser energy densities, lower polyamide contents were obtained in the SLSed parts due to the smoke formation (see fourth column of table 3.2). The lower amount of polyamide between the alumina particles also caused the alumina particles to lie closer to each other. After CIPing and debinding, the difference in alumina packing density after SLS was maintained. This resulted after furnace sintering in a corresponding density difference between the ceramic parts.
Figure 3.12 also shows the densities of the two QIPed samples after furnace sintering. The ceramic part QIPed at 165°C and 20 MPa for 15 minutes had a density of 92.6%. This density is even higher as the furnace sintered density of 90.4% for sample 1 (table 3.2) which was SLSed at the same laser energy density and CIPed at 200MPa for 1 minute at room temperature. This indicates that QIPing the SLS samples at 165°C was a good alternative for CIPing.

By using the geometrical data of table 3.3, the percentage volumetric shrinkage after SLS, CIPing and furnace sintering was calculated for the parts produced in the main set of experiments. As depicted in figure 3.13, after SLS, CIPing and furnace sintering, the percentage volumetric shrinkage was located in respectively the 0-20% zone (80-100% of nominal volume), the 60-80% zone (20-40% of nominal volume) and the 80-96% zone (4-20% of nominal volume). The calculated volumetrical shrinkage increased with decreasing laser energy density for the different stages of the powder metallurgy process.

After furnace sintering, there were still cracks in the center of most parts produced in the main parametrical SLS study of section 3.3.2 (figure 3.14). Possible causes for these cracks are:

- The heating rate of 0.15°C/min was still too high for debinding the polyamide (see section 3.3.4), resulting in internal damage during debinding. This is the most likely cause of the cracks in the center of the parts.

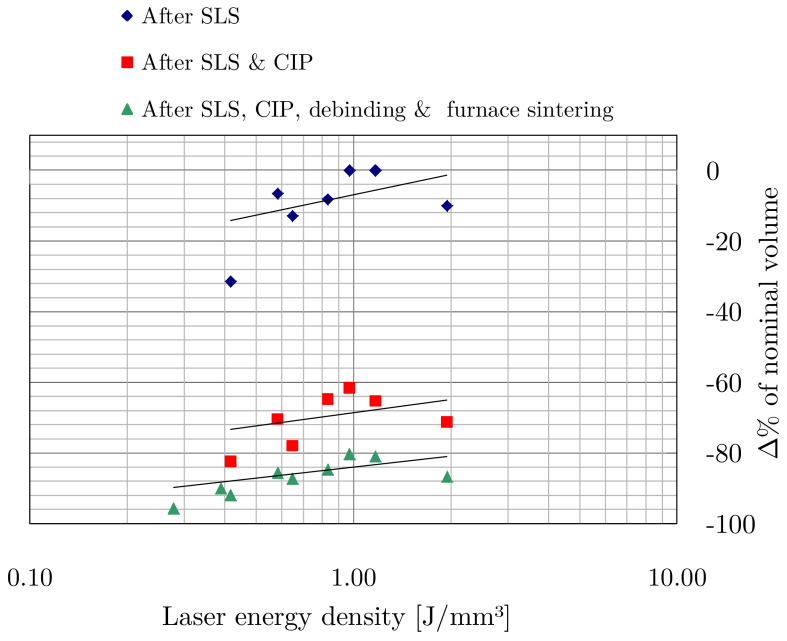

Figure 3.13: Laser energy density versus percentage volumetric shrinkage during different stages of the powder metallurgy process.

- An inhomogeneous shrinkage during furnace sintering, caused by an inhomogeneous microstructure formed in one of the stages of the powder metallurgy process.
- A too high heating rate (10-20°C/min) during furnace sintering, resulting in a thermal gradient in the part with preferential surface sintering accompanied by internal shrinkage cracks.

One of the major causes of the inhomogeneous microstructure observed in the produced green samples was the poor flowability of the ball milled starting powder, due to the non-spherical shape of the milled agglomerates (figure 3.2c). The poor flowability of the starting powder made it impossible to produce voluminous parts with good geometrical accuracy or green density after SLS. Using an alternative composite powder preparation route which allows to generate spherical agglomerates could be a solution for making the green microstructure more homogeneous and stronger.
Another way to homogenize the microstructure of the green parts could be to change the PA binder content or the isostatic pressing conditions. In this chapter, QIPing at elevated temperatures was investigated as an alternative for CIPing at room temperature. The first experiments showed very good results for QIPing during 15 minutes at 165°C and 20 MPa. A possible explanation for this higher density after QIPing was that the elevated temperature and pressure enabled the PA to deform plastically and enabled the large elongated

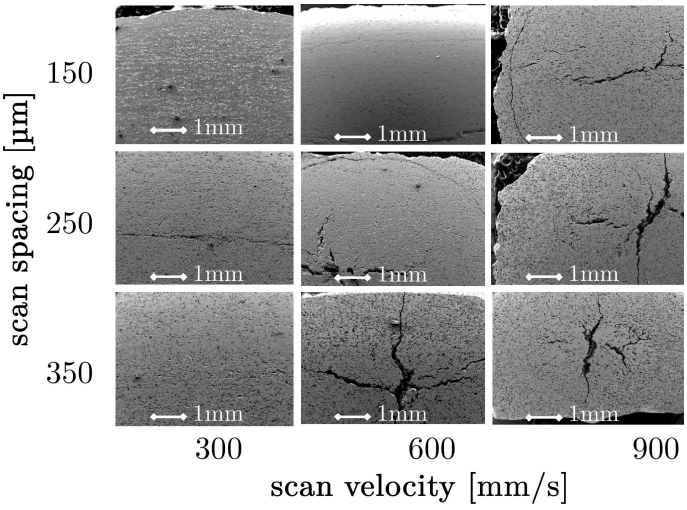

Figure 3.14: SEM micrographs of cross-sectioned sintered ceramics showing large cracks in the center of the parts.

pores to shrink or even to collapse during isostatic pressing. Although Liu et al. [139] already used CIPing to densify parts produced by SLS of a composite glass-ceramic/epoxy powder, QIPing had not been previously performed on SLSed ceramic parts.

In summary:

- The furnace sintered parts contain cracks. These cracks might be caused by the application of too high heating rates during debinding or furnace sintering, or by the inhomogeneous microstructure which is observed in the produced green samples. One of the major causes of this inhomogeneous microstructure is the poor flowability of the milled starting powder, due to the non-spherical shape of the milled agglomerates (figure 3.2c).
- The vol% of alumina after SLS is respectively 16.6-19.1%. Both CIP and furnace sintering double the vol% alumina up to respectively 33.2-40.8% and 83.3-90.4%. The vol% of alumina slightly increases with increasing laser energy density during SLS. This is due to the formation of larger melt pools (and resulting capillary attraction of the alumina particles) and the higher amount of polymer degradation when laser scanning at higher laser energy densities.

3.4 Conclusions

The possibility of processing alumina ceramics from a ball milled alumina - 22 wt% polyamide mixture by means of selective laser sintering, followed by cold isostatic pressing, debinding and sintering was assessed through density measurements, geometrical assessments and microstructural analyses. Despite the irregular shape of the ball milled agglomerates, they could be joined into a shape by applying the SLS powder preheating parameters of pure polyamide and a laser energy density higher than 0.2 J/mm^3. The density of the SLS parts was very low, but slightly increased with increasing laser energy density. When applying too high laser energy densities, the binder material degraded. The strength of the parts after SLS at high laser energy densities, was a compromise between this material degradation and plastic flowing of the binder material to bind the composite powder agglomerates.
No complex shapes could be produced from the ball milled composite alumina-PA agglomerates. This was due to the occurrence of small craters on the powder bed after layer deposition and due to the fragility of the parts after SLS.

The density of the SLS parts could be almost doubled by cold isostatic pressing

for 1 minute at 200 MPa. Polymer debinding at 0.15°C/min and furnace sintering at 1600°C again almost doubled the density, resulting in final parts with a density ranging from 83.3-90.4 %. The slightly increased green density with increased laser energy during SLS was directly reflected in an increased furnace sintered density. QIPing was a good alternative for CIPing, since the material QIPed for 15 minutes at 165°C (i.e. above the glass transition temperature of polyamide) and 20 MPa showed a sintered density of 92.6%. Geometrical assessments revealed a larger shrinkage of the parts in the z-direction (SLS build direction) than in the x- and y-directions during the powder metallurgy process. Further, less shrinkage was obtained if the parts were laser sintered with higher laser energy densities.

The sintered parts contained cracks. The sintered microstructure was composed of a $\sim$5 μm grain sized alumina matrix with long elongated isolated 100 μm pores and substantially smaller 10 μm sized residual pores. The large elongated pores originated from the inter-agglomerate space after SLS due to an improper agglomerate packing or insufficient flow of the PA during SLS. During CIP, these inter- or intra-layer pores were deformed into elongated pores, but not completely eliminated. The smaller pores originated from a local incomplete densification due to an inhomogeneous particle packing.
Homogenizing the microstructure in the SLS stage is the key challenge to further improve the density of the final product. Possible ways to homogenize the packing density of the powder bed during SLS are optimizing the composite starting powder by increasing the flowability and binder content of the ball milled material or the use of alternative composite powder preparation routes allowing to generate spherical agglomerates.

Chapter 4

Production of alumina parts through Laser Sintering of polystyrene-alumina agglomerates produced via dispersion polymerization

References:

Deckers, J., Kruth, J, Cardon, L., Shahzad, K., Vleugels, J. (2013). Densification and geometrical assessments of alumina parts produced through indirect Selective Laser Sintering of alumina-polystyrene composite powder. Strojniški vestnik - Journal of Mechanical Engineering , 59 (11), 646-661. [56]

Deckers, J., Cardon, L., Shahzad, K., Vleugels, J., Kruth, J. (2012). Production of alumina parts through indirect Selective Laser Sintering of alumina-polystyrene composite powder. Proceedings of PMI 2012, 5th International Conference on Polymers and Moulds Innovations. PMI. Ghent, Belgium, 12-14 September 2012 (art.nr. 28) (pp. 178-183). [54]

4.1 Structured abstract

Purpose The purpose of this chapter is to assess a new powder metallurgy (PM) process to make alumina parts through indirect Selective Laser Sintering (SLS).

The definition of the problem The main aim of this chapter is to produce high density technical ceramic parts through indirect Selective Laser Sintering. In order to do so, densification strategies are introduced as extra steps of the PM process. These densification strategies are warm isostatic pressing (WIP) and infiltration. In the latter, an alumina-ethanol suspension is used to fill open porosities.

Methodology Parts are produced through the synthesis of alumina/polystyrene (PS) composite agglomerates through dispersion polymerization, SLS, debinding and solid state sintering (SSS). Warm isostatic pressing and different infiltration strategies are introduced as extra steps of the PM process to increase the final densities of the produced parts. Pressure infiltration, i.e. applying an external pressure to press the suspension into the pores of the parts, as well as pressureless infiltration experiments are performed. Moreover infiltration of green, pre-sintered and solid state sintered parts is investigated. Density measurements, geometrical assessments and scanning electron microscopy (SEM) microstructural analyses are performed at different stages in the process.

Results, Findings Without extra densification steps, the linear shrinkage of the SLS parts during debinding and SSS was about 30%. The final parts contained a large amount of small cracks and the density was 66%.
WIPing could successfully increase the density of the green parts, but not the final density. Each of the final WIPed parts contained one large crack.
Infiltration generally decreased the shrinkage of the SLS parts during debinding and solid state sintering. Most solid state sintered parts, which were produced with the help of infiltration, contained one large crack. The application of pressure infiltration led to an increase of the part density up to 84%, since the cracks which occurred during the debinding process could be filled with alumina. Nevertheless micro-cracks arose. The micro-cracks probably occurred due to non-homogeneous shrinkage during solid state sintering.

Research limitations, implications Cracks remained in the solid state sintered parts. Homogenizing the microstructure of the parts through optimizing as

well the composite starting powder, as the deposition during SLS, the SLS parameters, WIPing parameters and infiltration parameters, is essential to overcome these limitations.

Contribution, Novelty, Value Amorphous thermoplastic polystyrene was not yet used to produce pure alumina parts by indirect SLS. The combined use of SLS and WIPing is new in the field of indirect SLS of ceramics. Moreover, the combined use of SLS and different infiltration techniques (pressureless and pressure infiltration; infiltration of green, pre-sintered and solid state sintered parts) is innovative.

4.2 Introduction

4.2.1 AM of polystyrene

Polystyrene is one of the most popular polymers used in the additive manufacturing (AM) technology. It has been used to demonstrate newly developed AM technologies like Layered Electro-Photographic Printing by Cormier et al. [43], Selective Inhibition Sintering by Khoshnevis et al. [106] or various kinds of Laminated Object Manufacturing (LOM) technologies (see Brooks and Aitchison [31]), de Smit and Broek [52], or Mahale et al. [144]. Moreover, polystyrene has been used to demonstrate that AM technologies can improve the investment casting (IC) process by reducing tooling costs and production lead-times (see Cheah et al. [40]).

The combined use of AM technology and investment casting technology, is called rapid investment casting. As illustrated by Cheah et al. [40], two main application areas exist: Firstly, AM technology can be applied to produce inserts to e.g. injection mold polystyrene parts as illustrated by Kinsella et al. [109]. Secondly, AM technologies can be applied to produce polystyrene IC patterns. These patterns can be master patterns (e.g. for silicone rubber molding), but are mostly sacrificial patterns.

The amorphous polystyrene is more suitable than other (semi-crystalline) polymer materials for the production of sacrificial rapid investment casting patterns due to its geometrical stability during the burning out step of the IC process (Kruth et al. [114]). This stability results from the porosity inside the polystyrene patterns and the low thermal expansion that prevents breaking of the (ceramic) IC mold during burn out (see figure 2.19). The polystyrene sacrificial patterns are sometimes produced through Three

Dimensional Printing (3DP) (Levy et al. [126]), but are mainly produced through SLS. In order to increase the polystyrene pattern strength, AM of high quality polystyrenes is investigated (e.g. SLS of High Impact Polystyrene by Yang et al. [230]) and/or wax infiltration of the patterns is applied (Ku et al. [121]). Wax infiltration of the polystyrene parts can also seal surface porosities (Cheah et al. [40]).

A difference has to be made between the production of metal and ceramic parts through rapid investment casting with (polystyrene) sacrificial patterns. When producing metal parts, the sacrificial polystyrene patterns have the shape of the part to be produced. From the sacrificial pattern, sometimes a plaster mold (see Liu et al. [134] or Niino and Yamada [155]), but generally a ceramic molding shell is fabricated. Finally, the molds are used to fabricate the metal parts through a casting process: e.g. vacuum pressure casting of aluminum parts, as applied by Hongjun et al. [101]. Applications of this technology can be found in the production of titanium, aluminum, steel alloys or super alloys for competitive motorsports (Cevolinni et al. [36]). When producing ceramics parts, the sacrificial polystyrene patterns have the negative geometry of the parts to be produced. Through high pressure slip casting, followed by debinding of the polystyrene and a furnace sintering treatment, Si_3N_4 parts parts could be obtained (Pfeifer et al. [165]).

4.2.2 AM of alumina through the use of polystyrene

In this study, an amorphous thermoplastic polystyrene is chosen to be used as binder material for the production of alumina through SLS of powder agglomerates. As illustrated in the previous section, polystyrene is a preferred polymer for investment casting due to its geometrical stability during the burning out step. It is believed that also during the burning out step (i.e. the debinding step) of indirect laser sintered alumina-polystyrene parts, the parts will benefit from the geometrical stability of polystyrene. Although amorphous thermoplastic polystyrene was already used by Zheng et al. [246] to produce composite alumina-polystyrene parts through SLS, it was not yet used to produce pure alumina parts by indirect SLS.

4.3 The powder metallurgical process

Figure 4.1 schematically presents the main steps of the powder metallurgy process assessed in this work to produce alumina parts through AM. In a first step the composite starting powder was produced. Afterwards the SLS

parameters were optimized to produce green parts. The final alumina parts were produced by subsequently debinding (deb.) and solid state sintering (SSS) of the green parts. Geometrical assessments were used to assess the dimensional changes of the SLSed parts. These changes occurred during the debinding and SSS step. In order to improve the final density of the alumina parts, two possible densification treatments were used, namely Warm Isostatic Pressing (WIP) and infiltration (inf.).

This chapter investigates the quality of the components during the different processing steps through density measurements, geometrical assessments and microscopic imaging. The density was measured by the Archimedes method (Analytical Balance, Sartorius, Germany). The geometrical assessments were realized with a coordinate measuring machine (CMM, FN905, Mitutoyo, Japan) or a vernier caliper (Mitutoyo, Japan). The roughness was measured with a Talysurf-120L (Taylor-Hobson, UK). The microscopic images were assessed with a digital camera, 3D microscopy (Discovery.V20, Carl Zeiss Inc., Germany) or scanning electron microscopy (SEM, XL30 FEG, FEI, The Netherlands). The outer shapes of the parts were figured with the digital camera. Internal, cross-sectional images were taken with the 3D microscope or SEM. In order to take the cross-sectional images, the parts were cut with a diamond blade, embedded in an epoxy resin, and ground. Secondary (SE-SEM), and backscattered electron (BSE-SEM) SEM images were taken.

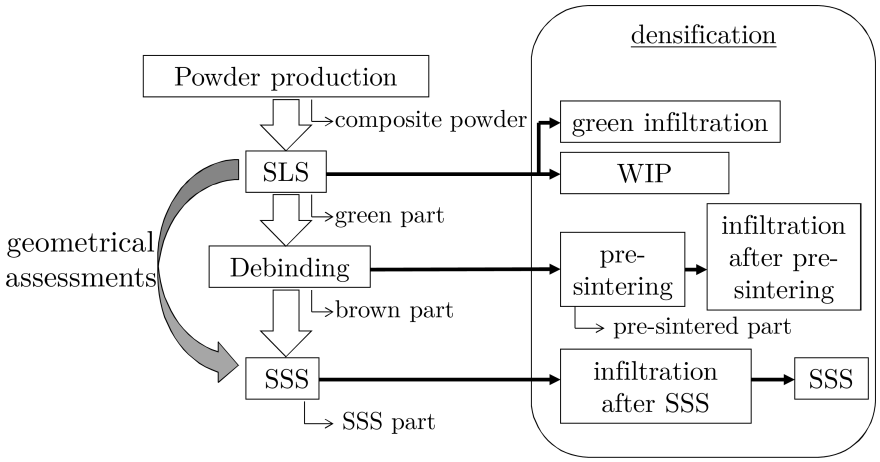

Figure 4.1: Powder metallurgy processing flow chart.

4.3.1 Difference with PM process described in previous chapter

In summary, the PM process described in this chapter differs from the one described in chapter 3 in three ways:

1. Amorphous polystyrene is used instead of semi-crystalline polyamide (PA) as polymer binder.
2. The synthesis of the initial polymer-ceramic powder is done by in-situ dispersion polymerization instead of ball milling (section 3.3.1).
3. Other post-densification strategies are tested: a.o. warm isostatic pressing (WIP), green infiltration and infiltration after solid state sintering.

4.4 Production of alumina parts

4.4.1 Powder production

Zheng et al. [246] used an emulsion polymerization process to produce alumina-polystyrene powder for SLS of composite parts. In this chapter, no emulsion polymerization, but a dispersion polymerization process was used to produce alumina-polystyrene powder. Different batches of powder were prepared in a 2 liter three-neck flask equipped with a thermometer and a reflux condenser. The flask was covered with aluminum foil and immersed in a water bath on a heating plate with magnetic stirrer capacity. A mixture of 1134 g ethanol (99,9%, Merck Millipore, USA) and 66 g water was heated above 50°C and 222.32 g of the monomer styrene (99,5%, Acros Organics, USA), 2.32 g divinylbenzene to make the styrene reactive (98% DVB, Merck Millipore, USA) and 120.44 g α-alumina powder (figure 4.2a: grade SM8, Baikowski, France) with a mean particle size of 0.3 μm were poured into the solution and stirred with a magnetic stirrer. The mixture was heated to 65°C and finally the polymerization reaction was initiated by adding 2.26 g 2,2-azobisisobutyronitrile (AlBN, Acros Organics, USA). Figure 4.2b schematically presents the dispersion polymerization reaction. The polymerization was carried out at 65°C for 6.5 hours. After reaction, the final product was cooled to room temperature. The next day, the mixture was filtered and three times washed with water. The solid product was dried in an oven at 50°C for 2 hours to remove all solvents. After drying, the cake material prepared in the 2000 ml flask was ground in a ball mill (Fritsch, Germany) to obtain fine powder that

was sieved (Retsch, Germany) with a mesh of 160 μm. For a more detailed description of the powder production method: see Cardon et al. [33].

The presented powder production route led to composite powder containing 39wt% polystyrene. As depicted in figure 4.2c, the composite particles were not spherical in shape. Some pristine α-alumina particles, with a d_{50}~0.3 μm (figure 4.2a), could still be observed in the powder (figure 4.2d).

4.4.2 Selective laser sintering (SLS)

Green samples were fabricated on a Sinterstation 2000 machine (DTM Corporation / 3DSystems, USA) equipped with a 100 W CO_2 laser (f100, Synrad, USA) with a wavelength of 10.6 μm and a laser beam diameter ϕ_{1/e^2} of 400 μm. Powder layers could be well deposited by a counter current roller.

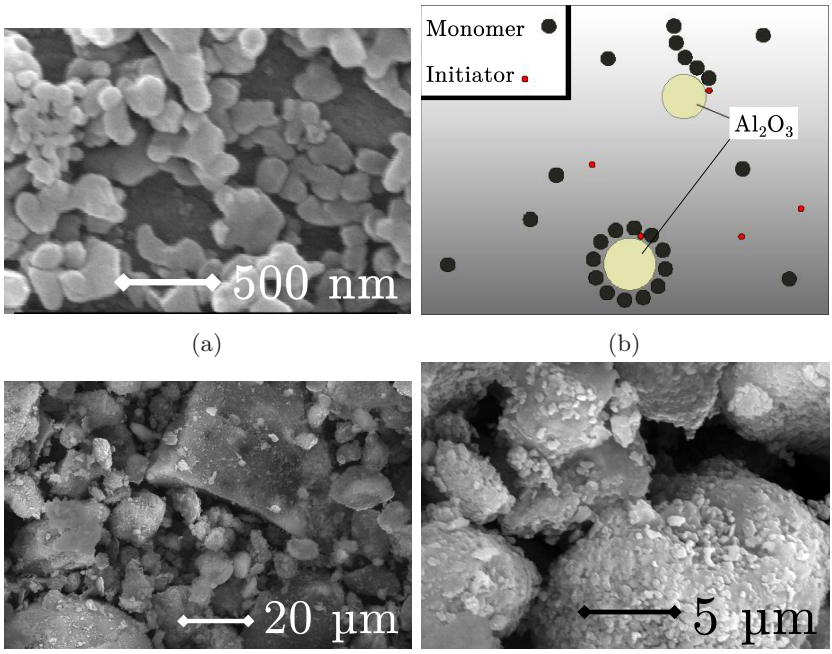

(a) (b)

(c) SE-SEM micrograph (d) BSE-SEM micrograph

Figure 4.2: Powder production: SEM micrograph of alumina starting powder (a); schematic of the dispersion polymerization process (b); micrographs of the produced alumina/polystyrene composite powders (c,d).

The powder layers were irradiated with the laser beam in N_2 atmosphere (L'Air Liquide, Belgium, $[O_2] < 5$ ppm). In order to improve the laser sinterability of the powder, the parts were produced at a powder bed of ∼90°C. The energy required to melt the amorphous polystyrene phase was partly supplied by preheating of the powder bed (distributed cylinder heating and surface IR heating) and by extra laser irradiation which locally raised the temperature.
Besides SLS tests to investigate the powder production route and to investigate the powder preheating and cooling conditions, a parametrical study was performed to investigate other crucial SLS parameters. During one of the SLS tests performed during this parametrical study, 18 cubic parts of 10x10x10 mm^3 were produced with a laser power 'P', scan speed 'v' and scan spacing 's' varying between respectively 13-17 W, 900-1200 mm/s and 0.1-0.2 mm. The layer thickness 'l' was fixed at 250 μm. The laser energy density 'e' which combines these parameters (see section 3.3.2), varied from 0.22 to 0.76 J/mm^3.

$$e = \frac{P}{s.v.l} \tag{4.1}$$

After SLS, the relative green density of the parts was measured (bold percentages in table 4.1). The relative density is the ratio of the absolute density and the theoretical density (TD). Assuming a TD of 1.05 g/cm^3 for polystyrene and 3.98 g/cm^3 for Al_2O_3, the green TD of the SLSed 61wt% alumina - 39wt% polystyrene powder should be 1.91 g/cm^3. Relative green densities varied from 51% to 66%, depending on the laser energy density. When scanning with low laser energy densities, the amount of melted polystyrene was too low to consolidate the powder particles. When scanning with too high laser energy densities, the polystyrene could degrade.
As depicted in figure 4.3a, dross was formed at the bottom of the parts during

s [mm]	900 mm/s			s [mm]	1200 mm/s		
0.1	**66%**	**66%**	**65%**	0.1	**64%**	**64%**	**55%**
	66%	66%	66%		66%	63%	63%
0.15	**63%**	**61%**	**60%**	0.15	**57%**	**55%**	**52%**
	61%	62%	64%		62%	65%	64%
0.2	**59%**	**57%**	**55%**	0.2	**54%**	**51%**	**52%**
	66%	63%	60%		62%	63%	62%
	17	15	13 P [W]		17	15	13 P [W]

Table 4.1: Green Al_2O_3-PS composite densities after SLS (i.e. before debinding; top, bold) and final sintered Al_2O_3 densities after solid state sintering (bottom). The densities are expressed in % of the theoretical density (TD).

the SLS process. The amount of dross increased when applying higher laser energy densities. At higher laser energy densities, the polystyrene was heated more. As a result, the polystyrene had a lower viscosity and flowed into the underlying powder. Figure 4.3b is a cross-sectional image that shows the different layers which were formed during the SLS process. No cracks are visible. A SEM image of the cross-section (figure 4.3c) illustrates the low green density of the SLSed parts. A large inhomogeneous network of pores is still visible as dark gray (epoxy resin) and black (air) zones, which surround the consolidated powder particles (light zones).

4.4.3 Debinding and solid state sintering

In order to know the optimal SLS parameters for producing alumina parts, all green samples obtained during the parametrical study went through at least two furnace treatments, namely debinding (deb.) and solid state sintering (SSS)

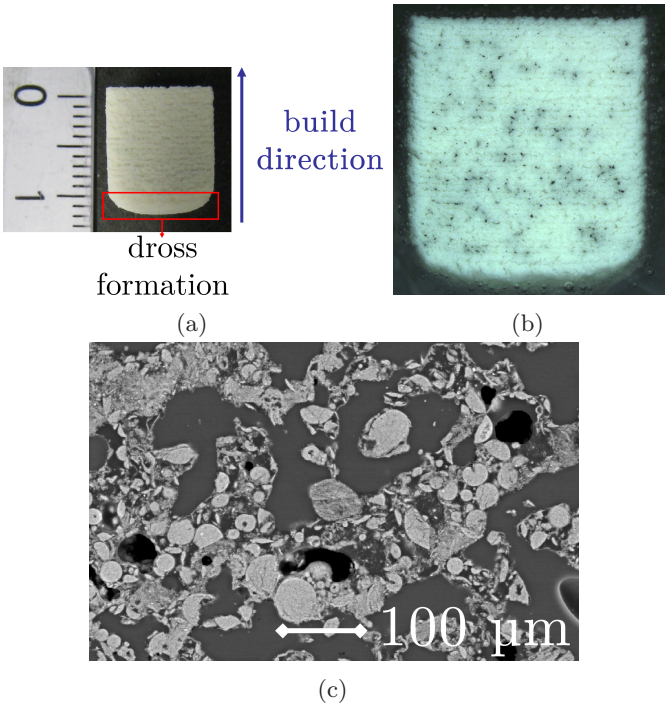

Figure 4.3: Green part after SLS: camera image (a), 3D microscope cross-sectional image (b) and BSE-SEM cross-sectional image (c).

(see figure 4.1). In the debinding step, the polystyrene was removed from the 'green' parts and a 'brown' part was formed. This was done at a heating rate of 0.1°C/min with a 2 hours dwell time at 600°C, followed by furnace cooling. Afterwards, the submicrometer alumina particles of the brown part were solid state sintered (SSS) to form the final part. This means that the brown part underwent the initial, intermediate and final stage of the SSS process. In this second step, a heating rate of 5°C/min was applied with a dwell time of 2 hours at 1600°C, followed by furnace cooling. Sometimes pre-sintering was used to strengthen the brown parts by forming necks between the submicrometer particles. By applying a heating rate of 5°C/min and a dwell time of 2 hours at 1050°C, these brown parts only went through the initial stage (i.e. neck formation) of the SSS process.
The densities of the samples of the parametrical study were measured (i) after SLS (i.e. before debinding) and (ii) after the final SSS furnace treatment (see table 4.1).
As depicted in table 4.1, relative composite densities between 60% and 66% were obtained. The part SLSed with the highest laser energy density (i.e. 0.76 J/mm^3), also had the highest density of 66% both after SLS and after SSS in a furnace. Therefore, the following optimized SLS parameters of this part were used for all further part production reported: a laser power of 17 W, a scan speed of 900 mm/s, a scan spacing of 0.1 mm and a layer thickness of 250 μm. Although complex shaped parts could be produced with the optimized parameter set (see figure 4.5), all resulting alumina parts of the parametrical study contained a large amount of cracks (figure 4.4a). Only small porosities could be observed between the cracks (figure 4.4b).
Figure 4.5a and 4.5b illustrate that the smaller parts (i.e. a cross-section $<$ 1 cm^2) produced through the presented powder metallurgical process did not have surface cracks, despite their internal cracks (see e.g. figure 4.4a). On the contrary, larger parts contained large surface cracks (figure 4.5c and 4.5d)

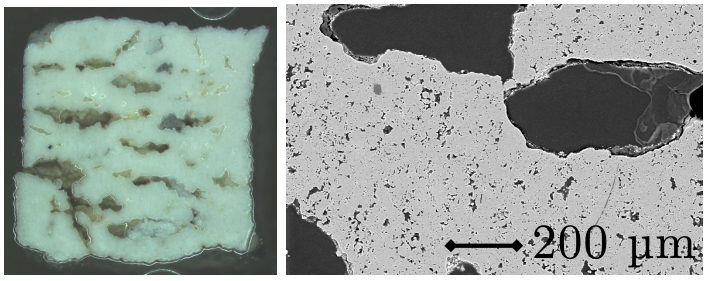

(a) 3D image (b) BSE-SEM image

Figure 4.4: Final part with optimized SLS parameters.

after debinding and solid state sintering. The larger parts also curled due to inhomogeneous shrinking.

In summary:

- Complex shaped alumina parts could successfully be produced through SLS of polystyrene-alumina powder synthesized by a dispersion polymerization process.
- When using higher laser energy densities during SLS, the resulting green and final density of the parts is also higher. Nevertheless, dross formation (and polymer degradation) might occur. The amount of dross increases when applying higher laser energy densities.
- The final parts, produced with optimized SLS parameters, contain a large amount of small cracks.

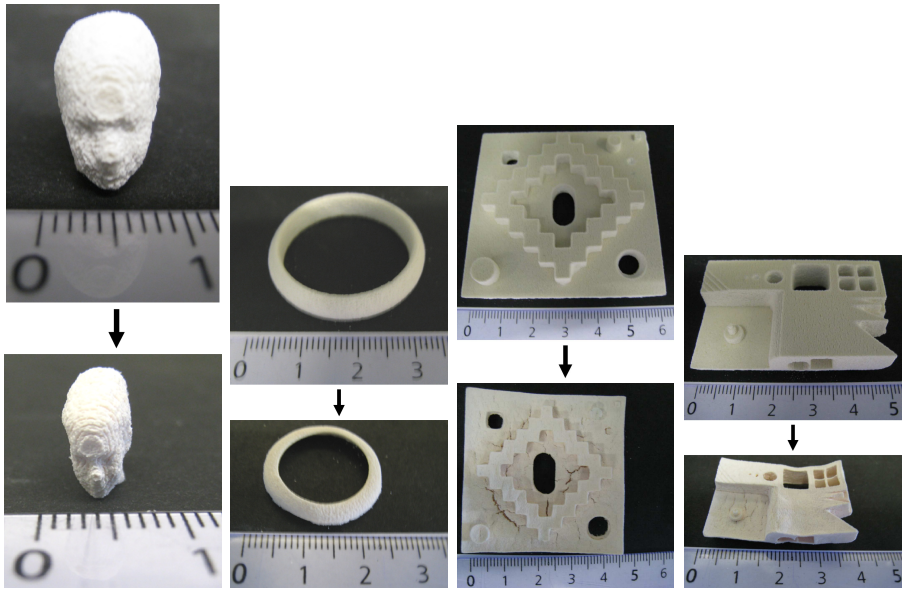

(a) (b) (c) (d)

Figure 4.5: Demo parts before (top) and after (bottom) debinding and sintering: small demo parts (a,b) and large geometrical benchmark parts (c,d).

4.5 Geometrical assessments

The benchmark parts depicted in figures 4.7a/4.5c and 4.7b/4.5d were used to investigate the percentage linear shrinkage across debinding and SSS. The research did not focus on the dimensional changes which occurred during the SLS process. This kind of study, which can be used to determine compensation strategies to geometrically match SLSed parts with the corresponding CAD files, was beyond the scope of the research.
The percentage linear shrinkage (% linear shrinkage) which occurred across debinding and solid state sintering was defined as

$$\%\ linear\ shrinkage\ =\ \frac{dimension\ after\ SSS\ -\ green\ part\ dimension}{green\ part\ dimension} \tag{4.2}$$

In order to investigate the directional dependence of the shrinkage, the scan, cross-scan and build direction were defined as x, y and z direction as illustrated in figure 4.6.
At last, the benchmark part shown in figure 4.5d has been used to investigate the roughness change in the x and y direction during debinding and SSS. Different roughness values (Ra, Rt and Rz) were obtained in the x and y direction. A Gaussian filter with a lower (Ls) and higher (Lc) cut-off value of respectively 0.008 mm and 2.5 mm was used to process the measured data.

Figure 4.8a describes the % linear shrinkage of different features of the benchmark parts (i.e. the parts depicted in figures 4.7a/4.5c and 4.7b/4.5d) as a function of the corresponding green dimension. By looking at the larger dimensions (>20 mm), it can be seen that the % linear shrinkage was about 30%. The % linear shrinkage seemed to vary a lot for the smaller green dimensions. When comparing outer and inner dimensions, the outer dimensions shrunk more.
Figure 4.8b describes the % linear shrinkage of the benchmark parts in x 'scan'

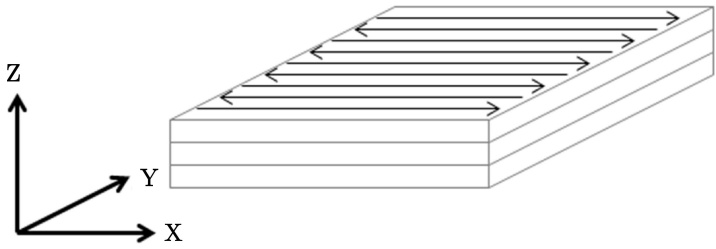

Figure 4.6: Directional dependency of shrinkage during debinding and furnace sintering: definition of x 'scan', y 'cross-scan' and z 'build' direction.

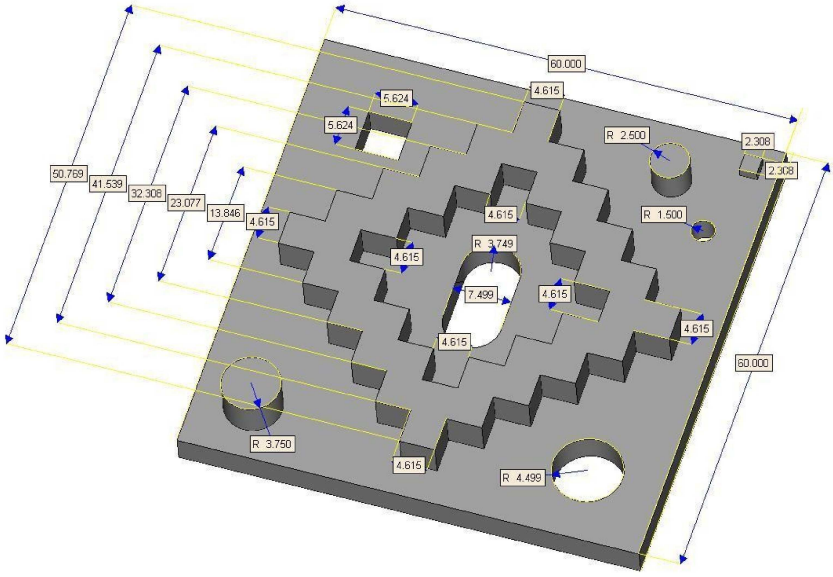

(a)

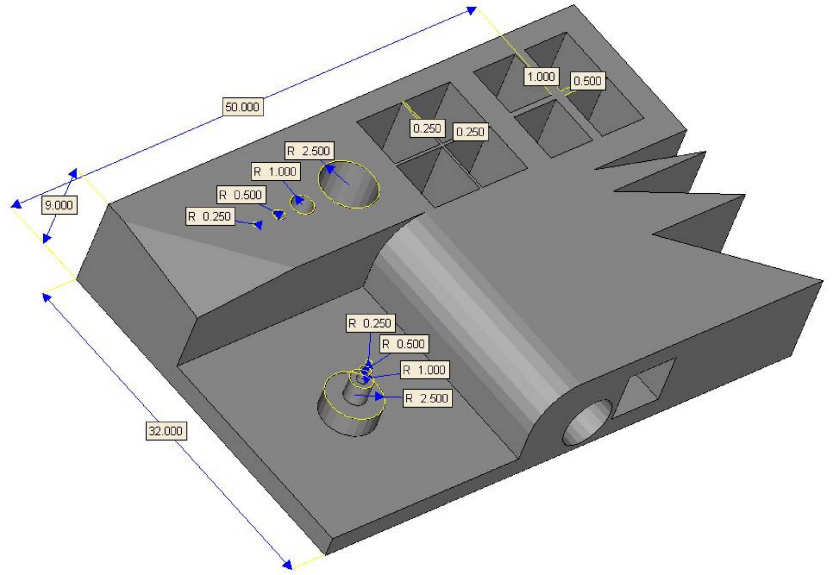

(b)

Figure 4.7: CAD dimensions of the benchmark parts depicted in figures 4.5c (a) and 4.5d (b).

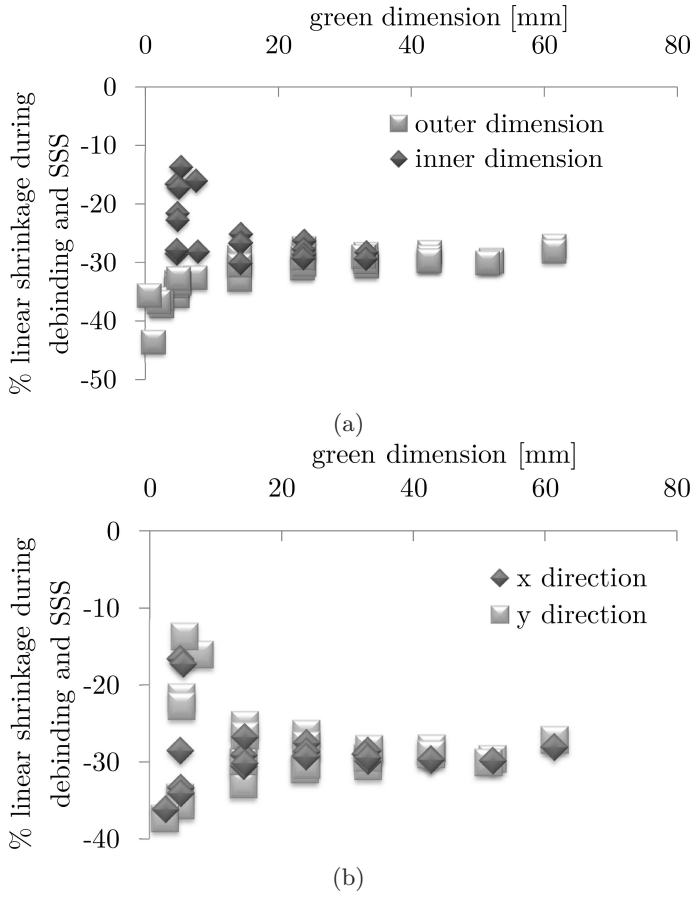

Figure 4.8: Percentage of linear shrinkage of the benchmark parts depicted in figures 4.5c and 4.5d: shrinkage of outer and inner dimensions (a); shrinkage in x and y direction (b).

and y 'cross-scan' direction during debinding and SSS. Although the measured variation of % shrinkage was slightly larger in the y direction compared to the x direction, no large difference could be observed. In the remaining of the chapter, no distinction will be made between shrinkages in the x and y direction.
The cubic parts produced to study the SLS parameters, were also used to investigate the % shrinkage in the z direction. In figure 4.9 the % linear shrinkages of the cubic parts are plotted as a function of the laser energy density. The shrinkage in the z direction was systematically larger than in the x/y direction. This might be related to the presence of a high concentration of pores between the SLSed layers (i.e. inter-layer pores). As the more porous areas were more free to shrink during debinding and SSS, the amount of shrinkage in the z direction was larger.
As depicted in table 4.2, the roughness in the x 'scan' direction was slightly lower than the roughness in the y 'cross-scan' direction. Furthermore, the final part was smoother than the green part.

The benchmark parts depicted in figures 4.7a/4.5c and 4.7b/4.5d were used to investigate the % shrinkage across debinding and SSS. As described in section 2.4.7.2, the shrinkage during debinding and SSS was mainly shrinkage due to the sintering stresses (i.e. sintering pressure). Cracks did not contribute to the shrinking process. This means that if no cracks had occurred during the debinding cycle, a linear shrinkage larger than -30% would have been observed. The large variety of the shrinkage for smaller green dimensions (figure 4.8) was probably due to measurement errors, which were relatively larger for smaller dimensions. A possible explanation for the observation that outer dimensions shrunk more than inner dimensions (figure 4.8a), could be found by looking

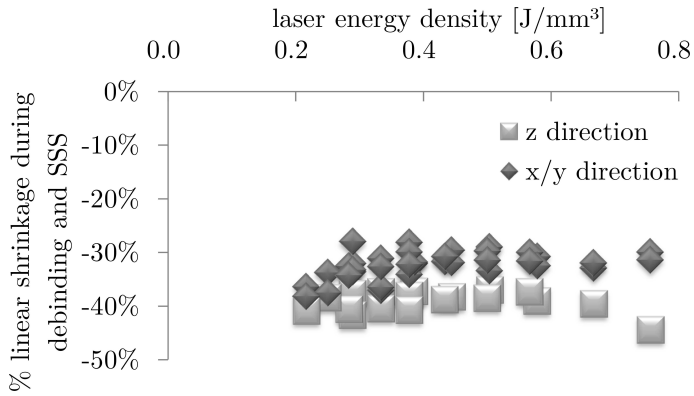

Figure 4.9: Percentage linear shrinkage of cubic parts in x/y and z direction as a function of laser energy density.

	x direction	y direction
Green part: Ra [μm]	18μm	22μm
Green part: Rt [μm]	142μm	202μm
Green part: Rz [μm]	107μm	152μm
Final part: Ra [μm]	19μm	22μm
Final part: Rt [μm]	128μm	167μm
Final part: Rz [μm]	103μm	138μm

Table 4.2: Mean roughness values of the benchmark part, depicted in figures 4.7b and 4.5d, after SLS (green) and after SSS (final).

at the shrinkage during sintering. As illustrated in figure 4.10a, the sintering stress was not constrained and tended to reduce the outer contours. In this case the reduction of the outer contours and the shrinkage of the debinded part acted in the same direction. On the contrary, the sintering stress tended to increase internal contours (figure 4.10b). The shrinkage of the debinded part counteracted this increase, resulting in a lower total shrinkage of the internal geometry.

In summary:

- The shrinkage during debinding and SSS is mainly caused by sintering stress. Sintering stress causes outer part dimensions to shrink more than inner part dimensions.
- Dimensions in the x 'scan' and y 'cross-scan' directions shrink about the

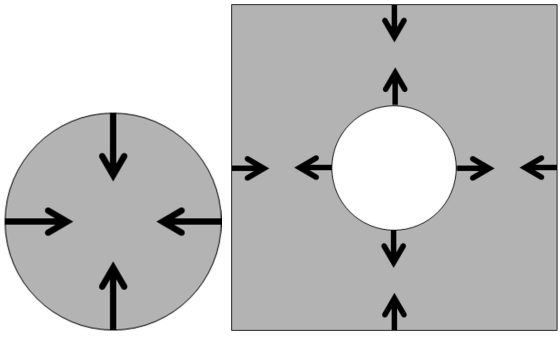

(a) outer geometry (b) inner geometry

Figure 4.10: Compressive sintering stresses during furnace sintering.

same amount across debinding and SSS. The x/y shrinkage was about −30%. In the remaining of the chapter, no distinction will be made between shrinkages in the x and y direction.

- Dimensions in the z 'build' direction shrink more than dimensions in the x/y direction.
- Roughness values become slightly lower during debinding and SSS.

4.6 Densification strategies

4.6.1 Warm isostatic pressing (WIP)

Two WIPing tests were performed. In the first test, the vacuum packed SLSed part ('part 2' in table 4.3) was heated in silicone oil to 100°C, which is above the glass transition temperature of polystyrene. The second vacuum packed sample, which was SLSed in another run ('part 3' in table 4.3), was heated in silicone oil to 110°C. On both samples, a uniform pressure of 16.1 MPa was applied for 5 minutes.

WIPing of the green parts resulted in an increase of the green density and the geometrical shrinkage (not reported in table 4.3). For part 2, WIPing increased the green density from 66% to 94% and resulted in a geometrical shrinkage of -10% (x/y direction) and -7% (z direction). Although the WIPing temperature of part 3 was 10°C higher than part 2, the green density increased from 67% to 79% and the resulting geometrical shrinkage was only -3% (in all directions).
After debinding and solid state sintering, the final densities and measured shrinkages of part 2 and 3 were respectively 52-48% and about 23% (in all directions): see table 4.3. This is lower than the density and shrinkage of reference 'part 1' (see table 4.3), which was produced with the optimized SLS

Part nr	Additional densification steps (besides SLS, deb. and SSS)	ρ [%]	x-y [%]	z [%]
1	No, i.e. only deb. and SSS	66%	-31%	-44%
2	$WIP_{100°C}$	52%	-22%	-24%
3	$WIP_{110°C}$	48%	-24%	-23%

Table 4.3: Influence of warm isostatic pressing (WIP) on sintered densities and linear shrinkages of the cubic (10x10x10 mm^3) alumina parts.

parameter set and not WIPed.

The different densities of part 2 and part 3 after the WIPing process, might be related to aging of the composite material of the SLSed sample. Aging is the thermal degradation over time when re-using the same powder repeatedly. Re-using the same polymer powder repeatedly results in an increase of the molecular weight of the polymer. Consequently, a decay of the MFI (Mold Flow Index), which is linearly related to the molecular weight, and a rise in melt viscosity occurs [119]. Part 3 was produced some time after part 2 and due to the aging process, the polystyrene of part 3 had a higher viscosity and worse WIPing behavior.
Although no cracks could be observed after WIPing (figure 4.11a), one large internal crack could be observed in the cross-sections of the parts after debinding and solid state sintering (figure 4.11c). This was in contrast with the large amount of smaller cracks in part 1 (figure 4.4a), which was not WIPed. The large crack might be at the origin of the lower densities and lower shrinkages of the WIPed samples after SSS (see table 4.3). Besides the difference in amount and size of cracks, the green and final microstructure of a WIPed part (figure 4.11b and 4.11d) was similar to that of a part which was not WIPed (figure 4.3c and figure 4.4b).

In summary:

- WIPing increases the green density of the SLSed parts.
- The final densities and final shrinkages of the WIPed parts after solid state sintering is lower than the part without WIPing. This is probably due to the formation of a large internal crack.

4.6.2 Pressureless and pressure infiltration

Green, pre-sintered and/or solid state sintered parts (SSS parts) were infiltrated with suspensions containing alumina particles (grade SM8, Baikowski, France) with a mean particle size of 0.3 μm to improve the final density of the produced parts (figure 4.1). Pressureless infiltration tests, i.e. dipping without external pressure, as well as pressure infiltration was applied to infiltrate the suspension into the pores of the part. An ethanol based suspension containing 20 or 30 vol% alumina was used during pressureless infiltration. An ethanol based suspension containing 40 vol% alumina was used during pressure infiltration, i.e. applying an external pressure to press the suspension into the pores of the

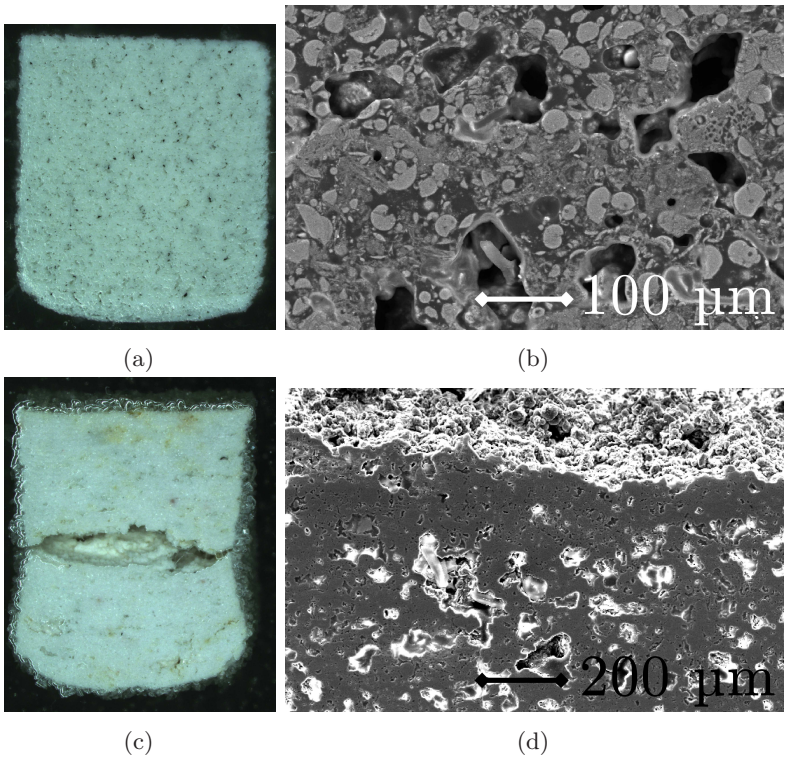

(a) (b)

(c) (d)

Figure 4.11: Images of WIPed parts: 3D microscope (a) and BSE-SEM image (b) of a part after WIPing; 3D microscope (c) and SE-SEM image (d) of part 3 after WIPing, debinding and SSS.

part. All suspensions were stabilized with 0.3 wt% citric acid (Anhydrous p.a., Acros, USA) and mixed on a Turbula mixer for 24 hrs.

4.6.2.1 Continuous green pressureless infiltration

The weight gain during continuous green pressureless infiltration for 30 hours was assessed with a 20 vol% (part 4) and 30 vol% (part 5) alumina suspension. The dried mass (without ethanol) was calculated from the wet mass, which was measured after respectively 1, 2, 3 and 30 hours of infiltration.
As depicted in table 4.4, the largest weight gain occurred during the first hour of infiltration. The 30 vol% alumina suspension led to a higher weight gain than the 20 vol% alumina suspension. Furthermore, comparing 'part 4' and 'part 5'

in table 4.5 with 'part 1' reveals that 30 hours of green pressureless infiltration decreased both the density after solid state sintering and the shrinkage during debinding and solid state sintering. Moreover, it reduced the difference between the shrinkage in the x/y direction and the shrinkage in the z direction.

In summary:

- The infiltration time does not need to be longer than 1 hour.
- Continuous green pressureless infiltration decreases the final density of the parts.
- Continuous green pressureless infiltration decreases and homogenizes the shrinkages in the x/y and z direction.

Part nr	0 hr [g]	1 hr [g]	2 hr [g]	3 hr [g]	30 hr [g]
4	1.26	1.48	1.49	1.48	1.53
5	1.28	1.57	1.57	1.58	1.63

Table 4.4: Measured weight values during continuous infiltration.

Part nr	Additional densification steps (besides SLS, deb. and SSS)	ρ [%]	x-y [%]	z [%]
1	No, i.e. only deb. and SSS	66%	-31%	-44%
4	green cont. pressureless inf.: 20 vol.%, 30 hrs	53%	-19%	-17%
5	green cont. pressureless inf.: 30 vol.%, 30 hrs	50%	-20%	-18%

Table 4.5: Influence of continuous green pressureless infiltration on sintered density and linear shrinkages of the cubic (10x10x10 mm^3) alumina parts.

4.6.2.2 Stepwise green pressureless infiltration

The weight gain during stepwise green pressureless infiltration for some hours was assessed with 20 vol% (part 6) and 30 vol% (part 7) alumina suspensions. After each infiltration step and before measuring the weight, the samples were placed for 2 hours in a drying furnace at 70°C to evaporate the ethanol. In total 4 infiltration steps were performed.
As depicted in table 4.6, the largest increase of weight could be observed after the first infiltration step. Again the highest weight gain was observed when infiltrating with the 30% alumina suspension. Comparing 'part 6' and 'part 7' in table 4.7 with 'part 1' reveals that green pressureless infiltration decreased both the density after solid state sintering and the shrinkage during debinding and solid state sintering. Green pressureless infiltration reduced the difference between shrinkage in respectively the x-y and z direction.

In summary:

- When applying stepwise infiltration, the highest weight gain is observed during the first infiltration step.
- Stepwise green pressureless infiltration decreases the final density of the parts.
- Stepwise green pressureless infiltration decreases and homogenizes the shrinkages in the x/y and z direction.

Part nr	green [g]	step 1 [g]	step 2 [g]	step 3 [g]	step 4 [g]
6	1.28	1.47	1.54	1.57	1.59
7	1.26	1.54	1.61	1.64	1.66

Table 4.6: Measured weight values during stepwise infiltration.

Part nr	Additional densification steps (besides SLS, deb. and SSS)	ρ [%]	x-y [%]	z [%]
1	No, i.e. only deb. and SSS	66%	-31%	-44%
6	4 x stepwise gr. inf.: p=0MPa; 20 vol.%; 4 hrs	47%	-20%	-18%
7	4 x stepwise gr. inf.: p=0MPa;30 vol.%; 4 hrs	47%	-17%	-15%

Table 4.7: Influence of stepwise green (pressureless) infiltration (gr. inf.) on sintered densities and linear shrinkages of the cubic (10x10x10 mm^3) parts.

4.6.2.3 Pressureless infiltration at different stages of the PM process

As schematically presented in figure 4.1, infiltration can be performed at different stages of the PM process: before the debinding step (i.e. green infiltration), after the debinding and a pre-sintering step or after solid state sintering. As described in the section 4.4.3, the debinded part has to be pre-sintered at 1050°C to give it some strength before infiltration is to be applied. After infiltrating the pre-sintered part, the part is further solid state sintered at 1600°C.
In order to investigate the combined influence of green infiltration and/or infiltration after pre-sintering and infiltration after SSS, 4 parts ('part 8', 'part 9', 'part 10' and 'part 11') underwent a pressureless infiltration treatment at different stages of the PM process. Each infiltration treatment, in which the 30 vol% suspension was used, lasted for 4 hours.
Table 4.8 and table 4.9 describe for each part, at which stages of the PM process infiltration was performed. Table 4.8 and table 4.9 also describe respectively the changes in relative density and geometrical shrinkage during the different steps of the PM process. *Higher densities were obtained without green infiltration.* On the contrary, infiltration after pre-sintering and SSS increased the final densities of the parts. *Infiltration after pre-sintering was the most successful densification step and led to densities up to 71% after SSS* (part 9 in table 4.8). Green infiltration decreased the part shrinkage. On the contrary, infiltration after pre-sintering and SSS did not seem to influence the part shrinkage much. Comparing parts 8-11 with part 1 in table 4.9, indicates that infiltration decreased the difference between shrinkages in x-y direction and z direction.

Part nr	gr. inf.	deb.	pre-sint. 1050°C	inf. after pre-sint.	SSS 1600°C	inf. after SSS	SSS 1600°C
1	o	x	o	o	66%	o	-
8	o	x	o	o	65%	x	65%
9	*o*	*x*	*37%*	*x*	*71%*	*x*	*68%*
10	x	x	o	o	54%	x	60%
11	x	x	31%	x	57%	x	60%

Table 4.8: Densities obtained at different stages of the PM process during the application of different pressureless infiltration strategies. The performed post-treatments are signed with an 'x'. The post-treatments which are not performed, are signed with an 'o'.

Part nr	gr. inf.	deb.	pre-sint. 1050°C		inf. after pre-sint.	SSS 1600°C		inf. after SSS	SSS 1600°C	
			x-y	z		x-y	z		x-y	z
1	o	x	o	o	o	-31%	-44%	o	-	-
8	o	x	o	o	o	-32%	-31%	x	-34%	-32%
9	o	x	-19%	-24%	x	-32%	-37%	x	-33%	-37%
10	x	x	o	o	o	-24%	-23%	x	-24%	-21%
11	x	x	-8%	-8%	x	-23%	-22%	x	-23%	-20%

Table 4.9: Percentage shrinkage obtained at different stages of the PM process during the application of different pressureless infiltration strategies. The performed post-treatments are signed with an 'x'. The post-treatments which are not performed, are signed with an 'o'.

In summary:

- Green pressureless infiltration decreases the final density of the parts.
- Green pressureless infiltration decreases the shrinkage of the parts during debinding and SSS.
- Pressureless infiltration after pre-sintering increases the final density of the parts and was the most successful densification step (densities up to 71% were obtained).
- Pressureless infiltration after solid state sintering may increase the final density of the parts (part 10-11), or may not have a positive influence on the final density (part 8-9).
- Pressureless infiltration after pre-sintering and solid state sintering did not seem to influence the part shrinkage much.
- Pressureless infiltration seems to homogenize the shrinkage in the x/y and z direction.

4.6.2.4 Pressure infiltration

A last strategy investigated to increase the density of the parts, was pressure infiltration. The pressure infiltration experiments were performed using an ethanol suspension containing 40 vol% alumina. Eight different pressure infiltration experiments were performed. Four parts (parts 12-15) were infiltrated after SLS (i.e. green infiltration) and after SSS. Four other parts (parts 16-19) were infiltrated after SLS, pre-sintering and SSS. During most infiltration experiments, the ethanol suspension was squeezed into the open porosity of the parts for 5 minutes at a pressure of 1.61 MPa, 16.1 MPa or 48.3 MPa. Two parts, parts 15 and 19, were pressure infiltrated for 30 minutes at 48.3 MPa.

Comparing parts 12-15 from table 4.10 with part 10 of table 4.8 reveals that when only applying green infiltration, the application of pressure did not increase the final densities much: for example, as well for the green pressure infiltrated as for the green pressureless infiltrated parts, the densities after the first SSS step were 51-54%. Comparing parts 16-19 in table 4.10 with part 11 in table 4.8, reveals that *applying pressure during an extra infiltration step after pre-sintering had a more pronounced influence on the final densities*: densities up to 84% were reached after the last SSS step (compared to 60% for part 11 in table 4.8). Applying the pressure for a longer time decreased the final densities: consider part 19 in table 4.10.

The shrinkages in x-y and z direction after SSS were somewhat less when applying pressure infiltration instead of pressureless infiltration: for example, when applying infiltration after SLS and pre-sintering, x-y shrinkages of -19 to -22% (table 4.11, parts 16-19) instead of -23% (table 4.9, part 11) were obtained after the first SSS step. Comparing parts 12-19 with part 1 in table 4.11, confirms that pressure infiltration also decreased the difference between the x-y shrinkage and the z shrinkage.

A drawback of the application of the pressure infiltration method was fracturing of the parts. This might be caused by air which was entrapped in the part and squeezed during the infiltration process. On the other hand, not only pores but also cracks could be filled with alumina and densities up to 84% were obtained. Figure 4.12a shows a 3D microscope image of part 18, which had a density of 83%. A large crack, pressure infiltrated with alumina is clearly visible. When having a closer look at the large infiltrated crack, micro-cracks surrounded by dense alumina become visible (figure 4.12b). Smaller micro-cracks, surrounded by dense alumina are also visible in the bulk material, i.e. in the infiltrated zones next to the large crack (figure 4.12c).

Part nr	p [MPa]	time [min.]	gr. inf.	deb.	pre-sint. 1050°C	inf.	SSS 1600°C	inf.	SSS 1600°C
1	-	-	o	x	o	o	66%	o	-
12	1.61	5	x	x	o	o	53%	x	63%
13	16.1	5	x	x	o	o	51%	x	62%
14	48.3	5	x	x	o	o	53%	x	61%
15	48.3	30	x	x	o	o	54%	x	62%
16	1.61	5	x	x	30%	x	65%	x	70%
17	16.1	5	x	x	31%	x	79%	x	84%
18	48.3	5	x	x	31%	x	80%	x	83%
19	48.3	30	x	x	31%	x	71%	x	74%

Table 4.10: Densities obtained at different stages of the PM process during the application of different pressure infiltration strategies. The performed post-treatments are signed with an 'x'. The post-treatments which are not performed, are signed with an 'o'.

Part nr	gr. inf.	deb.	pre-sint. 1050°C		inf.	SSS 1600°C		inf.	SSS 1600°C	
			x-y	z		x-y	z		x-y	z
1	o	x	o	o	o	-31%	-44%	o	-	-
12	x	x	o	o	o	-19%	-16%	x	-17%	-16%
13	x	x	o	o	o	-21%	-17%	x	-21%	-17%
14	x	x	o	o	o	-20%	-16%	x	-21%	-16%
15	x	x	o	o	o	-18%	-16%	x	-20%	-18%
16	x	x	-2%	-2%	x	-19%	-19%	x	-17%	-17%
17	x	x	-3%	-2%	x	-20%	-18%	x	-18%	-17%
18	x	x	-5%	-4%	x	-22%	-18%	x	-20%	-16%
19	x	x	-3%	-1%	x	-21%	-18%	x	-19%	-17%

Table 4.11: Percentage shrinkage obtained at different stages of the PM process during the application of different pressure infiltration strategies. The performed post-treatments are signed with an 'x'. The post-treatments which are not performed, are signed with an 'o'.

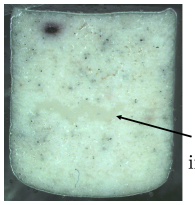

(a) 3D microscope image showing a crack pressure infiltrated with alumina.

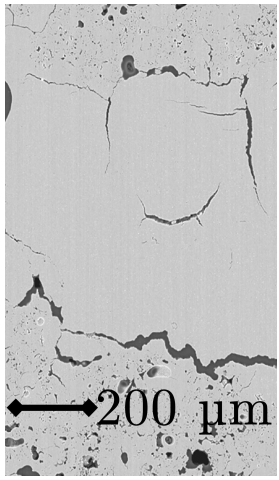

(b) BSE-SEM micrograph of an infiltrated crack.

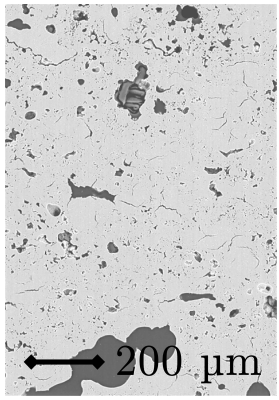

(c) BSE-SEM micrograph of the zone around the infiltrated crack.

Figure 4.12: Microscope images of the pressure infiltrated part 18.

In summary:

- Pressure infiltration after pre-sintering and solid state sintering increases the densities of the parts more than pressureless infiltration.
- Pressure infiltration decreases the shrinkage of the parts more than pressureless infiltration.
- Pressure infiltration for a longer time period can result in lower final densities.
- The application of pressure during infiltration might lead to fracturing of the parts.
- By applying pressure infiltration, not only pores, but also cracks can be filled.

4.6.2.5 Discussion

Unfortunately, all the infiltrated parts contained big internal cracks and voids (see e.g. figure 4.13a) after the solid state sintering process. This was in contrast with the large amount of small cracks, which occurred when no infiltration was applied (see figure 4.4a). As illustrated by figure 4.13b, only small porosities were obtained between the cracked zones.
A dense alumina shell was also observed at the edges of the parts (figure 4.13c). This shell was probably created when the alumina suspension was entering the pores and obstructed further infiltration. Since the suspension was too heavily loaded with alumina particles, the infiltrated part acted as a filter. It can be assumed that the dense shell prohibited the part to shrink uniformly. This can be explainedd as follows: part shrinkage, which mainly occurred during SSS (see section 2.4.7.2), was generally larger at the more porous areas of the part. As a result, the dense shell shrunk less, compared to the more porous core.
The assumption, that part shrinkage is generally larger at more porous areas, and the consequence, that the dense shell prohibits the part to shrink uniformly, might explain the following observations:

- The decrease of part shrinkage and concomitant final density when green (pressureless) infiltration was applied. As the pores were filled with infiltrant material, the amount of porosity decreased. As a result, also the amount of shrinkage during debinding and SSS decreased.
- The decrease of part shrinkage when pressure infiltration instead of pressureless infiltration was applied. The application of pressure increased the amount of infiltrant material entering the part.
- The formation of large internal cracks and voids when applying infiltration, instead of the large amount of smaller cracks when no infiltration was applied.
- The lower final densities when applying pressure infiltration for a longer time period. In this case, the application of pressure infiltration for a longer time caused the formation of a thicker shell.
- The difference between shrinkages in x/y direction and z direction.

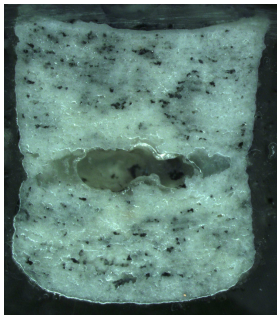

(a) 3D microscope image of part 11.

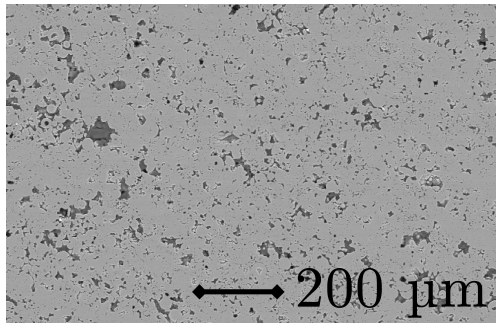

(b) BSE-SEM micrograph taken in a non-cracked area of part 8.

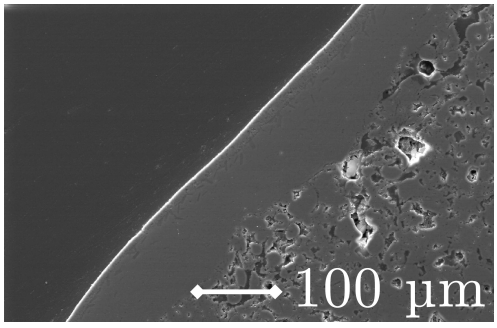

(c) SE-SEM micrograph taken at the edge of part 9.

Figure 4.13: Images of infiltrated parts.

4.7 Cause of the cracks

A disadvantage of the presented PM process is the occurrence of multiple cracks in the final parts without post-densification step (figure 4.4). Since the green SLSed parts did not contain cracks, they either originated during the debinding treatment, or during solid state sintering. In order to examine when exactly the cracks originated, two green (pressureless) infiltrated parts were further investigated. One part was debinded and pre-sintered at 1050°C to give the brown part some strength without causing too much shrinkage. The other part was debinded and solid state sintered at 1600°C. Both parts were cut with a diamond blade and the cross-sections were visualized by 3D microscopy. It could be clearly observed that the pre-sintered part (figure 4.14a) had some big cracks. This means that the cracks originated during debinding. As shown in figure 4.14b, the cracks were still visible in the part which was solid state

sintered at 1600°C.
Two strategies were investigated to eliminate the cracks of the final alumina parts. The first strategy was exploring the possibilities of infiltration: see section 4.6.2. The second strategy was to investigate the behavior of the produced powder during SLS and the debinding cycle. In order to do so, multiple differential scanning calorimetry and thermogravimetry (DSC-TGA) analyses (STA 449, Netzsch, UK) and Fourier transform infrared spectroscopy (FTIR) analyses (Bruker, Germany) were performed. It was found that the glass transition temperature Tg of the composite powder after production through the dispersion polymerization process was only 54°C instead of the expected 110°C for standard pure polystyrene. Since the polymerization reaction was not completed, the produced polystyrene had a rather low molecular weight or chain length. When using the composite powder for the first time in the Sinterstation 2000 SLS machine, the powder was preheated to 90°C. This caused the polymerization process to continue, which resulted in a higher glass transition temperature T_g of 90°C. During the debinding cycle, a complex degradation process occurred. The degradation process could be summarized in the following scheme:

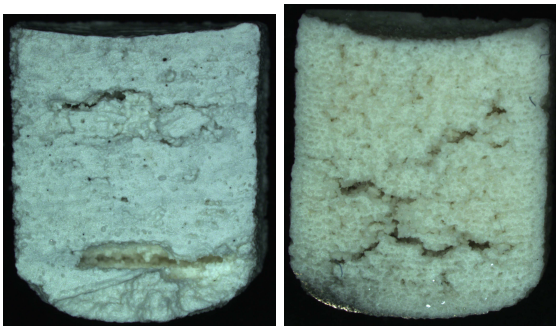

(a) (b)

Figure 4.14: 3D microscope image of parts, which underwent a green (pressureless) infiltration step: after pre-sintering at 1050°C (a); after SSS at 1600°C (b)

1. Evaporation of unreacted styrene
2. Thermal cracking of polystyrene molecules
3. Reorganization of the main chain to a stable aromatic structure
4. Combustion of the stable aromatic structure

In order to eliminate the formation of cracks in the parts, an optimized debinding scheme was proposed which maintained the heating rate of 0.1°C/min, but introduced a dwell time of 15 minutes at 250°C (for the reorganization of the main chain) and at the final temperature of 600°C. However, the final parts still contained cracks after the optimized debinding cycle. It can be concluded that the cracks were probably caused by either inhomogeneous distribution of alumina and polystyrene concentrations in the composite starting powder (which led to inhomogeneous shrinkage and resulting cracks during the debinding step), either by the occurrence of other phenomena which induced swelling (figure 3.8) during the debinding process.

4.8 Summary and conclusions

A PM process was developed and presented to produce freeform alumina parts through indirect SLS. The PM process comprised a dispersion polymerization process to produce composite alumina (61wt%) - polystyrene (39wt%) powder particles, as well as a tuned SLS process, a debinding and solid state sintering sintering step. When no extra densification step was applied, the final density amounted 66% (see table 4.12).
When using higher laser energy densities during SLS, the resulting green and final density of the parts was also higher. Nevertheless, dross formation (and polymer degradation) might occur. The amount of dross increased when applying higher laser energy densities.
The final alumina parts produced through the PM process contained a large amount of small cracks, which were formed during debinding. The larger parts (i.e. a cross-section > 1 cm^2), contained cracks which were also visible at the outer surface. Furthermore, the larger parts tended to curl during the debinding and SSS step. The cracks and the curling were probably caused by an inhomogeneous distribution of alumina and polystyrene in the composite starting powder or by the occurrence of other phenomena (e.g. swelling) during the debinding process.
Through geometrical assessments, the percentage shrinkage which occurred during the debinding and SSS process was investigated. The measured shrinkages were mainly caused by atomic diffusion (i.e. sintering), but also

by capillary forces, Van der Waals forces, cracking and curling of the parts. The shrinkage was more or less the same in the scan and cross-scan directions (about -31%), but on the contrary much larger in the building direction (about -44%). Furthermore, the unconstrained compressive sintering stresses seemed to let outer dimensions shrink more compared to inner dimensions.
Densification strategies, namely WIPing and infiltration, were presented to improve the density of the fabricated parts and reduce the occurrence of cracks in the final parts: see table 4.12 for an overview. WIPing could increase green densities from 66% to 94%. However, after applying a WIPing step, the final density and shrinkage during debinding and solid state sintering was lower. This might be due to the presence of large cracks in the final parts.
Pressureless and pressure infiltration tests with alumina-ethanol suspensions were performed at different stages of the PM process: after SLS (i.e. green infiltration), after pre-sintering and after SSS. These tests resulted in the following empirical conclusions regarding the density of the final parts:

- The infiltration time does not need to be longer than 1 hour.
- When applying stepwise infiltration, the highest weight gain is observed during the first infiltration step.
- In this chapter, green infiltration decreases the final density of the parts.
- Infiltration after pre-sintering increases the final density of the parts. Pressure infiltration after pre-sintering is the most successful densification step of this chapter.
- Infiltration after solid state sintering may have diverse effects on the final density of the parts.
- Pressure infiltration after pre-sintering and solid state sintering increases the density of the parts more than pressureless infiltration.

Since the suspension was too heavily loaded with alumina particles, the infiltrated part acted as a filter. As a result, during infiltration a dense alumina shell was created at the edges of the parts. This dense shell obstructed further infiltration.
It was assumed that the part shrinkage is generally larger at more porous areas and that consequently, the dense shell prohibited the part to shrink uniformly. This assumption could explain different infiltration results, such as:

- The decrease of part shrinkage and, hence, the final density when green (pressureless) infiltration was applied.
- The decrease of part shrinkage when pressure infiltration instead of pressureless infiltration was applied.
- The formation of big internal cracks and voids when applying infiltration, instead of the large amount of smaller cracks without infiltration.
- The difference between shrinkages in x/y direction and z direction.

The application of pressure during infiltration sometimes led to fracturing of the parts. This might be caused by air which was entrapped in the part and squeezed during the infiltration process. On the other hand, the application of pressure infiltration after pre-sintering led to an increase of the part densities up to 84% (table 4.12, part 17), since the cracks which occurred during the debinding process could be filled with alumina. Nevertheless micro-cracks arose. The micro-cracks probably occurred due to non-homogeneous shrinkage during solid state sintering.

Part nr	Additional densification steps (besides SLS, deb. and SSS)	ρ [%]	x-y [%]	z [%]
1	No, i.e. only deb. and SSS	66%	-31%	-44%
2	$WIP_{100°C}$	52%	-22%	-24%
3	$WIP_{110°C}$	48%	-24%	-23%
4	green continuous pressureless inf.: 20vol%;30hrs	53%	-19%	-17%
5	green continuous pressureless inf.: 30vol%;30hrs	50%	-20%	-18%
6	4 x stepwise green pressureless inf.: 20vol%;4hrs	47%	-20%	-18%
7	4 x stepwise green pressureless inf.: 30vol%;4hrs	47%	-17%	-15%
8	pressureless inf. after SSS: 30vol%	65%	-34%	-32%
9	pressureless inf. after pre-sint. & SSS: 30vol%	68%	-33%	-37%
10	pressureless inf. after SLS & SSS: 30vol%	60%	-24%	-21%
11	pressureless inf. after SLS, pre-sint. & SSS: 30vol%	60%	-23%	-20%
12	p-inf. after SLS & SSS: 1.61MPa;5min.;40vol%	63%	-17%	-16%
13	p-inf. after SLS & SSS: 16.1MPa;5min.;40vol%	62%	-21%	-17%
14	p-inf. after SLS & SSS: 48.3MPa;5min.;40vol%	61%	-21%	-16%
15	p-inf. after SLS & SSS: 48.3MPa;30min.;40vol%	62%	-20%	-18%
16	p-inf. after SLS, pre-sint. & SSS: 1.61MPa;5min.;40vol%	70%	-17%	-17%
17	p-inf. after SLS, pre-sint. & SSS: 16.1MPa;5min.;40vol%	84%	-18%	-17%
18	p-inf. after SLS, pre-sint. & SSS: 48.3MPa;5min.;40vol%	83%	-20%	-16%
19	p-inf. after SLS, pre-sint. & SSS: 48.3MPa;30min.;40vol%	74%	-19%	-17%

Table 4.12: Overview: sintered densities and linear shrinkages of the cubic (10x10x10 mm^3) alumina parts after additional densification steps. The dimensional shrinkages indicate the geometrical changes that appear after the SLS process (i.e. the geometry after SLS is the reference geometry). Part 1 was not densified, parts 2 and 3 were WIPed, parts 4-11 were pressureless infiltrated and parts 12-19 were pressure infiltrated (p-inf.) with an alumina suspension. The pressureless infiltration experiments were performed with 20 and 30 vol% alumina suspensions. The pressure infiltration experiments were performed with a 40 vol% alumina suspension.

Chapter 5

Production of alumina parts through Laser Sintering of polyamide-alumina agglomerates produced via dissolution-precipitation

References:

Deckers, J., Kruth, J., Shahzad, K., Vleugels, J. (2012). Density improvement of alumina parts produced through selective laser sintering of alumina-polyamide composite powder. CIRP Annals. Manufacturing Technology, 61 (1), 211-214. [57]

Deckers, J., Shahzad, K., Vleugels, J., Kruth, J., Boury, S. (2012). Production of alumina parts through Selective Laser Sintering of alumina-polyamide composite powder. In Bartolo, J. (Ed.), Innovative Developments in Virtual and Physical Prototyping. The International Conference on Advanced Research in Virtual and Rapid Prototyping (VRAP). Leira (Portugal), September 28 - October 1 (pp. 319-327). London: Taylor & Francis Group. [59]

5.1 Abstract

A powder metallurgy (PM) process to fabricate alumina parts through indirect Selective Laser Sintering (SLS) of spherical alumina-polyamide composite powder particles is presented and geometrically assessed. The PM process includes powder production, SLS, debinding and furnace sintering. Laser remelting and several isostatic pressing (IP) and infiltration techniques are investigated in order to improve the density of the final alumina parts. The investigated IP techniques are cold isostatic pressing (CIP), quasi isostatic pressing (QIP) and warm isostatic pressing (WIP). The investigated infiltration techniques, which use alumina containing suspensions, include both pressureless infiltration and infiltration under pressure (i.e. squeeze infiltration). Furthermore, microstructural and geometrical changes which occur during the PM process are investigated.

5.2 Introduction

In chapter 3, alumina parts could be produced, starting from ball-milled alumina-polyamide composite powder. Since the flowability of the ball-milled powder was not optimal, the powder could not be well deposited by the counter current roller of the DTM Sinterstation 2000 machine. As a consequence, no geometrically accurate parts could be produced. As depicted in this chapter, the homogeneity and flowability of conventionally deposited layers was increased by turning the submicrometer alumina powders into spherical alumina-PA composite agglomerates. An innovative temperature induced phase separation (TIPS; also called thermally induced phase separation) technique was used to produce spherical agglomerates of about 50 μm consisting of submicrometer alumina encapsulated in a polyamide matrix. This agglomerate size was large enough to avoid the unwanted clustering of submicrometer particles due to electrostatic forces. Moreover, the agglomerate size was fine enough to produce parts with a good geometrical quality.

5.3 The powder metallurgical process

Figure 5.1 schematically presents the main steps of the powder metallurgy process assessed in this chapter to produce alumina parts through AM. In a first step, the composite starting powder was produced. Afterwards the SLS parameters were optimized to produce green parts. The final alumina parts

were produced by subsequently debinding (deb.) and solid state sintering (SSS) of the green parts in a furnace. Geometrical assessments of the same benchmark part as shown in figure 4.7a, were used to assess the dimensional changes of the SLSed parts. These changes occurred during the debinding and SSS steps. In order to improve the final density of the alumina parts, densification treatments were used, namely: polymer remelting, Cold Isostatic Pressing (CIP), Quasi Isostatic Pressing (QIP), Warm Isostatic Pressing (WIP) and different infiltration (inf.) techniques.

The chapter investigates the quality of the components during the different processing steps. Density measurements were performed applying the Archimedes method (Analytical Balance, Sartorius, Germany) or applying the geometrical method by using a vernier caliper (Mitutoyo, Japan) to estimate the volume of the cuboid parts. In the tables of this chapter, the density of the parts, marked with *, were measured by the geometrical method. The initial CAD dimensions of these cuboid parts were 15x15x10 mm^3. The density of the parts which are not marked with an *, were measured by the Archimedes method. The initial CAD dimensions of these cubic parts were 10x10x10 mm^3. The geometrical assessments performed in section 5.5 were obtained by a coordinate measuring machine (CMM, FN905, Mitutoyo, Japan). A scanning electron microscope (SEM, XL30 FEG, FEI, The Netherlands) was utilized for the microstructural analyses.

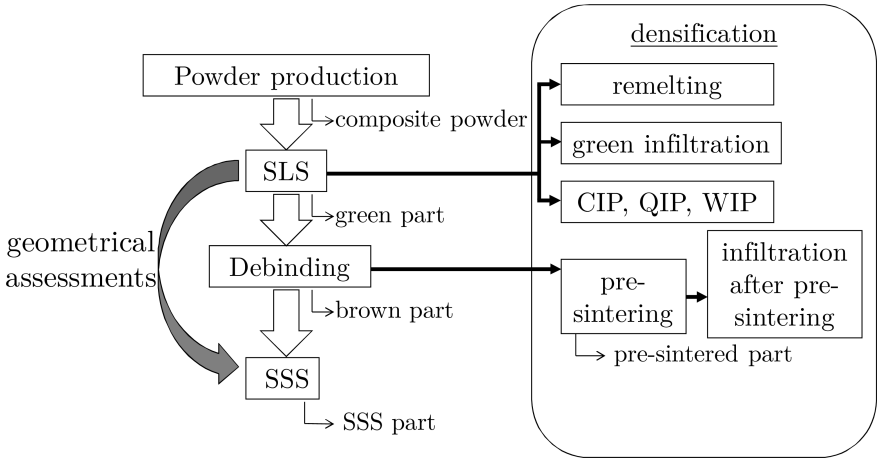

Figure 5.1: Powder metallurgy processing flow chart.

5.3.1 Difference with PM processes described in previous chapters

In summary, the PM process described in this chapter differs from the ones described in chapters 3 and 4 in three ways:

1. Semi-crystalline polyamide (PA) is used instead of amorphous polystyrene (PS; see chapter 4) as polymer binder.
2. The synthesis of the initial polymer-ceramic powder is done by temperature induced phase separation (TIPS), rather then by in-situ dispersion polymerization, as described in section 4.4.1, or ball milling, as described in section 3.3.1.
3. Other post-densification strategies are tested: a.o. remelting.

5.4 Production of alumina parts

5.4.1 Powder production

An innovative TIPS (or dissolution-precipitation) technique was used to produce 50vol% alumina - 50vol% PA and 40vol% alumina - 60vol% polyamide (PA) composite spheres (Yuan and Williams, 2007 [244]). The phase separation technique generally involves the dissolution of polymer in a suitable solvent by mixing, heating or increasing the pressure. The polymer is then allowed to precipitate from the homogeneous polymer solution by cooling the solution, also known as thermally induced phase separation (TIPS), reducing the pressure, evaporation of the solvent or adding a non-solvent (Van de Witte et al., 1996 [53]).
The first stage is the dissolution of polymer in a solvent. To do so, high purity α-alumina (grade SM8, Baikowski, France) powder with a d_{50}~0.3 μm and PA powder (grade Duraform PA, 3DSystems, USA) were added to DMSO (dimethyl sulfoxide) in a ratio 5/5/90 or 4/6/90 vol% alumina/PA/DMSO. This suspension was externally stirred in a 2 liter flask. The suspension was heated to 140°C (above the dissolution temperature of ~135°C) for 15 minutes under N_2 atmosphere to dissolve PA in DMSO. While stirring, the suspension was allowed to naturally cool to room temperature. Cooling of the PA solution led to a liquid-liquid phase separation to form two phases consisting of a DMSO rich phase and a PA rich phase. Upon further cooling, the PA rich phase solidified while incorporating the alumina submicrometer particles. Vacuum filtration was used to separate the PA-alumina precipitates from the DMSO and about

80% of the DMSO could be recovered. The precipitates were subsequently washed multiple times with ethanol and dried in an oven at 80°C for 24 hours. Fourier transformed infrared spectroscopy (FTIR) (Avatar 370, Thermo Optek, USA) confirmed that the polyamide did not experience structural changes during the powder production process: dissolution and reprecipitation at temperatures up to 140°C. Differential scanning calorimetry (DSC) and thermal gravimetric analysis (TGA) (Model-2920, TA instruments, USA) confirmed that the thermal properties of the composite powder were more or less the same as the thermal properties of the PA starting powder: the melting onset temperature, T_{om} was measured to be 184°C, while the crystallization temperature, T_{oc} was about 157°C [182]. The particle size of the composite microspheres was measured by laser diffraction (Mastersizer Plus, UK). As shown in figure 5.2, the composite powder had a monomodal distribution with an average diameter of ∼53 μm and an agglomerate size ranging from 2 to 105 μm. The morphology of the PA starting powder and produced composite powder was studied by scanning electron microscopy. As depicted in figure 5.3a, the pure PA powder had a honeycomb pattern. As a result of the phase separation process, the channels of this honeycomb pattern were filled with the submicrometer alumina particles (figure 5.3b). The result of the powder production process were ∼53 μm spherical alumina-PA composite agglomerates. A more detailed description of the powder production process can be found in [182].

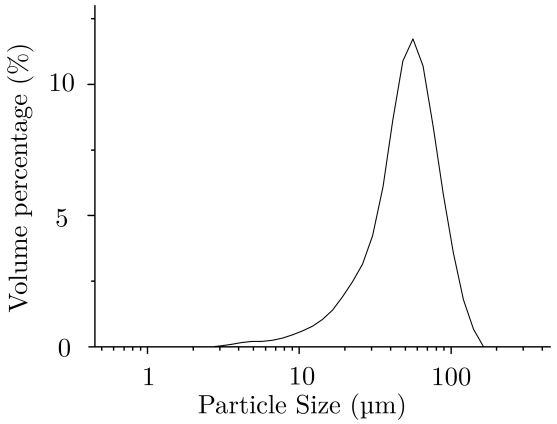

Figure 5.2: Particle size distribution of composite microspheres.

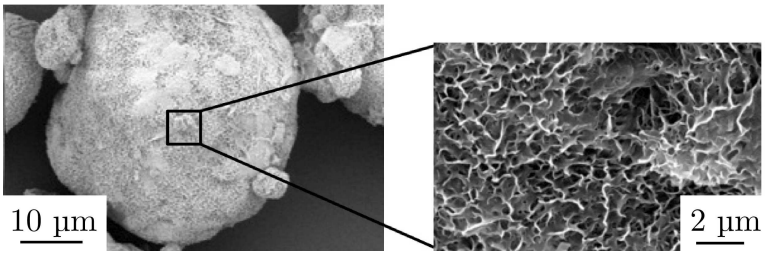

(a) Honeycomb pattern in pure PA powder.

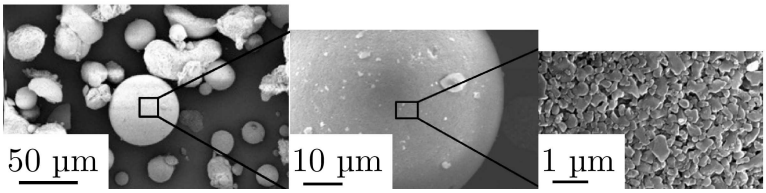

(b) Alumina particles filling the honeycomb pattern in Al_2O_3-PA microspheres.

Figure 5.3: Powder production.

5.4.2 Selective Laser Sintering (SLS) of the produced powder

Green samples were fabricated using a Sinterstation 2000 (DTM Corporation / 3DSystems, USA) equipped with a 100 W CO_2 laser (f100, Synrad, USA) with a wavelength of 10.6 μm and a laser beam diameter ϕ_{1/e^2} of 400 μm. Powder layers were deposited by a counter current roller and irradiated with the laser beam. In order to avoid thermal oxidation, SLS was performed in N_2 atmosphere (Air Liquide, Belgium, $[O_2] < 5$ %). In order to improve the laser sinterability of the powder and to avoid thermal cracks, the parts were produced at an elevated powder bed temperature (∼175°C). These powder preheating parameters were the standard preheating parameters for SLS of pure Duraform PA powder (without alumina addition). The energy required to melt PA was partly supplied by preheating of the powder bed to about 175°C, i.e. a temperature slightly below the melting onset temperature of 184°C (distributed cylinder heating and surface IR heating), and by extra laser irradiation which locally raised the temperature above the melting point.
According to the Quasi Isothermal Theory (Drummer D. et al., 2010 [65]), the composite powder is to be preheated to a temperature between the crystallization and melting temperature of polyamide during the SLS process. Afterwards, the laser energy is used to melt the PA and the PA-alumina remains in a molten state until all layers of the component are produced. The

surrounding composite powder that is not melted, supports the generated melt. During the final cooling down stage of the process, the PA crystallizes and a solid alumina-PA component is formed.
Initial tests were performed to investigate the powder preheating and cooling conditions. Moreover, initial tests revealed that the 40vol% alumina - 60vol% PA composite spheres showed a higher green density compared to the 50vol% alumina - 50vol% PA composite spheres [182]. This implied that a quite large amount (60 vol%) of PA was necessary to enable the production of sufficiently strong green parts.
After the initial tests, a parametrical study was performed to investigate other crucial SLS parameters. In this parametrical study, parts of 15x15x10 mm^3 were produced with a laser power 'P', scan speed 'v', scan spacing 's' and layer thickness 'l' varying between respectively 3-7 W, 300-1200 mm/s, 100-500 μm and 80-150 μm. The laser energy density, e, combining these parameters was an important parameter, and was defined as (see section 3.3.2):

$$e = \frac{P}{s.v.l} \tag{5.1}$$

When scanning with low laser energy densities, the melted PA phase was insufficient to consolidate the agglomerates (figure 5.4a). When scanning with too high laser energy densities, the PA degraded (figure 5.4b). Both too low and too high laser energy densities resulted in fragile green parts, which could not be used for further processing. The green parts produced by SLS in the 0.176 and 0.37 J/mm^3 laser energy density range allowed manufacturing green parts with a strength allowing non-destructive manipulation of the green parts.

During the SLS process, the scanned layers could delaminate (figure 5.4c). Delamination especially occurred when a too low layer thickness (e.g. $\sim$80 μm) was used: during layer deposition, the surface roughness peaks hit the roller and dragged along the parts being produced. After also inspecting the amount of delamination, four parts were selected to further investigate the geometrical accuracy by using a vernier caliper and the green density by applying the geometrical method. Finally, the following parameter set was chosen: 5 W laser power, 600 mm/s scan speed, 150 μm scan spacing and 150 μm layer thickness (table 5.1). This parameter set resulted in a relative green density of 55% of the theoretical density TD of the composite powder (=2.19 g/cm^3). The theoretical density (TD) was calculated assuming that the TD of PA was 1.00 g/cm^3 (Duraform PA datasheet) and the TD of alumina was 3.98 g/cm^3 (see chapter 2). The optimized set of SLS parameters was used for all further parts produced in this chapter.
Figure 5.5 shows a fractured surface of a part SLSed with the optimized parameter set (i.e. 5 W laser power, 600 mm/s scan speed, 150 μm scan spacing and 150 μm layer thickness). There is an indication of flowing of the PA during

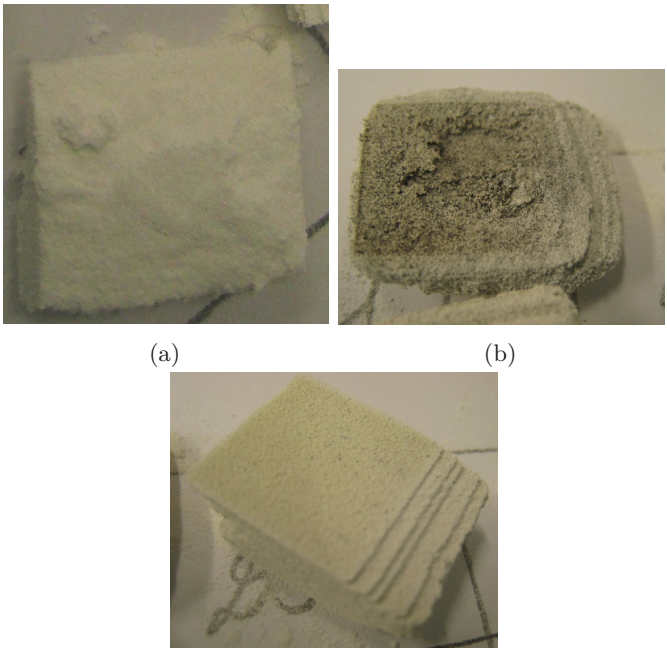

(a) (b)

(c)

Figure 5.4: Results of a parametrical SLS test, showing: a part produced with too low laser energy density (a); a part produced with too high laser energy density (b); delamination of a part with a relatively low (∼80 μm) layer thickness (c).

	laser power	scan speed	scan spacing	layer thickness	green density	relative green density
	W	mm/s	μm	μm	g/cm^3	% of TD
Part 1a*	3	600	150	150	1.18	54
Part 1b*	**5**	**600**	**150**	**150**	**1.20**	**55**
Part 1c*	5	1250	150	150	1.16	53
Part 1d*	5	600	300	150	1.17	53

Table 5.1: SLS parameters and concomitant green density of parts which were strong enough for non-destructive manipulation (i.e. laser energy density between 0.176 and 0.37 J/mm^3) and which did not delaminate. The optimized parameter set is shown in bold. The densities of the parts were measured by the geometrical method (as indicated by *).

laser sintering, but the microstructure is inhomogeneous. A distinction can be made between regions which were well melted and where even some powder particles collapsed, and regions where no melting of the powder particles could be observed and where the granular morphology of the starting powder was still visible.

5.4.3 Debinding and solid state sintering

In a debinding step, the polymer was removed from the green parts. A heating rate of 0.1°C/min was applied with a 2 hours dwell time at 275°C and 600°C, followed by furnace cooling. The submicrometer alumina particles were solid state sintered in a furnace sintering step. In this step a heating rate of 5°C/min was applied with a dwell time of 60 minutes at 1600°C, followed by furnace cooling. Sometimes furnace pre-sintering (pre-sint.) was used before the furnace sintering cycle to strengthen the brown parts by forming necks between the submicrometer particles. By applying a heating rate of 5°C/min and a dwell time of 2 hours at 1050°C, these brown parts only went through the initial stage (i.e. neck formation) of the SSS process.
As depicted in table 5.2, the parts produced with optimized parameters had a mean density of about 47% of the TD of alumina (= 3.98 g/cm^3, see chapter 2) after the solid state sintering step. As shown in a 3D microscope image of the final part after cutting with a diamond blade (figure 5.6a), no large no cracks or large porous regions could be observed in the final part. A SEM image of an alumina part, produced with optimized parameters, after debinding and solid state sintering (figure 5.6b) shows that the agglomerates did not collapse (i.e.

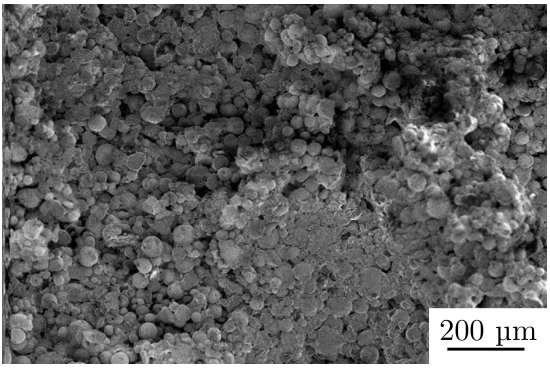

Figure 5.5: Scanning electron microscope (SEM) image of the fracture surface of a part SLSed with the optimized parameter set.

break) during debinding. Instead, an inhomogeneous porous microstructure consisting of dense interconnected agglomerates was obtained. Solid state sintering resulted in neck formation between the agglomerates which helped the parts to retain their shape, but also resulted in the presence of large inter-agglomerate pores and concomitant low final density.

In summary:

- Alumina parts can be successfully produced through SLS of alumina-PA composite powder synthesized by a temperature induced phase separation (TIPS) process.
- By increasing the PA content of the starting powder from 50 to 60vol%, parts with a higher green density can be produced.
- When using too high or too low laser energy densities during SLS, the resulting green parts are too fragile for further processing.
- When applying a too low layer thickness during SLS, the parts delaminate.
- The final parts, produced with optimized SLS parameters, do not contain cracks. Nevertheless the parts contain inter-agglomerate pores which restrict the final density to 47%.

Part nr	Additional densification steps (besides SLS, deb. and SSS)	ρ_{FS} [%]	x-y [%]	z [%]
1b	No, i.e. only deb. and SSS	47%	-21%	-24%

Table 5.2: Sintered density (Archimedes method) and linear shrinkage after SSS of an alumina part produced with optimized SLS parameters. The dimensional shrinkages indicate the geometrical changes that appeared after the SLS process (i.e. the geometry after SLS is the reference geometry).

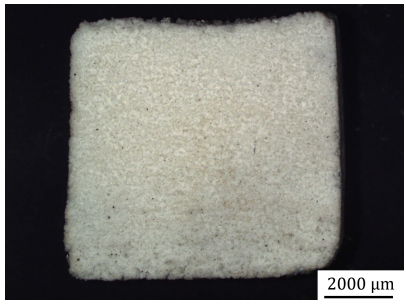

(a)

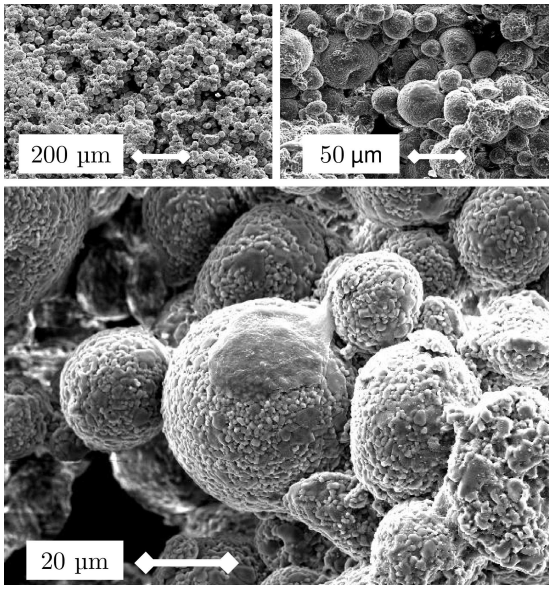

(b)

Figure 5.6: Final part after debinding and SSS after cutting with a diamond blade: overview image (a); SEM images (b).

5.5 Geometrical assessments

The investigated PM process enabled the production of freeform parts with a good geometrical accuracy through indirect SLS (see figure 5.7). The production of parts with a good geometrical accuracy was possible since the particle size of the starting powder was relatively low ($\sim$50μm). Moreover, due to the spherical shape of the powder, the small particles could be well deposited by the counter current roller system which was used during SLS. Figure 5.8 represents the famous Belgian statue 'Manneken Pis' as a green and final part. The figure illustrates that the produced green parts underwent a large but seemingly uniform shrinkage during debinding and furnace sintering.

A benchmark part (figure 4.7a) was used to quantitatively investigate the percentage linear shrinkage during debinding and SSS. The percentage linear

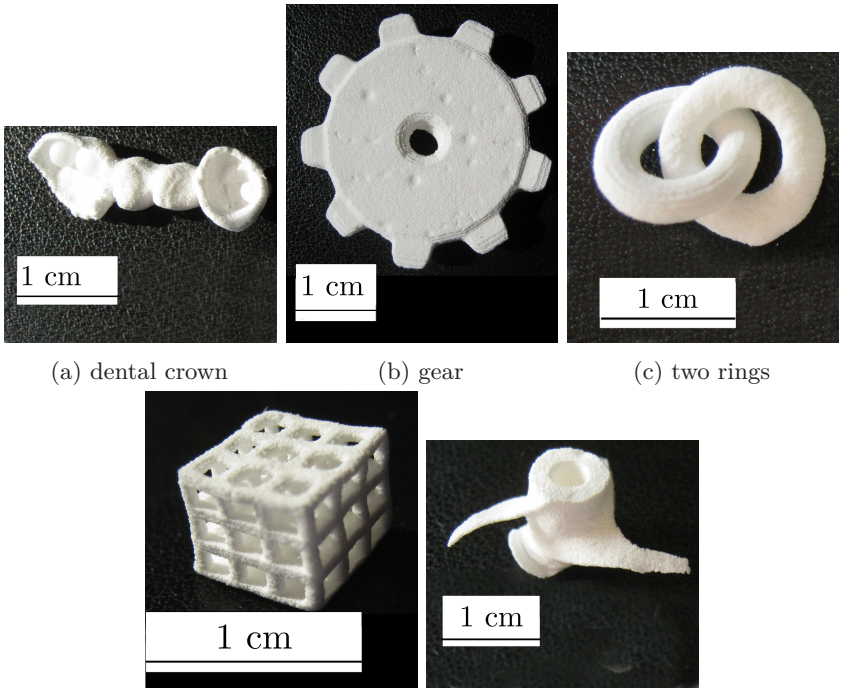

(a) dental crown (b) gear (c) two rings

(d) lightweight cube (e) turbine blades

Figure 5.7: Complex shaped solid state sintered alumina parts, produced by the PM process.

Figure 5.8: Seemingly uniform shrinkage of a part during debinding and solid state sintering.

shrinkage (% linear shrinkage) which occurred during debinding and solid state sintering was mainly shrinkage due to the sintering stresses (see section 2.4.7.2) and was defined as

$$\%\ linear\ shrinkage\ =\ \frac{dimension\ after\ SSS\ -\ green\ part\ dimension}{green\ part\ dimension} \tag{5.2}$$

Figure 5.9 describes the % linear shrinkage of different features of the benchmark part as a function of the corresponding green dimension. By looking at the larger dimensions (>20 mm), it can be seen that the % linear shrinkage was about -23%. The % linear shrinkage seemed to vary a lot for the smaller green dimensions. This was probably due to measurement errors, which were relatively larger for smaller dimensions. When comparing outer and inner dimensions, it can be observed that the outer dimensions shrunk more. This observation was also made in the previous chapter (see section 4.5). As described in the previous chapter, a possible explanation for this observation can be found by looking at the sintering stress which occurred during shrinkage. As illustrated in figure 4.10a, the sintering stress was not constrained and tended to reduce the outer contours. In this case, the reduction of the outer contours and the shrinkage of the debinded part acted in the same direction.

On the contrary, the sintering stress tended to increase internal contours (figure 4.10b). The shrinkage of the debinded part counteracted this increase, resulting in a lower total shrinkage of the internal geometry.
Figure 5.10 describes the % linear shrinkage of the benchmark parts in x 'scan' and y 'cross-scan' direction (figure 4.6) during debinding and SSS. Although the measured variation of % shrinkage seemed to be slightly larger for the x direction compared to the y direction, no large difference could be observed. In the remaining of the chapter no distinction will be made between shrinkages in the x and y direction.
In order to investigate the uniformity of the shrinkage, a distinction was made between the mean shrinkage in the 'scan/cross-scan' directions (respectively x-direction and y-direction) and the shrinkage in the build direction (z-direction). Table 5.2 indicates that after solid state sintering (part 1b) a quite uniform shrinkage of -21 to -24% was obtained.
At last, the benchmark part shown in figure 4.7a was used to investigate the roughness change in x and y direction during debinding and SSS. Different roughness values (Ra, Rt and Rz) were obtained in x and y direction. A Gaussian filter with a lower (Ls) and higher (Lc) cut-off value of respectively 0.008 mm and 2.5 mm was used to process the measured data. As depicted in table 5.3, there seemed to be no significant directional dependency between the roughness values in the x 'scan' and y 'cross-scan' direction. On the other hand, the roughness values of the final parts were somewhat lower than the roughness values of the green parts. This may be due to the shrinkage of the part during debinding and solid state sintering.

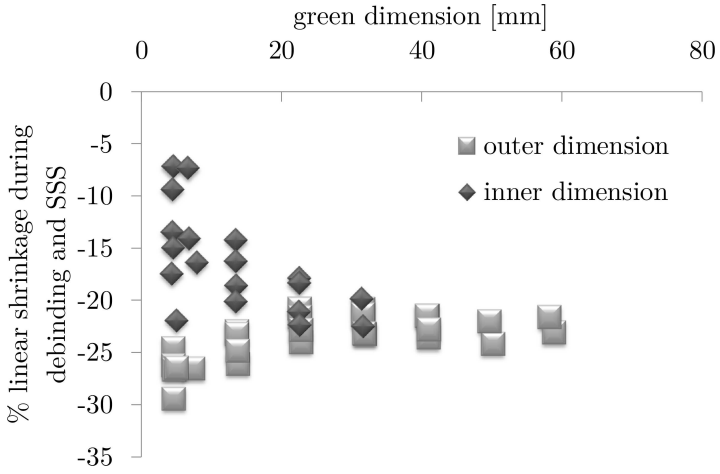

Figure 5.9: Percentage linear shrinkage of outer and inner dimensions.

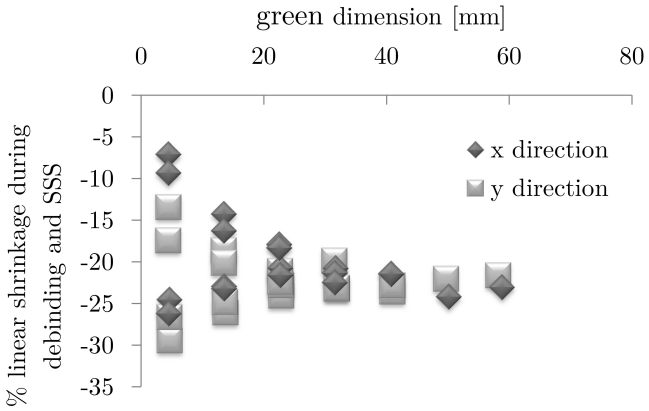

Figure 5.10: Percentage of linear shrinkage in x and y direction.

	x direction	y direction
Green part: Ra [μm]	17μm	17μm
Green part: Rt [μm]	140μm	140μm
Green part: Rz [μm]	110μm	112μm
Final part: Ra [μm]	16μm	15μm
Final part: Rt [μm]	112μm	104μm
Final part: Rz [μm]	98μm	88μm

Table 5.3: Mean roughness values after SLS (green) and SSS (final), of the benchmark part depicted in figure 4.7a.

The conclusions of this section are similar to the conclusions of section 4.5:

- Complex shaped alumina parts could successfully be produced by the PM route presented in the previous section.
- The shrinkage during debinding and SSS is mainly caused by sintering stress. Sintering stress causes outer part dimension to shrink more than inner part dimensions.
- Dimensions in the x 'scan' and y 'cross-scan' directions shrink about the same amount during debinding and SSS. The x/y shrinkage was about -23%. In the remaining of the chapter, no distinction will be made between shrinkages in the x and y direction.
- Roughness values become slightly lower during debinding and SSS.

5.6 Densification strategies

Although the described PM process could be used to produce freeform, complex shaped objects (figure 5.7), the density of the final parts was modest. In the next sections, the following strategies will be studied to improve the final density: remelting, isostatic pressing (IP) and infiltration (inf.).

5.6.1 Remelting

A first strategy to improve the part density was to laser scan every powder layer two or more times instead of only once, i.e. laser remelting. Two polymer remelting experiments, namely 'experiment a' and 'experiment b', were performed. During each of the remelting tests, every powder layer was scanned once with the optimized parameter set for SLS (5 W laser power, 600 mm/s scan speed, 150 μm scan spacing) and also one or two times with different remelting parameters. The remelting parameters were: laser power 'P' of 5-10 W, scan speed 'v' of 320-1280 mm/s and scan spacing 's' of 150 μm. The density of the parts of the first remelting test (parts 2a to 19a) were analyzed by the geometrical method (table 5.4a, table 5.5). The density of the parts of the second remelting tests (parts 2b to 19b) were analyzed by the Archimedes method (table 5.4b, table 5.5).
As depicted in table 5.4, applying the remelting scan strategy could increase the green density of the parts up to 63% - 62% ('experiment a' - 'experiment b'). Generally, when using higher remelting laser energy densities (by increasing the laser power and/or decreasing the scan speed), higher green densities were obtained. Only when too high laser energy densities were used, the green densities of the produced parts tended to decrease due to degradation of the PA. Also, when laser sintering with too high laser energy density, the melted PA tended to stick powder particles which were not laser scanned to the produced parts. This caused unwanted 'dross formation' which is visualised in figure 5.11a.
Although remelting could increase the green densities of the parts, the final density after debinding and furnace sintering was only increased up to 50% - 51% ('experiment a' - 'experiment b') of the theoretical density (parts 2-19 in table 5.5). This non significant increase in final density could not be clearly observed by comparing SEM images of figure 5.11b and figure 5.6b. Further, the remelting strategy did not cause the wanted collapsing of the composite microspheres. At last, the dimensional shrinkage of the remelted parts during debinding and furnace solid state sintering was -18 to -24% in the x-y direction and -12 to -25% in the z direction (table 5.5).

P [W]	320	640	1280 v [mm/s]
10	**59** / 47	**57** / 46	**54** / 47
7	**60** / 47	**55** / 46	**53** / 48
5	**59** / 50	**54** / 46	**53** / 47

P [W]	320	640	1280 v [mm/s]
10	**55** / 42	**61** / 47	**57** / 49
7	**60** / 47	**59** / 47	**56** / 49
5	**63** / 48	**59** / 46	**57** / 50

(a) Experiment a (parts 2a to 19a): the densities were measured geometrically.

P [W]	320	640	1280 v [mm/s]
10	**61** / 48	**62** / 50	**56** / 48
7	**61** / 50	**56** / 48	**57** / 50
5	**59** / 51	**57** / 49	**55** / 49

P [W]	320	640	1280 v [mm/s]
10	**55** / 41	**61** / 50	**57** / 48
7	**60** / 48	**59** / 50	**56** / 48
5	**59** / 49	**57** / 49	**56** / 47

(b) Experiment b (parts 2b to 19b): the densities were measured by the Archimedes method.

Table 5.4: Relative green densities (bold) and densities after solid state furnace sintering [%] of two different remelting experiments. The parts at the left and right side, represent parts which were respectively remelted once and twice.

Part nr	Additional densification steps (besides SLS, deb. and SSS)	ρ_{FS} [%]	x-y [%]	z [%]
1b	No, i.e. only deb. and SSS	47%	-21%	-24%
2a-19a*	Laser remelting	46-50%	-20 to -24%	-14 to -25%
2b-19b	Laser remelting	47-51%	-18 to -23%	-12 to -25%

Table 5.5: Sintered density and linear shrinkage of the alumina parts after remelting. The density of the parts, marked by *, were measured by the geometrical method. Other densities were measured by the Archimedes method.

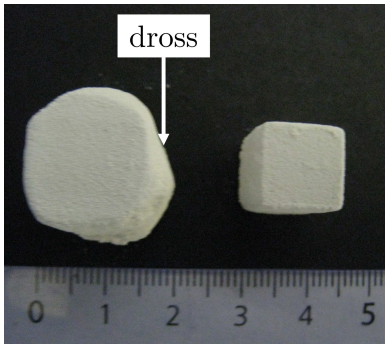

(a) Green part with (left) and without (right) 'dross formation'.

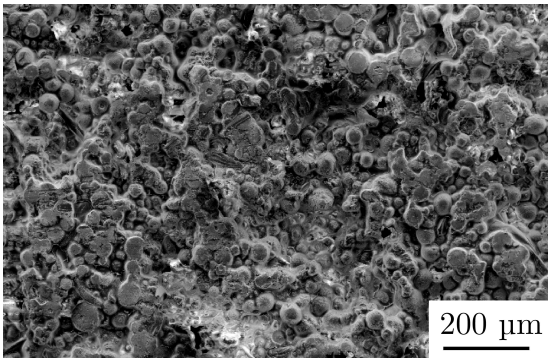

(b) SEM micrograph of solid state sintered part, produced by laser remelting.

Figure 5.11: Remelting

In summary:

- Remelting increases the green density of the parts, but not the final density after SSS.
- Remelting causes unwanted 'dross formation' when too high laser energy densities are applied.

5.6.2 Isostatic pressing (IP)

Three isostatic pressing (IP) techniques were investigated to increase the density of the green SLSed parts, and as a result also the density of the final SSS parts: (wet bag) cold isostatic pressing (CIP), quasi isostatic pressing (QIP) and warm isostatic pressing (WIP).

5.6.2.1 Cold isostatic pressing (CIP)

A first isostatic pressing (IP) strategy to improve the final density was to (wet bag) CIP the green SLS parts before debinding and solid state sintering. Samples, produced by SLS with optimized parameters, were vacuum packed in a rubber sheath or bag. The vacuum packed samples were placed in a pressure vessel and isostatically pressed at respectively 100, 150 and 200 MPa.
CIP could increase the relative green density of the parts from 55% to 78% (table 5.6), i.e. about 20%. This corresponded to a % linear shrinkage of -6% to -8% in the x-y direction and -11% to -13% in the z direction. As depicted in table 5.7, the total % linear shrinkage of the final parts was -20 % to -27% in the x-y direction and -32% to -33% in the z direction. These shrinkages were larger than the shrinkages obained when CIP was not applied (part 1b in table 5.7). Final sintered densities up to 62% were obtained (table 5.7). The increase in final density could be observed by comparing the microstructure of the final parts with (figure 5.12) and without (figure 5.6b) the CIP step. CIPing at higher pressures seemed to give slightly higher green densities and according to the SEM images (figure 5.12) also higher final densities. Nevertheless, the hypothesis that the final density increases by increasing the CIP pressure, could not be confirmed by the density measurements (table 5.7). Inter-agglomerate pores were still visible in the final parts (figure 5.12).

5.6.2.2 Quasi isostatic pressing (QIP)

The difference between QIPing and (wet bag) CIPing, is that powder particles are used instead of a liquid as pressure transmitting medium during QIPing. Moreover, the samples do not need to be vacuum packed before QIPing and QIPing can be performed at elevated temperatures. QIPing tests at 100°C and 160°C were performed for 5 and 30 minutes.
Compared to QIPing at 100°C, QIPing at 160°C clearly resulted in higher green densities (table 5.6). At 160°C, PA had a higher plasticity and therefore the green part could be compressed to higher densities. QIPing for a short period of time (5 minutes) seemed to result in higher green densities, compared to QIPing for longer time periods (30 minutes). This counterintuitive result

Part nr	Additional densification steps (besides SLS, deb. and SSS)	ρ_{SLS} [%]	ρ_{IP} [%]	x-y [%]	z [%]
20*	$CIP_{100\ MPa;\ <5\ minutes}$	55%	74%	-7%	-13%
21*	$CIP_{150\ MPa;\ <5\ minutes}$	55%	78%	-8%	-13%
22*	$CIP_{200\ MPa;\ <5\ minutes}$	54%	75%	-6%	-11%
23*	$QIP_{100°C;\ 50\ MPa;5\ minutes}$	54%	65%	+2%	-15%
24*	$QIP_{100°C;\ 50\ MPa;30\ minutes}$	57%	63%	+2%	-12%
25*	$QIP_{160°C;\ 50\ MPa;5\ minutes}$	59%	82%	+1%	-29%
26*	$QIP_{160°C;\ 50\ MPa;30\ minutes}$	55%	72%	+7%	-32%
27	$WIP_{110°C;\ 16.1\ MPa;\ 30\ minutes}$	52%	72%	-4%	-6%
28	$WIP_{110°C;\ 16.1\ MPa;\ 30\ minutes}$	49%	73%	-9%	-9%

Table 5.6: Green density and linear shrinkage of green parts after additional isostatic pressing (IP) steps. The dimensional shrinkage indicates the geometrical changes that appeared after the SLS process (i.e. the geometry after SLS is the reference geometry). The density of the parts, marked by *, were measured by the geometrical method. Other densities were measured by the Archimedes method.

Part nr	Additional densification steps (besides SLS, deb. and SSS)	ρ_{FS} [%]	x-y [%]	z [%]
1b	No, i.e. only deb. and SSS	47%	-21%	-24%
20*	$CIP_{100\ MPa;\ <5\ minutes}$	62%	-27%	-32%
21*	$CIP_{150\ MPa;\ <5\ minutes}$	53%	-20%	-33%
22*	$CIP_{200\ MPa;\ <5\ minutes}$	59%	-26%	-32%
23*	$QIP_{100°C;\ 50\ MPa;\ 5\ minutes}$	63%	-27%	-33%
24*	$QIP_{100°C;\ 50\ MPa;\ 30\ minutes}$	53%	-19%	-34%
25*	$QIP_{160°C;\ 50\ MPa;\ 5\ minutes}$	63%	-19%	-42%
26*	$QIP_{160°C;\ 50\ MPa;30\ minutes}$	56%	-13%	-46%
27	$WIP_{110°C;\ 16.1\ MPa;\ 30\ minutes}$	62%	-29%	-29%
28	$WIP_{110°C;\ 16.1\ MPa;\ 30\ minutes}$	63%	-29%	-30%

Table 5.7: Density and linear shrinkage after SSS of alumina parts, which were isostatically pressed after SLS. The density of the parts, marked by *, were measured by the geometrical method. Other densities were measured by the Archimedes method.

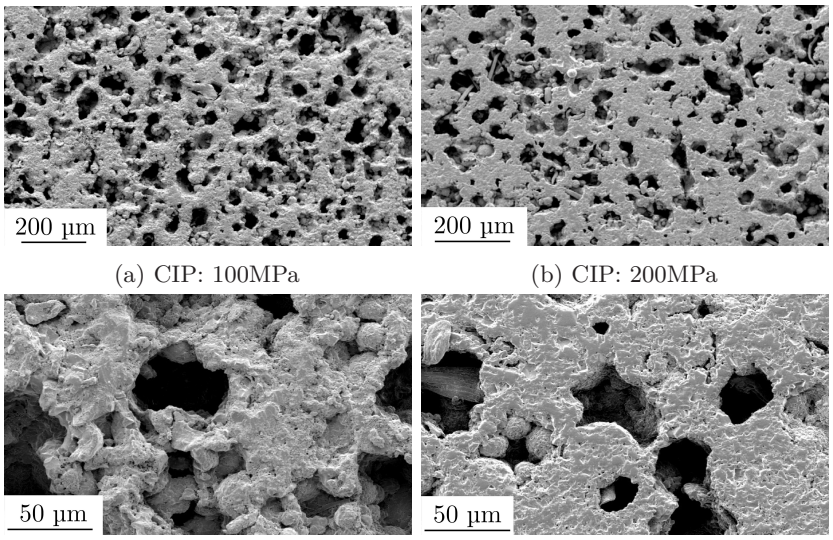

(a) CIP: 100MPa (b) CIP: 200MPa

(c) CIP: 100MPa (d) CIP: 200MPa

Figure 5.12: SEM images of CIP parts after solid state sintering.

might be related to the nonuniform pressure distribution during QIP.
A drawback of the QIP process was the nonuniform shrinkage due to the uniaxial compression in the z direction. The axial compression led to a % linear shrinkage of -12% to -32% in the z direction, but a % linear expansion (!) of +1% to +7% in the x-y direction (table 5.6).
Finally, a % linear shrinkage of -13% to -27% in the x-y direction, and -33% to -46% in the z direction were obtained after furnace solid state sintering (table 5.7). Final densities up to 63% of TD (table 5.7) were reached. The increase in final density could be observed by comparing the microstructure of the produced parts with (figure 5.13) and without (figure 5.6b) the QIP step. Inter-agglomerate pores were still visible in the final parts after QIPing (figure 5.13).

5.6.2.3 Warm isostatic pressing (WIP)

The WIPing process comprises vacuum packing and immersing an SLSed part in a heated liquid that transmits the pressure uniformly to the part. WIPing combines the advantages of both CIPing and QIPing, i.e. a heated pressure transmitting medium and a uniformly applied pressure.
During all WIPing tests, the vacuum packed SLSed samples were first heated in

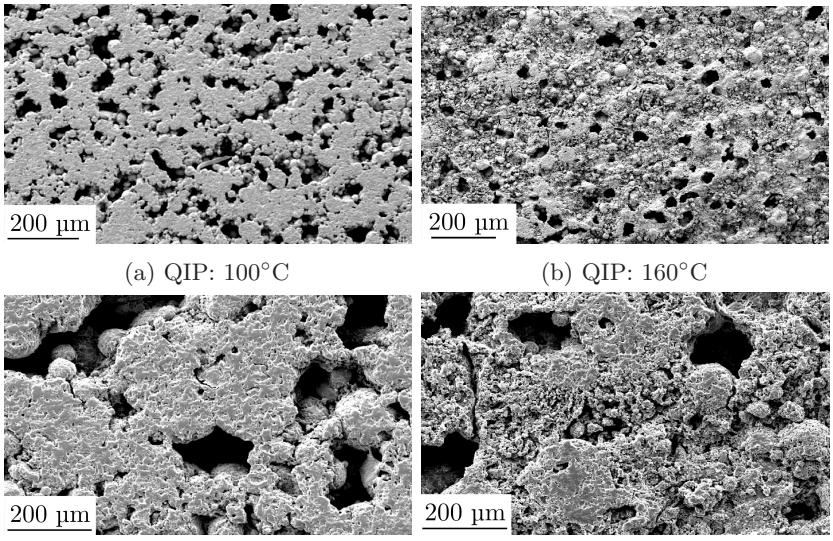

(a) QIP: 100°C (b) QIP: 160°C

(c) QIP: 100°C (d) QIP: 160°C

Figure 5.13: SEM images of QIP parts after solid state sintering.

silicon oil to 110°C. For 5 minutes (min.) a uniform pressure of 16.1 MPa was applied. WIPing of the green parts resulted in an increase of the green density up to 73% and a quite uniform shrinkage of -4% to -9% (table 5.6). After debinding and solid state sintering, the final densities and measured (uniform) shrinkages were respectively 62% to 63% and -29% to -30% (see parts 27 and 28 in table 5.7). The shrinkages were larger than the shrinkages obained when WIP was not applied (part 1b in table 5.7).
Although no cracks could be observed after WIPing (figure 5.14a), unwanted circular cracks could be observed in the cross sections of the parts after debinding and solid state sintering (see arrow in figure 5.14b). Possible reasons for these cracks are an inhomogeneous pressure or temperature distribution, air entrapment during the WIPing process and too fast debinding or furnace sinter rates. As can be seen in figure 5.14c and figure 5.14d, WIPing also could not cause the breaking of the composite microspheres. Inter-agglomerate pores were still visible.

In summary:

- CIP, QIP and WIP increase the green density of the SLSed parts and the final densities of the parts after solid state sintering. Inter-agglomerate pores are still visible.

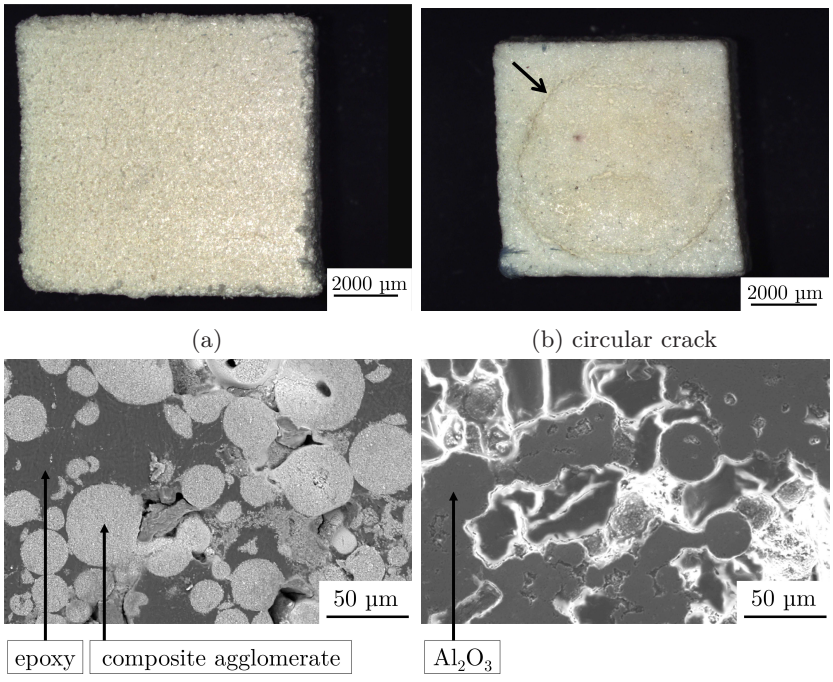

Figure 5.14: Cross-sectional 3D microscope and SEM images of a WIPed green part (a resp. c) and a WIPed part after solid state sintering (b resp. d).

- QIPing leads to a nonuniform shrinkage due to the uniaxial compression in the z direction.
- CIP and WIP lead to an increased shrinkage of the final sintered parts.
- WIP leads to a quite uniform final % linear shrinkage of about -30%.
- WIP seems to be a more promising IP technique than CIP and QIP, since an isostatic pressure can be uniformly applied on the SLSed sample and the heated liquid allows the binder material to be plastically deformed. Nevertheless, circular cracks in the final parts should be avoided.

5.6.3 Infiltration (inf.)

A last method investigated to improve the green density was to infiltrate the green parts or the pre-sintered parts with a suspension (susp.) containing

submicrometer alumina particles (grade SM8, Baikowski, France). The infiltration experiments were performed by using ethanol based suspensions.

5.6.3.1 Green pressureless infiltration with 10 and 20 vol% Al_2O_3-ethanol suspensions

During the first ethanol based infiltration experiments, the behavior of two suspensions with different alumina content (10 and 20vol%) was investigated. The suspensions were prepared by pouring an appropriate amount of alumina powder into ethanol fluidum. The suspension was mixed in a Turbula mixer and no stabilizer (e.g. citric acid) was added to the supsension. The infiltration time was varied between 2 and 12 hours.
As illustrated in table 5.8, infiltrating with a 20vol% alumina suspension seemed to result in a slightly higher weight increase compared to infiltrating with a 10vol% alumina suspension. After infiltration with a 20vol% alumina suspension, a (dry) weight increase of +20wt% to +23wt% was observed. After infiltration with a 10 vol% alumina suspension, the (dry) weight increase was only +9wt% to +18wt%.
Infiltrating for longer period of time also seemed to result in a slightly higher weight increase (up to +23%). Final densities (ρ_{FS}) up to 54% of the TD of alumina were reached after solid state sintering. These densities were measured by the geometrical method.
At last, it could be observed that infiltration reduced the % linear shrinkage: compare the final shrinkages of parts 29 to 40 with the final shrinkage of part 1b in table 5.8. No microstructural changes could be clearly observed by comparing the SEM images of figure 5.15 with the SEM images of figure 5.6b.

In summary:

- Green infiltration can increase the final density of the parts and reduces the part shrinkage after SSS.

5.6.3.2 Green pressureless and pressure infiltration with a stabilized Al_2O_3-ethanol suspension

During a second set of infiltration experiments, both pressureless and pressure infiltration, where an external pressure was applied to press the suspension into the pores of the part, were performed. A 30vol% alumina - 70vol% ethanol suspension was used during the pressureless infiltration experiments. A 40vol%

Part nr	Additional densification steps (besides SLS, deb. and SSS)	ρ_{SLS} [%]	Δweight [wt%]	ρ_{FS} [%]	x-y [%]	z [%]
1b	No	51-55%	-	47%	-21%	-24%
29*	Pressureless, 10vol% susp., 2h	51%	+9%	47%	-19%	-16%
30*	Pressureless, 10vol% susp., 4h	53%	+9%	47%	-18%	-17%
31*	Pressureless, 10vol% susp., 6h	53%	+12%	49%	-18%	-17%
32*	Pressureless, 10vol% susp., 8h	53%	+12%	48%	-20%	-19%
33*	Pressureless, 10vol% susp., 10h	54%	+18%	54%	-19%	-23%
34*	Pressureless, 10vol% susp., 12h	55%	+13%	46%	-18%	-17%
35*	Pressureless, 20vol% susp., 2h	52%	+21%	48%	-14%	-16%
36*	Pressureless, 20vol% susp., 4h	54%	+21%	47%	-13%	-19%
37*	Pressureless, 20vol% susp., 6h	53%	+22%	50%	-12%	-19%
38*	Pressureless, 20vol% susp., 8h	53%	+21%	48%	-17%	-18%
39*	Pressureless, 20vol% susp., 10h	54%	+20%	51%	-19%	-18%
40*	Pressureless, 20vol% susp., 12h	54%	+23%	50%	-17%	-18%

Table 5.8: Green (ρ_{SLS}) and final (ρ_{FS}) densities, (dry) weight increase after green infiltration (Δweight) and linear shrinkages of the final parts. The weight increase is expressed as weight percentage, wt%, of the green part. The dimensional shrinkages indicate the geometrical changes that appeared after the SLS process (i.e. the geometry after SLS is the reference geometry). The density of the parts, marked by *, were measured by the geometrical method. Other densities were measured by the Archimedes method.

alumina - 60vol% ethanol suspension was used during pressure infiltration. In contrast to the infiltration experiments described in the previous section, the suspensions were stabilized by adding 0.3wt% of citric acid (Anhydrous p.a., Acros, USA) and by mixing in a Turbula mixer for 24 hrs.
Four SLSed green parts were infiltrated: see parts 41 to 44 in table 5.9. Part 41 was pressureless infiltrated for 4 hours. Part 42 and part 43 were pressure infiltrated respectively once and twice. Part 44 was WIPed after pressure infiltration. All pressure infiltrated tests of this section were performed for 5 minutes under a pressure of 1.6 MPa.
As can be seen in table 5.9, green infiltration of the parts caused a reduction in dimensional shrinkage during debinding and furnace sintering: parts 41-43 had a dimensional shrinkage of -15 to -17% (compared to -21 to -24% for part 1b which was not green infiltrated) and part 44 had a shrinkage of -24 to -25% (compared to -29 to -30% of part 27 and part 28 which were not green infiltrated). The final density seemed to be increased when green pressure infiltration was applied for two times and when WIPing was applied after green pressure infiltration.

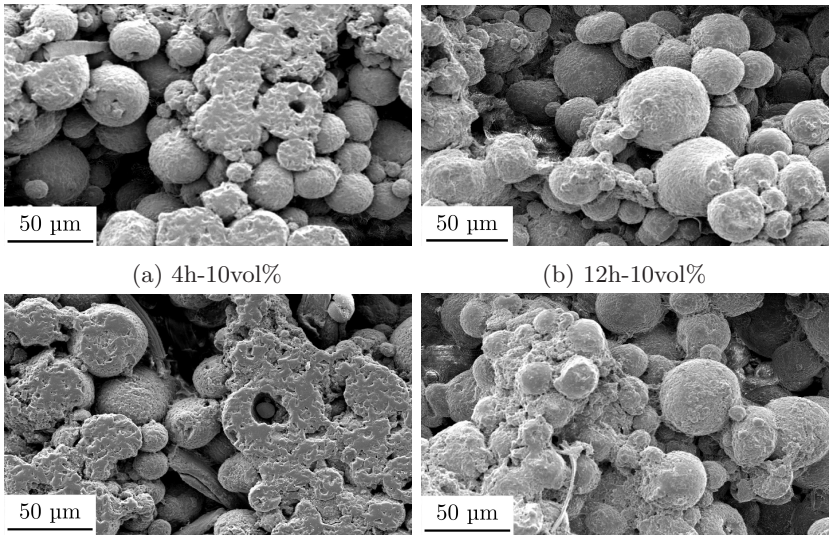

(a) 4h-10vol% (b) 12h-10vol%

(c) 4h-20vol% (d) 12h-20vol%

Figure 5.15: SEM images of green infiltrated parts after solid state sintering.

Part nr	Additional densification steps (besides SLS, deb. and SSS)	ρ_{FS} [%]	x-y [%]	z [%]
1b	No, i.e. only deb. and SSS	47%	-21%	-24%
41	Green pressureless inf.: 30 vol% Al_2O_3 susp.	48%	-15%	-16%
42	Green pressure inf.: 40 vol% Al_2O_3 susp.	46%	-17%	-17%
43	2x Green pressure inf.: 40 vol% Al_2O_3 susp.	53%	-16%	-16%
44	Green pressure inf. + WIP: 40 vol% Al_2O_3 susp.	61%	-25%	-24%

Table 5.9: Sintered density and linear shrinkage of the alumina parts after green pressureless and pressure infiltration with a stabilized Al_2O_3-ethanol suspension. The density of the parts was measured by the Archimedes method.

When investigating the cross-sections of the solid state sintered parts, irregularities could be observed (figure 5.16): part 41 (pressureless infiltrated) and part 42 (pressure infiltrated) had a horizontal crack/porous zone, part 43 (two times pressure infiltrated) had a denser region near the edges and part 44 (pressure infiltrated and WIPed) had a circular crack, due to the WIPing process, and a horizontal crack. It seemed that due to the relative high viscosity of the alumina suspensions and air entrapment during infiltration (as the suspension was entering the part from all directions at the same time), the suspension could only fill the pores at the edges of the green parts. This nonuniformity introduced local porosity differences and concomitant cracks during deb. and SSS.

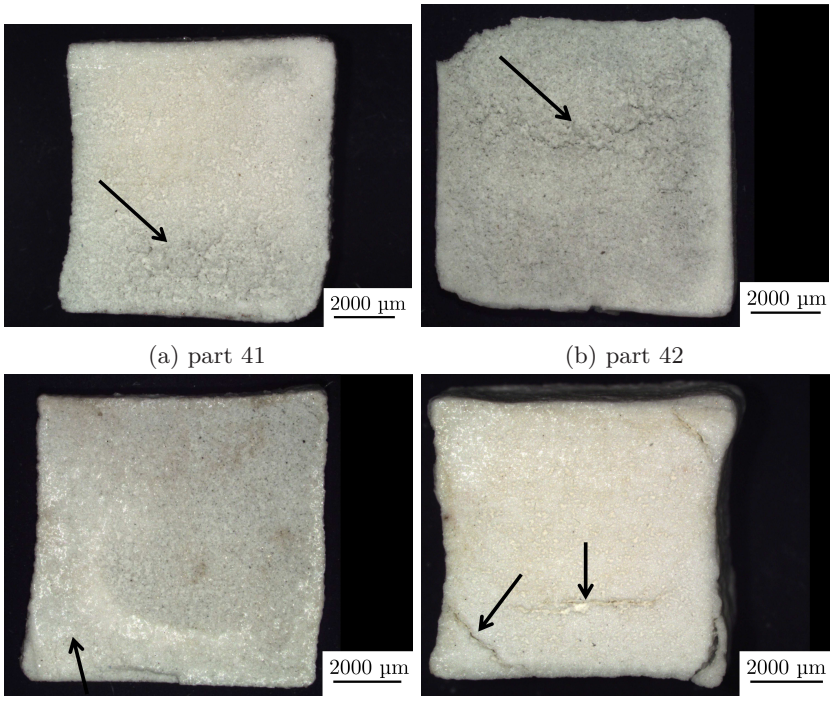

(a) part 41 (b) part 42

(c) part 43 (d) part 44

Figure 5.16: 3D microscope images after cutting with a diamond blade.

In summary:

- It seems that due to the relative high viscosity of the alumina suspensions and air entrapment during pressureless and pressure infiltration, the suspension can only fill the pores at the edges of the green parts. As a result, a denser region near the edge of the parts is created, which leads to a nonuniform shrinkage and (consequently) the formation of cracks/porous zones.
- Green (pressureless and pressure) infiltration reduces the part shrinkage during debinding and SSS.
- Applying green pressure infiltration for two times or applying green pressure infiltration after WIPing increases the final density after SSS.

5.6.3.3 Pressureless and pressure infiltration of a pre-sintered part with a stabilized Al_2O_3-ethanol suspension

In order to improve the final density of the infiltrated parts and in order to homogenize the obtained microstructure, the infiltration process was adapted. Firstly, a pre-sintered part (see section 5.4.3) was infiltrated instead of the green part. The suspension was expected to more easily infiltrate the low density pre-sintered part (table 5.10), compared to the less porous green part. A multi step infiltration procedure was performed after pre-sintering. The procedure had 3 steps: firstly the part was placed in pure ethanol (i.e. without alumina) and a negative pressure (i.e. vacuum) was applied, afterwards the ethanol infiltrated part was placed in the alumina suspension and again a negative pressure was applied, and finally infiltration at atmospheric pressure (pressureless infiltration) or at 16.1 MPa (pressure infiltration) was applied to the already infiltrated parts. By infiltrating first with ethanol, which has a lower viscosity compared to the alumina suspension, and by applying the negative pressure, the multi step procedure aimed to avoid that the infiltration only occurred at the edges of the part. On the other hand, pre-infiltration with pure ethanol could prevent further infiltration of the alumina suspension.
Parts 45, 46 and 47 were infiltrated according to the procedure described above. Part 45 was pressureless infiltrated for 4 hours. Part 46 was pressure infiltrated for 5 minutes under a pressure of 16.1 MPa. Part 47 was WIPed as a green part and also pressure infiltrated for 5 minutes under a pressure of 16.1 MPa as a pre-sintered part.
After pre-sintering in a furnace, parts 45 and 46 had densities of only 30% and dimensional shrinkages of -10% to -12% (table 5.10). Due to the WIPing process, part 47 had already a density of 36% and a dimensional shrinkage of -17% to -18%.

Part nr	Additional densification steps (besides SLS, deb. and SSS)	$\rho_{pre-sint.}$ [%]	x-y [%]	z [%]
45	Pressureless inf. after pre-sint.: 30vol%	30%	-11%	-12%
46	P-inf. after pre-sint.: 40vol%	30%	-10%	-10%
47	WIP + p-inf. after pre-sint.: 40vol%	36%	-17%	-18%

Table 5.10: Densities and shrinkages of parts after pre-sintering, before infiltration with a 30 vol% or 40 vol% alumina-ethanol suspension.

Part nr	Additional densification steps (besides SLS, deb. and SSS)	ρ_{FS} [%]	x-y [%]	z [%]
1b	No, i.e. only deb. and SSS	47%	-21%	-24%
45	Pressureless inf. after pre-sint.: 30vol%	63%	-25%	-26%
46	P-inf. after pre-sint.: 40vol%	70%	-23%	-23%
47	WIP + p-inf. after pre-sint.: 40vol%	67%	-29%	-31%

Table 5.11: Sintered density and linear shrinkage of the alumina parts, additionally infiltrated with a with a 30 vol% or 40 vol% alumina-ethanol suspension after pre-sintering. The density of the parts was measured by the Archimedes method.

The dimensional shrinkage of the final parts, which were infiltrated after pre-sintering, was uniform and similar to the shrinkage of the corresponding parts produced without infiltration: e.g. compare part 45, 46 with part 1b in table 5.11. Part 45 (pressureless infiltrated) had a final density of 63% and no visible cracks (figures 5.17a and 5.17d). Part 46 (pressure infiltrated) had a final density of 70%. The microstructure comprised a dense shell, where the inter-granular (i.e. inter-agglomerate) pores were clearly filled with infiltrated alumina, at the edge of the part (figure 5.17b and 5.17f) and a more porous core (figure 5.17b and 5.17e). Since the presented multi step procedure did not allow air entrapment in the part, the dense alumina shell might be created at the edges of the parts since the viscous alumina suspension obstructed further infiltration when entering the part. The dense alumina shell might also be created due to the pre-infiltration with pure ethanol, which possibly prevented further infiltration of the alumina suspension. Part 47 (WIPed and pressure infiltrated) also had an improved density of 67%, but contained an unwanted circular crack, due to the WIPing process (figure 5.17c).

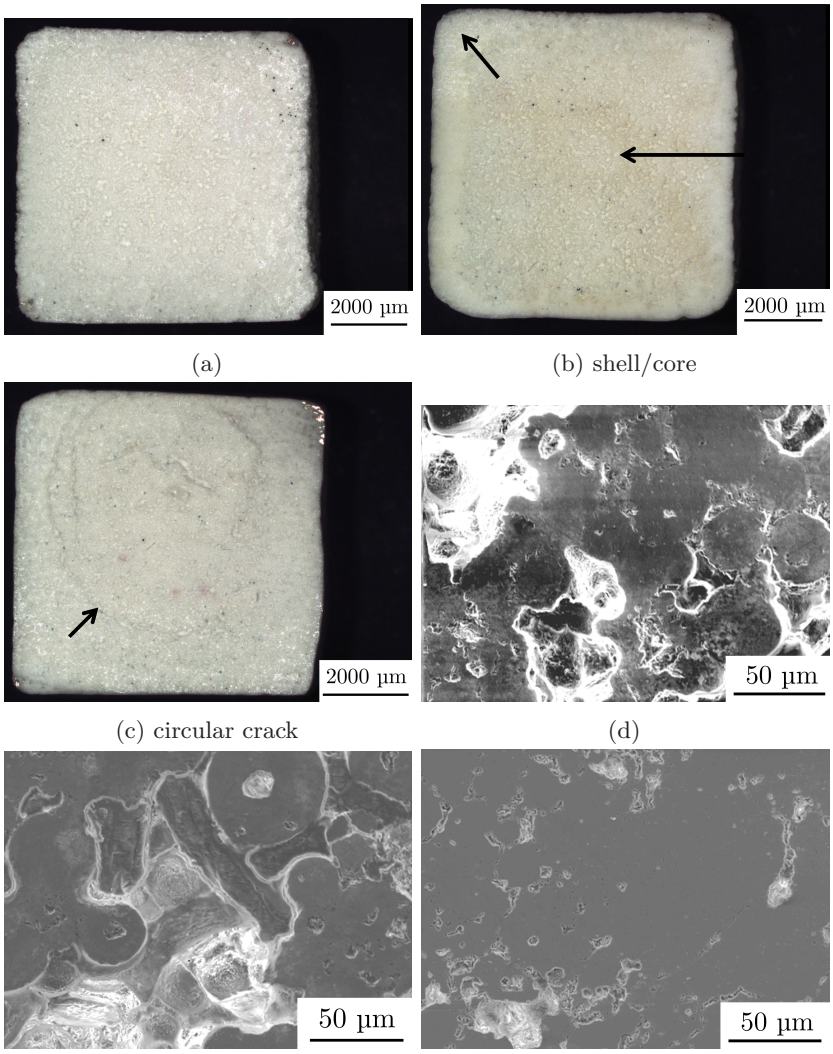

(a) (b) shell/core

(c) circular crack (d)

(e) (f)

Figure 5.17: 3D microscope images and SEM micrographs of part 45 (a, d), part 46 (b, e, f) and part 47 (c).

In summary:

- Infiltrating a pre-sintered part increases the final density after SSS.
- Infiltrating a pre-sintered part does not seem to decrease the part shrinkage during SSS.
- By applying pressure during infiltration, higher densities are obtained after SSS.
- After infiltrating a pre-sintered part, a dense shell can be formed at the edge of the part. The dense shell consists of inter-granular (i.e. inter-agglomerate) pores which are filled with infiltrated alumina. Since the presented multi step procedure did not allow air entrapment in the part, the dense alumina shell might be created at the edges of the parts since the viscous alumina suspension obstructed further infiltration when entering the part. The dense alumina shell might also be created due to the pre-infiltration with pure ethanol, which possibly prevented further infiltration of the alumina suspension.

5.6.3.4 Discussion

Similar to section 4.6.2.5, the following infiltration phenomena can be explained by assuming that part shrinkage is generally larger at more porous areas and the consequence that porosity differences (e.g. introduced through infiltration) prohibit the part to shrink uniformly:

- The decrease of part shrinkage during debinding and SSS, when applying green (pressureless and pressure) infiltration.
- The formation of cracks and porous zones when applying green (pressureless and pressure) infiltration.

In this chapter, no such phenomena could be observed on parts, infiltrated after pre-sintering. These parts were infiltrated with ethanol, before infiltration with the 40 vol% alumina suspension. The ethanol probably diluted the 40 vol% alumina suspension, causing the resulting suspension (which had a lower viscosity) to enter more uniformly the high-porosity, pre-sintered part. For example, despite part 46 (which was pressure infiltrated after pre-sintering) contained a shell, this nonuniformity was not large enough to cause an observable decrease of part shrinkage, crack or porous zone.

5.7 Summary and conclusions

A PM process was presented to produce freeform and complex shaped alumina geometries. The PM process comprised an innovative temperature induced phase separation (TIPS) technique to produce alumina-PA composite microspheres, as well as a tuned SLS process, a thermal debinding step and a furnace solid state sintering step.
When using too high or too low laser energy densities during SLS, the resulting green parts were too fragile for further processing. When applying a too low layer thickness during SLS, the parts delaminated.
The final parts, produced with optimized SLS parameters, did not contain cracks. Nevertheless the parts contained inter-agglomerate pores which restricted the final density to 47% (table 5.12). The shrinkage during debinding and SSS was mainly caused by sintering stress during SSS. Sintering stress caused outer part dimensions to shrink more than inner part dimensions. The dimensional shrinkage was about -23% in the x 'scan' and y 'cross-scan' directions (figure 5.10). The % linear shrinkage in the z 'build' direction was about -24% (table 5.12).

Three strategies were presented to improve the density of the fabricated parts (table 5.12): laser remelting, isostatic pressing and infiltration. Remelting was found to improve the green densities, but not the final densities. Remelting could also cause unwanted 'dross formation' when too high laser energy densities were applied.

Three different isostatic pressing techniques were assessed: cold isostatic pressing (CIP), quasi isostatic pressing (QIP) and warm isostatic pressing (WIP). CIP, QIP and WIP increased the green density of the SLSed parts and the final densities of the parts after solid state sintering. Nevertheless, inter-agglomerate pores were still visible. Due to the uniaxial compression, the QIPing process led to a part shrinkage in the z direction, but a part expansion in the x-y direction. WIP seemed to be a more promising IP technique than CIP and QIP, since an isostatic pressure could be uniformly applied on the SLSed sample, which led to a quite uniform % linear shrinkage of about -30% during debinding and SSS. Also, during WIPing, the heated liquid allowed the binder material to be plastically deformed. Nevertheless, circular cracks in the final parts arose during the WIPing process. These cracks should be avoided in future.

Green infiltration (e.g. applying pressure infiltration for two times) and WIP after green (pressure) infiltration could increase the final density of the parts. However, green infiltration reduced the part shrinkage during debinding and

SSS. Further, it seemed that due to the relatively high viscosity of the alumina suspensions and air entrapment during pressureless and pressure infiltration, the suspension could only fill the pores at the edges of the green SLSed parts. As a result, a denser region near the edge of the parts was created, which led to a nonuniform shrinkage and (consequently) the formation of cracks/porous zones after SSS. The reduction of shrinkage during debinding and SSS and the formation of cracks/porous zones due to green infiltration can be explained by assuming that part shrinkage is generally larger at more porous areas and the consequence that porosity differences (e.g. introduced through infiltration) prohibit the part to shrink uniformly.

Only if pressure was applied, infiltration after pre-sintering by applying the presented multi step procedure caused the formation of a dense shell at the edge of the part. The dense shell consisted of inter-granular (i.e. inter-agglomerate) pores which were filled with infiltrated alumina. Since the presented multi step procedure did not allowed air entrapment in the part, the dense alumina shell might be created at the edges of the parts since the viscous alumina suspension obstructed further infiltration when entering the part. The dense alumina shell might also be created due to the pre-infiltration with pure ethanol, which possibly prevented further infiltration of the alumina suspension.
Infiltration after pre-sintering did not cause an observable decrease in part shrinkage, crack or porous zone. During the multi step infiltration procedure, these parts were first infiltrated with ethanol. The ethanol probably diluted the 40 vol% alumina suspension, causing the resulting suspension (which had a lower viscosity) to enter more uniformly the high-porosity, pre-sintered part. As a result, even if a thin shell was formed (e.g. part 46, figure 5.17b), this nonuniformity was not large enough to cause an observable decrease of part shrinkage, crack or porous zone.
By applying pressure during infiltration, higher densities (up to 70%) were obtained after SSS without introducing observable unwanted phenomena. Therefore, pressure infiltration after pre-sintering seemed to be the most promissing infiltration route.

Part nr	Additional densification steps (besides SLS, deb. and SSS)	ρ_{FS} [%]	x-y [%]	z [%]
1b	No, i.e. only deb. and SSS	47%	-21%	-24%
2-19a*	Laser remelting	46-50%	-20 to -24%	-14 to -25%
2-19b	Laser remelting	47-51%	-18 to -23%	-12 to -25%
20*	$\mathrm{CIP}_{100\ MPa;\ <5\ minutes}$	62%	-27%	-32%
21*	$\mathrm{CIP}_{150\ MPa;\ <5\ minutes}$	53%	-20%	-33%
22*	$\mathrm{CIP}_{200\ MPa;\ <5\ minutes}$	59%	-26%	-32%
23*	$\mathrm{QIP}_{100°C;\ 50\ MPa;\ 5\ minutes}$	63%	-27%	-33%
24*	$\mathrm{QIP}_{100°C;\ 50\ MPa;\ 30\ minutes}$	53%	-19%	-34%
25*	$\mathrm{QIP}_{160°C;\ 50\ MPa;\ 5\ minutes}$	63%	-19%	-42%
26*	$\mathrm{QIP}_{160°C;\ 50\ MPa;\ 30\ minutes}$	56%	-13%	-46%
27	$\mathrm{WIP}_{110°C;\ 16.1\ MPa;\ 30\ minutes}$	62%	-29%	-29%
28	$\mathrm{WIP}_{110°C;\ 16.1\ MPa;\ 30\ minutes}$	63%	-29%	-30%
29-34*	Green pressureless inf.: 10vol%	46-54%	-18 to -20%	-16 to -23%
35-40*	Green pressureless inf.: 20vol%	47-51%	-12 to -19%	-16 to -19%
41	Green pressureless inf.: 30vol%	48%	-15%	-16%
42	Green p-inf.: 40vol%	46%	-17%	-17%
43	2x Green p-inf.: 40vol%	53%	-16%	-16%
44	Green p-inf. + WIP: 40vol%	61%	-25%	-24%
45	Pressureless inf. after pre-sint.: 30vol%	63%	-25%	-26%
46	P-inf. after pre-sint.: 40vol%	70%	-23%	-23%
47	WIP + p-inf. after pre-sint.: 40vol%	67%	-29%	-31%

Table 5.12: Sintered density and linear shrinkage of the alumina parts after additional densification steps. The dimensional shrinkages indicate the geometrical changes that appeared after the SLS process (i.e. the geometry after SLS is the reference geometry). The density of the parts, marked by *, was measured by the geometrical method. Other densities were measured by the Archimedes method. Part 1 was not densified. Parts 2a-19a and 2b-19b were remelted. Parts 20-22, 23-26 and 27-28 were respectively CIPed, QIPed and WIPed. Parts 29-41 and 45 were pressureless infiltrated and parts 42-44 and 46-47 were pressure infiltrated (p-inf.) with an alumina suspension. The pressureless infiltration experiments were performed with 10, 20 and 30vol% alumina suspensions. The pressure infiltration experiments were performed with a 40vol% alumina suspension.

Chapter 6

Production of alumina parts through Laser Sintering of polypropylene-alumina agglomerates produced via dissolution-precipitation

6.1 Abstract

A powder metallurgy (PM) process to fabricate crack-free alumina parts through indirect Selective Laser Sintering (SLS) of spherical alumina - polypropylene composite powder particles is presented. The PM process included powder synthesis, SLS, debinding and solid state sintering (SSS) in a furnace. The resulting parts had a density of about 39% and contained inter-agglomerate pores.
Infiltration and/or warm isostatic pressing (WIP) were investigated as extra steps of the PM process to eliminate the inter-agglomerate pores and to improve the density of the sintered alumina parts. Infiltration was performed on both SLSed samples (i.e. green infiltration) and/or samples which were pre-sintered at 1050°C. Different suspensions were used to investigate the infiltration behavior: a 40vol% alumina - ethanol suspension, a 40wt% silica - water suspension, a 10wt% boehmite (AlOOH) - water suspension and molten

carnauba wax containing 22wt% alumina. Furthermore, microstructural and geometrical changes which occurred during the PM process were investigated and the fabrication of complex and fragile shapes was qualitatively assessed.
During infiltration, a dense shell was formed. This shell prohibited the part to shrink uniformly during further debinding and/or solid state sintering. This could result in the formation of cracks perpendicular to the z 'build' direction and along the inter-layer porosities. The results of the infiltration experiments could be further explained by considering the porosity of the part prior to infiltration and the suspension used. Infiltrating a pre-sintered part 3 times with the alumina suspension allowed to increase the sintered density up to 91.4%. Infiltrating once after SLS and after pre-sintering with the silica suspension allowed to increase the sintered density up to 76.6%. At last, it was found that a pressure between 48 and 64 MPa was needed to break the composite alumina (40vol%) - polypropylene (60vol%) agglomerates during WIPing at 135-140°C.

6.2 Introduction

According to the Quasi Isothermal Theory (Drummer D. et al., 2010 [65]), semi-crystalline powders are preheated to a temperature between the crystallization and melting temperature during the SLS process. The laser energy is used to melt the material, which remains in a molten state until all layers of the component are produced. The surrounding composite powder that is not melted, supports the generated melt. During the final cooling down stage of the process, the semi-crystalline material crystallizes and a solid polymer is formed. The difference between the melting onset temperature, T_{om}, and the crystallization onset temperature, T_{oc}, is called the 'SLS window'.
During laser irradiation, the induced thermal stresses can result in curling of the consolidated material towards the laser beam. This phenomenon is known as 'warpage'. Since the powder deposition system of an SLS device can hit curled parts and drag them out of the powder bed, warpage is unwanted. If the material is pre-heated up to a temperature in the range of the SLS window, the part will not shrink and, as a result, not curl after irradiation as it stays in a molten state. Therefore, a big SLS window generally implies a better controllable SLS process.
In chapter 3 and 5 of the dissertation, a semi-crystalline polymer, namely polyamide 12 (PA12), was used as binder material in order to indirect selective laser sinter alumina parts. Polyamide 12 is the most common semi-crystalline material to SLS polymers. The success of PA12 can be explained by the following reasons:

- PA12 has a large SLS window of 25 °C, which facilitates the SLS process.
- PA12 has a good mechanical strength and can be used for many applications.

For laser sintering of composite powder agglomerates to produce ceramics, the mechanical strength of the green parts after SLS is not as critical as it is for laser sintering of pure polymers. Therefore, other semi-crystalline polymers might be more qualified than PA12 for indirect SLS of ceramics.
Advantage of polypropylene: In order to find a semi-crystalline polymer which has a better SLS behavior than PA12, the melting onset temperature, T_{om}, and the crystallization onset temperature, T_{oc}, of different semi-crystalline polymers were investigated. It was concluded that polypropylene (PP) might have a better SLS behavior than PA12. The SLS window of PP is also 25 °C, but *the melting onset temperature is about 30°C lower*. This makes it easier for the SLS device to control the temperature of the SLS process.

6.3 The powder metallurgical process

Figure 6.1 schematically presents the main steps of the powder metallurgy process assessed in this chapter to produce alumina parts through additive manufacturing (AM). In a first step, the composite starting powder was produced through a thermally induced phase separation (TIPS) process. Afterwards, the SLS parameters were optimized to produce green parts. The final alumina parts were produced by subsequently debinding (deb.) and solid state sintering (SSS) of the green parts in a furnace. Sometimes, a furnace pre-sintering step was applied after debinding and before final SSS, in which the debinded parts only underwent the initial stage of the SSS process. In order to improve the final density of the alumina parts, two possible densification treatments were used, namely warm isostatic pressing (WIP) and infiltration (inf.). Infiltration was applied on SLSed parts (green) as well as on pre-sintered parts. Moreover, infiltration was applied using 4 different infiltrants. The combination of different densification treatments was also investigated: e.g. WIP after green infiltration. Finally, the limits of the presented PM process were investigated by qualitatively assessing the fabrication of complex and fragile shapes.

This chapter investigates the quality of the components during the different processing steps through density measurements, geometrical assessments and microscopic imaging. When optimizing SLS parameters, the green densities were measured by the geometrical method using a vernier caliper (Mitutoyo,

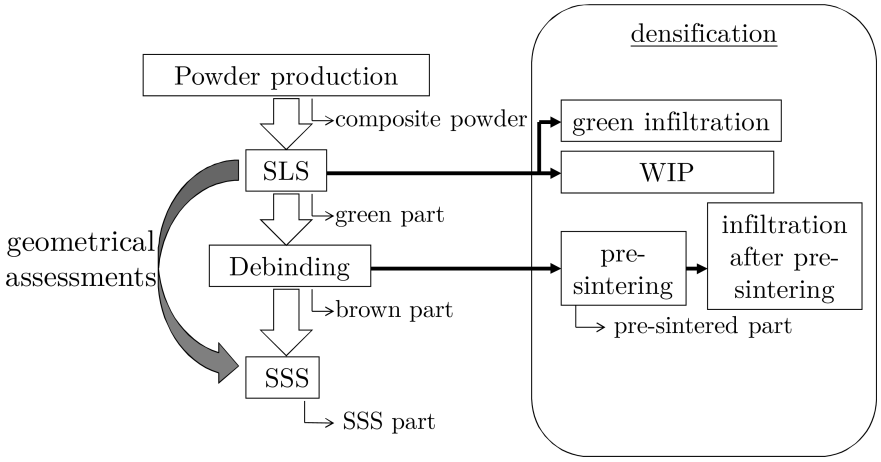

Figure 6.1: Powder metallurgy processing flow chart.

Japan). All other densities reported in this chapter were measured by the Archimedes method (Analytical Balance, Sartorius, Germany). The Archimedes densities of the green parts, not used to optimize the SLS parameters, were obtained by measuring the weight of the parts in air, immersed in ethanol and again in air after immersion. The last measurement was needed to compensate for open porosities. The Archimedes densities after SSS were measured by covering the sintered parts with a green lacquer (Enplate Stop-off No. 1, Enthone-Omi Inc., US). The mass of the sintered parts was measured before and after addition of the lacquer, and after immersing the parts in ethanol. Relative densities were calculated, starting from the following theoretical densities:

- $\rho_{Al_2O_3} = 3.98 g/cm^3$
- $\rho_{PP} = 0.90 g/cm^3$
- $\rho_{SiO_2} = 2.65 g/cm^3$
- $\rho_{boehmite} = 3.05 g/cm^3$
- $\rho_{carnauba\,wax} = 0.97 g/cm^3$

The geometrical assessments were realized with a vernier caliper. In sections 3.3.5, 4.5 and 5.5 it was demonstrated that the linear shrinkage in the x 'scan' and y 'cross-scan' directions was similar, but different from the linear shrinkage in the z 'build' direction. Therefore, the shrinkage in x and y direction will be

denoted as x/y shrinkage. The z shrinkage will be reported separately.
Outer shapes of the parts were figured with a digital camera. Microscopic images were assessed by 3D microscopy (Discovery.V20, Carl Zeiss Inc., Germany) or scanning electron microscopy (SEM, XL30 FEG, FEI, The Netherlands). The SEM device was also equipped with an energy-dispersive X-ray spectroscopy (EDX) device. Internal, cross-sectional images were taken both with the 3D microscope and SEM. Secondary (SE-SEM) and backscattered electron (BSE-SEM) SEM images were taken. In order to take the cross-sectional images, the parts were cut with a diamond blade, embedded in an epoxy resin, ground and polished if the sintered density of the parts was above 70%. If the furnace sintered density was high enough, the parts were strong enough to be polished without damaging the polishing cloths. After the polishing step, the epoxy resin in the parts was dissolved in acetone and the parts were thermally etched by the following furnace treatment in air atmosphere: a heating rate of 10°C/min, a 30 minutes dwell time at 1200°C followed by furnace cooling. The furnace treatment did not only engrave the grain boundaries, but also removed the dirt which entered the part during grinding and polishing. Before taking the SEM images, the parts were coated with a thin layer of paladium-gold alloy to make the surface conductive.

6.3.1 Difference with PM processes described in previous chapters

In summary, the PM processes described in this chapter differ from the ones described in chapters 3, 4 and 5 in three ways:

1. Semi-crystalline polypropylene (PP) is used instead of semi-crystalline polyamide (PA; chapter 3 and 5) or amorphous polystyrene (PS; see chapter 4) as polymer binder.

2. The synthesis of the initial polymer-ceramic powder is done by temperature induced phase separation (TIPS), rather then by in-situ dispersion polymerization, as described in section 4.4.1, or ball milling, as described in section 3.3.1.

3. Another post-densification strategy is tested: i.e. vacuum infiltration.

6.4 Production of alumina parts

6.4.1 Powder production

Thermally induced phase separation (TIPS) was used to produce 40 vol% alumina - 60 vol% polypropylene (Al_2O_3-PP) composite agglomerates. High purity α-alumina (grade SM8, Baikowski, France) powder with a d_{50} of 0.3 μm was used as structural material and isotactic polypropylene (PP) with an average molecular weight (Mw) of 12,000 (Mw/Mn= 2.4, Sigma-Aldrich) was used as binder phase. Al_2O_3 powder was first deagglomerated in a polyethylene bottle for 24 hours in xylene (p-xylene, reagent grade, Sigma-Aldrich, US) during multi-directional mixing at 70 rpm (TypeT2A, WAB, Basel, Switzerland) with 5 mm diameter ZrO_2 balls (TZ-3Y, Tosoh, Japan). An amount of 200 ml of this suspension was added to a 500 ml glass flask. The suspension was mechanically stirred at 300 rpm and heated to 133°C to dissolve 9 wt% PP in the xylene solution, containing 40 vol% alumina particles. In the next step, the suspension was naturally cooled to room temperature to induce precipitation. The precipitates were allowed to settle, allowing decantation of the xylene. The powders were washed multiple times with ethanol to remove residual xylene and subsequently dried in air at 65°C.
The size of the agglomerates was measured by laser diffraction (Mastersizer Plus, Malvern, UK). As depicted in figure 6.2a, the average agglomerate particle size was 8 μm. The agglomerates had a spherical shape (figure 6.2b) and showed a good flowability. Homogeneous layers could be deposited by a counter current roller. The thermal properties of the microspheres, as determined by differential scanning calorimetry (DSC, Model-2920, TA instruments, USA), are shown in figure 6.2c. The lower and upper curves represent the heating and cooling curves, respectively. The agglomerates showed a melting onset temperature T_{om} of 149 °C and a crystallization temperature T_{oc} of 125 °C. An SLS window of 24 °C was available to avoid the distortion of the green parts during SLS.
For a more detailed description and analysis of the powder production method: see Shahzad et al. [185].

6.4.2 Selective laser sintering (SLS)

Green samples were fabricated using a Sinterstation 2000 (DTM Corporation / 3DSystems, USA) equipped with a 100 W CO_2 laser (f100, Synrad, USA) with a wavelength of 10.6 μm and a laser beam diameter ϕ_{1/e^2} of 400 μm. Powder layers were deposited by a counter current roller and irradiated with the laser beam. In order to avoid thermal oxidation, SLS was performed under

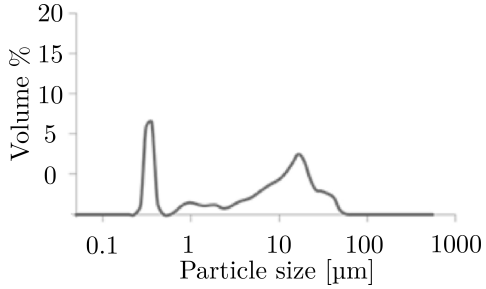

(a) Particle size distribution.

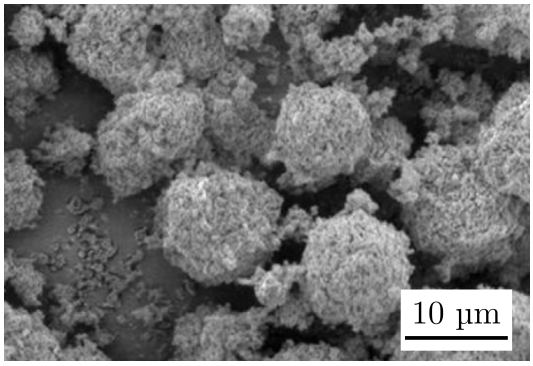

(b) Morphology of the powder particles/agglomerates.

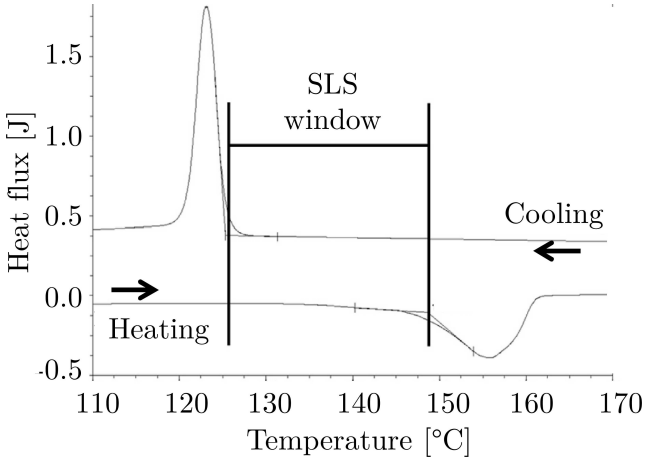

(c) DSC curve.

Figure 6.2: Production of the 40 vol% alumina - 60 vol% polypropylene powder [185].

N_2 atmosphere (Air Liquide, Belgium, $[O_2] < 5$ %). In order to improve the laser sinterability of the powder and to avoid warpage, the parts were produced at an elevated powder bed temperature (∼138°C). The energy required to melt PP was partly supplied by preheating of the powder bed to that temperature slightly below the melting onset temperature (distributed cylinder heating and surface IR heating) and by extra laser irradiation which locally raised the temperature above the melting point.

Preliminary SLS experiments were performed by using 50-50 vol% PP-alumina agglomerates. As it was the case for the 50-50 vol% PA-alumina powder produced by TIPS (see section 5.4.2), these tests demonstrated that a quite large amount (60 vol%) of polymer material was necessary to enable the production of strong green parts.
By increasing the PP content of the starting powder up to 60vol%, stronger parts with a better geometrical accuracy could be produced. In order to optimize the SLS parameters, a parametrical study was performed. In this study, 27 parts of 15x15x5 mm^3 were produced with a laser power 'P', scan speed 'v' and scan spacing 's' varying between respectively 3-5-7 W, 500-850-1250 mm/s and 100-150-200 μm. The layer thickness 'l' was kept constant at 130 μm.
The laser processability (i.e. the easiness to find appropriate laser parameters) of the alumina-PP agglomerates was very good and seemed to be better than the laser processability of alumina-PA agglomerates (section 5.4.2). All 27 different SLS parameters, with a laser energy density 'e' (=P/s.v.l, see section 3.3.2) ranging between 0.092 to 1.077 J/mm^3, led to parts which could be taken out of the DTM Sinterstation. For the alumina-PA agglomerates, only SLS parameters with a laser energy density ranging between 0.176 and 0.37 J/mm^3 were strong enough for non-destructive manipulation (table 5.1). The green density of 27 parts was measured by the geometrical method and could be plotted against the laser energy density, as depicted in figure 6.3a. The density after SLS was quite low and between 48.5 and 56.8%. Applying higher laser energy densities resulted in higher green densities. However, when applying too high laser energy densities, the green density did not increase anymore. This was probably due to degradation of the PP binder material.
It was observed that applying higher laser energy densities also led to a loss in geometrical accuracy (see rounded curves of the right part in figure 6.3b). Due to the higher laser energies, the viscosity of PP decreased rapidly during irradiation. This caused the PP to flow outside the part contours and to consolidate powder particles which were not irradiated by the laser beam. This phenomenon is known as 'dross formation'.
Finally, two SLS parameter sets were chosen (table 6.1). Parameter set 1 resulted in parts with the highest green density without the formation of

extensive dross (i.e. 50.7%): see left arrow in figure 6.3a and left part in figure 6.3b. This parameter set led to parts with the highest accuracy and will be used in the remaining of the chapter, unless stated otherwise. Parameter set 2 resulted in parts with the highest green density (i.e. 56.8%): see right arrow in figure 6.3a and right part in figure 6.3b. This parameter set resulted in the strongest parts.
Shahzad et al. [185] investigated the green microstructure of the parts produced through SLS of the composite powder. Although these parts were produced with other SLS parameters (P=5W; v=875mm/s; s=150μm; l=200μm; e=0.190J/mm^3), the microstructure should be quite similar to the microstructure of parts obtained with parameter set 1 and 2. Figure 6.3c confirmed the low green density values. A network of composite powder agglomerates, consolidated during SLS, and inter-agglomerate pores were visible as a quite inhomogeneous green microstructure.

6.4.3 Debinding and furnace sintering

The same debinding and furnace sintering parameters as described in section 4.4.3 (see table 6.2) were used to remove the PP from green SLSed parts and to furnace solid state sinter or pre-sinter the resulting brown parts. As depicted in table 6.3, after the solid state sintering step, parts SLSed with parameter set 1 showed a uniform % linear shrinkage of about -20%. The parts had a low mean density of about 39%. The density after SSS was slightly lower for larger parts: compare part 1 (initial CAD dimensions: 10x10x10 mm^3) with part 2 (initial CAD dimensions: 20x20x20mm^3) in table 6.3. This might be due to the applied contour scanning during SLS, by which the surface of the parts was laser irradiated two times instead of only once. As a result, the density at the surface of the parts after SLS and SSS was larger than the internal density. Since larger parts have a lower surface to volume ratio, the final density was

	Parameter set 1	Parameter set 2
P [W]	3	5
v [mm/s]	1250	500
s [μm]	150	100
l [μm]	130	130
e [J/mm^3]	0.123	0.769

Table 6.1: SLS parameters optimized for accuracy (parameter set 1) and green density (parameter set 2).

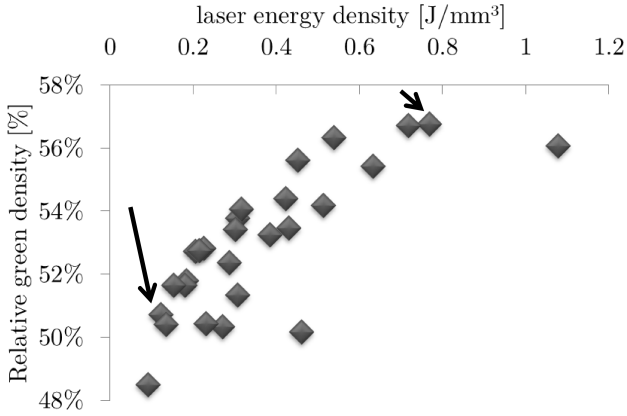

(a) Green density after SLS versus laser energy density. The left and right arrows indicate respectively parameter set 1 and parameter set 2.

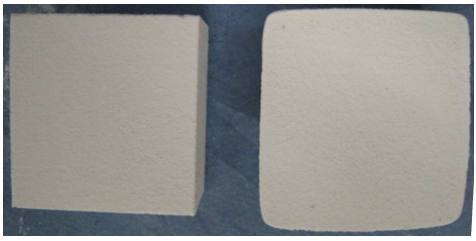

(b) Two parts produced with respectively parameter set 1 (left) and parameter set 2 (right).

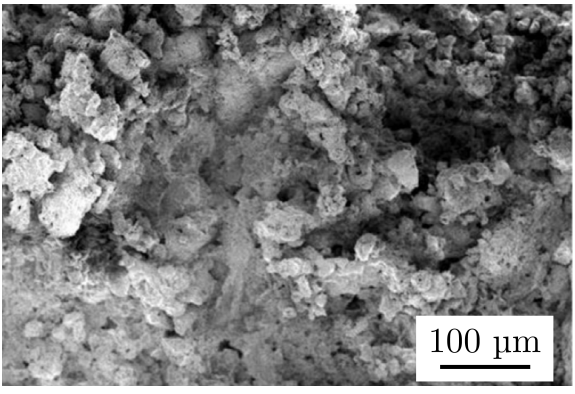

(c) Green microstructure of an SLSed part [185].

Figure 6.3: Optimizing SLS parameters.

	debinding	SSS	pre-sintering
heating rate [°C/min.]	0.1	5	5
heating temperature [°C]	600	1600	1050
dwell time [min.]	120	120	120
cooling rate	furnace cooling	furnace cooling	furnace cooling
atmosphere	air	air	air

Table 6.2: Parameters of the different furnace treatments used in this chapter.

also lower.
After furnace solid state sintering, no cracks could be observed by 3D microscopy of part 1 and 2 (figure 6.4a). SEM images of part 1 and 2 (figure 6.4b) revealed a microstructure quite similar to the green microstructure after SLS (see previous section) and the microstructure after SSS of parts obtained by SLS of spherical PA-alumina agglomerates (see section 5.4.3): an inhomogeneous microstructure consisting of slightly connected agglomerates and inter-agglomerate pores. Figure 6.4c, which is a detail SEM image of a solid state sintered agglomerate (see square in figure 6.4b), revealed that the agglomerates do not have intra-agglomerate pores at their outer surface, but have a very fine grain size after furnace SSS.
In order to simulate the ideal SLS process, composite alumina (40vol%) - PP (60vol%) agglomerates were heated in a crucible above the melting point of PP and cooled afterwards. In this way parts with a relative green density of 97.2% were obtained. After debinding and SSS in a furnace, the microstructure depicted in figure 6.5 was obtained. This microstructure revealed that the powder agglomerates did not collapse during melting. Instead, the molten PP flew out of the spherical agglomerates and closely packed ceramic spheres remained after SSS.
Some agglomerates depicted in figure 6.5 are hollow. A possible explanation

Part nr	Additional densification steps (besides SLS, deb. and SSS)	ρ [%]	x-y [%]	z [%]
1	No, i.e. only deb. and SSS	39.8	-20	-21
2	No, i.e. only deb. and SSS	38.4	-17	-21

Table 6.3: Sintered (Archimedes) density and linear shrinkage after SSS of two alumina parts produced with parameter set 1. The initial CAD dimensions of part 1 and part 2° were respectively 10x10x10 mm^3 and 20x20x20mm^3.

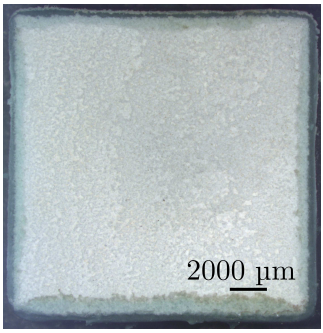

(a) part 2: 3D microscope

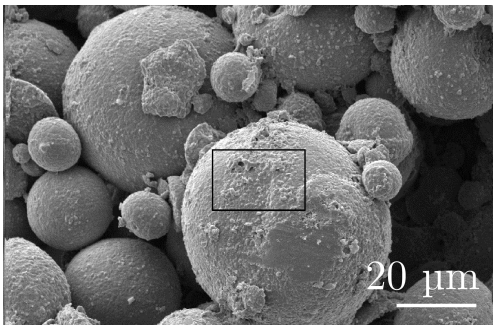

(b) part 2: SE-SEM

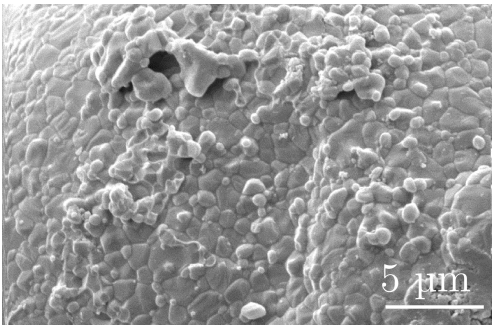

(c) part 2: SE-SEM

Figure 6.4: 3D microscope image (a) and SEM images (b,c) of part 2 (20x20x20 mm^3) SLSed with parameter set 1, after solid state sintering. SEM image (c) is a detail of the square depicted in SEM image (b).

for this phenomenon is that during the TIPS process, the agglomerates did not always nucleate from a ceramic particle, but also from the polymer phase. As a result, some agglomerates had a polymer core, which disappeared during thermal debinding, and a composite shell, which became an alumina shell. It is also possible that the hollow agglomerates were not created during the TIPS process, but during the melting process.

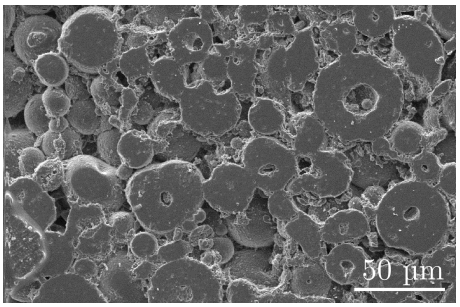

Figure 6.5: SEM image, showing the microstructure of thermally treated powder after debinding and SSS.

In summary:

- Crack-free alumina parts can be produced through SLS of alumina-PP composite powder synthesized by a temperature induced phase separation (TIPS) process.
- By increasing the PP content of the starting powder from 50 to 60vol%, stronger green parts with a better geometrical accuracy can be produced.
- The laser processability of alumina-PP agglomerates seems to be better than the laser processability of alumina-PA agglomerates. All 27 different SLS parameter sets, with a laser energy density 'e' ranging between 0.092 to 1.077J/mm^3, lead to parts which can be taken out of the DTM Sinterstation. For the alumina-PA agglomerates, only SLS parameters with a laser energy density ranging between 0.176 and 0.37 J/mm^3 are strong enough for non-destructive manipulation. The better processability of the PP containing agglomerates might be related to the the lower pre-heating temperature needed.
- High laser energy densities lead to higher green densities after SLS. When using too high laser energy densities, dross formation and/or polymer degradation occurs.
- The microstructure after SLS and SSS is inhomogeneous and consists of dense interconnected agglomerates as well as inter-agglomerate pores. As a result, the density after SLS and solid state sintering is low and respectively about 51% (after SLS) and 39% (after SSS) for the parts SLSed with optimized parameter set 1 (i.e. highest accuracy).
- The % linear shrinkage during debinding and solid state sintering is uniform and about -20% in the x-, y- and z-directions.

6.5 Densification strategies

As described in the previous sections, crack-free alumina parts could be produced through SLS of alumina-PP composite powder, synthesized by temperature induced phase separation (TIPS). However, both the green and final parts had a low density due to the occurrence of inter-agglomerate pores. In this section, an attempt is made to eliminate the inter-agglomerate pores by different infiltration techniques, warm isostatic pressing (WIP), or a combination of infiltration and WIP.

6.5.1 Vacuum infiltration

In chapter 4 and 5 of this dissertation, different infiltration studies were reported which all aimed to improve the density of alumina parts after SSS. These experiments showed that the formation of a dense shell at the edges of the parts should be avoided to improve the infiltration results. Chapter 4 and 5 revealed two phenomena which both caused the formation of the dense shell:

- Air entrapment: as during infiltration the suspension enters the part from all directions at the same time, a central air bubble arises. If the air bubble gets clogged, further infiltration is prohibited. The application of pressure during infiltration might dissolve the air bubble, but might also lead to breaking of the part (see section 4.6.2.4).
- Obstruction: infiltrated particles can impede further infiltration. In this case, the porous infiltrated part acts as a filter.

In order to prevent air entrapment during infiltration, an experimental setup was constructed to apply a vacuum atmosphere before infiltration. A schematic of the experimental setup is depicted in figure 6.6a. The setup consisted of a vacuum chamber (1) in which a cup (2), containing the ceramic suspension, was placed. The suspension could be heated by a heating plate (3) and stirred by a magnetic stirrer (4). The vacuum chamber also consisted of a cage (5) in which the sample (6), to be infiltrated, was placed between two grids (7). After pumping the chamber vacuum (8), the cage could be dipped into the suspension by pushing a rod (9) through a vacuum seal (10).
All the vacuum infiltration experiments were performed by first evacuating the chamber down to the vapor pressure of the suspension: 5800 Pa for ethanol suspensions and 2300 Pa for aqueous suspensions at 20°C. When reaching the vapor pressure, the suspension started to boil. Secondly, the sample was moved into the suspension. After bringing the chamber back to atmospheric pressure, the parts were infiltrated for 100 seconds and taken out of the suspension.

Vacuum infiltration frequently resulted in the formation of an external shell (figure 6.6b). Since the external shell decreased the part accuracy, it was always removed prior to further processing.
The infiltration experiments were performed after SLS (green infiltration) and/or after furnace pre-sintering. All parts, unless the parts indicated with an °, had initial CAD dimensions of 10x10x10mm^3. Parts indicated with an ° had initial CAD dimensions of 20x20x20mm^3. Sometimes, the parts were infiltrated multiple times. In this case the parts were dried, before infiltrating them again. The following suspensions were used to infiltrate the parts:

- An ethanol suspension containing 40 vol% alumina (grade SM8, Baikowski, France) particles with a mean diameter of 0.3 μm. This suspension was stabilized by adding 0.3wt% of citric acid (Anhydrous p.a., Acros, USA) and by mixing in a Turbula mixer (TypeT2A, WAB, Basel, Switzerland) for 24 hrs.

- An aqueous suspension containing 40wt% silica (Ludox TM-40, Sigma Aldrich, US) particles with a mean diameter of 22 nm [98]. The aim of using this infiltrant was to study how the structural (Al_2O_3) material got infiltrated by the infiltrant (SiO_2) material. Silica also enabled the occurrence of a liquid state sintering process (see section 2.4.5) during furnace sintering.

- An aqueous suspension containing 10wt% boehmite (AlOOH, Disperal P2, Sasol, South Africa) particles with a mean diameter of 45 nm. The aim of using this infiltrant was to study if obstruction during infiltration could be avoided by infiltrating with nano-size boehmite particles, which become alumina after SSS.

- Molten carnauba wax (melting point: 82−86°C), containing 22wt% alumina particles (grade SM8, Baikowski, France). The aim of using this infiltrant, was to produce 100% dense green parts by the application of an infiltration step.

6.5.1.1 Green infiltration

Part 3 to 9 were green infiltrated with the alumina, silica, boehmite and carnauba wax containing infiltrants described above. Some parts (parts 4, 7 and 8) were infiltrated multiple times.

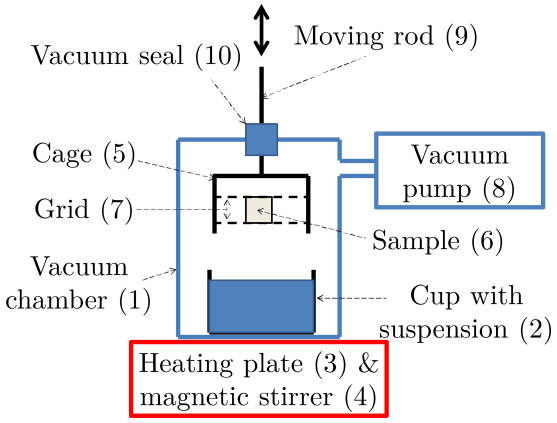

(a)

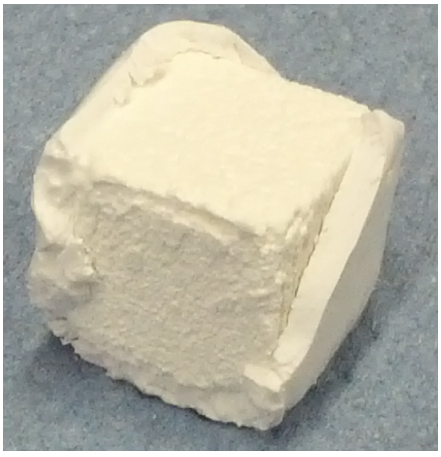

(b)

Figure 6.6: Vacuum infiltration: schematic of the experimental setup (a); an external shell, formed during infiltration (b).

Part nr	Additional densification steps (besides SLS, deb. and FS)	ρ_{SLS} [%]	$\rho_{green\ inf.}$ [%]
1	No, only SLS	50.7	/
3	1x green infiltration (alumina)	46.6	69.4
4	2x green infiltration (alumina)	45.9	71.0
5	1x green infiltration (silica)	47.1	56.2
6°	1x green infiltration (silica)	47.5	57.1
7	4x green infiltration (silica)	45.1	67.0
8	4x green infiltration (boehmite)	48.9	54.2
9	1x green infiltration (alumina-carnauba wax)	46.4	60.9

Table 6.4: Density after SLS and green infiltration.

Part nr	Additional densification steps (besides SLS, deb. and FS)	ρ [%]	x-y [%]	z [%]
1	No, i.e. only deb. and FS	39.8	-20	-21
3	1x green infiltration (alumina)	63.3	-14	-13
4	*2x green infiltration (alumina)*	*73.9*	*-16*	*-16*
5	1x green infiltration (silica)	50.0	-11	-12
6 °	1x green infiltration (silica)	44.4	-8	-9
7	4x green infiltration (silica)	57.4	-3	-1
8	4x green infiltration (boehmite)	45.1	-20	-20
9	1x green infiltration (alumina-carnauba wax)	48.9	-10	/

Table 6.5: Density and linear shrinkage of green infiltrated parts after FS.

Green infiltration with an alumina suspension Parts 3 and 4 were green infiltrated with an alumina suspension. Part 3 was infiltrated once and part 4 twice. After infiltration and drying, part 3 had a density of 69.4% (table 6.4). As depicted in table 6.5, green infiltration with an alumina suspension increased the density after solid state sintering up to 63.3%. Green infiltration decreased the linear shrinkage to about -14%. As discussed in sections 4.6.2.5 and 5.6.3.4, this phenomenon can be explained by assuming that the part shrinkage is generally larger for more porous parts: as infiltration reduced the porosity inside part 3, the shrinkage after infiltration was less.
Figure 6.7a and 6.7b illustrated that part 3 did not contain cracks, but was not completely infiltrated: a non-infiltrated zone in the middle of the part was surrounded by a large infiltrated zone. This means that the application of a vacuum prior to infiltration was not sufficient to fully infiltrate the parts. Further, the infiltrated zone consisted of a porous zone and a dense

shell. Probably infiltrated particles impeded further infiltration. Moreover, the viscosity of the alumina suspension was too high and the infiltration time too short to fully infiltrate the parts.
As illustrated in figure 6.7b, the alumina suspension penetrated between the SLS layers during infiltration. Inter-layer porosities probably gave the lowest resistance for the suspension to flow into the part. Figure 6.7c illustrates that in the infiltrated zone, the alumina agglomerates were covered by the infiltrated alumina.

Infiltrating twice increased the green density of part 4 up to 71.0% (table 6.4) and the density after SSS up to 73.9% (table 6.5). As green infiltration decreased the porosity of the green parts, the linear shrinkage decreased to -16%.
The microstructure of part 4 was similar to the microstructure of part 3: no cracks could be observed and an infiltrated zone, consisting of a porous zone and a dense shell was clearly visible (figures 6.7d and 6.7e). The dense shell seemed to have a limited amount of closed pores. In contrast to part 3, no non-infiltrated zone could be detected in the 3D microscope images (figure 6.7d). This means that either the part was fully infiltrated by the alumina suspension, either the diamond blade did not cut through the porous core when making the cross-section.
Part 4 was polished and thermally etched to reveal the grain size of the produced parts. Figure 6.7g is a close-up image of the powder agglomerate depicted in figure 6.7f and illustrates that the grain size inside the powder agglomerates was about 5μm.

Shahzad et al. [185] and Cuypers [44] applied pressure infiltration, where vacuum was not applied before infiltration, on parts produced through SLS of 40 vol% alumina - 60 vol% polypropylene agglomerates. Cuypers infiltrated SLSed parts obtained by using parameter set 1. After SSS, parts with a relative density of 70.9% were obtained by pressure infiltrating with a stabilized 40vol% alumina - ethanol suspension (i.e. the same suspension as applied above) at 1.75 MPa for 5 minutes. This means that, for these infiltration conditions, the application of a single pressure infiltration step led to higher sintered densities, compared to the application of a single vacuum infiltration step: after SSS, the density of part 3 was only 63.3%. However, despite the higher density, the (single) pressure infiltrated parts contained large cracks.
Shahzad also applied pressure infiltration on parts, produced with different SLS parameters: P=5W; v=875mm/s; s=150μm; l=200μm (see section 6.4.2 above). Shahzad used a stabilized 30vol% alumina-ethanol suspension and a pressure of 13 MPa. After SSS, parts with a relative density of 62.8% were obtained and no cracks were reported. It seems that, for these infiltration

conditions, applying single pressure infiltration with a less viscous suspension (i.e. a 30vol% instead of 40vol% ceramic suspension), led to about the same results as applying the single vacuum infiltration described above.

Green infiltration with a silica suspension Parts 5, 6° and 7 were green infiltrated with a silica suspension. Parts 5 and 6° were infiltrated once. Part 7 was infiltrated 4 times. After green infiltrating part 5, the weight gain was measured. Since the density of the part before infiltration and the density of the silica suspension was known, the density after infiltration and before drying could be calculated and was 96.4%. This means that part 5 was almost completely infiltrated by the low viscosity ($\leq$ 10.0 cps [12]) silica suspension. After drying, part 5 had a green density of 56.2% after infiltration (table 6.4). As depicted in table 6.5, green infiltration with a silica suspension increased the density after furnace sintering at 1600°C up to 50.0%. As green infiltration decreased the porosity of the parts, the linear shrinkage decreased to about -11%.
Figure 6.8a illustrates that part 5 did not contain macrocracks after furnace sintering. Despite the SLSed part was almost fully infiltrated with silica suspension, the SiO_2 was mainly visible at the edges of the part after furnace sintering (figure 6.8b). This could be explained by the following two hypotheses:

- Obstruction: the infiltrated nanoparticles impeded further infiltration. In this case, the porous infiltrated part acted as a filter which prohibited the small nanoparticles to further migrate inside the part.
- Capillary flow: during drying of the infiltrated parts, capillary flow transported the silica nanoparticles to the edges of the part.

Figure 6.8b also illustrates that the silica suspension seemed to flow inside the inter-layer porosities between the SLS layers during infiltration.

The size of infiltrated parts did not influence the green density after infiltration and drying. Both part 6° (initial dimensions 20x20x20mm^3) and part 5 (initial dimensions 10x10x10mm^3) had a density of 56-57% after infiltration and drying (table 6.4). Due to a lower amount of porosity compared to part 1 which was not infiltrated, part 6° shrunk only about -8 to -9% during debinding and SSS (table 6.5). Further, part 6° tended to crack horizontally after furnace sintering at 1600°C. The cracks were probably caused by a denser SiO_2 containing zone at the edge of the part. The dense edge prohibited part 6° to shrink uniformly during debinding and furnace sintering, causing the cracks and, as a result, a lower final furnace sintered density of 44.4% (table 6.5). Probably the parts cracked horizontally (i.e. perpendicular to the build direction), since the

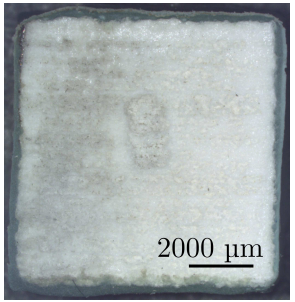

(a) part 3: 3D microscope

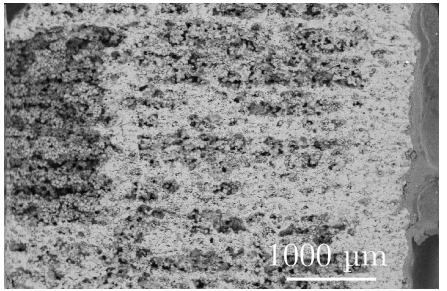

(b) Part 3: BSE-SEM

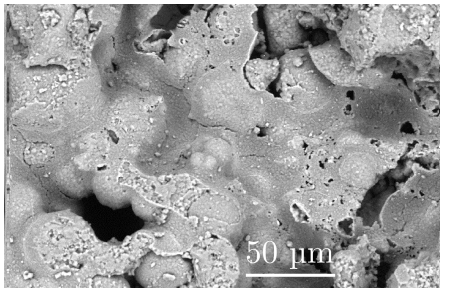

(c) part 3: BSE-SEM

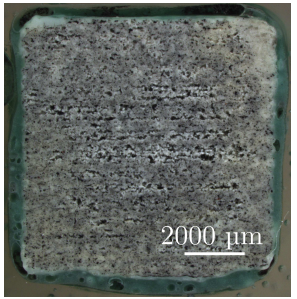

(d) part 4: 3D microscope

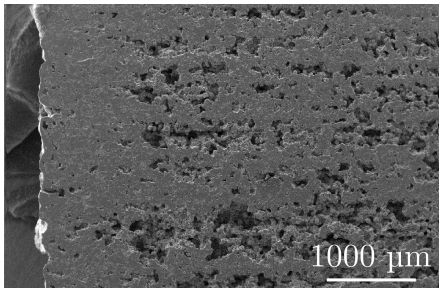

(e) part 4: SE-SEM

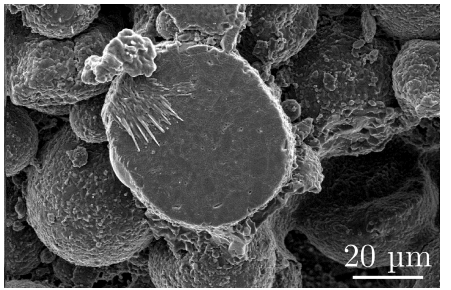

(f) part 4: SE-SEM

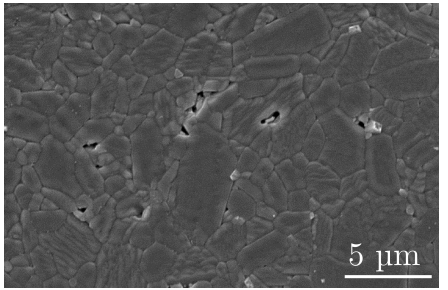

(g) part 4: SE-SEM

Figure 6.7: 3D microscope and SEM images showing the microstructure of parts which were green infiltrated with an alumina suspension: part 3 (a,b,c; 1x infiltrated), part 4 (d,e,f,g; 2x infiltrated).

strength of the parts was less in the build direction due to the porous inter-layer zones.

Part 7 illustrated that green infiltrating a part 4 times also resulted in cracks after furnace sintering at 1600°C (figure 6.8c). Part 7 had a density of 67% after the last infiltration and drying step (table 6.4). After furnace sintering, the density was 57.4% (table 6.5) and again a large dense edge could be observed in the micrographs (figure 6.8d). Figure 6.8e is a close-up of the dense shell depicted in figure 6.8d. EDX measurements confirmed that this shell consisted of SiO_2 material. The dense shell probably prohibited the part to shrink uniformly, causing the cracks. The lower amount of porosity after infiltration caused a reduced part shrinkage of about -1 to -3% (table 6.5).
Figure 6.8f is a detail of the more porous zone around the dense edge depicted in figure 6.8d. It seems that after furnace sintering, the powder agglomerates in the porous zone were covered by a thin layer of SiO_2. This observation confirms that the parts were almost completely infiltrated.

Green infiltration with a boehmite suspension Part 8 was green infiltrated 4 times with a boehmite suspension. After the infiltration (and drying) steps, the green density of part 8 was increased only up to 54.2% (table 6.4). Due to the small amount of boehmite particles (only 10wt%) in the suspension, the green density could not be increased much, despite the multiple infiltration steps. As a result, the boehmite infiltration only slightly increased the density after SSS: up to 45.1% (table 6.5). Since not many boehmite particles filled the pores, green infiltration did not affect the shrinkage: both part 1 (not infiltrated) and part 8 shrunk uniformly about -20%.
The microstructure of part 8 and part 1 (not infiltrated) were similar. No dense shell could be observed in the micrographs and no cracks could be observed in the 3D microscope images (figure 6.9a). Nevertheless, some alumina 'flakes' were present between the agglomerates (figure 6.9b). Figure 6.9c and figure 6.9d are details of these flakes. Probably, after green infiltration and drying, boehmite flakes were formed between the agglomerates. During debinding and SSS, the boehmite transformed into alumina.

Green infiltration with molten carnauba wax, containing alumina particles Part 9 was green infiltrated with melted carnauba wax, containing 22wt% alumina particles with a mean diameter of 0.3 μm. Due to the high viscosity of the melted carnauba wax, it could not fully penetrate the green part. Nevertheless, the green density increased almost 15% up to 60.9% (table 6.4). After SSS, the density was increased about 10% up to 48.9% (table 6.5). A thin and dense shell was formed at the edge of the part (left side of figure

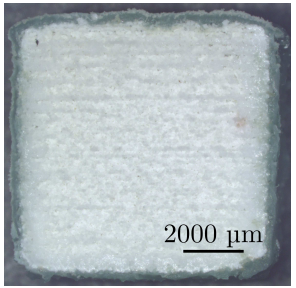

(a) part 5: 3D microscope

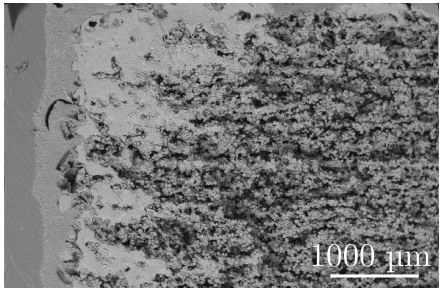

(b) part 5: BSE-SEM

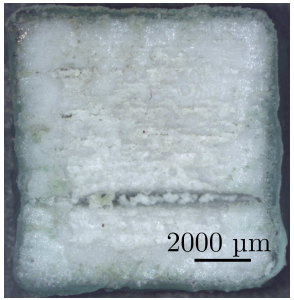

(c) part 7: unpolished

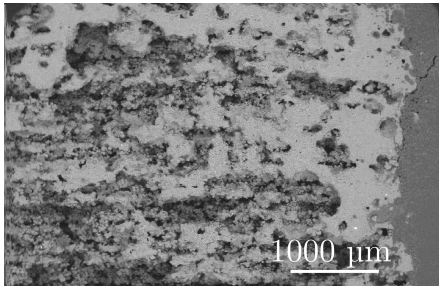

(d) part 7: BSE-SEM

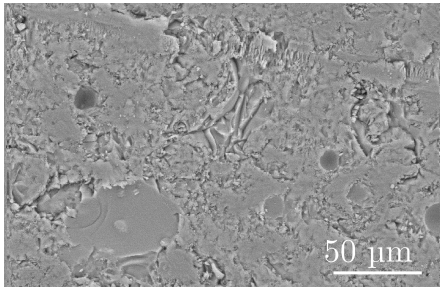

(e) edge of part 7: BSE-SEM

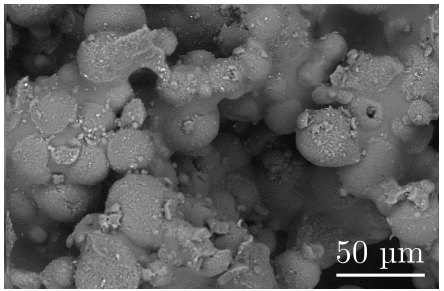

(f) middle of part 7: BSE-SEM

Figure 6.8: 3D microscope images (a,c) and SEM images (b,d,e,f) of unpolished cross sections of furnace sintered (1600°C) parts which were green infiltrated with a silica suspension: part 5 (a,b; 1x green infiltrated) and part 7 (c,d,e,f; 4x green infiltrated).

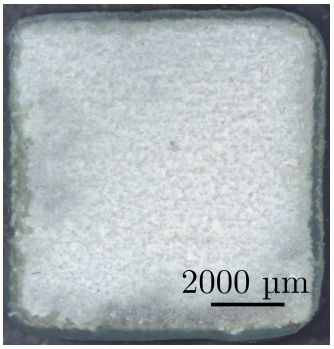

(a) part 8: 3D microscope

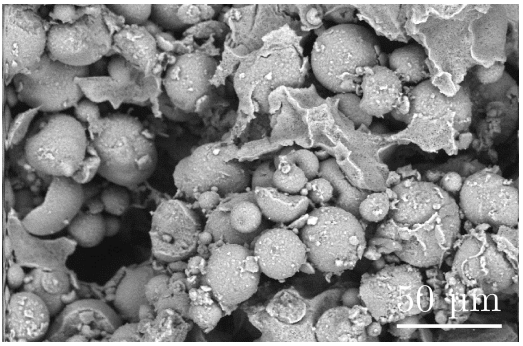

(b) part 8: BSE-SEM

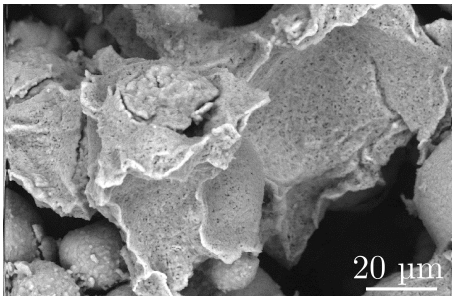

(c) part 8: BSE-SEM

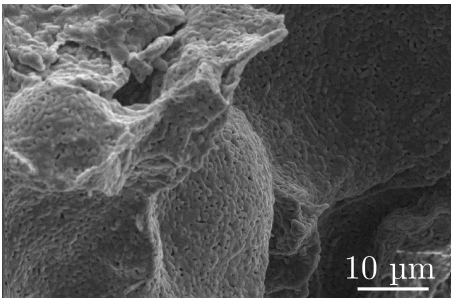

(d) part 8: SE-SEM

Figure 6.9: 3D microscope image (a) and SEM images (b,c,d) showing the microstructure of part 8 which was green infiltrated with a boehmite suspension.

6.10b). This shell prohibited the parts to shrink uniformly during debinding and SSS. The part shrinkage was -10% in the x/y direction (table 6.5). Due to the nonuniformity after infiltration, part 8 broke in the z 'build' direction during debinding and SSS (figure 6.10a).

In summary:

- Green vacuum infiltration increases the green density and the density after SSS. Vacuum infiltrating multiple times increases the green and sintered density.
- Green vacuum infiltration with the alumina suspension, the silica suspension and the carnauba wax infiltrant leads to the formation of a dense shell. The formation of the dense shell can be explained by assuming that: (i) the infiltrated particles impede further infiltration (alumina and

silica suspension), (ii) during drying capillary flow transports infiltrated nanoparticles towards the edge of the part (silica suspension), (iii) the viscosity of the suspension is too high (carnauba wax infiltrant, alumina suspension) and/or (iv) the infiltration time too short (alumina suspension) to fully infiltrate the parts.

- The dense shell prohibits the parts to shrink uniformly during debinding and SSS. This results in possible cracking or breaking of the parts.
- As infiltration reduces the porosity inside a part, green infiltrated parts tend to shrink less during debinding and SSS.
- The parts produced with SLS parameter set 1 seem to have inter-layer porosities. Due to these porosities, the infiltrant material tends to flow between the SLS layers during vacuum infiltration. If cracking or breaking of the part occurs, these inter-layer porosities can make the part crack/break perpendicular to the z 'build' direction.

6.5.1.2 Infiltration after pre-sintering

Since the polymer material of a green SLSed part might obstruct particles to infiltrate deeply inside a part, the possibility to infiltrate parts after the debinding step was investigated. In order to give the debinded 'brown' parts some strength, a pre-sintering step at 1050°C was applied prior to infiltration. During pre-sintering, the parts went through the initial SSS step (see table 6.2 for the furnace sintering parameters). Afterwards, the alumina and silica suspensions were used to infiltrate the low density pre-sintered parts.

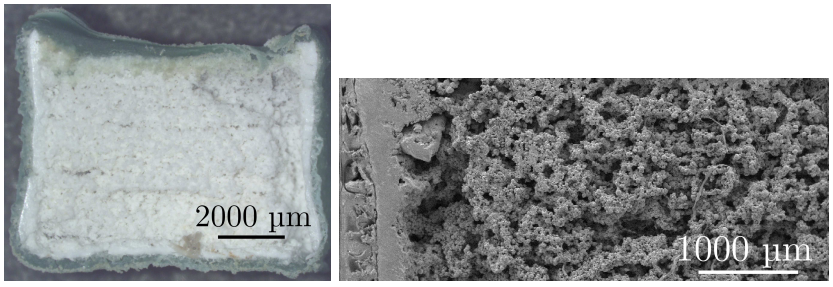

(a) part 9: 3D microscope (b) part 9: SE-SEM

Figure 6.10: 3D microscope (a) and SEM image (b), showing the microstructure after SSS of part 9 which was green infiltrated with molten carnauba wax containing Al_2O_3 particles.

Infiltration after pre-sintering with an alumina suspension After pre-sintering, part 10 was infiltrated 3 times with a 40vol% alumina containing ethanol suspension. After drying, the weight of part 10 was increased by +143wt% (table 6.6). A density of 91.4% was obtained after SSS (table 6.7). This is the highest sintered density of an alumina part, obtained in this dissertation. During debinding and SSS, part 10 shrunk about -15 to -19%, which is slightly lower than the part shrinkage of part 1 (table 6.7). Similar to the lower amount of part shrinkage after green infiltration, the lower amount of part shrinkage after infiltrating a pre-sintered part is probably caused by the reduced porosity.
The 3D microscope images (figure 6.11a) revealed that part 10 contained a porous, non infiltrated core, surrounded by a very large and densely infiltrated shell. The dense shell contained closed porosities (figure 6.11b). The initial powder agglomerates could not be differentiated from the infiltrant material. Furthermore, the alumina grain size was small (<5 μm; figure 6.11c). At one place of the dense shell, a small micro-crack could be observed (figure 6.11d). This micro-crack was probably caused by non-homogeneous shrinking during SSS.
The microstructure of the porous core (figure 6.11e) was similar to the microstructure of part 1 (not infiltrated). It consisted of connected alumina agglomerates and inter-agglomerate porosities. Figure 6.11f confirms that the agglomerates consisted of small alumina grains (< 5μm).

Part nr	Additional densification steps (besides SLS, deb. and FS)	ρ_{SLS} [%]	Δweight [wt%]
1	No, only SLS	50.7	/
10	3x infiltration after pre-sintering (alumina)	47.2	+143
11	1x infiltration after pre-sintering (silica)	46.8	+38

Table 6.6: Densities after SLS and weight increase during infiltration after pre-sintering.

Part nr	Additional densification steps (besides SLS, deb. and FS)	ρ [%]	x-y [%]	z [%]
1	No, i.e.only deb. and FS	39.8	-20	-21
10	3x infiltration after pre-sintering (alumina)	91.4	-15	-19
11	1x infiltration after pre-sintering (silica)	56.3	-19	-13

Table 6.7: Densities and linear shrinkages after FS of parts infiltrated after pre-sintering.

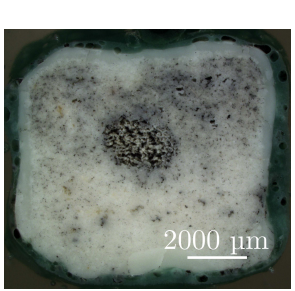

(a) part 10: 3D microscope

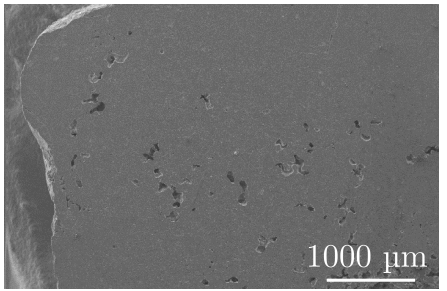

(b) part 10: dense shell, overview

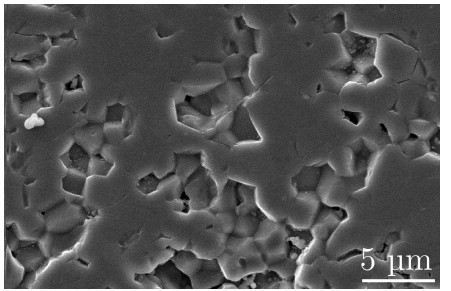

(c) part 10: dense shell, detail

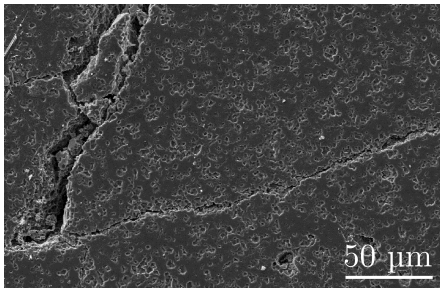

(d) part 10: dense shell, micro-crack

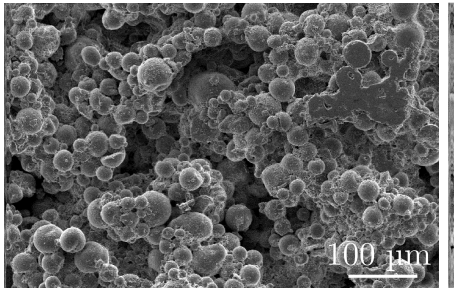

(e) part 10: porous core, overview

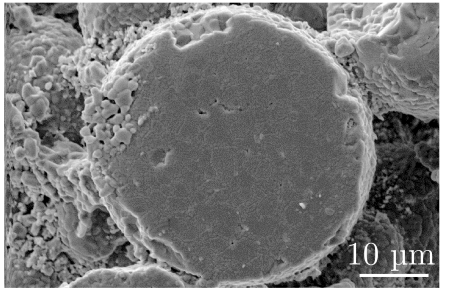

(f) part 10: porous core, powder particle

Figure 6.11: 3D microscope image (a) and SE-SEM images (b,c,d,e,f) showing the microstructure of part 10, which was 3 times infiltrated with an alumina suspension after pre-sintering.

Infiltration after pre-sintering with silica suspension After pre-sintering, part 11 was infiltrated once with the silica suspension, which led to a weight increase of +38wt% after drying (table 6.6). After furnace sintering at 1600°C, the obtained sintered density of 56.3% (table 6.7) was similar to the obtained sintered density of part 7 (i.e. 57.4%, see table 6.5), which was green infiltrated 4 times. Also the microstructure of part 11 (figure 6.12b) and part 7 (figure 6.8d) were similar. At the edge of the part, a dense SiO_2 shell could be observed (figure 6.12c). At the end of the infiltrated zone, alumina agglomerates covered by a thin layer of SiO_2 were obtained (figure 6.12d). In the middle of part 11, almost no infiltrated SiO_2 could be distinguished (figure 6.12e).
Opposite to part 7, part 11 did not contain cracks (figure 6.12a). Further, the final shrinkage of part 11 (-13 to -19% in table 6.7) was larger compared to the final shrinkage of part 7 (-1 to -3% in table 6.5).
It can be concluded that infiltration with a silica suspension after pre-sintering led to a sintered part with about the same density as a sintered part which was green infiltrated 4 times. However, when infiltrating after pre-sintering, no cracks were observed in the sintered part. Also, infiltration after pre-sintering caused more part shrinkage than infiltration after SLS. A possible explanation for these phenomena is that the part shrinkage during the debinding step was not prohibited if only infiltration after pre-sintering was applied.

In summary:

- Vacuum infiltration after pre-sintering increases the density after furnace sintering at 1600°C effectively: e.g. an alumina part with a density of 91.4% can be obtained by infiltrating 3 times with a 40vol% alumina - ethanol suspension.

- Vacuum infiltration after pre-sintering leads to the formation of a shell. However, infiltration after pre-sintering causes more part shrinkage than infiltration after SLS. A possible explanation for this phenomenon is that the part shrinkage during the debinding step is not prohibited if only infiltration after pre-sintering is applied.

- Infiltration with a silica suspension after pre-sintering leads to a sintered part with about the same density as a sintered part which is green infiltrated 4 times. However, when infiltrating after pre-sintering, no cracks are observed in the sintered part. This phenomenon can also be explained by assuming that the (nonuniform) shrinkage is less, if only infiltration after pre-sintering is applied.

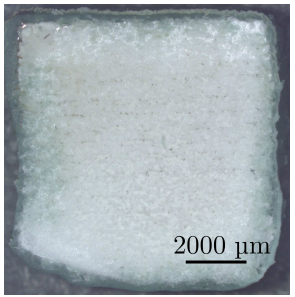

(a) part 11: 3D microscope

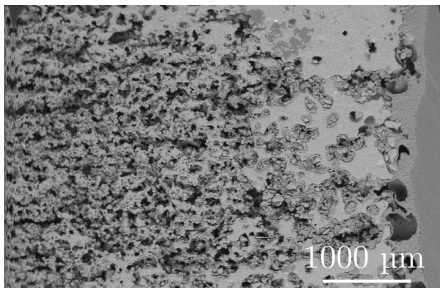

(b) part 11: BSE-SEM, detail

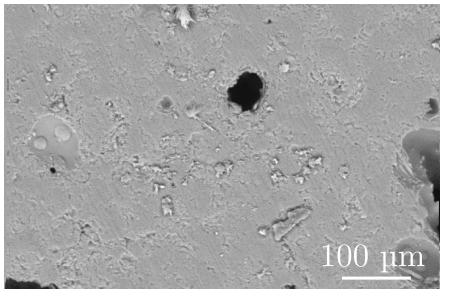

(c) part 11: BSE-SEM, infiltrated zone

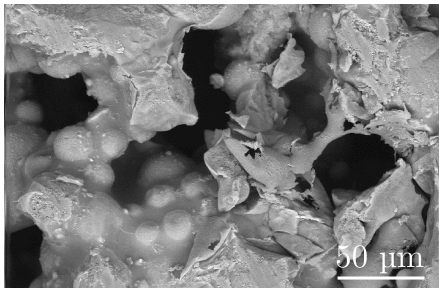

(d) part 11: BSE-SEM, edge

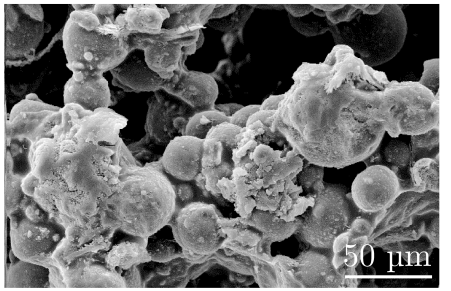

(e) part 11: SE-SEM, middle

Figure 6.12: 3D microscope image (a) and SE-SEM images (b,c,d,e) of the microstructure of part 11 which was 1 time infiltrated with a silica suspension after pre-sintering.

6.5.1.3 Green infiltration and infiltration after pre-sintering

The two previous subsections demonstrated that both green infiltration and infiltration after pre-sintering increase the density of the parts after SSS. This subsection explores whether the combination of these two infiltration techniques is beneficial. Infiltration experiments were performed using an alumina and a silica suspension.

Green infiltration and infiltration after pre-sintering with an alumina suspension Both after SLS and after pre-sintering, part 12 was infiltrated with an alumina suspension. During green infiltration, the green density increased about +20% up to 68.9% (table 6.8). This was similar to the green density of part 3, which increased up to 69.4% after green infiltration with an alumina suspension (table 6.4). Infiltrating part 12 three times after pre-sintering led to a weight increase of +7wt% (table 6.8). This was much lower than the weight increase after pre-sintering of +143wt% for part 10, which was not green infiltrated, but also infiltrated after pre-sintering (table 6.6). This means that green infiltration partially prohibited the infiltration after pre-sintering to be effective: as many inter-agglomerate pores were already filled during the first green infiltration step, not many inter-agglomerate pores could be filled during the second infiltration step after pre-sintering.
3D microscope images (figure 6.13a) and SE-SEM images (figure 6.13b) revealed that after solid state sintering, part 12 consisted of a dense shell and a more porous core. Probably, the dense shell was formed after green infiltration and also partially prohibited the infiltration after pre-sintering to be effective. When having a closer look at the dense shell (figure 6.13c and 6.13d), closed pores seemed to be present. The obtained grain size was again smaller than 5 μm. A detail of the porous zone (figure 6.13e) revealed that alumina particles were infiltrated up to the middle of the part. The alumina agglomerates and the infiltrated alumina could not be differentiated.
Infiltration after SLS and after pre-sintering doubled the sintered density, without affecting the part shrinkage much. After SSS, the density of part 12 was 81.0% instead of 39.8% for part 1 (table 6.9). The linear shrinkage of part 12 was -18 to -19%, which is slightly lower than the linear shrinkage of about -20% for part 1 (table 6.9).

Green infiltration and infiltration after pre-sintering with a silica suspension Both after SLS and after pre-sintering, part 13 was infiltrated with a silica suspension. The results were similar to the results of part 12, which also was infiltrated after SLS and after pre-sintering, but with an alumina suspension instead of a silica suspension. After green infiltrating the SLSed part, the green

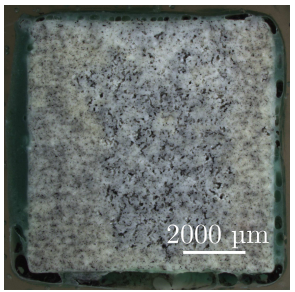

(a) part 12: 3D microscope

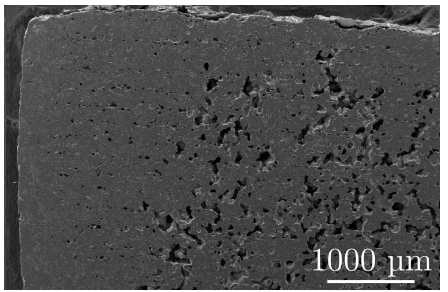

(b) part 12: overview

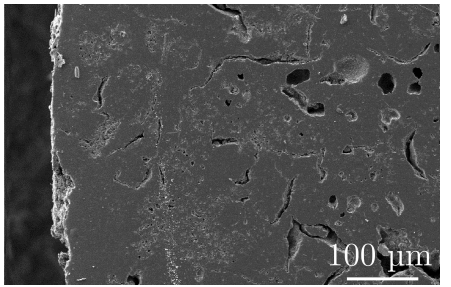

(c) part 12: edge, medium magnification

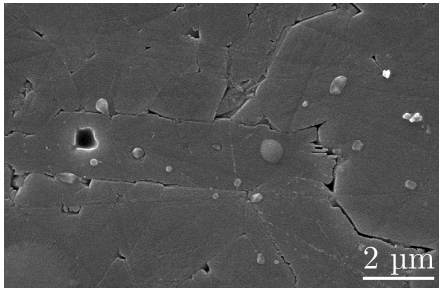

(d) part 12: edge, high magnification

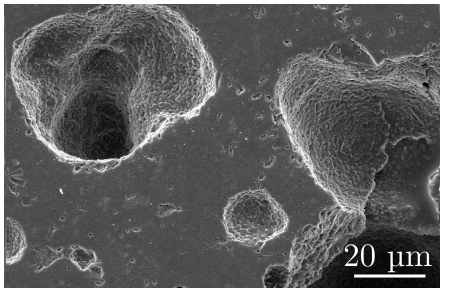

(e) part 12: core, medium magnification

Figure 6.13: 3D microscope image (a) and SE-SEM images (b,c,d,e) showing the microstructure of part 12 which was 1 time green infiltrated and 3 times infiltrated after pre-sintering with an alumina suspension.

Part nr	Additional densification steps (besides SLS, deb. and FS)	ρ_{SLS} [%]	$\rho_{gr.\ inf.}$ [%]	Δweight [wt%]
1	No, only SLS	50.7	/	/
12	1x gr. inf. & 3x inf. after pre-sint. (Al_2O_3)	48.6	68.9	+7
13	1x gr. inf. & 1x inf. after pre-sint. (SiO_2)	47.2	57.4	+18

Table 6.8: Densities after SLS, densities after green infiltration and weight increase during infiltration after pre-sintering.

Part nr	Additional densification steps (besides SLS, deb. and FS)	ρ [%]	x-y [%]	z [%]
1	No, i.e. shrinkage resulting from deb. and FS only	39.8	-20	-21
12	1x gr. inf. & 3x inf. after pre-sint. (Al_2O_3)	81.0	-19	-18
13	1x gr. inf. & 1x inf. after pre-sint. (SiO_2)	76.6	NM	NM

Table 6.9: Densities and linear shrinkages after FS of parts infiltrated after SLS and pre-sintering.

density increased about +10% up to 57.4% (table 6.8). This was similar to the green density of part 5, which increased up to 56.2% after infiltration with a silica suspension (table 6.4). Infiltrating part 13 after pre-sintering led to a weight increase of +18wt% (table 6.8). This was lower than the weight increase after pre-sintering of +38wt% for part 11, which was not green infiltrated, but infiltrated after pre-sintering (table 6.6). This means that, similar to part 12, green infiltration partially prohibited the infiltration after pre-sintering to be effective: as many inter-agglomerate pores were already filled during the first green infiltration step, not many inter-agglomerate pores could be filled during the second infiltration step after pre-sintering.
3D microscope images (figure 6.15a) and BSE-SEM images (figure 6.15b) revealed that after furnace sintering at 1600°C, part 13 consisted of a dense shell that seemed to have closed pores, and a more porous core. Probably, the dense shell was formed after green infiltration and also partially prohibited the infiltration after pre-sintering to be effective. EDX measurements revealed two phases in the dense shell: a phase which consisted of SiO_2 filling the inter-agglomerate pores and a phase which consisted of alumina and SiO_2 (figure 6.15c). The latter phase might contain mullite (figure 6.14). The porous zone did not contain the SiO_2 phase (figure 6.15d). High magnification BSE-SEM images (figure 6.15e) in the middle of the part revealed that the alumina-SiO_2 phase consisted of small alumina particles, covered by a thin layer of silica: as the weight averaged mean atomic number $\overline{Z}$ is higher for silica ($\overline{Z}_{SiO_2}$=10.8)

than for alumina ($\overline{Z}_{Al_2O_3}$=10.4), silica looks slightly brighter in the BSE-SEM images [102].
After furnace sintering at 1600°C, part 13 had a density of 76.6%. This was the highest density obtained in this chapter by using infiltration with silica. However, the 3D microscope images (figure 6.15a) revealed that part 13 cracked horizontally during furnace sintering. The dense shell probably prohibited part 13 to shrink uniformly. This resulted in a crack perpendicular to the z 'build' direction, along the inter-layer porosities.

In summary:

- Vacuum infiltration after SLS and after pre-sintering increases the density of the sintered parts.
- When infiltrating after SLS and after pre-sintering, a part is formed which has a dense shell and a more porous core. When infiltrating with the SiO_2 suspension, the dense shell consists of two phases: a SiO_2 phase filling the inter-agglomerate pores and a alumina-SiO_2 phase which might contain mullite. The porous core only consists of the alumina-SiO_2 phase.
- After green infiltration, already filled inter-agglomerate pores and the dense shell partially prohibit effective infiltration after pre-sintering. Nevertheless, densities up to 76.6% (table 6.9) can be obtained by infiltrating with the 40wt% silica suspension. This is the highest density obtained in this chapter by infiltrating with a silica suspension. A sintered density of only 81.0% (table 6.9) can be obtained by infiltrating with the more viscous 40vol% alumina suspension. This is lower than the sintered density which can be obtained by only applying infiltration after pre-sintering (i.e. about 91.4%, table 6.7).
- If the dense shell prohibits a part to shrink uniformly, cracks perpendicular to the z 'build' direction and along the inter-layer porosities can arise.

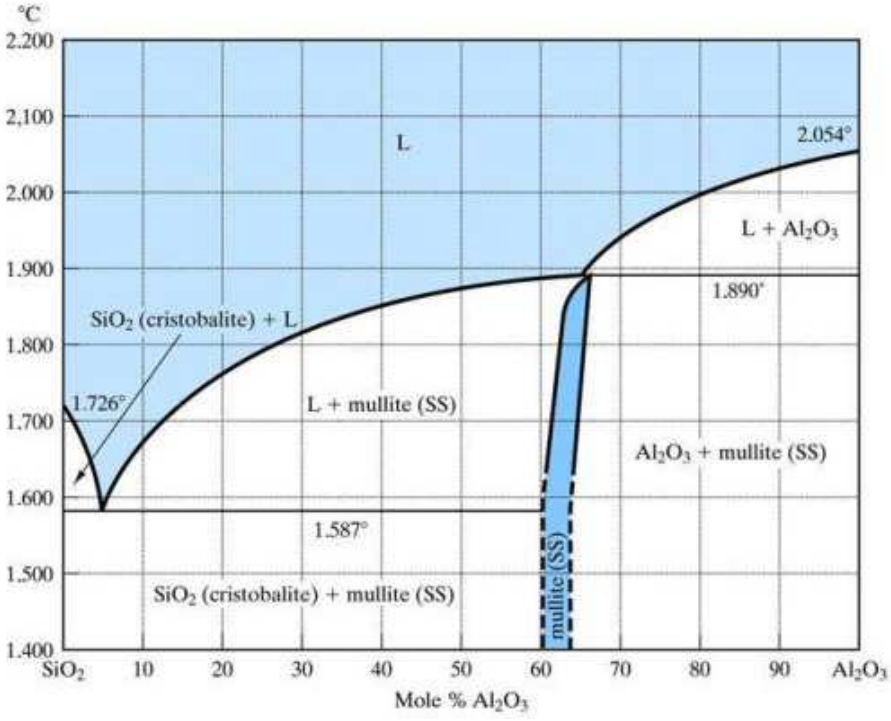

Figure 6.14: Al_2O_3 - SiO_2 phase diagram. Mullite is an intermediate compound with ideal stoichiometry $3Al_2O_3$. $2SiO_2$.

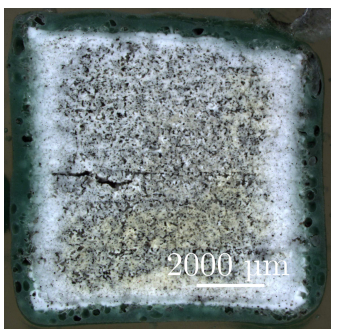

(a) part 13: 3D microscope

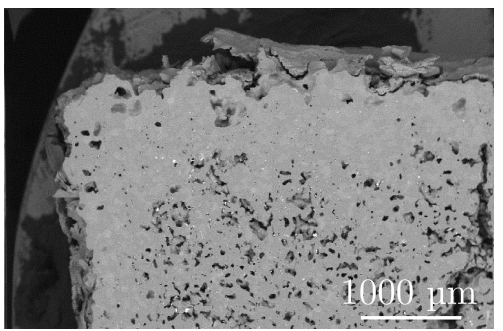

(b) part 13: overview

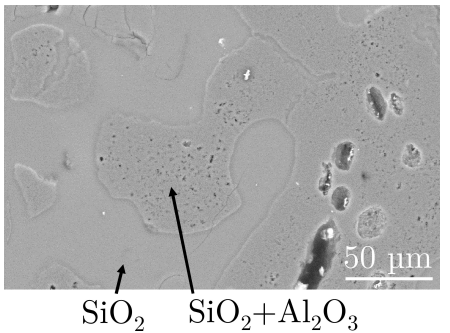

(c) part 13: edge, medium magnification

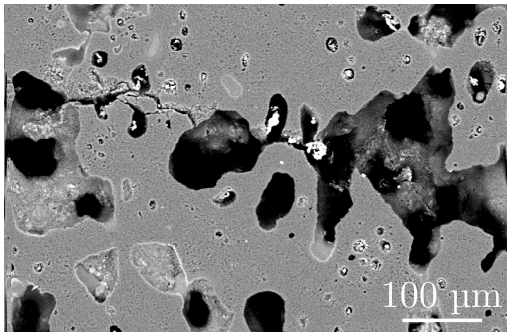

(d) part 13: core, medium magnification

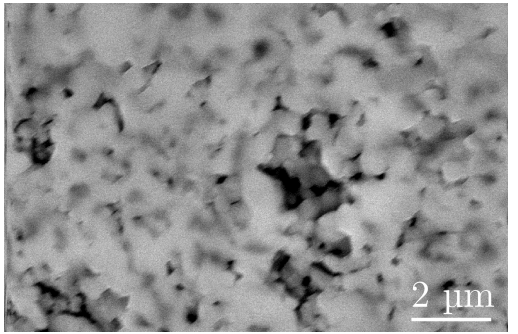

(e) part 13: core, high magnification

Figure 6.15: 3D microscope image (a) and BSE-SEM images (b,c,d,e) showing the microstructure of part 13 which was green infiltrated and infiltrated after pre-sintering with a silica suspension.

6.5.2 Warm isostatic pressing

As described in the previous chapters, the WIPing process comprises vacuum packing and immersing the part in a heated liquid that transmits the pressure uniformly to the part. WIPing combines the advantages of both CIPing and QIPing, i.e. a uniformly applied pressure and a heated pressure transmitting medium.
WIPing was investigated with or without infiltration after SLS and/or after pre-sintering. The infiltration experiments were performed with the stabilized 40vol% alumina - ethanol suspension. In order to obtain a good plastic deformation behaviour during WIPing, the samples were vacuum packed in bags of polypropylene (i.e. same material as the polymer binder material). All parts were WIPed for 15 minutes at 48 MPa and 140°C. After the WIPing step, the polypropylene (PP) bags of parts 15, 16 and 17 could not be manually removed from the WIPed part without having the risk to break the part. Therefore, the PP bags were removed during the debinding step. The PP bag of part 14 could be manually removed after WIP and before debinding.

Only WIP Part 14 was only densified by WIP. As a result, the green density became 87.7% (table 6.10). The WIPing step increased the density after SSS up to 64.2% (table 6.11). WIPing also increased the linear shrinkage during debinding and SSS. The linear shrinkage of -35% in the z 'build' direction was larger compared to the linear shrinkage of -19% in the x/y 'scan'/'cross-scan' directions.
No cracks could be observed in the 3D microscope images (figure 6.16a) and SEM images (figure 6.16b). The microstructure consisted of densely packed agglomerates and inter-connected pores. At some places, the agglomerates seemed to be fused together (figure 6.16c).
Shahzad et al. [185] also used warm isostatic pressing on parts produced through SLS of 40 vol% alumina - 60 vol% polypropylene agglomerates. The parts were produced with different SLS parameters: P=5W; v=875mm/s; s=150μm; l=200μm (see section 6.4.2 above). The SLSed samples were vacuum packed in nitrile rubber bags (TNT Blue disposable gloves, Ansel limited, Malaysia) and WIPed for 5 minutes at 64 MPa and 135°C. After WIP, the green density of the parts was increased up to 91.9%. After SSS, the density was 88.1% and the agglomerates seemed to be broken. *The higher densities after WIPing were probably obtained due to the application of a higher WIPing pressure: 64 MPa instead of 48 MPa was used. The WIPing pressure of 64 MPa was just high enough to break the agglomerates at 135°C.*

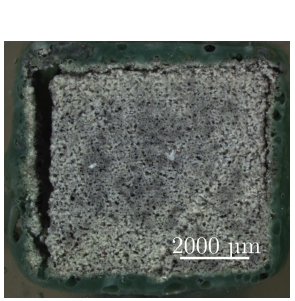

(a) part 14: 3D microscope

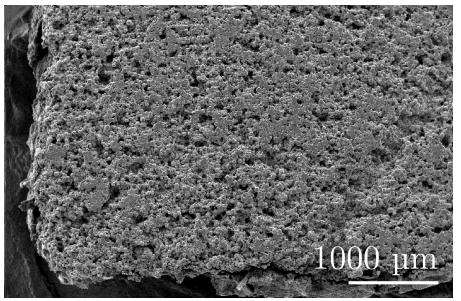

(b) part 14: overview

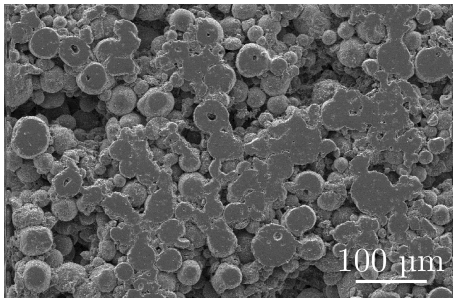

(c) part 14: bulk

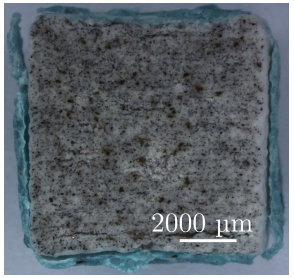

(d) part 15: 3D microscope

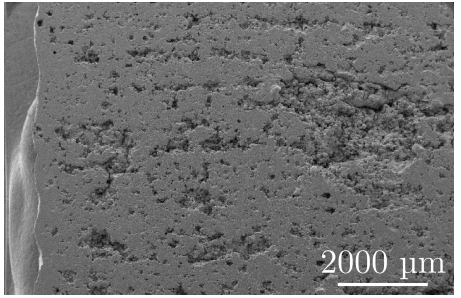

(e) part 15: overview

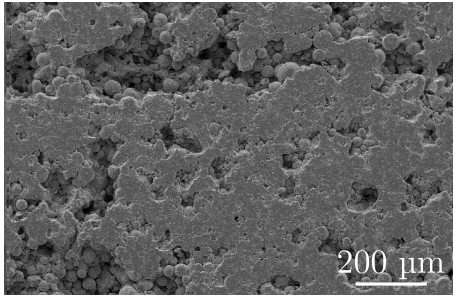

(f) part 15: porous infiltrated zone

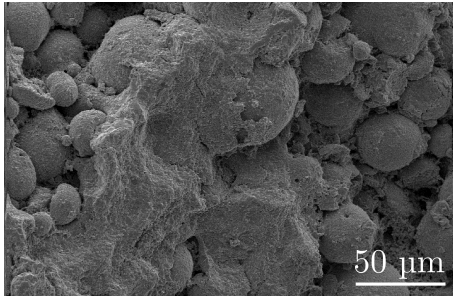

(g) part 15: core

Figure 6.16: 3D microscope (a,d) an SE-SEM images (b,c,e,f,g) showing the microstructure after SSS of part 14 (a,b,c) which was WIPed and part 15 (d,e,f,g) which was green infiltrated with an alumina suspension and WIPed afterwards.

Part nr	Additional densification steps (besides SLS, deb. and SSS)	ρ_{SLS} [%]	$\rho_{gr.\,inf.}$ [%]	ρ_{WIP} [%]	Δweight [wt%]
1	No, only SLS	50.7	/	/	/
14	WIP, 140°C, 48 MPa, 15 minutes	46.0	/	87.7	/
15	gr. infiltration & WIP	49.0	73.9	NM	/
16	WIP & 3x inf. after pre-sint.	45.7	/	85.5	+1
17	gr. inf., WIP, 3x inf. after pre-sint.	46.4	67.8	NM	+3

Table 6.10: Densities after SLS, densities after green infiltration, densities after warm isostatic pressing and weight increase during infiltration after pre-sintering (NM = not measured).

Part nr	Additional densification steps (besides SLS, deb. and SSS)	ρ [%]	x-y [%]	z [%]
1	No, i.e. only deb. and SSS	39.8	-20	-21
14	WIP, 140°C, 48 MPa, 15 minutes	64.2	-27	-35
15	*gr. infiltration (Al_2O_3) and WIP*	*78.5*	*-17*	*-18*
16	WIP and 3x inf. after pre-sint. (Al_2O_3)	70.0	/	/
17	gr. inf., WIP, 3x inf. after pre-sint. (Al_2O_3)	77.0	-18	-19

Table 6.11: Densities and linear shrinkages after SSS of parts: infiltrated after SLS, WIPed and/or infiltrated after pre-sintering.

Green infiltration and WIP Part 15 was first green infiltrated with the alumina suspension and WIPed afterwards. During green infiltration, the green density was increased up to 73.9% (table 6.10). After WIP, debinding and SSS, the density of part 15 was 78.5% and the part shrinkage -17 to -18% (table 6.11). Compared to part 14, which was only WIPed, *the application of green infiltration before WIPing increased the sintered density and reduced the amount of shrinkage during debinding and SSS.* Similar to green infiltration without WIPing, the reduced part shrinkage can be explained by assuming that shrinkage is generally larger for more porous parts: as infiltration reduced the porosity inside part 15, the shrinkage after infiltration was less.
The 3D microscope images (figure 6.16d) and the SEM images (figure 6.16e) revealed a microstructure similar to the microstructure of part 3 which was only green infiltrated with alumina (figure 6.7a and 6.7b): a (quasi) non-infiltrated zone at the middle of the part, surrounded by a large infiltrated zone, consisting of a porous zone and a dense shell. The dense shell was probably formed during green infiltration. The porous infiltrated zone consisted of inter-agglomerate pores which were infiltrated with alumina and compressed during WIPing (e.g.

figure 6.16f). The quasi non-infiltrated zone at the middle of the part consisted of agglomerates which were not collapsed during WIPing and a small remnant of infiltrated alumina (figure 6.16g).
Shahzad et al. [185] investigated the application of warm isostatic pressing after pressure infiltration on parts produced through SLS of 40 vol% alumina - 60 vol% polypropylene agglomerates. The SLS parameters (P=5W; v=875mm/s; s=150μm; l=200μm), pressure infiltration parameters (p=13MPa; 30vol% alumina-ethanol suspension) and WIP parameters (5 minutes at 64 MPa and 135°C) were respectively the same as described in sections 6.4.2, 6.5.1.1 and 6.5.2. After SSS, the density was 86.1% and the agglomerates seemed to be broken. As it was the case for part 14 (see previous paragraph), also in this case the *higher densities after SSS were probably obtained due to the application of a higher WIPing pressure (64MPa instead of 48MPa).*

WIP after SLS and infiltration after pre-sintering Part 16 was WIPed after SLS and infiltrated with the alumina suspension after pre-sintering. After WIP, the green density was increased up to 85.5% (table 6.10). During infiltration after pre-sintering, the weight of the part increased only +1wt%. This was much lower than the weight increase after pre-sintering of +143wt% for part 10, which was not WIPed, but also infiltrated after pre-sintering (table 6.6). This means that the WIPing process partially prohibited the infiltration after pre-sintering to be effective. Probably, the WIPing process decreased the pore size after pre-sintering. As a result, the alumina suspension could not flow into the pre-sintered part anymore.
After SSS, a density of 70.0% was obtained (table 6.11). As depicted in the 3D microscope image (figure 6.17a), part 16 had a quite irregular outer shape after SSS. The weak strength of the part after pre-sintering caused some eroding of the outer shapes. Due to this erosion, the measured shrinkages of the part did not represent the shrinkage due to only the debinding and SSS. Therefore, the shrinkage after SSS for part 16 was not presented in table 6.11.
The SE-SEM images of part 16 (figure 6.17b and 6.17c) were similar to part 14 (figure 6.16b and 6.16c). No cracks could be observed and the microstructure consisted of densely packed agglomerates and inter-connected pores. No clear traces of infiltrated alumina could be detected.

Green infiltration, WIP and infiltration after pre-sintering Part 17 was infiltrated after SLS, WIPed before debinding and infiltrated with the alumina suspension after furnace pre-sintering. After green infiltration, the density of the part was 67.8% (table 6.10). This was similar to the green density of part 3, which increased up to 69.4% after infiltration with an alumina suspension (table 6.4). During infiltration after pre-sintering, the weight of the part increased

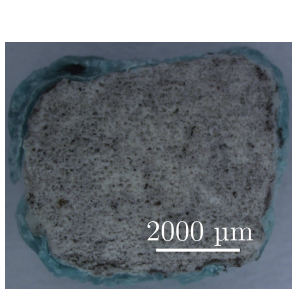

(a) part 16: 3D microscope

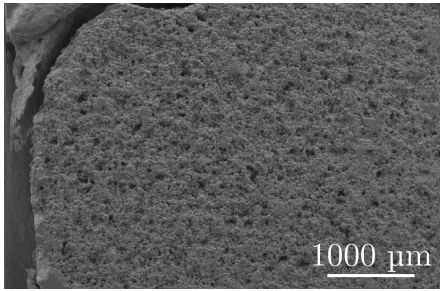

(b) part 16: overview

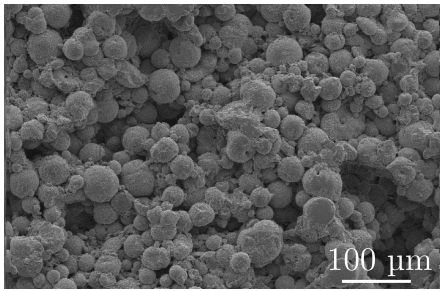

(c) part 16: bulk

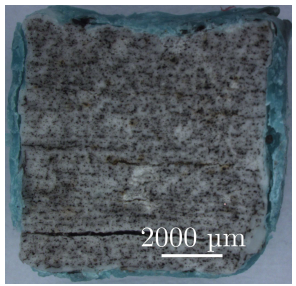

(d) part 17: 3D microscope

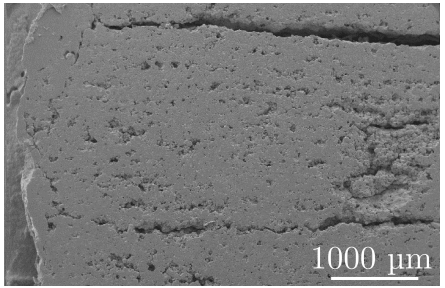

(e) part 17: overview

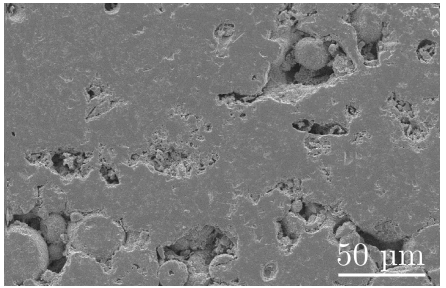

(f) part 17: dense shell

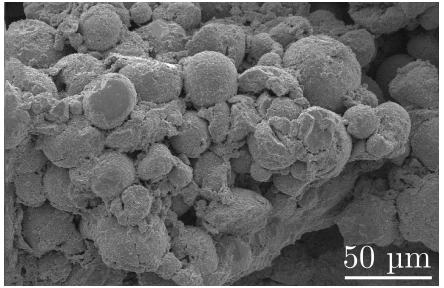

(g) part 17: porous core

Figure 6.17: 3D microscope images (a,d) and SE-SEM (b,c,e,f,g) images showing the microstructure of part 16 (a,b,c) which was WIPed and 3 times infiltrated after pre-sintering with an alumina suspension and part 17 (d,e,f,g) which was 1 time green infiltrated, WIPed and 3 times infiltrated after pre-sintering with an alumina suspension.

only +3wt% (table 6.10). Similar to part 16, the weight increase after pre-sintering was much lower than the weight increase of +143wt% for part 10, which was only densified by infiltrating after pre-sintering (table 6.6).
The 3D microscope images (figure 6.17d) revealed that part 17 contained horizontal cracks. The microstructure of part 17 (figure 6.17e) was similar to the microstructure of part 15, which was green infiltrated and WIPed, but not infiltrated after pre-sintering: a (quasi) non-infiltrated zone at the middle of the part surrounded by a large infiltrated zone, consisting of a porous zone and a dense shell. Similar to part 15, the dense shell was probably formed during green infiltration. The porous infiltrated zone consisted of inter-agglomerate pores which were infiltrated with alumina and compressed during WIPing (figure 6.17f). The quasi non-infiltrated zone consisted of agglomerates which were not collapsed during WIPing and less densely infiltrated alumina (figure 6.17g).
For part 17, the low weight gain during infiltration after pre-sintering can be explained by its microstructure. Probably the infiltration after pre-sintering was impeded by the green infiltration (i.e. the filling of the inter-agglomerate pores and the formation of the dense shell) and the WIPing process (i.e. the decrease of pore size).

In summary:

- WIPing increases the green density, the density after SSS and the part shrinkage, even when the composite agglomerates do not collapse.
- During WIPing at 135-140°C, the composite alumina (40vol%) - PP (60vol%) agglomerates break at a pressure between 48 and 64 MPa.
- Green infiltration before WIPing is an effective method to increase the sintered density. As green infiltration reduces the amount of porosity inside a part, the application of green infiltration also decreases the part shrinkage.
- Infiltration after pre-sintering can become a non-effective densification step after WIPing. Since WIPing decreases the pore size after pre-sintering, the infiltrant might no longer flow inside the part.
- The temperature of 1050°C is rather a lower bound for pre-sintering. If not handled with care, parts which are pre-sintered at 1050°C erode.

6.6 Qualitative geometrical assessments

The geometrical limits of the production of alumina parts through indirect SLS of composite alumina (40vol%) - PP (60vol%) agglomerates were qualitatively assessed. In order to do so, non cubic alumina parts were fabricated.

In a first geometric experiment, complex shapes (figure 6.18a) were SLSed using parameters optimized for accuracy and green density: respectively parameter set 1 and 2 of table 6.1. After SLS, composite powder got stuck in the SLSed shapes. Sticking of the powder is a phenomenon which especially occurred when the same composite powder was used multiple times to fabricate parts: i.e. when using 'aged' powder[1]. During manual removal of this powder with a spatula, all complex shapes which were SLSed using parameter set 1 broke. All complex shapes which were SLSed using parameter set 2 survived the powder removal step. However, these parts broke during the subsequent debinding and SSS steps. During the debinding step, the strength of the complex shape was probably too low to bear its own weight without additional support. In order to increase the strength during debinding and to prevent breaking of the parts, an infiltration step was successfully applied on the SLSed parts. Since the experimental vacuum infiltration setup could only be used to infiltrate samples smaller than about 25x25x25 mm^3, pressure infiltration was applied: a stabilized 40vol% alumina - ethanol suspension was squeezed into the part for 5 minutes at a pressure at 1.75 MPa. Figure 6.18b depicts the result after SSS of the applied procedure.
The difference between SLS parameter set 1 (optimized accuracy) and 2 (optimized green density) was further explored. Both parameter sets were used to produce thin walls (figure 6.18c). The scanning system of the DTM Sinterstation 2000 was able to produce all the walls, except the wall with a CAD thickness of 0.4 mm. After SLS, composite powder got stuck between the SLSed walls. The walls of 0.5 and 0.6 mm CAD thickness and SLSed with parameter set 1 broke during manually removing the powder (figure 6.18d). All the walls that could be SLSed with parameter set 2 survived the powder removal step. In order to increase the strength of the walls during debinding, the same pressure infiltration step as for the complex shapes (40vol% Al_2O_3 - ethanol suspension; 1.75 MPa; 5 min.) was applied on the SLSed parts. The result after SSS is depicted in figure 6.18e.
Finally, benchmark parts (figure 4.7b) were SLSed with parameter set 1 and 2. After pressure infiltration (40vol% Al_2O_3 - ethanol suspension; 1.75 MPa;

[1]The properties of polymer powder can change (i.e. 'age') over time. Aging might be caused by modifications of the polymer chains during iterative heating when reusing the powder multiple times during different SLS experiments. Aging might also be caused by the absorption of moisture from the surrounding atmosphere.

5 min.), debinding and SSS, the final parts were obtained (figure 6.18f and 6.18g). All features with a CAD size below 0.5 mm could not be laser scanned by the DTM Sinterstation 2000. Parameter set 1 was more appropriate than parameter set 2 to produce the other features. The high laser energy of parameter set 2 decreased the viscosity of the PP during irradiation. As a result, the melted PP flowed into the surrounding powder and solidified, forming dross. As the melted PP flowed into underlying powder, dross formation prohibited the accurate production of overhang structures (not depicted in figure 6.18f and 6.18g). The flowing of the PP also caused silting of the internal holes (figure 6.18g). Silting of the internal holes was also caused by the formation of an external shell (figure 6.6b) during infiltration. This external shell always had to be removed with a spatula after the infiltration step.
Other complex shapes, which were also produced through SLS, pressure infiltration and SSS are depicted in figure 6.19.

In summary:

- Complex shapes can be produced through SLS of composite alumina (40vol%) - PP (60vol%) agglomerates. However, features with a CAD size below 0.5 mm can not be laser scanned by the DTM Sinterstation 2000. Parameter set 1 can be used to accurately SLS small features. However, these features might break when manually removing composite powder sticking between the SLSed shapes. Sticking of the powder is a phenomenon which especially occurs when the same composite powder is used multiple times to fabricate parts: i.e. when using 'aged' powder. If parameter set 2 is applied during SLS, the powder sticking to the fabricated shapes can be manually removed, without breaking them. However, the high laser energy of parameter set 2 decreases the viscosity of the PP during irradiation and causes the PP to flow. As a result dross is formed, prohibiting the accurate production of overhang structures and internal holes.

- During the debinding step, the strength of complex shapes is too low to bear its own weight without additional support. Green pressure infiltration can increase the strength of these shapes during debinding. However, green infiltration causes the formation of an external shell. If not removed properly with e.g. a spatula, this shell can lead to silting of internal geometries.

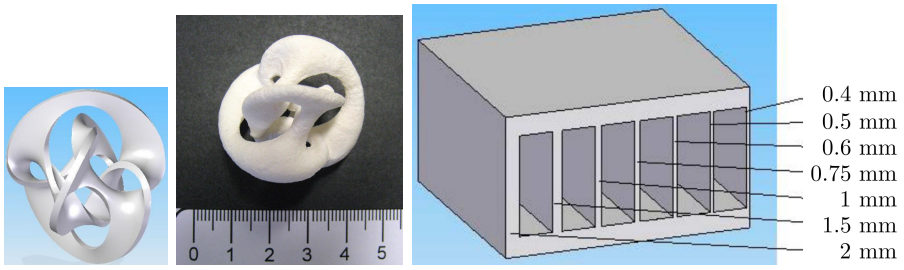

(a) CAD image (b) after SSS (c) CAD image

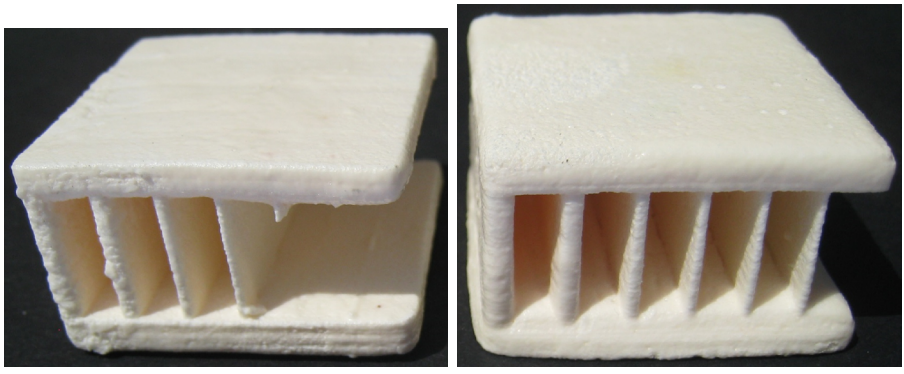

(d) after SSS (e) after SSS

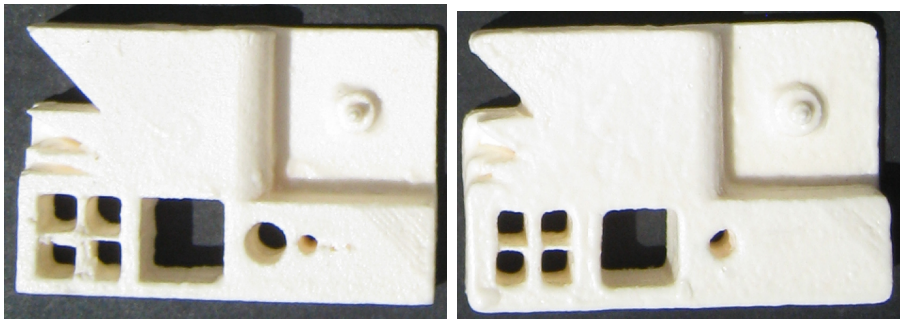

(f) after SSS (g) after SSS

Figure 6.18: Geometrical assessments: the fabrication of a complex shaped part (a,b), thin walls (b,c,d) and a benchmark part (e,f). The parts were produced through SLS, pressure infiltration, debinding and SSS. Some parts (d,f) were SLSed by using parameter set 1; other parts (b,e,g) by using parameter set 2.

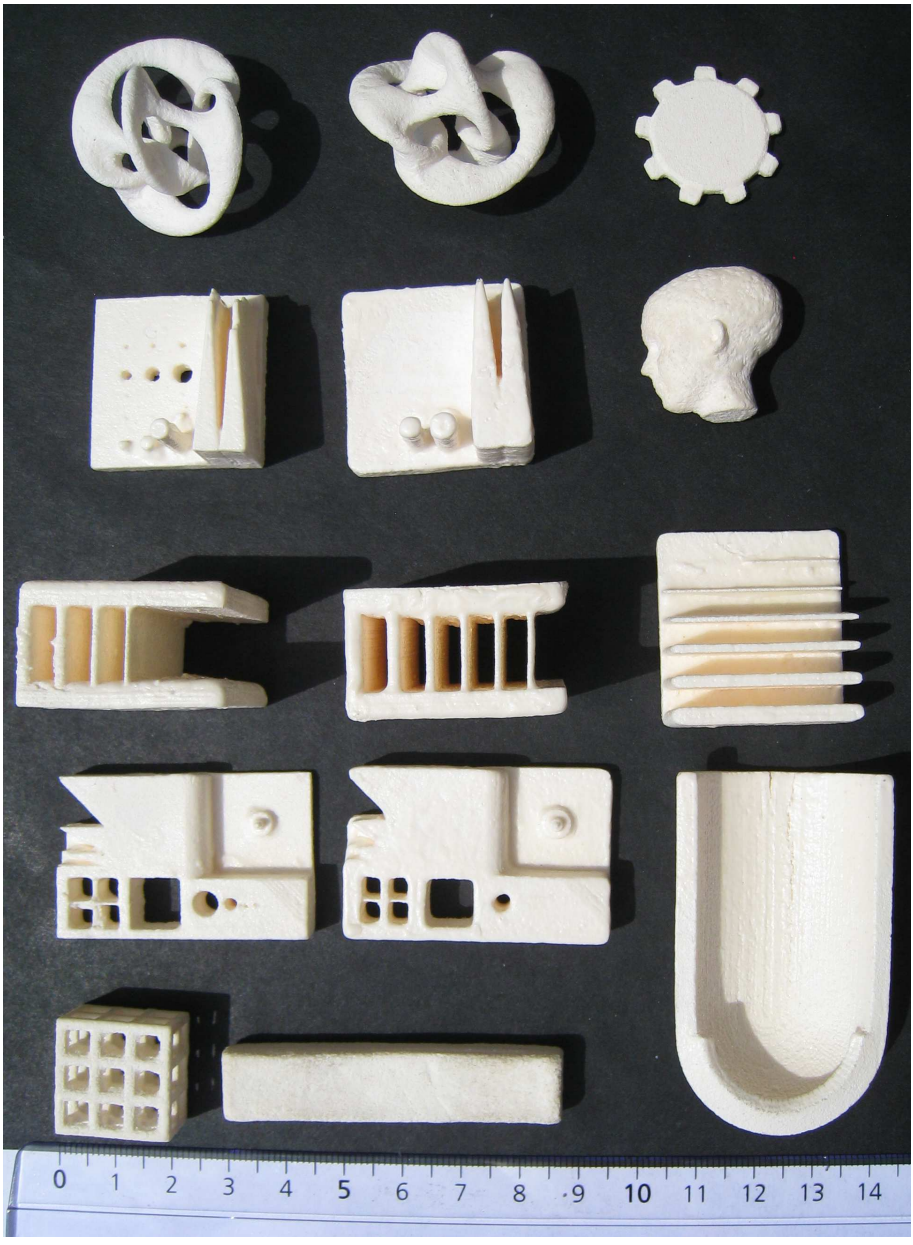

Figure 6.19: Overview of non cubic parts produced through SLS, pressure infiltration, debinding and SSS.

6.7 Conclusions

A powder metallurgy process was developed to produce crack-free alumina parts through SLS, starting from alumina - PP composite powder synthesized by temperature induced phase separation (TIPS). Since PP has an SLS window at a lower temperature range than PA, PP seemed to be a binder material which is easier to SLS: all 27 different SLS parameters, with a laser energy density 'e' ranging between 0.092 to 1.077J/mm^3, led to parts which could be taken out of the DTM Sinterstation. For the alumina-PA agglomerates, only SLS parameters with a laser energy density ranging between 0.176 and 0.37 J/mm^3 were strong enough for non-destructive manipulation. Furthermore, by increasing the PP content of the starting powder from 50 to 60vol%, stronger parts with a better geometrical accuracy could be produced. Applying high laser energy densities during SLS resulted in green parts with a higher density and strength.
After SLS with parameters optimized for accuracy and subsequent debinding and SSS, an inhomogeneous microstructure consisting of interconnected agglomerates as well as inter-agglomerate pores was formed. The density of the sintered parts was 39% (table 6.12, part 1 and 2). The linear shrinkage during debinding and solid state sintering was homogeneous and about -20%.

In order to eliminate the inter-agglomerate pores after furnace sintering, vacuum infiltration, warm isostatic pressing (WIP) or a combination of both was applied (table 6.12). Vacuum infiltration was performed on both SLSed samples (i.e. green infiltration) and/or samples which were pre-sintered at 1050°C. Different infiltrants were used: a 40vol% alumina - ethanol suspension, a 40wt% silica - water suspension, a 10wt% boehmite - water suspension and molten carnauba wax containing 22wt% of alumina powder.
Green infiltration, infiltration after pre-sintering and warm isostatic pressing all improved the density of the parts after furnace sintering. When WIPing at 135-140°C, a pressure between 48 and 64 MPa was needed to break the composite alumina (40vol%) - PP (60vol%) agglomerates. The infiltration behavior was dependent on the infiltrant used. When infiltrating with the alumina suspension, the highest sintered density (i.e. 91.4%, table 6.12, part 10) was obtained by infiltrating 3 times after pre-sintering. When infiltrating with the silica suspension, the highest sintered density (76.6%, table 6.12, part 13) was obtained by infiltrating once after SLS and once after pre-sintering.
Vacuum infiltration reduced the amount of porosity inside a part. As a result, the infiltrated parts tended to shrink less. Vacuum infiltration with the alumina suspension, the silica suspension and carnauba wax infiltrant also led to the formation of a dense outer shell. The formation of the dense shell could be explained assuming that (i) the infiltrated particles impeded further infiltration

(alumina and silica suspension), (ii) during drying a capillary flow transported infiltrated nanoparticles towards the outside of the part (silica suspension), (iii) the viscosity of the suspension was too high (carnauba wax infiltrant, alumina suspension) and (iv) the infiltration time was too short to fully infiltrate the parts (alumina suspension). No dense shell was formed when infiltrating with the boehmite suspension.
The dense shell prohibited the parts to shrink uniformly during debinding and furnace sintering: the more porous areas shrunk more than the less porous areas. As a result, cracks perpendicular to the z 'build' direction and along the inter-layer porosities could be formed. These cracks could drastically reduce the density of the sintered parts.
Infiltration after pre-sintering caused more part shrinkage than infiltration after SLS. A possible explanation for this phenomenon is that the part shrinkage during the debinding step was not prohibited if only infiltration after pre-sintering was applied.
Infiltration after pre-sintering was a non-effective densification step when applied after a green infiltration and/or WIPing step. After green infiltration, already filled inter-agglomerate pores and the dense shell prohibited the infiltration after pre-sintering. Also, since WIPing decreased the pore size after pre-sintering, the infiltrant could not flow inside the part anymore.

For the production of fragile complex shapes, SLS with high laser energy was sometimes needed to increase the green strength. Only if the SLSed part was strong enough, composite powder, sticking between the SLSed shapes, could be manually removed with a spatula without breaking the fragile shapes. However, when using too high laser energy densities, dross formation and/or polymer degradation occurred. Dross formation prohibited the accurate production of overhang structures and internal holes.
The strength of complex shapes was too low to bear its own weight without additional support during debinding. Green pressure infiltration could increase the strength of these shapes during debinding. However, green infiltration caused the formation of an external shell. If not removed properly with a spatula, this shell led to silting of the internal geometries.

Part nr	Additional densification steps (besides SLS, deb. and SSS)	ρ [%]	x-y [%]	z [%]
1	No, i.e. only deb. and SSS	39.8	-20	-21
2°	No, i.e. only deb. and SSS	38.4	-17	-21
3	1x green vacuum infiltration (Al_2O_3)	63.3	-14	-13
4	2x green vacuum infiltration (Al_2O_3)	73.9	-16	-16
5	1x green vacuum infiltration (SiO_2)	50.0	-11	-12
6°	1x gren vacuum infiltration (SiO_2)	44.4	-8	-9
7	4x green vacuum infiltration (SiO_2)	57.4	-3	-1
8	4x green vacuum infiltration (boehmite)	45.1	-20	-20
9	1x green vacuum infiltration (Al_2O_3-carnauba wax)	48.9	-10	/
10	*3x vac. infiltration after pre-sint. (Al_2O_3)*	*91.4*	*-15*	*-19*
11	1x vac. infiltration after pre-sint. (SiO_2)	56.3	-19	-13
12	1x gr. vac. inf. & 3x vac. inf. after pre-sint. (Al_2O_3)	81.0	-19	-18
13	1x gr. vac. inf. & 1x vac. inf. after pre-sint. (SiO_2)	76.6	NM	NM
14	WIP, 140°C, 48 MPa, 15 minutes	64.2	-27	-35
15	gr. vacuum infiltration (Al_2O_3) and WIP	78.5	-17	-18
16	WIP and 3x vac. inf. after pre-sint. (Al_2O_3)	70.0	/	/
17	gr. vac. inf., WIP, 3x vac. inf. after pre-sint. (Al_2O_3)	77.0	-18	-19

Table 6.12: Sintered densities and linear shrinkages of the cubic (10x10x10 mm^3; samples indicated with °, are 20x20x20mm^3) alumina parts after additional densification steps. The dimensional shrinkages of the table indicate the geometrical changes that appear after the SLS process, i.e. the geometry after SLS is the reference geometry (NM=not measured). The vacuum infiltration (vac. inf.) experiments were performed using the following suspensions: 40 vol% Al_2O_3 - ethanol, 40 wt% SiO_2 - water, 10 wt% boehmite - water and 22 wt% Al_2O_3 - molten carnauba wax.

Chapter 7

Direct selective laser sintering/melting of high density alumina powder layers at elevated temperatures

> What we agree with leaves us inactive, but contradiction makes us productive.
>
> von Goethe, Johann Wolfgang

7.1 Abstract

In order to direct laser sinter (SLS) or laser melt (SLM) technical alumina ('direct' means without binder), a low laser energy density should be applied on high density powder layers of submicrometer alumina, preheated to a uniform and high ($\pm$ 800°C) temperature. In order to do so, an experimental setup was designed and constructed. The experimental setup consisted of a vertical tube furnace, which was mounted on the building platform of a DTM Sinterstation 2000. In this furnace, a cylindrical zone could be homogeneously heated within a margin of $\pm$ 50°C up to a temperature of 800°C. The experimental setup also

consisted of a deposition mechanism, which could deposit high density powder layers through electrophoretic deposition (EPD).
Two samples, with a density up to 85%, were produced after optimizing the layer deposition and laser scanning parameters. Despite the formation of a liquid phase during direct SLS/SLM of the high density and preheated powder layers, an alumina microstructure with a grain size close to or smaller than 5 μm could be formed. When the laser energy density input increased, the resulting size of the grains also increased. The samples still contained pores, due to improper layer deposition, and surface cracks appeared. The surface cracks were caused by the following reasons, or a combination thereof: thermal stresses, shrinkage of the powder due to densification during SLS/SLM and/or improper layer deposition.

7.2 Introduction

As depicted in section 2.3 of this dissertation, the long term goal of the ceramic research at KU Leuven is to rapidly produce technical and thus high quality ceramics through additive manufacturing. Direct Selective Laser Sintering/Melting seemed to be the best AM process to fulfill this goal. According to the conclusions of the literature review (section 1.5), direct AM processes can produce more rapidly ceramic parts compared to indirect AM processes. The direct AM processes which are commonly investigated to produce ceramics are direct SLS and direct SLM. In those processes, the distinction between sintering and melting might not always be very clear. The process developed by the author using preheating to 800°C is rather a mixture of sintering the ceramic powder (i.e. SLS) and fully melting the ceramic powder (i.e. SLM). This process will therefore be designated as direct Selective Laser Sintering/Melting or direct SLS/SLM.

In order to investigate whether alumina parts could be produced through direct SLS/SLM in a conventional laser sintering machine, some preliminary experiments were performed. During these experiments, spray dried agglomerates with a diameter of about 50 μm and consisting of submicrometer α-Al_2O_3 particles (grade SM8, Baikowski, France), were deposited by a conventional powder deposition device and scanned with a laser beam afterwards.
Firstly, an attempt was made to produce alumina parts by using an Yb:YAG fiber laser (laser beam diameter ϕ_{1/e^2} of 53 μm, maximal laser power of 300 W, IPG Photonics, USA) in combination with a monitoring and control system which attempted to adapt the laser power according to the melt pool size. Secondly, a DTM Sinterstation 2000 was used in combination with a CO_2 laser (firestar f100, Synrad Inc., USA) to directly melt alumina powder. By scanning

12 layers of 10x10 mm^2 and a layer thickness of 80 μm with a laser power of 90 W, a scan velocity of 25 mm/s and a scan spacing of 80 μm, the part depicted in figure 7.1a was obtained. A very bad surface finish was clearly visible. Due to the expulsion of molten alumina particles during the SLS/SLM process (in this case mainly SLM), sparks were formed (figure 7.1b). After consolidation, the alumina droplets were visible as spheres on the unpolished part surface (figure 7.1c). Figure 7.1d shows the microstructure of the top-surface of the part after polishing and thermal etching. A crack could be seen which arose due to thermal gradients caused by the laser irradiation process. Cross-sectional images revealed the formation of unwanted large cross layer grains ($>$ 20 μm, figure 7.1e). These grains were assumed to be formed due to a too large amount of molten alumina during the SLS/SLM process.
As described in section 1.4.1, Wilkes [222] also performed experiments to fully melt (pure) alumina powder. The results of these experiments were similar, i.e., microcracks and large grains of about 100 μm were formed.
Based on the preliminary tests of the author, it was concluded that direct SLS/SLM of alumina is only possible when low laser energy densities are applied. In this way, thermal gradients and also large grain sizes which are assumed to originate from the large melt pools can be avoided. Direct SLS/SLM of alumina with low laser energy densities is only possible by applying *a high preheating temperature* to the powder before laser scanning. Preheating the powder to a high temperature reduces thermal gradients, since it reduces the amount of laser energy required during consolidation of the powder particles. *A uniform preheating temperature* is also required to direct SLS/SLM alumina powder. After consolidation, a uniform temperature avoids thermal stresses inside the produced part. A uniform temperature also improves the reliability of the SLS/SLM process, i.e., one laser scanning parameter set will induce the same consolidation behavior if the powder particles are preheated to the same temperature.

After the preliminary experiments, some attempts were made to design an SLS/SLM machine to laser sinter at a high and uniform temperature. In order to reach the high and uniform temperature, electrical heating was preferred over combustion heating. Combustion heating was considered to be too dangerous and dealing with the exhaust gases could make the design too complex. Therefore, the following possibilities to electrically heat the ceramic powder, were considered: resistance heating, induction heating, dielectric heating, infrared heating, arc heating, plasma heating, laser heating and electron beam heating. In order to avoid a complex design, heating by electrical resistance heating elements was preferred.

Some of the preliminary designs, which incorporated electrical resistance

(a) The produced part.

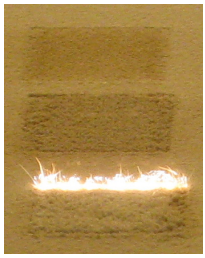

(b) Sparks.

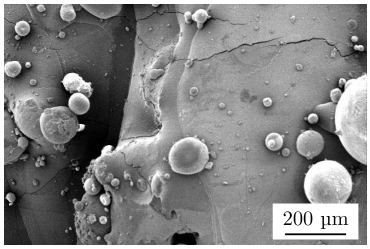

(c) Consolidated sparks.

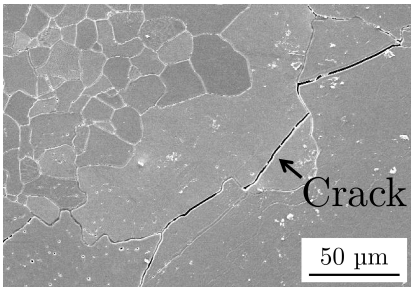

(d) SEM micrograph: top surface.

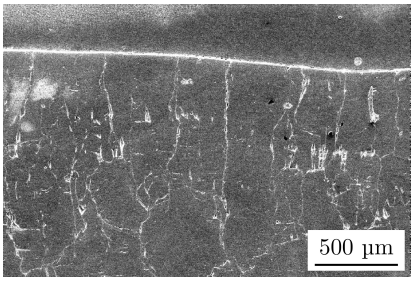

(e) Large cross layer grains.

Figure 7.1: SLS/SLM (in this case mainly SLM) of pure alumina at room temperature.

heating elements, are depicted in figure 7.2. During the design process, two main concerns could be formulated.

1. If the powder would be preheated at a too high temperature, the concomitant energy losses could cause some parts of the machine to overheat. As a result, the machine could be damaged.

2. Due to energy losses, it might not be possible to preheat the powder bed at a uniform temperature.

In a first design (figure 7.2a), the idea was to build a new SLS/SLM device. This machine resembled the Phenix PM-100 machine as the building chamber consisted of refractive materials. In order to avoid radiation losses, the laser window was not above the preheated powder. Instead, a copper (Cu) mirror was used to reflect the incoming laser irradiation.

Since the building of a new SLS/SLM device would require a lot of resources, it was decided to design an experimental setup and incorporate it inside the

DTM Sinterstation 2000. The resulting design is depicted in figure 7.2b. In order to preheat the powder to a uniform temperature, two heating modules were designed. Each heating module heated the powder from respectively the bottom and the top. In order to avoid heating of the DTM Sinterstation 2000 machine, the two heating modules were water cooled. During layer deposition a horizontal cam should move together with the counter current roller. During the deposition of a new powder layer, the horizontal cam should lift, through a follower, the upper heating unit.

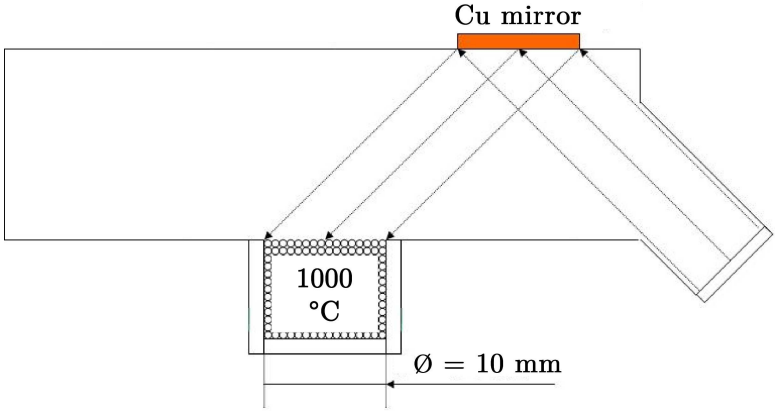

(a) Making a new SLS/SLM device

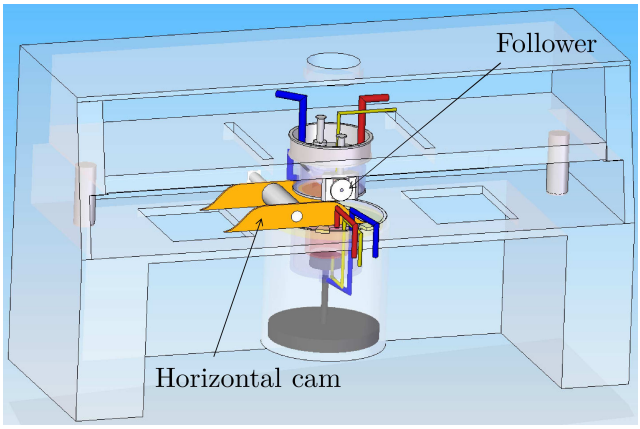

(b) Incorporating a first experimental setup inside the DTM Sinterstation 2000.

Figure 7.2: Preliminary designs of a device to direct SLS/SLM alumina.

Also the second design had a shortcoming. As explained in section 2.4.2, processing fine submicrometer ceramic powder is not straightforward but needed in order to get a good final microstructure with small grain sizes (< 5 μm). In order to deposit submicrometer powder with the conventional powder deposition device of the DTM Sinterstation 2000, the submicrometer particles need to be clustered in agglomerates. However, the density of the agglomerates, deposited with a conventional deposition system, is generally low due to the large inter-agglomerate porosities. In order to eliminate these porosities, a high laser energy density is needed to fully melt the agglomerates. As a result, large grain sizes, which are assumed to originate from the large melt pools, are obtained. Also large thermal stresses are induced when laser melting the agglomerates without applying appropriate preheating. For example, as depicted in the literature review (section 1.4.1), a preheating temperature of 1730°C was required to fully melt alumina-zirconia powder with a size of 50μm [222].

In order to avoid extremely high preheating temperatures and too large melt pools during SLS/SLM, it was decided to use non-agglomerated, submicrometer alumina powder (grade SM8, Baikowski, France) as starting material and to densely pack this powder during layer deposition. If the SM8 powder layers could be densely packed and homogeneously deposited, a homogeneous and large 'driving force for pore closure' (i.e. 'sintering pressure' of about 6.7 to 13.3 MPa according to equation 2.3) would be obtained before the laser sintering step.

Densely packing submicrometer powder is not straightforward. The bulk density (i.e. the density after pouring the powder) and the tap density (i.e. the density after vibrating a certain volume of powder until no volume reduction occurs anymore) of the used SM8 powder are respectively 0.8 g/cm^3 (i.e. about 20%) and 1.1 g/cm^3 (i.e. about 28%) [3]. According to Liu et al. [130] and Olakanmi [160], the density of a powder after deposition with a roller or scraper should be between the bulk density and the tap density. This is much lower than the density of randomly closed packed monomodal spheres, which is about 64% [169].
Two options were considered to increase the density of the powder layers after deposition:

1. Compressing the powder: as illustrated by Souriou et al., the relative density of SM8 powder after compression under a pressure of 450 MPa is about 70% ([189], figure 7.3). A relative density of 60% can be obtained by applying a pressure of about 100 MPa.

2. Use colloidal processing techniques: for example, when using electrophoretic deposition (EPD) as a colloidal processing technique to produce an SM8 powder layer, the density of the resulting layer is about 52-60% [15, 154, 158, 245].

The packing density obtained by colloidal processing techniques such as electrophoretic deposition (EPD) is similar to the packing density obtained through mechanically pressing at about 100 MPa. This assessment explains the trend observed during the literature review of this dissertation, i.e. AM processes which incorporate colloidal processing techniques can produce more easily high quality ceramic parts than AM processes which do not incorporate colloidal processing techniques (section 1.5).
For the final design of the experimental setup, it was decided to use electrophoretic deposition (EPD) as the colloidal processing technique to deposit high density submicrometer SM8 alumina powder layers. In this way, the construction of a mechanical press could be avoided. Furthermore, it was decided to optimize the preheating system. Instead of using two heating modules and the cam-follower system (figure 7.2b), it was decided to preheat the powder inside a vertical furnace tube. In this way, a homogeneous and high temperature could be assured at a certain region of the furnace tube.

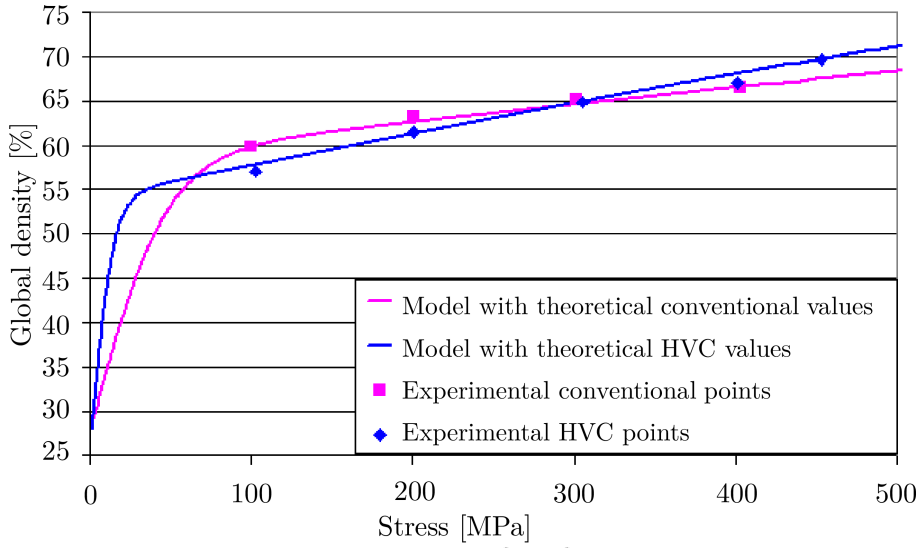

Figure 7.3: Theoretical pressure - density curve and experimental points for SM8 powder compacted by high velocity compaction (HVC) or conventional pressing [189].

The next section details the final designed experimental setup which has been constructed and tested.

In summary:

- A low laser energy density should be applied during direct melting of alumina powder. Only in this way, thermal gradients and large grain sizes which are assumed to originate from large melt pools, can be avoided during and after laser irradiation.
- High laser energy densities can only be avoided by applying a high preheating temperature to the powder before laser scanning. Preheating the powder to a high temperature reduces thermal gradients, since it reduces the amount of laser energy required during consolidation of the powder particles.
- A uniform preheating temperature is required for direct SLS/SLM alumina powder. After consolidation, a uniform temperature avoids thermal stresses inside the produced part. A uniform temperature also improves the reliability of the SLS/SLM process.
- In order to have a homogeneous and large 'driving force for pore closure', densely packed layers of submicrometer powder have to be deposited homogeneously before laser scanning. In this way, extremely high preheating temperatures (e.g. 1730°C) and too large melt pools can be avoided during direct SLS/SLM of ceramics.
- The packing density obtained by colloidal processing techniques, such as electrophoretic deposition (EPD), is similar to the packing density obtained through mechanically pressing at about 100 MPa. This assessment explains the trend observed during the literature review of this dissertation, i.e. AM processes which incorporate colloidal processing techniques can produce more easily high density ceramic parts than AM processes which do not incorporate colloidal processing techniques (section 1.5).

7.3 The experimental setup

The final design of the experimental setup consisted of a novel building platform which was mounted on the (old) building platform of the DTM Sinterstation 2000 and a deposition mechanism (figure 7.4). The new building platform (figure 7.5a) consisted of a vertical tube furnace which was mounted on the (old) building platform. The furnace consisted of a threaded alumina tube of

110 mm length, which could be heated by a resistance wire (diameter = 1 mm; Kanthal A-1, Sandvik Heating Technology, Sweden). Around the threaded tube, insulation and water cooling was provided. In this way, radial energy losses could not damage the Sinterstation 2000. Inside the threaded tube, an alumina inner tube, which had an inner diameter of 32 mm, was placed. The inner tube was a spare part, which protected the threaded tube from the powder environment. The inner tube also fixed the position of the preheated zone. A thermocouple (type K) was used to measure the temperature inside the preheated zone.
Temperature measurements revealed that between 50 and 110 mm from the top of the vertical furnace, a cylindrical zone with an inner diameter of 32 mm could be homogeneously heated within a margin of ± 50°C up to a temperature of 800°C. Possibly, the margin of ± 50°C could be improved by optimizing the temperature controller (T162, Red Lion Control, US). If temperatures above 800°C were applied, the following failures started to occur: breaking of the resistance heating wire, cracking of the treaded alumina tube and cracking of the alumina inner tube.
Six springs (Lesjöfors, The Netherlands), each with a stiffness of 10 N/mm, three linear ball bearings (LVCD16-2LS, SKF, Sweden) and three accompanying shafts provided vertical flexibility and prohibited horizontal flexibility between the furnace and the (old) building platform. An optical sensor (OPB916 Series, Optek, US) was used as a contact sensor, as a needle blocked its light pad if the furnace was pushed downwards.

The electrophoretic powder deposition mechanism (figure 7.5b) consisted of a 'frame' which was comprised of two triangular metal plates. The frame was attached to the DTM Sinterstation 2000 by three clamping magnets. Between the two plates of the frame, a gearbox was mounted. On this gearbox, which was driven by a DC motor, a holder for the deposition electrode (i.e. electrode holder) could be attached. The electrode holder could be axially positioned by its conical shape (see also figure 7.6a) and fixed by a screw nut. On the electrode holder, the deposition electrode could be mounted. The deposition electrode was used to extract submicrometer powder from an alumina containing suspension and to deposit this powder into the furnace of the new building platform.

More specifically, the layer deposition process consists of two steps. In a first step, a powder layer is deposited on the deposition electrode through the EPD process in a so called EPD cell (figure 7.6a). The EPD cell consists of a positively charged alumina suspension. At the bottom of the cell a counter electrode is mounted and at the top of the cell, the deposition tool (i.e. electrode holder and deposition electrode). During the EPD process, a DC

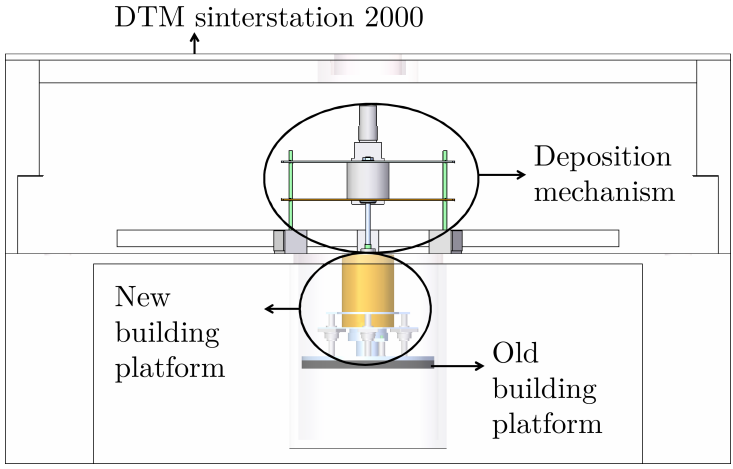

(a) schematic

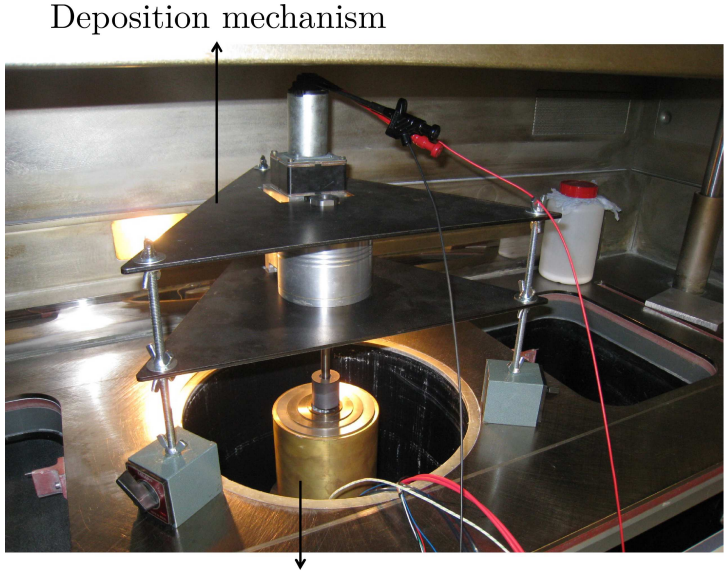

(b) as built

Figure 7.4: Overview of the experimental setup.

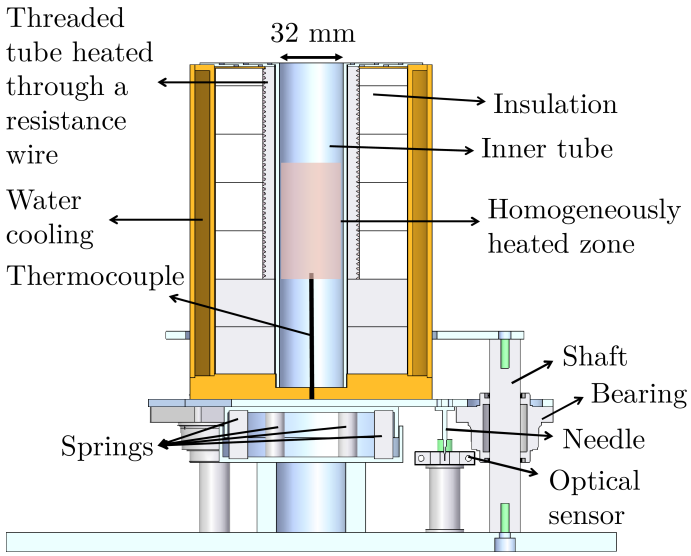

(a) New building platform

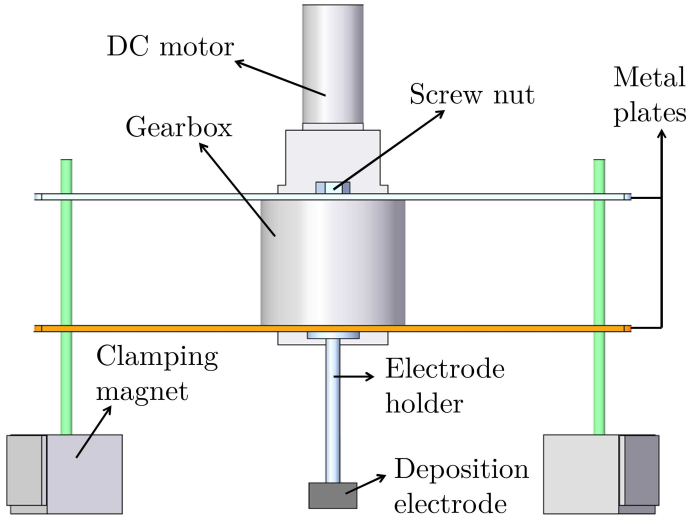

(b) Deposition mechanism

Figure 7.5: Two modules of the experimental setup.

source negatively charges the deposition electrode and positively charges the counter electrode. As a result, submicrometer alumina particles move from the suspension to the deposition electrode. In this way, a densely packed powder layer is formed on the deposition electrode.
In a second step, the electrode holder is mounted into the gearbox to deposit the new powder layer in the new building platform (figure 7.6b). For deposition inside the furnace, the old building platform moves upwards until contact between the electrode and the powder bed is detected by the contact sensor. To get a full contact between the powder bed and the deposition electrode, a force of 40±10 N is applied between the electrode and the powder bed. Afterwards, the deposition tool is rotated by the DC motor. Friction causes the powder layer to slide off the deposition electrode, into the new building platform.
In order to have a free path for the laser beam, the deposition tool is then taken out of the gearbox after layer deposition. After moving the new powder layer into the focus of the laser beam, the new layer is scanned.

In summary:

- An experimental setup to direct SLS/SLM uniformly preheated high density submicrometer alumina powder layers has been designed and constructed. The experimental setup consists of a vertical tube furnace, which is mounted on the building platform of a DTM Sinterstation 2000. In this furnace, a cylindrical zone with an inner diameter of 32 mm and a height of about 60 mm can be homogeneously heated within a margin of ± 50°C up to 800°C. The experimental setup also consists of a deposition mechanism, which can deposit high density (52-60%, section 7.2) powder layers through electrophoretic deposition (EPD).

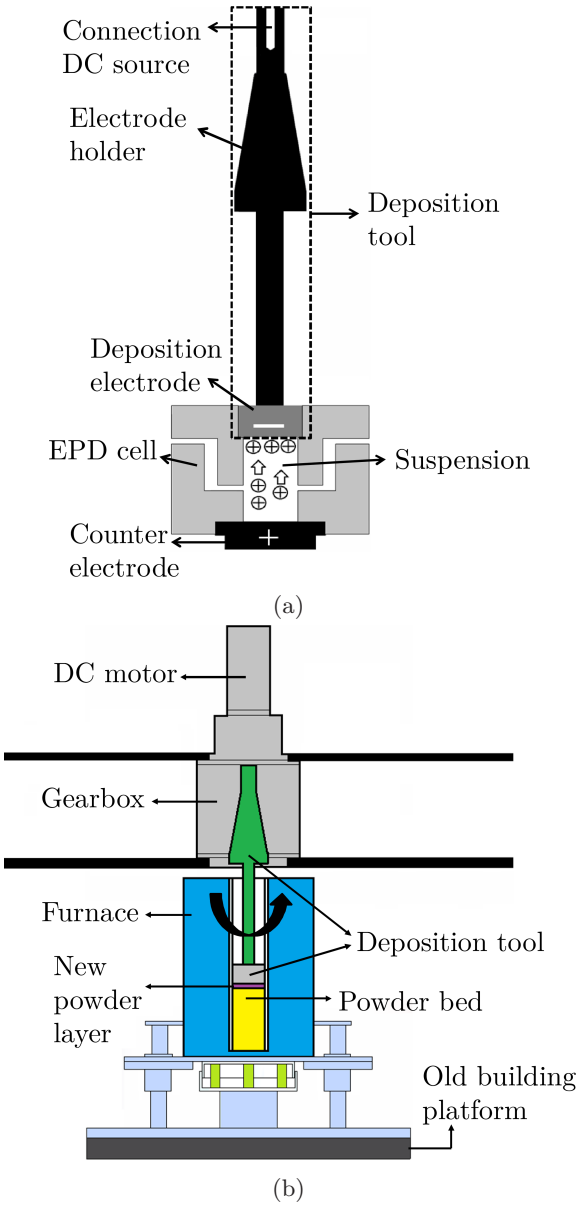

Figure 7.6: Layer deposition steps: electrophoretical deposition (EPD) on the deposition electrode (a); deposition of a fresh powder layer on the powder bed (b).

7.4 The powder metallurgical process

In figure 7.7, the powder metallurgy (PM) process is depicted which was used to test the experimental setup. The PM process consists of 3 subprocesses: powder deposition, laser irradiation and solid state sintering in a furnace. Non-agglomerated submicrometer alumina powder (grade SM8, Baikowski, France), produced through a modified Bayer loop process, was used as starting powder (see figure 3.2a). The experimental setup was used to directly SLS/SLM this powder by applying a low laser energy density to avoid the occurrence of large grains and thermal stresses. Since no binder material was used during SLS/SLM, no time consuming debinding step was needed. However, to be sure that all powder particles were sintered (if not melted) at the end of the PM process, the SLS/SLMed samples were solid state sintered (SSS) in a furnace (Nabertherm, Germany). The samples were furnace sintered at 1600°C for 2 hours in air at a heating rate of 5°C/min.

The SLS/SLMed samples were assessed visually (see camera images). The SSS samples, obtained after the furnace sintering step, were assessed through density measurements, stereo microscopy and scanning electron microscopy (SEM, XL30 FEG, FEI, The Netherlands). The density was measured by the Archimedes method (Analytical Balances, Sartorius, Germany): the weight of the samples was measured in air, in Disinfectol (denatured ethanol with up to 5 vol% ether, Chem-Lab, Belgium) and again in air. In order to calculate relative densities, a theoretical density of 3.984 g/cm^3 was used for alumina. After the density measurements, the samples were embedded in epoxy and polished in a surface perpendicular to the scan tracks. Next, digital images were taken using a stereo microscope (SteREO Discovery.V20, Zeiss, Germany). The epoxy was dissolved in acetone (Chem-Lab, Belgium). To reveal the grain boundaries after polishing, the samples were thermally etched in air at 1350°C for 30 minutes

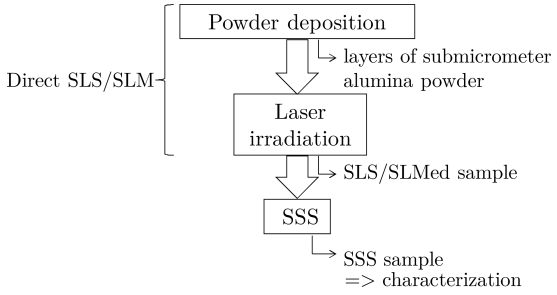

Figure 7.7: Powder metallurgy processing flow chart.

at a heating rate of 20°C/min in a furnace (Nabertherm, Germany). For the subsequent morphology investigation with a scanning electron microscope (SEM, XL30-FEG, FEI, The Netherlands), the samples were coated with gold-palladium using a sputtering device (Balzers, Switzerland).

In the following sections, first the performed SLS/SLM experiments will be detailed. Secondly, some characteristics (density and morphology) of the SLS/SLMed parts after solid state sintering in a furnace (SSS parts), will be assessed.

7.4.1 Difference with PM processes described in previous chapters

In summary, the PM process described in this chapter differs from the ones described in chapter 3, 4, 5 and 6 in two ways:

1. No polymer binder material is used.
2. Besides solid state sintering in a furnace, no extra PM process steps were applied after SLS/SLM.

7.5 Selective laser sintering/melting

The investigated selective laser sintering/melting process can be divided into two sub-processes: layer deposition and laser scanning.

7.5.1 Layer deposition

As described in section 7.3, the deposition of the layers was performed through electrophoretic deposition (EPD). For the EPD-process, a slurry was used with 95 vol% Disinfectol, 5 vol% high purity α-Al_2O_3 powder (SM8 grade, Baikowski, France) with d_{50} of 0.3 μm, and 1.5 mM HNO_3 (Chem-Lab, Belgium). The nitric acid provided positive charging of the Al_2O_3 surface, resulting in electrostatic repulsion of the charged particles and a stable suspension. The slurry was ball mixed on a Turbula mixer (TypeT2A, WAB, Basel, Switzerland) at 70 rpm for 12 hours. The density of a powder layer after EPD using this slurry was approximately 57% [15].

Equation 7.1 is an approximation to determine the mass m deposited on the

electrode during EPD (figure 7.6a). In this approximation, which is valid for short deposition times, all variables were assumed to be constant during EPD [61]. Suspension concentration C_s and electrophoretic mobility μ_e were properties of the slurry and remained unchanged. The size of the deposition surface S and distance between the two electrodes d also remained constant at respectively 6.61 cm^2 and 4.3 cm. The EPD-voltage U and deposition time t were varied until a full deposition of each layer was guaranteed. If a too thin layer was deposited during the EPD step, the powder layer did not slide off the deposition electrode during deposition inside the new building platform. If a too thick layer was deposited during the EPD step, the powder layer slid off the deposition electrode before deposition inside the new building platform.

$$m = \frac{C_s.\mu.S.U.t}{d} \tag{7.1}$$

An EPD-voltage of 150 V and deposition time of 40 s were eventually found to be reliable parameters to allow a good deposition of each layer.
For the material of the deposition electrode, both MAX phase[1] and graphite were tested. A MAX phase (MAXTHAL® 211 powder based) consisting of Ti_2AlC and Ti_3AlC_2 was tested because of its electric conductivity, good machinability, thermal shock resistance, wear resistance and a low dry friction coefficient with Al_2O_3 [69, 88, 89, 168]. In practice, its wear resistance was insufficient. Further, the powder bed was sometimes contaminated with MAX phase powder when depositing a new layer. Graphite was eventually used because of the even lower friction coefficient. Graphite also contaminated the powder bed during deposition, but was easily burned away during selective laser sintering/melting.

7.5.2 Laser scanning

Samples were fabricated using a DTM Sinterstation 2000 machine, equipped with a 100 W CO_2-laser (f100, Synrad, USA) with a wavelength of 10.6 μm and a laser beam diameter ϕ_{1/e^2} of 400 μm. Parametric tests were performed using a 2x2 matrix of 4x4 mm^2 squares. Laser power, scan speed, scan spacing, scan strategy and preheating temperature were varied until a sample was produced. The optimized parameter set was subsequently used to produce a 10x10 mm^2 sample.

To allow time for neck formation during SLS/SLM, the scan speed v was

[1] MAX phases are layered, hexagonal carbides and nitrides. They have the general formula: $M_{n+1}AX_n$ where n = 1 to 3, M is an early transition metal, A is an A-group (mostly IIIA and IVA, or groups 13 and 14) element and X is either carbon and/or nitrogen.

initially kept as low as possible (5.2 mm/s). The preheating temperature was kept at the maximum temperature of 800±50°C in an attempt to prevent cracks due to thermal stresses. Higher temperatures were not possible in the current setup. The first test was performed with a scan spacing s of 40 μm and a laser power P of 5 W. Due to the occurrence of unwanted balling[2] of the molten powder (figure 7.8), the laser energy density e (=P/s.v.l, see section 3.3.2) was subsequently lowered, by lowering the laser power P and increasing the scan spacing, until a complete sample was produced. The layer thickness l was assumed to be constant and was approximately 50-200 μm.
Figure 7.9 shows the result of the parametrical test that first produced a complete sample of sufficient strength for further research. During this first parametrical test, four samples were scanned as a 4x4 mm^2 square, with a thickness of 5 layers, using a MAX phase electrode for layer deposition. The sample depicted in figure 7.9b, sample 1, and produced with parameters summarized in table 7.1, had sufficient strength for further investigation.
Another sample, sample 2, with a scan surface of 10x10 mm^2 and a thickness of 15 layers, was produced with the optimized laser scanning parameters. This time, the graphite electrode was used for layer deposition. Figure 7.10 shows the result. Despite not remaining intact after SLS/SLM, this sample also had sufficient strength for further research.

[2]Long thin melt pools are known to break up into balls, called 'balling' and commonly described as due to Rayleigh instabilities [119].

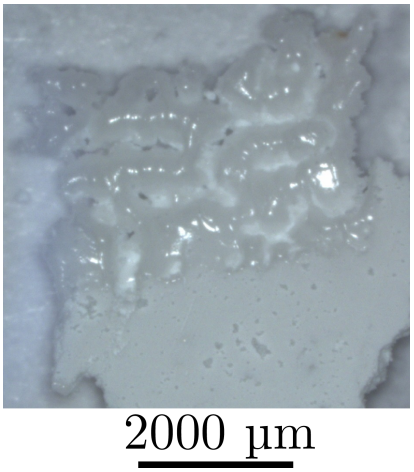

Figure 7.8: Melting and balling of the powder due to the use of an excessive laser energy density during laser sintering/melting.

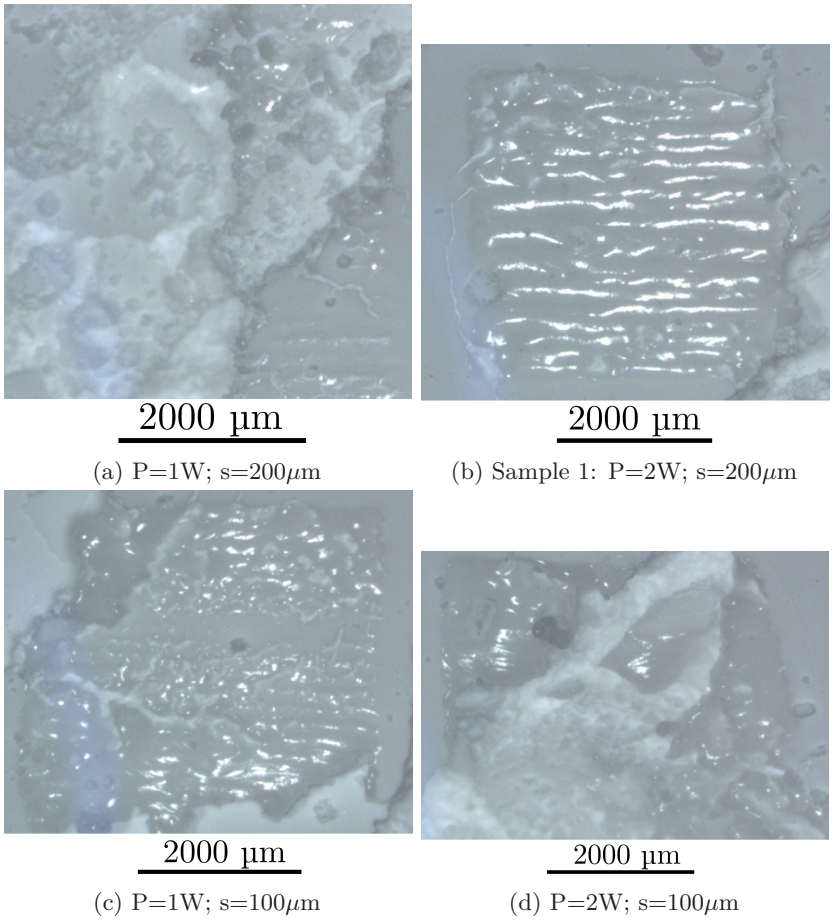

(a) P=1W; s=200μm (b) Sample 1: P=2W; s=200μm

(c) P=1W; s=100μm (d) P=2W; s=100μm

Figure 7.9: Results of the parametrical test that first produced a complete sample of sufficient strength for further research: i.e. sample 1 (b).

P	**s**	**v**	**T**
2 W	200 μm	5.2 mm/s	800°C

Table 7.1: Optimized laser scanning parameters.

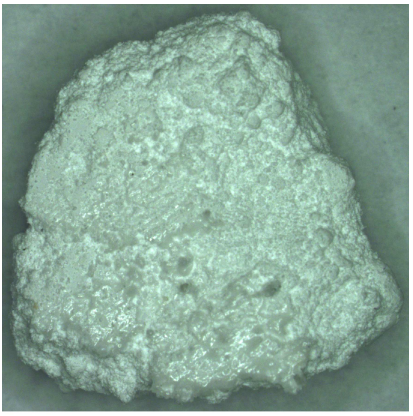

Figure 7.10: Second sample of sufficient strength (i.e. sample 2), produced with the parameter set in table 7.1.

In an attempt to improve the laser scanning process, the following variations on the parameter set in table 7.1 were investigated:

- Lower preheating temperatures (600 & 700°C)
- Lower laser power (1.5 W)
- Higher laser power (2.5 W) and larger scan spacing (250 μm)
- Lower laser power (1.8 W) and smaller scan spacing (150 μm)
- Higher laser power (4 W) and higher scan speed (7.35 mm/s)
- Scanning each scan vector multiple times at different scan speeds (2-100 times, at 5.2-520 mm/s)

None of these variations produced a sample of sufficient strength for further research. However, the removal of samples from the powder bed in the building platform was rather difficult, possibly breaking promising (but delicate) samples.

In summary:

- The *optimized parameters for layer deposition* through the presented EPD setup consisting of a deposition surface of 6.61 cm^2, a distance between

the two electrodes of 4.3 cm, and containing a 5 vol% α-Al_2O_3 (SM8 grade, Baikowski, France) suspension, stabilized with 1.5 mM HNO_3, are: an EPD voltage of 150 V and an EPD time of 40 seconds.

- The *optimized laser scanning parameters* to direct SLS/SLM the deposited powder layers at 800°C with a CO_2 laser, having a ϕ_{1/e^2} spot size of 400 μm, are: a laser powder of 2 W, a scan spacing of 200 μm and a scan velocity of 5.2 mm/s.
- The optimized parameters for layer deposition and direct SLS/SLM seem to be independent of the (electrically conductive and heat resistant) materials used for the deposition electrode: i.e. a MAX phase consisting of Ti_2AlC or Ti_3AlC_2, and graphite. However, graphite seems to be the preferred material since it does not contaminate the powder bed after laser scanning and has a lower friction coefficient.

7.6 Characterization of the solid state sintered parts

7.6.1 Density

After furnace sintering, the density of sample 1 and sample 2 was measured. The measurement of sample 1 was discarded. This sample was too small and had insufficient mass for a reliable measurement. Sample 2 had a relative density of 85%.

7.6.2 Stereomicroscopy

Samples 1 and 2 were investigated under a stereo microscope. Sample 1 (figure 7.11a) showed upward curling, towards the laser beam. This was most likely due to thermal gradients during SLS/SLM. Sample 2 (figure 7.11b) showed downward curling. It is unsure why this sample seemed to curl downwards. It is possible that upward curled pieces of sample 2 had broken off during removal from the powder bed after SLS/SLM.

7.6.3 Scanning electron microscopy

Figures 7.12 and 7.13 are SE-SEM images of respectively sample 1 and sample 2. Figures 7.12a and 7.13a, which depict the unpolished scan surfaces of these

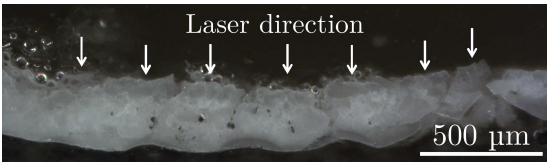

(a) Sample 1

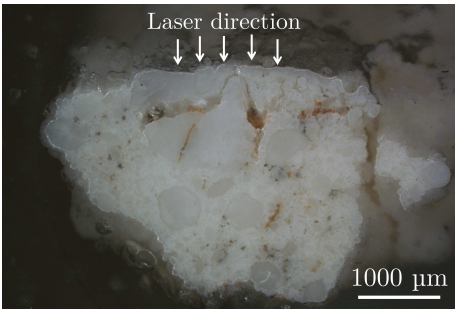

(b) Sample 2

Figure 7.11: Stereo microscope images of two produced samples after polishing.

samples, show a fully solidified scan surface. The size and shape of the grains shown in these figures should be carefully interpreted: the grains were distorted since the surface was, due to its irregular shape, not perpendicular to the electron beam during SEM.

Figure 7.13b shows a molten alumina droplet on the surface of sample 2. This proves that liquid phases were formed during the direct SLS/SLM process. At the edge of the surface of sample 1 (figure 7.12b), the laser beam evaporated alumina material. It seemed that, at the start (or end) of a scan track, the laser was not powered down when the scan mirrors did not move anymore. As a result, the start (or end) of each scan track received an elevated energy input, compared to the middle of a scan track and evaporation occurred. When having a closer look at the evaporated zone, a rough surface could be observed (figure 7.12c). Furthermore, the edges of the laser scan tracks were defined by an upwards ridge (figure 7.12b and 7.13a).

Not the entire scan surface seemed to be liquefied during SLS/SLM. This might be due to instability of the laser beam at low laser powers. Figure 7.13c shows a solidified liquid phase on the left and an almost powder-like structure to the right. The presence of a solidified liquid phase seems unlikely in the powder-like zones, which were probably densified purely by solid state sintering (SSS) in a furnace.

Figure 7.13c also illustrates that sample 2 contained surface cracks, which

seemed to stop where the solidified surface stopped. As depicted in figure 7.12d, sample 1 also contained surface cracks. These cracks could be caused by any of the following reasons, or a combination thereof:

1. Thermal stresses due to excessive thermal gradients during SLS/SLM is probably the main cause for the surface cracks. This is in correspondence to the curling of sample 1, shown in figure 7.11a.
2. Shrinkage of the powder due to densification during SLS/SLM.
3. Cracking of the EPD layers during sliding from the deposition electrode.

Figures 7.12e and 7.13d give an overview of the cross-sections of respectively sample 1 and sample 2, perpendicular to the scan tracks. Figure 7.12e is a cross-section at the edge of sample 1 and figure 7.13d is a cross-section at the middle of sample 2. The bulk microstructure of the samples (figures 7.12f and 7.13e) contained several dense zones which consisted of consolidated alumina. Pores were visible between the dense zones. Probably, the dense EPD layers broke during sliding from the deposition electrode, creating the pores. These pores remained after laser irradiation. During laser irradiation, some alumina powder melted, but not enough to fully eliminate all the pores.

More detailed SE-SEM images of the cross-sections of the samples, revealed that despite the laser melting and solidification process, fine alumina grain sizes could be obtained. Moreover, the grain size of the samples seemed to be dependent on the laser energy density used during scanning. Just below the scan surface, sample 1 seemed to have slightly larger grains (i.e. slightly bigger than 5 μm, figure 7.12g) than sample 2 (i.e. grain size close to or smaller than 5 μm, figure 7.13f). As sample 1 was cross-sectioned near the edge (i.e. the place where the scan mirrors did not move for some time during laser irradiation: figures 7.12b and 7.12c), the consolidated alumina of figure 7.12g received more laser energy than the consolidated alumina of figure 7.13f, which was taken just below the scan surface at the middle of sample 2 (i.e. at the middle of the scan tracks). The submicrometer alumina powder at the bottom of sample 1 (figure 7.12h) and further down the scan surface (i.e. bulk) at the middle of sample 2 (figure 7.13g) also received a lower amount of laser energy density. As a result, the consolidated alumina also had a grain size close to or smaller than 5 μm.
The finding that the grain size increased if the laser energy density increased, proved the assumption that large grains of ceramic parts, produced through direct SLS/SLM, originate from large melt pools.

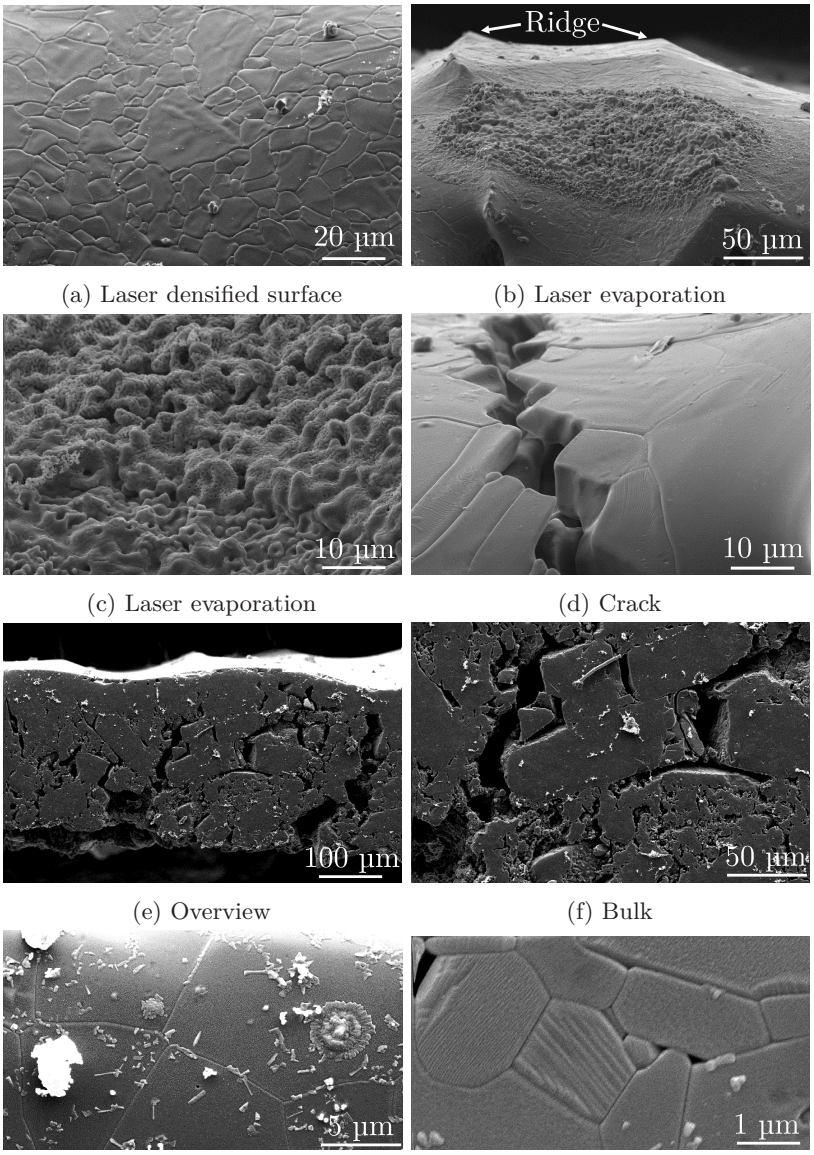

(a) Laser densified surface

(b) Laser evaporation

(c) Laser evaporation

(d) Crack

(e) Overview

(f) Bulk

(g) Top (i.e. just below the scan surface)

(h) Bottom (i.e. far below the scan surface)

Figure 7.12: Sample 1: SE-SEM images of a non-polished scan surface (a,b,c,d); SE-SEM images of a polished cross-section, taken at the edge of the sample (i.e. start or end of scan track) and perpendicular to the scan tracks (e,f,g,h).

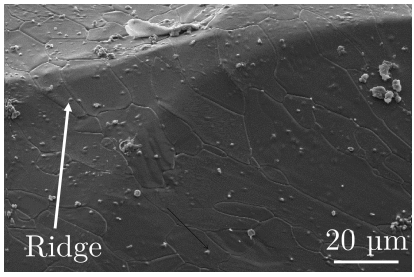

(a) Laser densified surface

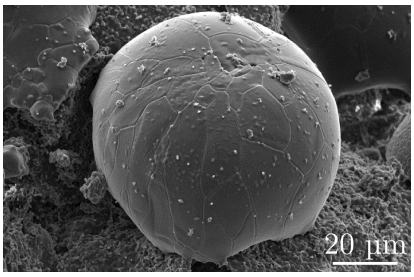

(b) Molten droplet

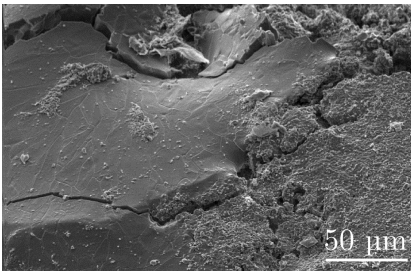

(c) Crack

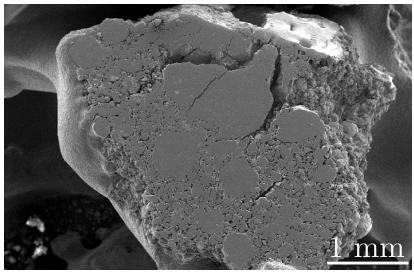

(d) Overview

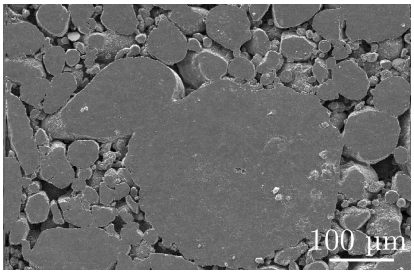

(e) Bulk

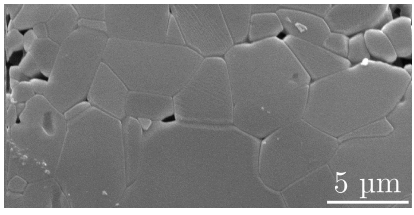

(f) Top (i.e. just below the scan surface)

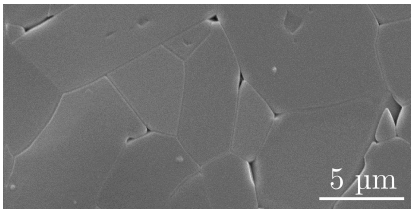

(g) Bulk (i.e. further down the scan surface)

Figure 7.13: Sample 2: SE-SEM images of a non-polished scan surface (a,b,c); SE-SEM images of a polished cross-section, taken at the middle of the sample (i.e. middle of scan tracks) and perpendicular to the scan tracks (d,e,f,g).

In summary:

1. The experimental setup can produce alumina samples with a density up to 85% through direct SLS/SLM. The microstructure of these samples consists of dense zones, which consist of consolidated molten alumina, and pores. Probably, the pores originate during breaking of the dense EPD layers during sliding from the deposition electrode.

2. Thermal stresses, which occur during the laser scanning, curl the samples towards the laser beam. These stresses might also result in cracking of the solidified scan surface. Cracking of the scan surface might also be caused by shrinkage of the powder due to densification during SLS/SLM or cracking of the EPD layers during sliding from the deposition electrode.

3. Despite the formation of a liquid phase during direct SLS/SLM of high density powder layers at 800°C, an alumina microstructure with a grain size close to or smaller than 5 μm can be formed. If the laser energy density input increases, the resulting size of the grains also increases. This proves the assumption that large grains of ceramic parts, produced through direct SLS/SLM, originate from large melt pools. If too high laser energy densities are applied, evaporation of the alumina occurs.

7.7 Conclusions

Direct melting of alumina and acquiring small grains upon solidification is only possible by applying low laser energy densities. In this way thermal gradients and also large grains which originate from large melt pools, can be avoided during laser irradiation. High laser energy densities can only be avoided by applying a high preheating temperature to the powder bed before laser scanning. Preheating the powder to a high temperature reduces thermal gradients, since it reduces the amount of laser energy required during consolidation of the powder particles. A uniform preheating temperature is required to direct SLS/SLM alumina powder. After consolidation, a uniform temperature avoids thermal stresses inside the produced part. A uniform temperature also improves the reliability of the SLS/SLM process.
In order to have a homogeneous and large 'driving force for pore closure', densely packed layers of submicrometer powder have to be deposited homogeneously before laser scanning. In this way, extremely high preheating temperatures (e.g. 1730°C) and too large melt pools can be avoided during direct SLS/SLM of ceramics. In order to deposit homogeneous and dense layers of submicrometer powder, colloidal processing techniques are favored: for example, the packing density obtained by colloidal processing techniques such as electrophoretic deposition (EPD) is similar to the packing density obtained through mechanically pressing at about 100 MPa.

An experimental setup to direct SLS/SLM uniformly preheated, high density submicrometer alumina powder layers by applying low laser energy densities, was designed and constructed. The experimental setup consisted of a vertical tube furnace, which was mounted on the building platform of a DTM Sinterstation 2000. In this furnace, a cylindrical zone with an inner diameter of 32 mm and a height of about 60 mm could be heated up to 800°C within a margin of ± 50°C. The experimental setup also consisted of a deposition mechanism which could deposit high density (52-60%) powder layers through electrophoretic deposition (EPD).

The optimized parameters for layer deposition through the EPD-process, consisting of a deposition surface of 6.61 cm^2 with an electrode distance of 4.3 cm, and containing a 5 vol% α-Al_2O_3 (SM8 grade, Baikowski, France) ethanol-based suspension electrostatically stabilized with 1.5 mM HNO_3, were: an EPD voltage of 150 V and an EPD time of 40 seconds. The optimized laser scanning parameters to direct SLS/SLM the deposited powder layers at 800°C with a CO_2 laser, having a ϕ_{1/e^2} spot size of 400 μm, were: a laser powder of 2 W, a scan spacing of 200 μm and a scan velocity of 5.2 mm/s.
The optimized parameters for layer deposition and direct SLS/SLM seemed

to be independent of the electrically conductive and heat resistant materials used for the deposition electrode: i.e. a MAX phase consisting of Ti_2AlC and Ti_3AlC_2 or graphite. Graphite seemed to be the preferred material for the deposition electrode since it did not contaminate the powder bed after laser scanning and had a lower friction coefficient.

The experimental setup could produce alumina layers with a density up to 85%. The microstructure of these samples consisted of dense zones, which consisted of consolidated molten alumina, and pores. Probably, the pores originated during breaking of the dense EPD layers during sliding from the deposition electrode.
Thermal stresses, which occurred during the laser scanning, curled the samples towards the laser beam. These stresses might also result in cracking of the solidified scan surface. Cracking of the scan surface might also be caused by shrinkage of the powder due to densification during SLS/SLM or cracking of the EPD layers during sliding from the deposition electrode.
Despite the formation of a liquid phase during direct SLS/SLM of high density powder layers at 800°C, an alumina microstructure with a grain size close to or smaller than 5 μm could be formed. When the laser energy density input increased, the resulting size of the grains also increased. This proved the assumption that large grains of ceramic parts produced through direct SLS/SLM, originate from large melt pools. Also, if too high laser energy densities were applied, evaporation of the alumina occurred.

Chapter 8

Conclusions

> If we knew what we were doing,
> it wouldn't be called research.
>
> Einstein, Albert

This chapter compares the different PM routes investigated throughout the previous chapters for the production of ceramic components by SLS/SLM. From this comparison a number of conclusions and achievements are synthesized, and hints are given for possible extensions of this research. The conclusions and achievements for indirect SLS and direct SLS/SLM are discussed separately in sections 8.2 and 8.3.

8.1 Introduction

Ceramics are currently not as widely used in industry as they should and could be. The main reason for the reluctance within industry is the high, both fixed and variable, production costs of ceramic parts. It was understood that, since additive manufacturing (AM) has the ability to produce near-net-shape ceramic functional prototypes, it has the ability to drastically reduce the fixed costs associated with the engineering of a ceramic part for a certain application. Moreover, as for all AM technologies, AM of ceramics has also the potential to shape freeform geometries, which can not be produced by any other conventional production method.
In this dissertation, AM was used as primary shaping step of a powder

metallurgical (PM) process to produce ceramic parts. In this way, a PM process consisting of the following main steps was investigated: powder production, AM, debinding and furnace sintering. Furthermore, in order to produce ceramic parts with increased density, the following post-AM densification techniques were investigated as additional steps of the PM process: remelting, isostatic pressing and infiltration.
Two different types of AM processes exist to shape ceramics: indirect and direct AM processes. The advantage of the indirect AM processes, which make use of a polymer binder material, is the ability to produce different types of ceramic materials. However, the indirect processes require a time consuming binder removal step. Therefore, indirect AM processes can not produce ceramic parts rapidly. On the contrary, the direct AM processes, which do not use a binder material, do not require a time consuming binder removal step. Therefore, direct AM processes can produce ceramic parts more rapidly compared to indirect AM processes. However, the direct AM processes are currently not able to produce as many different types of ceramics as the indirect AM processes.
The AM processes which currently are most widely investigated to produce ceramics, are laser based processes. In order to meet both the self-defined short term research goal (i.e. produce ceramics and join the international debate) and long term research goal (i.e. the fast production high quality ceramics), respectively indirect SLS and direct SLS/SLM were chosen in this dissertation as the AM processes to study. Since alumina is the most commonly used ceramic for technical applications, α-alumina was chosen as primary ceramic material.

8.2 Indirect SLS

Indirect SLS was the main AM process assessed in this dissertation to shape ceramics. A DTM Sinterstation 2000, the (only) SLS machine available at KU Leuven at the beginning of this dissertation, was refurbished with a new CO_2 laser for this purpose. As the DTM Sinterstation 2000 machine was equipped with a counter current roller for the deposition of dry powders, different powders had to be developed. In this section, these different powders will first be compared by comparing the main steps of the PM process: powder production, indirect SLS, debinding and SSS (table 8.1). Secondly, the post-AM densification techniques, which were investigated as extra steps of the PM process in order to produce ceramic parts with increased density, will be discussed.

synthesis method		ball milling	disp. polym.	$TIPS_1$	$TIPS_1$	$TIPS_2$
ceramic		Al_2O_3	Al_2O_3	Al_2O_3	Al_2O_3	Al_2O_3
binder		PA 22wt%	PS 39wt%	PA 60vol%	PP 60vol%	carn.+LDPE 22wt%
SLS	deposition	bad	good	excellent	excellent	excellent
	balling	no	no	no	no	yes
	curling	no	no	no	no	yes
	$e^{max}_{\rho_{SLS}}$ $[J/mm^3]$	0.97	0.76	0.37	0.77	0.38
	e^* $[J/mm^3]$	1.94	0.76	0.37	0.12	0.38
	$\rho^{e=e*}_{SLS}$	37%	66%	55%	51%	66%
deb.&SSS	$\Delta^{e=e*}_{x-y}$	NM	-31%	-21%	-20%	-21%
	$\Delta^{e=e*}_{z}$	NM	-44%	-24%	-21%	-26%
	$\text{cracks}_{deb+SSS}$	NM	yes	no	no	no
	$\rho^{e=e*}_{SSS}$	NM	66%	47%	39%	77%

Table 8.1: Comparison of the composite powders assessed in this dissertation, when applying them to the standard PM process without post-densification treatment, i.e. powder synthesis, Selective Laser Sintering, debinding and solid state sintering in a furnace. (NM = not measured)
$e^{max}_{\rho_{SLS}}$ = the laser energy density which led to the maximum green density
e^* = optimized laser energy density
$\rho^{e=e*}_{SLS}$ = relative density after SLS, for parts produced with optimized laser energy density
$\Delta^{e=e*}_{x-y}$ = % linear shrinkage during debinding and SSS in the scan x and cross-scan y directions, for parts SLSed with an optimized laser energy density
$\Delta^{e=e*}_{z}$ = % linear shrinkage during debinding and SSS in the z direction, for parts SLSed with an optimized laser energy density
$\text{cracks}_{deb+SSS}$ = cracking during debinding and solid state sintering: yes/no
$\rho^{e=e*}_{SSS}$ = relative density after SSS, for parts produced with optimized laser energy density

8.2.1 Comparison of the different composite powders

8.2.1.1 Powder production

Five different alumina containing composite powders were synthesized by four powder production methods: ball milling, dispersion polymerization (disp. polym.) - cake formation - ball milling, thermally induced phase separation ($TIPS_1$) and thermally induced phase separation - cake formation - ball milling ($TIPS_2$, see appendix A). The five composite powders had different binder materials and a different amount of binder: polyamide (PA, 53vol% and 60vol%), polystyrene (PS, 71vol%), polypropylene (PP, 60vol%) and a carnauba_wax-low_density_polyethylene combination (carn.+LDPE, 54vol%, see appendix A). PA and PP were chosen as binder material since they have an 'SLS window' due to their semi-crystalline behavior (PP has an SLS window at a lower temperature compared to PA). This SLS window improved the sinterability (i.e. the easiness to find appropriate SLS parameters) of the composite powders. Further, PS was chosen due to its geometrical stability during the debinding step, and the carnauba wax containing binder for its low melt viscosity. The amount of binder was always a lower bound: if a lower amount of binder was chosen, the strength of the parts after SLS was less.

8.2.1.2 Selective laser sintering

As craters were formed on the powder bed, the ball milled Al_2O_3-PA powder (chapter 3) behaved differently compared to the other powders during layer deposition by the counter current roller of the DTM Sinterstation 2000. Probably, the craters were formed due to the irregular shape of the composite powder agglomerates. As a result, the parts after SLS had a low green density (up to 37%) and no complex shapes could be produced. Since the other composite powder agglomerates had a more spherical shape, no problems occurred during deposition by the counter current roller.

Compared to the other powders, the Al_2O_3-carnauba_wax-LDPE powder behaved differently during laser irradiation. Firstly, the melt pools tended to break up into balls. This phenomenon, which is called 'balling', is commonly described as due to Rayleigh instabilities [119]. Probably, the low viscosity of the carnauba wax during irradiation caused the melt pools to break. The occurrence of balling could be avoided by producing the Al_2O_3-carnauba_wax-LDPE parts on a (cardboard) base plate.
During laser irradiation, the Al_2O_3-carnauba_wax-LDPE material also tended to curl, causing thermal cracks in the parts after SLS. The curling of the parts

during the SLS process might be related to the overlap between the melting onset temperature of carnauba wax and the recrystallization temperature of LDPE. As a result, no laser window could be defined for this binder system. According to the Quasi Isothermal Theory (Drummer D. et al., 2010 [65]), it was not possible to preheat this binder system up to a temperature where it stayed in a molten, stress-free state after laser irradiation, until all layers of the part were produced.
Due to the curling of the parts, the counter current roller hit the parts during layer deposition and tended to drag them along. This was however also prevented by the base plate, which anchored the parts during SLS.

The laser energy density e[1], which is defined by the laser energy per unit time which irradiates the powder particles (as an input parameter; P) divided by the material consolidation rate (as output parameter; MCR), is most important to describe the laser irradiation process during SLS. It combines the most important scanning parameters: laser power P, scan spacing s[2], scan speed v and layer thickness l (MCR = s.v.l).
When using too low laser energy densities during SLS of the powder agglomerates, insufficient powder material was consolidated and the resulting parts were too fragile. When using higher laser energy densities, the binder material was heated more, causing a decrease of the binder viscosity. If the viscosity was too low, the binder material flowed into the underlying powder and towards the sides of the parts. As a result, a dross was formed at the part contours. When too high laser energy densities were applied, the binder material started to degrade. The gases formed during binder degradation, sometimes led to the formation of extra pores in the green parts. Both binder degradation and pore formation also resulted in too fragile parts. The green density and concomitant strength of the SLSed parts was a compromise between the material degradation, pore formation and plastic flowing of the binder material to bind the alumina particles.
For the five investigated alumina containing composite powders, the laser energy density which led to the maximum green density ($e^{max}_{\rho_{SLS}}$, table 8.1) varied from 0.37 J/mm^3, for the Al_2O_3-PA powder produced through TIPS,

[1]In AM literature, the laser energy density e [J/mm^3] is widely used to optimize the density (as a macroscopic parameter) of parts after SLS and SLM. This is in contrast with the laser processing literature, where the fluence F [J/m^2] (i.e. the laser energy irradiating the powder surface) is widely used to optimize the laser parameters. Although not done in this dissertation, the fluence could be a very useful laser parameter in future research on optimizing the microstructures (e.g. by improving the connection between the different layers, or by avoiding the formation of pores originating from binder degradation/smoke formation) and geometrical accuracies (e.g. by avoiding the formation of dross) of parts, obtained after SLS and SLM. In this context, the spatiotemporal laser energy distribution/absorption caused by the incoming fluence should also be investigated.

[2]In literature, sometimes the term 'pitch' is used instead of 'scan spacing'.

up to 0.97 J/mm^3, for the Al_2O_3-PA powder produced through ball milling. This means that the powder synthesis method, together with the amount of binder used, had a more pronounced influence on the SLS behavior than the binder material itself.
In general, the parts which had the highest green density after SLS, also had the highest green strength. The higher the green strength, the easier complex shaped parts could be fabricated without the risk of breaking them during part manipulation. Nevertheless, not for all composite powders, the laser energy density was optimized for the highest green density. For the ball milled Al_2O_3-PA powder, the laser energy density was optimized to have the highest density after an additional cold isostatic pressing (CIP), debinding and solid state sintering (SSS) step. As the parts, SLSed with the highest laser energy densities contained the lowest amount of binder material due to binder degradation, these parts had the highest final density. For the Al_2O_3-PP powder, produced by the TIPS process, the laser energy density was optimized to have the highest geometrical accuracy (i.e. no dross formation) after SLS. The optimized laser energy density (e*, table 8.1) of 0.12 J/mm^3, was lower than the laser energy density of 0.77 J/mm^3 which resulted in the highest green density. In this case, the green density after SLS, corresponding to the optimized laser energy density ($\rho_{SLS}^{e=e*}$, table 8.1), was 51%.

8.2.1.3 Debinding and furnace sintering

During debinding and SSS, the green parts shrunk. This shrinkage, which is also called 'sintering shrinkage' or shrinkage due to the sintering pressure or sintering stress, was mainly caused by atomic diffusion (i.e. diffusion of aluminum and oxygen atoms) during SSS. Sintering stress caused the outer part dimensions to shrink more than the inner part dimensions. This means that the formation of pores in the green parts might lead to nonuniform shrinkage during subsequent debinding and SSS: pores can be considered as 'inner' geometries, which shrunk less compared to the surrounding material (i.e. 'outer' geometries). Furthermore, the shrinkage during debinding and SSS was generally more or less the same in the scan, x, and cross-scan, y, directions, but larger in the build, z, direction: see $\Delta_{x-y}^{e=e*}$ and $\Delta_{z}^{e=e*}$ in table 8.1 for the shrinkage in respectively the x-y and z direction for parts produced with optimized laser energy density (e=e*). This was probably due to pores between the different SLSed layers, i.e. inter-layer pores.
The final density after debinding and furnace solid state sintering of the parts SLSed with optimized laser energy densities ($\rho_{SSS}^{e=e*}$), varied between 39% and 77%. The solid state sintered parts (SSS parts) sometimes contained cracks: see cracks$_{deb+SSS}$ in table 8.1. These cracks were probably caused by an inhomogeneous distribution of alumina and binder material in the composite

starting powder or by the occurrence of other phenomena which induced swelling (figure 3.8) during the debinding process. Probably, this swelling was caused by a too high green density, which hindered the gases formed during the debinding step to escape, in combination with (i) a too high amount of binder material, (ii) the presence of solvents used during powder production and/or (iii) the presence of moisture in the starting powder. Optimizing the binder removal and SSS process parameters might reduce the amount and size of the cracks and result in a slightly increased final densities.

8.2.1.4 Discussion

From all the powder synthesis routes investigated in this dissertation to produce composite powder agglomerates to indirect SLS alumina parts, the TIPS process seemed to be the most appropriate. Firstly, the agglomerates produced by the TIPS process had a (near) spherical shape and could be well deposited by the counter current roller of the DTM Sinterstation 2000. Secondly, the TIPS process seemed to be very flexible, as composite agglomerates containing different binders (PA, PP, carnauba wax and LDPE) could be synthesized. The TIPS process could also be applied on other ceramics than alumina. For example, although not described in this dissertation, ZrO_2 parts were fabricated from ZrO_2-PP agglomerates synthesized by TIPS [186]. Also hydroxyapatite-tricalcium_phosphate-PP agglomerates could be synthesized through TIPS and SLSed.

It seemed that SLS of composite powders, containing low viscosity binders, resulted in green parts with the highest green density (table 8.1). During the SLS process, the low viscosity binders could fill the inter-agglomerate pores. Furthermore, the density after debinding and furnace sintering was generally also the highest for the parts with the highest green density after SLS. From all the binder materials investigated, the carnauba wax containing binders had the lowest viscosity during SLS and the highest density after SSS. Nevertheless, due to its low viscosity, a base plate and the addition of LDPE was needed during respectively SLS and debinding. In this way, the low viscosity of the carnauba wax made the production of complex shapes more difficult.
In this dissertation, PS seemed to be the most appropriate binder material to fabricate high density, complex shaped alumina parts through SLS of dry composite powders (without using a base plate), followed by a debinding and SSS step. The viscosity of this PS seemed to be high enough to have a relatively high green density after SLS at low temperatures, and low enough to avoid the use of a base plate. However, as only composite agglomerates, containing a large amount of PS (39wt%) were investigated and the alumina parts produced by the alumina-PS powder contained cracks, further research is needed to prove this

statement. In order to do so, alumina-PS composite powder, synthesized by the TIPS process rather than dispersion polymerization, should be investigated.

8.2.2 Post-AM densification

The main drawback of producing technical ceramic parts through indirect SLS of dry composite powder agglomerates, was the presence of inter-agglomerate pores in the final parts. These pores were already present as space between the agglomerates at the beginning of the PM process. Since the inter-agglomerate pores could not be eliminated during the SLS, debinding and SSS steps, the following post-AM densification steps were investigated to produce ceramic parts with an increased density: remelting, isostatic pressing and infiltration.[3] Figure 8.1 illustrates at which stages of the PM process, the different post-AM densification steps were performed in this dissertation: remelting was performed after SLS; isostatic pressing was performed before debinding; infiltration could be performed after SLS, after a debinding and pre-sintering step in a furnace (1050°C) and after SSS in a furnace (1600°C).

8.2.2.1 Remelting

During remelting, every powder layer is SLSed two or more times instead of only once. This was found to successfully improve the green density, but not the final density. Remelting could also cause unwanted 'dross formation' when

[3]Although in this dissertation, these three post-AM densification steps were applied to increase the density of SLSed polymer-ceramic composite parts, these steps also can be applied to increase the density of parts of any material, produced through AM: e.g. isostatic pressing can be applied on SLSed polymer parts.

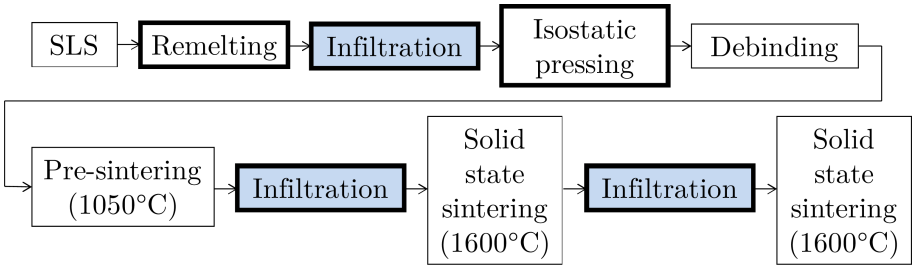

Figure 8.1: Powder metallurgy processing flow chart, illustrating at which stages of the PM process the different post-AM densification steps were performed.

too high laser energy densities were applied.
Although no significant increase of the final furnace sintered density could be obtained through remelting, it should be mentioned that the scanning system of the DTM Sinterstation 2000 was not appropriate to thoroughly investigate this densification step. For example, as it was not possible for the DTM Sinterstation 2000 machine to determine the scan order, the parts were sometimes firstly scanned with high laser energy density remelting parameters and afterwards with the lower laser energy density SLS parameters.

8.2.2.2 Isostatic pressing

During the isostatic pressing experiments, the SLSed parts were first vacuum packed in a rubber bag. By compressing the vacuum packed sample, the inter-agglomerate porosity was reduced. Three isostatic pressing (IP) techniques were investigated to increase the green density of the SLSed parts: cold isostatic pressing (CIP), quasi isostatic pressing (QIP) and warm isostatic pressing (WIP). CIP, QIP and WIP all led to an increase of the green density. In this dissertation, the pressure applied during the CIP experiments (up to 200 MPa) was not high enough to plastically deform the powder agglomerates. By heating the SLSed parts during QIP experiments, the strength of the composite agglomerates decreased. However, QIPing led to a uniaxial compression, resulting in a nonuniform shrinkage. WIP was a more promising IP technique than CIP and QIP, since an isostatic pressure could be uniformly applied on the SLSed samples and the heated liquid allowed the binder material to be plastically deformed. For example, during WIPing at 135-140°C, the 40vol%alumina-60vol%PP composite agglomerates broke at a pressure between 48 and 64 MPa. At a similar pressure, the 78wt%alumina-22wt%carnauba_wax-LDPE composite agglomerates broke at a WIPing temperature of 60°C. It can be concluded that WIP was the most promising IP techique investigated in this dissertation.
Many isostatically pressed parts cracked during debinding and SSS, although these parts did not crack without the IP step. Sometimes, the cracks could be attributed to improper vacuum packing. In this case, circular cracks arose after SSS, due to air entrapment during WIP (see section 5.6.2). After IP, debinding and SSS, the parts obtained by SLS of the ball milled Al_2O_3-PA powder (CIP), the Al_2O_3-PS powder (WIP) and the Al_2O_3-carnauba_wax-LDPE powder (WIP) contained non-circular cracks. These cracks could be attributed to swelling during the debinding process or inhomogeneous shrinkage during debinding and SSS. In the former case, the gases, formed during the thermal debinding step, could not escape from the dense, WIPed parts. In the latter case, the cracks were caused by an inhomogeneous distribution of alumina-binder concentrations in the composite starting powder.

It can be concluded that breaking the composite agglomerates through WIP was not sufficient to produce high density and crack free alumina parts. As described in the next section, applying an infiltration step after SLS and before WIP could prevent the formation of large cracks during debinding and SSS.

8.2.2.3 Infiltration

The infiltration experiments attempted to fill the inter-agglomerate pores of the parts with a (stabilized) suspension containing infiltrant material. Infiltration experiments were performed in vacuum (vacuum infiltration), atmospheric pressure (pressureless infiltration) and by applying an external pressure on the suspension (pressure infiltration). The following formula describes the total driving force for the infiltration, p_d, as function of the applied pressure [212].

$$p_d = p_c + p_a - p_i \tag{8.1}$$

The infiltration of the porous parts with a suspension was driven by two different mechanisms. The first involved the flow of infiltrating liquid into the porous structure under the combined effect of the capillary (p_c) and applied pressure (p_a, consisting of the hydrostatic and atmospheric pressure) until the internal pressure (p_i) of the compressed air became equal to $p_a + p_c$. The second mechanism involved the outward diffusion of gas because of its higher solubility at higher pressures. During pressureless infiltration ($p_a = 1$ atm) experiments, infiltration was mainly driven by the first mechanism: $p_c + p_a$ (1 atm) = p_i. When applying pressure infiltration ($p_a > 1$ atm), infiltration was also driven by the second mechanism (i.e. diffusion of air). This led to a better infiltration behavior. When applying vacuum infiltration ($p_i \approx 0$ atm; $p_a = 1$ atm), the air inside the pores of the SLSed was evacuated before infiltration. In this case, infiltration was again determined by the first mechanism: $p_c + p_a$ (1 atm) = p_i (0 atm).
The infiltration experiments revealed that both pressure infiltration and vacuum infiltration led to a better infiltration behavior compared to pressureless infiltration. It could not be determined whether pressure infiltration or vacuum infiltration was the best infiltration method. Perhaps, a combination of both methods is the most favorable: applying a vacuum prior to infiltration and applying an external pressure during infiltration. However, this infiltration method was not tested in this dissertation.

Generally, infiltration led to the formation of a dense outer shell and a more porous core. The formation of the dense shell could be explained assuming that (i) the infiltrated particles impeded further infiltration, (ii) during drying a capillary flow transported infiltrated nanoparticles towards the outside of the

part, (iii) the viscosity of the suspension was too high and/or (iv) the infiltration time was too short to fully infiltrate the parts. These findings suggest that the results of the infiltration experiments performed in this dissertation could be improved by infiltrating with less concentrated suspensions and for longer times: e.g. infiltrating 1 hour with an ethanol suspension, containing 25 vol% instead of 30 or 40 vol% alumina particles.

As infiltration filled the pores of the parts, the shrinkage during subsequent debinding and/or solid state sintering was prohibited. As a result, infiltration decreased the part shrinkage during subsequent debinding and SSS. Moreover, the dense shell, formed during infiltration, shrunk less than the more porous core. This nonuniform shrinkage sometimes led to the formation of cracks (usually cracks perpendicular to the build z direction and along the inter-layer porosities) and a decrease of the final density after SSS.

As depicted in figure 8.1, infiltration was performed at different stages of the PM process: after SLS, after the debinding and pre-sintering step 1050°C) and after SSS (1600°C). Since infiltration was a more effective densification step when applied on more porous parts, infiltration after pre-sintering (i.e. after the binder removal and the initial solid state sintering step) generally led to the highest density (higher than infiltrating after SLS or after furnace SSS): e.g. up to 91.4% for alumina parts produced with the Al_2O_3-PP powder. However, the strength of the parts during the debinding step was generally low. Green infiltration was sometimes needed to increase the strength of complex shapes during the debinding step. Without the application of additional support, the strength of these shapes would be too low to bear its own weight.
It could be stated that, if infiltration was only applied once during the PM process, the best stage of the PM to infiltrate depended on the complexity of the part: for non-complex shaped parts the best stage to infiltrate was after pre-sintering (i.e. highest density), and for complex shaped parts the best stage to infiltrate was after SLS (i.e. increased density and sufficient strength during debinding). The feasibility to infiltrate not once, but at different stages of the PM process, was also investigated: see next section.
At last, experiments also revealed that infiltration after pre-sintering resulted in an increase of the part shrinkage compared to infiltration after SLS. A possible explanation for this is that the part shrinkage during the debinding step was not prohibited if only infiltration after pre-sintering was applied.

8.2.2.4 Combination of different post-AM densification steps

The combined influence of infiltration after SLS, infiltration after pre-sintering and/or infiltration after SSS was investigated in sections 4.6.2.3 and 4.6.2.4.

The combined influence of infiltration after SLS, warm isostatic pressing and/or infiltration after pre-sintering was investigated in sections 6.5 and A.5. After green infiltration, already filled inter-agglomerate pores and the dense shell prohibited the infiltration after pre-sintering. Also, since WIPing decreased the pore size after pre-sintering, the infiltrant could not flow inside the part anymore. For infiltration after SSS, similar conclusions could be made.
It can be concluded that infiltration after pre-sintering was a non-effective densification step when applied after a green infiltration and/or WIPing step. However, further research is needed to investigate whether these results could be improved: e.g. by infiltrating with more dilute suspensions which have a lower viscosity.
Applying green infiltration before WIP seemed to be the most successful combination of post-AM densification steps for complex shapes. For example, after furnace sintering this combination led to densities up to 87.6% for alumina parts produced with the Al_2O_3-carnauba_wax-LDPE powder. Moreover, green infiltration increased the strength and prohibited the formation of cracks during the debinding step.

Conclusion: In this dissertation, the post-AM densification techniques which led to the highest increase of the furnace sintered density, depended on the complexity of the parts: for non-complex shaped parts the best post-AM densification technique was to infiltrate after pre-sintering (i.e. highest density), and for complex shaped parts the best post-AM densification technique was to infiltrate after SLS and to WIP afterwards (i.e. increased density and sufficient strength during debinding). However, since the densities after furnace solid state sintering can still be improved in various ways, this conclusion is not absolute.

8.2.2.5 Discussion

During the PM processes described above, material was removed (debinding) and added (infiltration) to the SLSed part. The mass of a ceramic part after solid state sintering m_{SSS} was a function of the mass after SLS m_{SLS}, the mass of the binder m_{binder} inside the SLSed part and the (dry) mass of the infiltrant material added during infiltration $m_{inf.}$. This could be expressed by the following formula:[4]

$$m_{SSS} = m_{SLS} - m_{binder} + m_{inf.} \tag{8.2}$$

[4]Generally, the mass of a part at the end of the PM process can always be written as a function of the mass of the part after the primary shaping step and (possible) mass addition/removal during the subsequent PM processing steps. This means that similar equations as equations 8.2 and 8.3 can be formulated for all PM processes.

This formula could be rewritten as the following formula, which correlates the density change and the part shrinkage after SLS:

$$\rho_{SSS,a} = \frac{\rho_{SLS,a}}{\rho_{SLSmax}} . \frac{\rho_{SLSmax} - \rho_{binder} . vol\%\ binder + \rho_{inf.} . vol\%\ inf.}{1 + vol\%\ shrinkage} \quad (8.3)$$

with:

- $\rho_{SSS,a}$: the absolute density of the part after solid state sintering.
- $\rho_{SLS,a}$: the absolute density of the part after selective laser sintering.
- ρ_{SLSmax}: the maximal possible (absolute) density of the part after selective laser sintering: i.e. the density of an SLSed part without pores.
- ρ_{binder}: the (absolute) density of the binder material.
- vol% binder: the volume binder material in the SLSed part, relative to the 'internal' volume (i.e. not including pores) of the SLSed material.
- $\rho_{inf.}$: the (absolute) density of the (dry) infiltrant material: e.g. 3.984 g/cm^3 for alumina.
- vol% inf.: the volume (dry) infiltrant material which entered the part during subsequent infiltration steps (i.e. after SLS, pre-sintering and/or SSS), relative to the 'internal' volume of the SLSed material.
- 1 + vol% shrinkage: the 'external' volume (i.e. including pores) of the part after solid state sintering, relative to the 'external' volume of the SLSed part. The volumetrical shrinkage (vol% shrinkage), which was mainly caused by atomic diffusion during SSS (section 2.4.7.2), could be calculated by the % linear shrinkage in the scan x, cross-scan y and build z directions:

$$(1 + vol\%\ shrinkage) = \prod_{i=x,y,z} (1 + \%\ linear\ shrinkage)_i \quad (8.4)$$

In order to verify formula 8.3, the measured density $\rho_{meas.}$ after SSS of a selection of parts produced in this dissertation, was compared with the corresponding calculated density $\rho_{calc.}$. As depicted in table 8.2, in about half of the cases, formula 8.3 could predict quite accurately the final density of the parts. In the other half of the cases, formula 8.3 seemed to be less accurate and differences of about 10% could be observed between the measured and calculated relative density. These differences were probably caused by:

- Dimensional measurement errors: the dimensions of the SLSed and SSS parts were (mostly) measured by a vernier caliper. Therefore the % linear shrinkages calculated in this dissertation could vary 1 or 2%. As the vol% shrinkage in formula 8.3 was calculated by multiplying the % linear shrinkage in scan x, cross-scan y and build z directions, these errors could accumulate. Furthermore, for the calculation of the vol % shrinkage, it was assumed that the parts had flat side and top surfaces. Part distortion (e.g. introduced during isostatic pressing) could make this assumption not valid anymore.
- Density measurement errors: similar to the dimensional measurements performed in this dissertation, the measured densities might vary 1 or 2%.
- Assumptions made on the theoretical density of the binder and infiltrant materials.
- Degradation of polymer material during the SLS process: for the calculation of the densities after SLS, it was assumed that the binder did not degrade during SLS.
- Erosion of the parts during manipulation.
- During many furnace treatments (debinding and SSS), the SLSed parts were placed on coarse alumina powder. Especially when low viscosity binders were used, the binder possibly flowed into this coarse powder during the debinding step. The concomitant sticking of some coarse powder particles to the part, might lead to inaccurate density or dimensional measurements.

Although formula 8.3 could not be validated by all results, it provided insight in how the density of the SSS parts, produced in this dissertation was influenced by the composite powder, the SLS process and the different post-AM densification steps. For example:

- Composite powder: the more binder present in the composite powder, the more material degraded during the debinding step. As a result, the density after SSS decreased if the concomitant increase of part shrinkage could not compensate for this phenomenon. However, a higher amount of binder material in the composite powder tended to increase the green density during SLS. As a result, also the density after SSS tended to increase.
- SLS: SLS with a high laser energy density led to plastic flow of the binder material and could also lead to binder degradation and concomitant

Part	powder	Additional densification steps (besides SLS, deb. and FS)	$\rho_{meas.}$ [%]	$\rho_{calc.}$ [%]
1	Al_2O_3-PS	None, i.e. only deb. and FS	66	72
1b	Al_2O_3-PA (TIPS)	None, i.e. only deb. and FS	47	46
1	Al_2O_3-PP	None, i.e. only deb. and FS	40	40
3	Al_2O_3-PP	1x gr. inf. (Al_2O_3)	63	64
4	Al_2O_3-PP	2x gr. inf. (Al_2O_3)	74	73
14	Al_2O_3-PP	WIP, 140°C, 48 MPa, 15 min.	64	53
1	Al_2O_3-carn.+LDPE	None, i.e. only deb. and FS	77	66
2	Al_2O_3-carn.+LDPE	1x gr. inf. (Al_2O_3)	80	82
3	Al_2O_3-carn.+LDPE	2x gr. inf. (Al_2O_3)	81	95
11	Al_2O_3-carn.+LDPE	WIP, 60°C, 48 MPa, 15 min.	83	71

Table 8.2: Comparison of the measured density $\rho_{meas.}$ after SSS of a selection of parts produced in this dissertation, with the corresponding density $\rho_{calc.}$, calculated according to formula 8.3.

formation of pores. Plastic flow and the formation of pores respectively increased and decreased the green density after SLS. According to formula 8.3, both high green densities after SLS ($\rho_{SLS,a}$) and binder degradation during SLS (lower vol% binder) tended to increase the density after SSS if the concomitant decrease of part shrinkage could not compensate for this phenomenon. Material degradation during SLS not only influenced the green density ($\rho_{SLS,a}$) and the amount of binder inside the SLSed part (vol% binder), but also the maximal possible (absolute) density of the SLSed part (ρ_{SLSmax}). As a result, the laser energy density which resulted in the highest green density, did not always resulted in the highest density after SSS: e.g. see figure A.3.

When comparing the different composite powders (section 8.2.1.4), it could be generally stated that high densities after SLS led to high densities after SSS. However, due to the formation of inter-agglomerate pores, the green densities of the SLSed parts which could be successfully debinded, did not exceed 66%. In order to further increase the green density of the SLSed parts, the inter-agglomerate pores should be eliminated. As depicted in section 8.2.2, in this dissertation post-AM densification techniques were explored to eliminate the inter-agglomerate pores. Alternatively, high densities can be obtained by either eliminating the inter-agglomerate pores during laser irradiation, either by preventing the formation of the inter-agglomerate pores during powder deposition. To eliminate the inter-agglomerate pores during laser irradiation, further research is needed on indirect SLS of composite agglomerates, containing

low viscosity binders. To eliminate the formation of inter-agglomerate pores during powder depositing, the agglomerates should be broken during powder deposition (e.g. by a powder compaction device) or fine (e.g. submicrometer sized) composite powder particles, instead of the large (10-50 μm) composite agglomerates should be deposited. In this way, also the amount of binder material needed to SLS parts of sufficient strength might be less. To deposit fine powder particles, clustering of the particles due to interparticle forces should be avoided by 'dry depositing' the particles (e.g. by a ring blade) or by 'wet depositing' powder containing slurries (e.g. by a tape casting or spray deposition device).[5]

- Remelting: the remelting experiments performed in this dissertation led to similar results as the SLS tests: although the green density of the parts could be significantly increased, the density after SSS was not.

- Isostatic pressing: isostatic pressing increased the density after SSS by increasing the vol% shrinkage after the SLS step. Although isostatic pressing was only performed after the SLS step in this dissertation, isostatic pressing during SSS (e.g. hot isostatic pressing, HIP) would also increase the final density.

- Infiltration: according to formula 8.3, the amount of infiltrated material was linearly related to the density increase after SSS. However, due to a decrease of the porosity of the part, infiltration also decreased the part shrinkage. Especially when infiltration led to inhomogeneous shrinkage (e.g. due to the formation of a dense shell), the density of the sintered parts could decrease.
  The infiltration experiments performed in this dissertation revealed that infiltration was more effective, when applied on more porous parts. This means that, in order to increase final density (i.e. the density after solid state sintering) by infiltration, the density prior to infiltration should be as low as possible. According to formula 8.3, a compromise should be made between the green density after SLS and the amount of material added during infiltration in order to optimize the density after SSS. Furthermore, it should be noticed that for the fabrication of complex shaped parts, the green density and concomitant part strength should be high enough to enable part manipulation.

[5]The elimination of inter-agglomerate pores after additive manufacturing is critical for all powder based AM processes. This means that similar techniques as described in this paragraph can be applied to improve the density obtained after other AM processes: e.g. SLS/SLM of metals and SLS of pure polymers.

8.3 Direct SLS/SLM

The experimental setup developed in this dissertation for direct SLS/SLM of alumina parts, proved that it might be possible to produce technical ceramics through direct SLS/SLM. In order to do so, a low laser energy density should be applied to consolidate the powder particles. Firstly, a low laser energy density reduces the thermal stresses during laser irradiation. Secondly, it seems that a low laser energy density reduces the melt pool size during SLS/SLM and the concomitant grain size[6] obtained after SLS/SLM. To consolidate ceramic powder particles by low laser energy densities, high density powder layers of submicrometer powder (e.g. deposited by using colloidal processing techniques) should be preheated to a high temperature:

- The *higher* the *preheating temperature*, the less energy is needed for the laser to consolidate the powder particles.
- *Submicrometer powder particles* have a large 'driving force for pore closure' (section 2.4.7.2). As a result, the powder particles can be consolidated by applying relatively low laser energy densities and without applying extremely high preheating temperatures (e.g. 1730°C; section 1.4.1).
- The small gaps between *densely packed* (submicrometer) *powder particles* can be filled by the small amount of melting phase, induced by the low laser energy density.

The experimental setup developed in this dissertation did not yet allow to direct SLS/SLM alumina in a reliable way. Future research on direct SLS/SLM should focus improving the reliability of the process by homogenizing:

- *the powder deposition process.* The experimental setup could deposit submicrometer powder layers through electrophoretical deposition. However, the layers cracked during deposition. As a result, dense but separated clusters of submicrometer powder were formed after deposition. Further improving the deposition device is needed to avoid the cracking of the layers. Other deposition processes (e.g. a ring blade or spray deposition device) might also be considered to deposit dense submicrometer powder layers in a more homogeneous way.

[6]The observation that small melt pools result in small grain sizes might be related to the cooling rates of the melt pools after laser irradiation. Since small melt pools cool faster than large melt pools, the resulting grain sizes are smaller.

- *the consolidation temperature during selective heating of the powder layers.* In the experimental setup a 'Gaussian shaped' laser was applied to selectively sinter the ceramic powder particles. The Gaussian shape caused the occurrence of a thermal gradient and concomitant thermal stresses and curling during consolidation. The thermal gradient might be reduced by selectively heating/consolidating the different layers of ceramic powder particles at once (e.g. by using a digital light projector device).

- *the preheating temperature of the powder layers.* In the current setup, the powder layers could be heated up to a temperature of 800°C within a margin of ± 50°C. As a result, thermal stresses could occur in the part after consolidation. Possibly, the margin of ± 50°C could be improved by optimizing the temperature controller. Applying another preheating configuration would be another option. For example, in order to preheat the ceramic powder, dielectric heating (e.g. microwave heating) instead of resistance heating might be applied.

8.4 General conclusion

This thesis investigated a large number of PM processing routes for the production of ceramic parts by SLS/SLM. More specifically, the potential of the following SLS/SLM processes was studied: indirect SLS of composite powder agglomerates and direct SLS/SLM of pure, submicrometer sized ceramic powder.
Through indirect SLS of composite powder agglomerates in combination with the application of post-AM densification techniques, freeform shaped alumina parts with densities up to approximately 90% could be obtained. In order to produce higher quality ceramics through indirect SLS, the inter-agglomerate pores should be avoided or completely eliminated.
An in-house developed experimental setup enabled the production of alumina samples with a grain size smaller than 5 μm by direct SLS/SLM. In order to produce high quality ceramics through direct SLS/SLM, the reliability of the of the experimental setup should be improved by homogenizing: (i) the powder deposition process, (ii) the consolidation temperature during selective heating of the powder layers and (iii) the preheating temperature of the powder layers.

Appendix A

Production of alumina parts through Laser Sintering of carnauba wax - alumina agglomerates produced via dissolution-precipitation

A.1 Abstract

A powder metallurgy process was developed to produce alumina parts through SLS, starting from 78wt% alumina - 18wt% carnauba wax - 4wt% low density polyethylene (LDPE) composite agglomerates synthesized by temperature induced phase separation (TIPS). The PM process included powder synthesis, SLS, debinding and solid state sintering (SSS) in a furnace. The resulting parts had a density of about 77% and contained inter-agglomerate pores.
Similar infiltration and/or warm isostatic pressing (WIP) experiments as described in chapter 6 were investigated as extra steps of the PM process. The aim of these experiments was to eliminate the inter-agglomerate pores and to improve the density of the sintered alumina parts. Infiltration was performed on both SLSed parts (i.e. green infiltration) and/or pre-sintered (1050°C) parts. Two suspensions were used to investigate the infiltration behavior: a 40vol% alumina - ethanol suspension and a 40wt% silica - water suspension.

During infiltration, a dense shell was formed. This shell prohibited the part to shrink uniformly during further debinding and/or solid state sintering. This resulted in the formation of cracks perpendicular to the z 'build' direction and decreased the part density after furnace sintering. The results of the infiltration experiments could be further explained by considering the porosity of the part prior to infiltration. WIPing at a sufficiently high temperature and pressure, allowed to break the composite agglomerates. By combining infiltration and WIPing, alumina parts with a sintered density up to 89.0% could be obtained.

A.2 Introduction

In chapters 3 to 6 of this dissertation, four different home-made composite powders to indirectly SLS alumina parts were presented, together with post-densification strategies to improve the density of the resulting alumina parts. Each chapter attempted to improve both the properties of the composite starting powder and the post-densification strategies.
In this appendix, another home-made composite powder will be presented. The initial experiments, performed with this powder, attempted to compare the properties of this powder and resulting parts with the properties of the powders/parts described in the previous chapters. Further, similar post-densification strategies as described in chapter 6 were applied. In this way, the influence of binder synthesis (and more specifically binder formulation) on the post-densification behavior could be assessed.

As described by Rombouts et al. [178], the binder formulation applied in this study was inspired on a wax based binder system that was developed by Nogueira et al. [156] for low pressure powder injection molding (LPIM). In LPIM, mixtures of ceramic or metal powder and low melting point binders (in the range of 30-40 vol%) are commonly used as feedstock material during the forming stage and subsequently the parts are post-processed by debinding and sintering [124]. The rheological and thermal requirements for the binder in LPIM and indirect laser sintering are to some extent similar. In LPIM low molecular weight paraffins and waxes are often employed as main ingredient, usually in combination with a minor proportion of a more viscous polymer [146]. The aim of the polymer is to increase the viscosity of the molten binder and to expand the removal of the binder over a broader temperature window so that a higher strength and geometrical stability during post-processing is obtained. Nogueira et al. produced alumina parts with a density of 3.7g/cm^3 by LPIM and subsequent furnace sintering using a carnauba wax based binder with 5-8% low density polyethylene (LDPE) and 1% stearic acid [156]. In this chapter, the production of alumina parts by indirect laser sintering of free-flowing alumina-

binder powder, based on such a binder formulation, will be presented, together with post-densification steps, wich were performed to increase the density of the produced parts.

A.3 The powder metallurgical process

The powder metallurgy (PM) processes, investigated in this chapter was similar to the PM processes investigated in chapter 6. Moreover, the quality of the components during the different processing steps was investigated with the same equipment, as described in section 6.3.

A.3.1 Difference with PM processes described in previous chapters

In summary, the PM process described in this chapter differs from the ones described in chapters 3, 4, 5 and 6 in five ways:

1. Wax based binders (pure carnauba wax with a theoretical density of 0.970 g/cm^3 and carnauba wax containing 18wt% LDPE with a theoretical density of 0.966 g/cm^3) are used instead of the semi-crystalline polypropylene (PP; chapter 6), semi-crystalline polyamide (PA; chapters 3 and 5) or amorphous polystyrene (PS; chapter 4).

2. The synthesis of the initial composite powder is done by temperature induced phase separation (TIPS), which is different than in-situ dispersion polymerization, as described in section 4.4.1, or ball milling, as described in section 3.3.1. Despite the use of the TIPS process, the powder synthesis route performed in this chapter is slightly different from the powder synthesis routes described in sections 5.4.1 and 6.4.1.

3. The parts are SLSed on a base plate instead of loose powder.

4. Compared to section 6.5, similar, but less post-densification strategies are tested: no vacuum infiltration tests are performed with the boehmite suspension and molten carnauba wax containing 22wt% of alumina powder. Also no vacuum infiltration experiments are performed on green parts with a size of 20x20x20 mm^3.

5. Other Al_2O_3 starting powder was used: 'CT3000SG' (Almatis GmbH, Germany) instead of 'grade SM8' (Baikowski, France).

A.4 Production of alumina parts

A.4.1 Powder production

A production method for free-flowing powder agglomerates consisting of submicron sized Al_2O_3 powder (CT3000SG, Almatis GmbH, Germany) and 22wt% organic binder was developed. Two different binder systems were applied: 100% carnauba wax and 72wt% carnauba wax + 18wt% low density polyethylene (LDPE; Coathylene HX1681, Dupont, US). The composite powder was synthesized by temperature induced phase separation (TIPS). The binder constituents were first dissolved in toluene at elevated temperature (70°C). The alumina powder was then added to the solution and milled in a planetary ball mill. After 15 minutes, the solution was cooled down to room temperature, which led to reprecipitation of the carnauba wax and LDPE on the alumina powder. The majority of the toluene was removed by centrifugation. The remainder was dried and granulated. Sieve fractions between respectively 50 μm and 250 μm (for both the 100% carnauba wax and 72wt% carnauba wax + 18wt% LDPE powder) or between 50 μm and 125 μm (only for the 72wt% carnauba wax + 18wt% LDPE powder) were retained.
The resulting powders were angular in shape (figure A.1a), but had a good flowability during deposition with the counter current roller. The scanning electron microscopy images indicated a homogeneous coverage of the organic phase on the alumina particles (figure A.1b).
A more detailed description of the applied powder production method and properties of the resulting composite powders can be found in Rombouts et al. [178].

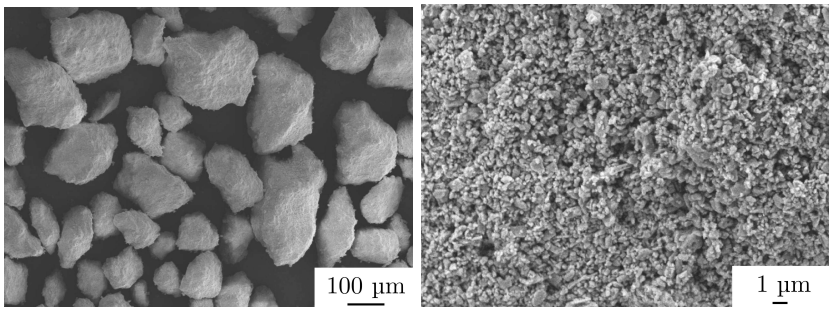

(a) (b)

Figure A.1: Scanning electron micrographs of alumina - 22wt% binder (carnauba wax + 18wt% LDPE) powder with sieve fraction of 50-125 μm

A.4.2 Selective laser sintering (SLS)

Selective laser sintering (SLS) experiments were performed on a DTM Sinterstation 2000. Due to the very low viscosity of the carnauba wax during laser irradiation, balling[1] occurred (figure A.2a). To avoid balling of the parts during SLS, it was necessary to produce the parts on a base plate. In this way, the balling phenomenon could be suppressed. Since the parts were anchored on the base plate during SLS, also less curling[2] of the parts occurred. Moreover, due to the anchoring on the base plate, the parts could not be dragged along with the roller or scraper during layer deposition.

A first parametric study was performed in the DTM Sinterstation 2000 using the alumina-carnauba wax powder, sieved between 50 and 125 μm (see section A.4.1), and a PMMA base plate. Cubes of 10x10x11 mm^3 were produced by applying the following scan parameters: a laser power P, scan speed v, scan spacing s and layer thickness l of respectively 4-8 W, 100-1200 mm/s, 100-300 μm and 250 μm. The preheating temperature was kept constant at 53°C.
The laser energy density e (=P/s.v.l, see section 3.3.2) tended to be a very important parameter to describe the SLS process. At first, it was observed that only parts scanned with a very high laser energy density, were attached to the PMMA base plate. At e values above about 1 J/mm^3, significant smoke formation during laser sintering (figure A.2b) and a black colored and rough laser sintered surface (figure A.2c) was observed. This indicated that the excessive high heat input led to decomposition and evaporation of the binder constituents. The formation of smoke was unwanted. Firstly, the SLS process was disturbed due to contamination of machine components such as the laser window. Further, microscopical analysis indicated gas bubble entrapment. This caused large spherical pores (figure A.2d) and as a result a lower green density. The parts produced using very low laser energy densities (e $<$ 0.3 J/mm^3) were only weakly bonded, which made part manipulation difficult. From these observations it was concluded that the use of an intermediate laser energy density (0.3 J/mm^3 $<$ e $<$ 1 J/mm^3) was preferred. At the high end of this intermediate laser energy density range (just before smoke formation) the highest green densities were obtained. The relative green densities varied between 45% and 83%.
As depicted in figure A.2c, also dross was formed at the sides of the parts during the SLS process. The amount of dross increased when applying higher

[1] Long thin melt pools are known to break up into balls, called 'balling' and commonly described as due to Rayleigh instabilities [119].

[2] Parts tend to curl towards the laser beam if the melt pools shrink after laser irradiation. This shrinkage occurs when the parts are not preheated to a temperature in the 'SLS window' (i.e. a temperature between the crystallization onset temperature T_{oc} and the melting onset temperature T_{om}).

laser energy densities. At higher laser energy densities, the carnauba wax was heated more. As a result, the carnauba wax had a lower viscosity and flowed towards the sides, consolidating powder particles which were not irradiated by the laser beam.

The second parametric study used the composite alumina - carnauba wax - LDPE powder with sieve fraction 50-250 μm and a nylon base plate. Cubes

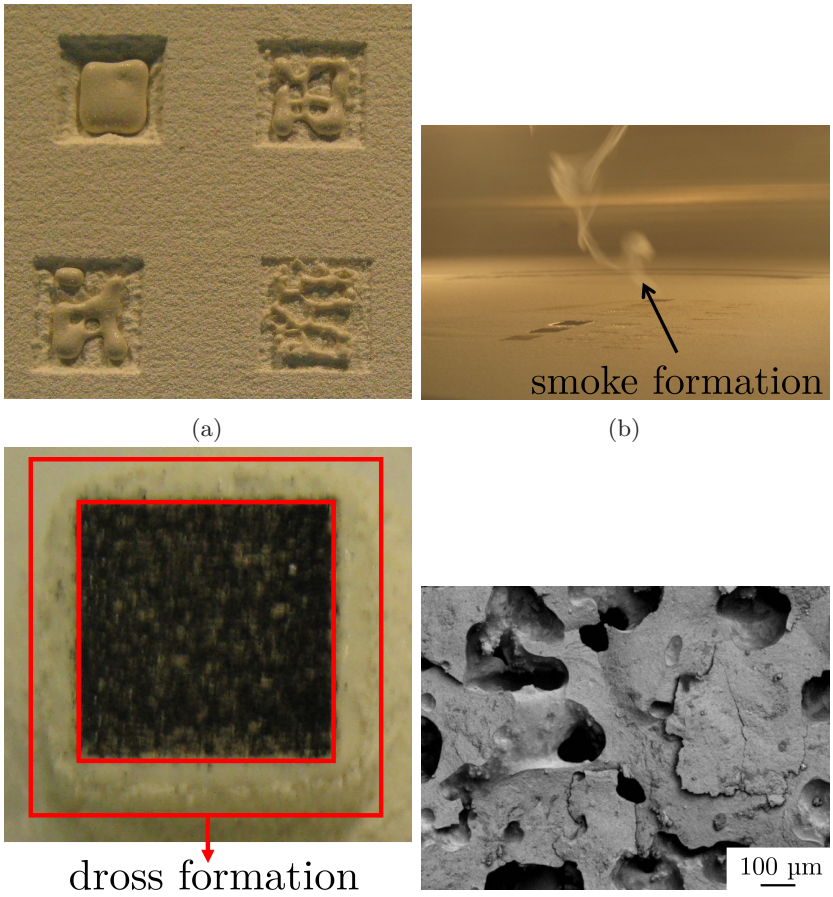

(a)

(b)

(c) e = 3.2 J/mm^3: P = 8 W, v = 100 mm/s, s = 0.3 mm, l = 0.25 mm

(d) e = 3.2 J/mm^3: P = 8 W, v = 100 mm/s, s = 0.3 mm, l = 0.25 mm

Figure A.2: SLS of alumina - carnauba wax composite agglomerates: balling (a); formation of smoke (b), a black colored and rough surface (c), dross (c) and spherical pores (d) during SLS at high laser energy densities.

of 10x10x6 mm^3 were produced by applying the following scan parameters: a laser power P, scan speed v, scan spacing s and layer thickness l of respectively 4-8 W, 300-1200 mm/s, 100-200 μm and 150 μm. The preheating temperature was kept constant at 53°C.
After SLS, the alumina - carnauba wax - LDPE parts were so strongly attached to the nylon base plate, that they could not be easily removed without breaking. Although the composite powder contained the same weight percentage of binder as used during the first parametrical study (i.e. 22wt%), the resulting parts had only a relative green density between 35% and 54%. The presence of LDPE probably lowered the viscosity of the binder and concomitant densification during laser irradiation. Similar to the first parametrical study, the highest green densities were obtained at laser energy densities just below 1 J/mm^3 (i.e. the laser energy density at which smoke formation started to occur).

The third parametric study again employed the composite alumina - carnauba wax - LDPE powder. In order to easily remove the parts from the base plate after SLS, a cardboard base plate was used. In order to increase the green density of the parts, smaller composite powder particles with a sieve fraction of 50-125 μm were used and a higher preheating temperature of 75°C was applied during SLS. Cubes of 10x10x10 mm^3 were produced by applying the following scan parameters: a laser power P, scan speed v, scan spacing s and layer thickness l of respectively 4-6 W, 400-800 mm/s, 80-120 μm and 250μm. As depicted in figure A.3a, the green densities after SLS were between 56 and 66%. This was about 10% higher than the green densities obtained in the second parametrical study. The highest green densities were obtained at laser energy densities of about 0.4 J/mm^3 instead of the 0.9 - 1 J/mm^3, which resulted in the highest green density during the first and second parametrical study. Probably, due to the finer starting powder and the higher preheating temperatures, less laser energy was needed to consolidate the same amount of material.

A.4.3 Debinding and furnace sintering

The green parts produced in the first parametrical study were debinded in air. In order to do so, the parts were heated to 500°C at different heating rates. However, all samples collapsed during debinding. This was attributed to the very low viscosity of the pure carnauba wax binder.

The parts produced in the second and third parametrical study were debinded and solid state sintered in a furnace. The parameters of these furnace treatments are depicted in table A.1: the 'debinding$_1$' and 'debinding$_2$'

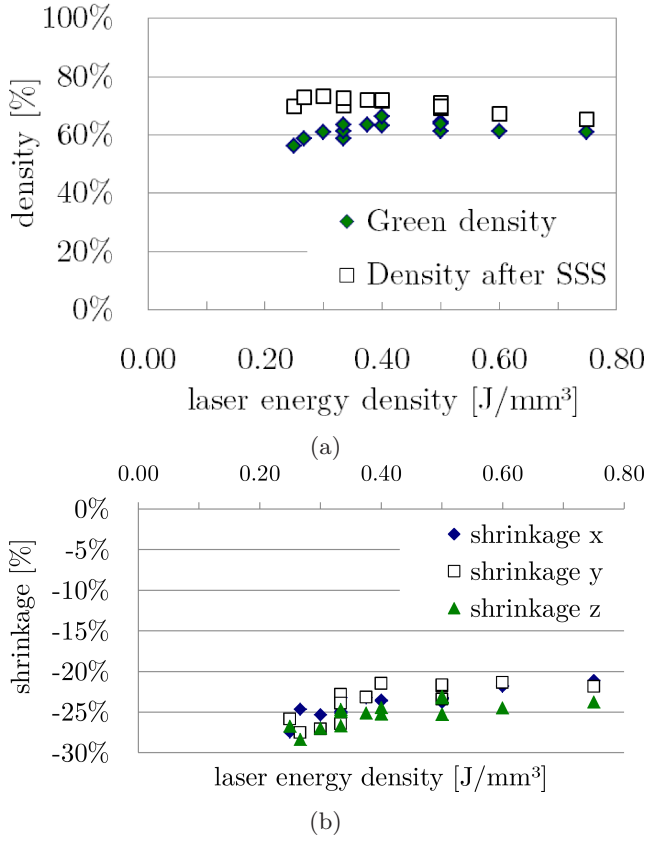

Figure A.3: SLS of alumina - 22wt% binder (carnauba wax + 18wt% LDPE) powder (sieve fraction 50-125 μm): green and final densities (a); linear shrinkage during debinding and solid state sintering in scan x, cross-scan y and build z directions (b).

parameters were applied to debind the parts of respectively the second and third parametrical study. Further, the shrinkage of the parts during debinding and solid state sintering was assessed.
Since the binders used during the second and third parametrical study contained 18wt% LDPE[3], no collapsing of the parts occurred. It was observed that the higher green density obtained during the third parametrical study did not lead to a higher density after SSS. However, for the parts produced in the second parametrical study, a larger shrinkage along the building direction z than along the scan directions x & y was observed. This was especially the case for parts produced at low laser energy densities.
Figure A.3a details the final densities after SSS of the parts produced in the third parametrical study as a function of the laser energy density. The final density did not vary significantly in the laser energy density range e $\sim$ 0.3-0.40 J/mm^3. Densities up to 73% were obtained.
Figure A.3b details the linear shrinkage during debinding and solid state sintering for the parts produced in the third parametrical study. No large difference between the shrinkage in the scan x, cross-scan y and build z directions were observed. The linear shrinkage decreased with increasing laser energy density. The amount of linear shrinkage was the largest for laser energy densities below 0.40 J/mm^3.

Finally, the following parameter set was chosen to be optimal for the alumina - 22wt% binder (carnauba wax + 18wt% LDPE) powder with sieve fraction 50-125 μm: a laser power P of 6 W, a scan speed v of 800 mm/s, a scan spacing s of 80 μm, a layer thickness of 250 μm and a preheating temperature of 75°C. This parameter set resulted in a laser energy density of 0.375 J/mm^3, which corresponded to an optimized density after SLS and SSS (figure A.3a). Moreover, this laser energy density corresponded to a relatively small amount of shrinkage during debinding and SSS (figure A.3b).
The optimized SLS parameter set was applied to produce many parts to study different post-densification strategies. However, some of these parts contained small inter-layer cracks (figure A.4a). These cracks were probably caused by thermal stresses which tended to curl the parts towards the laser beam. As a result, the composite powder was not always well deposited during SLS. In the remaining of this chapter, only parts which did not contain these visible

[3]Composite powders with binder systems ranging from 0% to 100% LDPE were produced and evaluated to determine the optimal LDPE content in combination with the carnauba wax. The screening experiments involved an evaluation of both the mechanical strength of loose powder, which was heated to above the melting temperature of the binder (120°C) as well as its thermal stability during subsequent thermal binder removal and furnace sintering. From these screening experiments, a binder formulation with 18wt% LDPE was selected. At too high LDPE concentrations the powder remained loose after the melting stage while at too low LDPE concentrations the pile of powder collapsed and lost its mechanical integrity during binder removal.

inter-layer cracks were selected for further processing.
As depicted in figure A.4b, the bulk microstructure consisted of the molten agglomerates which were glued together during laser irradiation. Despite the low viscosity of the binder, inter-agglomerate pores were visible.
Part 1 was SLSed with the optimized parameter set and debinded (using the 'debinding$_2$' parameter set of table A.1) and solid state sintered afterwards. In order to do so, the parts were placed on coarse alumina powder and covered by an alumina shell. During debinding and SSS, part 1 shrunk -21% in the scan/cross-scan x/y directions and -26% in the build z direction. Finally, a density of 77.2% was obtained (table A.2). This final density was about +5% higher than the final density of 72% which was obtained in the third parametrical test for parts SLSed with the same scanning parameters (i.e. a laser energy density of 0.375 J/mm^3 in figure A.3a). The lower sintered density of 72% for the parts of the third parametrical study might be caused by:

- the way the parts were placed in the furnace during debinding and SSS. The parts of the third parametrical study were completely covered by (thermally insulating) coarse alumina powder during debinding and SSS. The thermally insulating powder could have caused non-optimal sintering conditions, resulting in the lower sintered densities.

- small inter-layer cracks between the parts (figure A.4a): only parts which did not contain the visible inter-layer cracks were selected for further processing.

As depicted in figure A.4c, part 1 did not contain any cracks after furnace sintering. The final microstructure contained inter-agglomerate pores (figure A.4d) and Al_2O_3 grain sizes < 5 μm were obtained (figure A.4e).

	debinding$_1$	debinding$_2$	SSS	pre-sintering
heating rate [°C/min.]	0.5	0.1	5	5
heating temperature [°C]	500	600	1600	1050
dwell time [min.]	60	120	120	120
cooling rate	furnace cooling	furnace cooling	furnace cooling	furnace cooling
atmosphere	air	air	air	air

Table A.1: Parameters of the different furnace treatments used in this chapter.

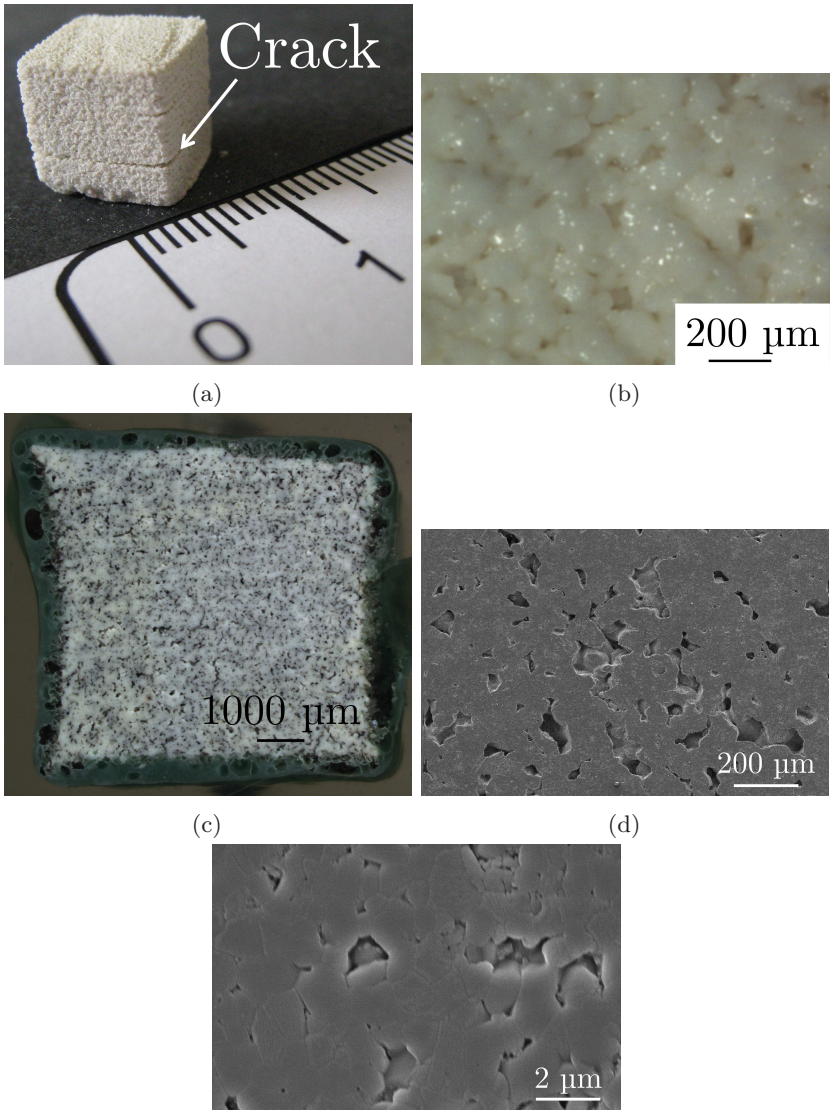

Figure A.4: Parts SLSed with the optimized parameter set: outer shape of a crack containing SLSed part (a); 3D microscope image of green microstructure (b); 3D microscope image (c) and SEM images (d,e) of part 1 after furnace sintering.

Part nr	Additional densification steps (besides SLS, deb. and SSS)	ρ [%]	x-y [%]	z [%]
1	None, i.e. only deb. and FS	77.2	-21	-26

Table A.2: Sintered (Archimedes) density and linear shrinkage after SSS of part 1, SLSed with the optimized parameter set.

In summary:

- Carnauba wax containing agglomerates are very difficult to SLS due to the occurrence of balling, thermal stresses (and resulting outer cracks) and dross formation. These phenomena are mainly a result of the low viscosity of carnauba wax at elevated temperatures.
- Using a base plate improves the SLS process of agglomerates, containing low viscosity binders. Cardboard seems to be the best base plate material: it provides sufficient rigidity to anchor the parts during the SLS process and the parts can be easily removed from the base plate after SLS.
- The SLS process is also improved by preheating the composite agglomerates up to a temperature just below the melting onset temperature T_{om} (i.e. up to 75°C), and by lowering the particle size of the agglomerates.
- The optimized laser scanning parameters for the alumina - 22wt% binder (carnauba wax + 18wt% LDPE) powder with sieve fraction 50-125 μm, are: a laser power P of 6 W, a scan speed v of 800 mm/s, a scan spacing s of 80 μm and a layer thickness of 250 μm. This parameter set results in a laser energy density of 0.375 J/mm^3.
- After optimizing the SLS parameters, parts with a green density up to 66% can be produced. These parts contain inter-agglomerate porosities and some of the parts contain cracks.
- In order to improve the strength during debinding of the SLSed wax containing parts, an optimized amount of polymer (i.e. 18wt% of LDPE) has to be added to the binder. However, the addition of a polymer can increase the viscosity of the binder during laser irradiation and, as a result, the green density after optimizing the SLS parameters.
- During debinding and SSS, the density of the parts SLSed with optimized parameters increases up to 77.2%. The linear shrinkage of these parts is about -21% (x/y direction) to -26% (z direction). The final parts have a grain size < 5 μm, but still contain inter-agglomerate pores.

A.5 Densification strategies

Similar densification strategies as already described in section 6.5 were applied to parts of 10x10x10 mm^3, produced with the optimized SLS parameters. Also similar debinding and SSS treatments were used: see $debinding_2$, SSS and pre-sintering in table A.1. This section will compare the post-densification behavior of the carnauba wax - LDPE binder system, reported in the previous section of this chapter, with the post-densification behavior of the PP binder system, described in section 6.5.

A.5.1 Vacuum infiltration

A.5.1.1 Green infiltration

Parts 2 to 5 were green infiltrated with the alumina and silica containing suspensions described in section 6.5.1. Some parts (parts 3 and 5) were infiltrated multiple times.

Part nr	Additional densification steps (besides SLS, deb. and FS)	ρ_{SLS} [%]	$\rho_{green\ inf.}$ [%]
1	None, only SLS	65.9	/
2	1x green infiltration (alumina)	66.7	82.4
3	2x green infiltration (alumina)	67.5	86.7
4	1x green infiltration (silica)	66.2	71.7
5	4x green infiltration (silica)	64.4	81.3

Table A.3: Density after SLS and green infiltration.

Part nr	Additional densification steps (besides SLS, deb. and FS)	ρ [%]	x-y [%]	z [%]
1	None, i.e. only deb. and FS	77.2	-21	-26
2	1x green vacuum infiltration (Al_2O_3)	80.2	-19	-14
3	2x green vacuum infiltration (Al_2O_3)	80.5	-19	-19
4	1x green vacuum infiltration (SiO_2)	65.1	-16	-13
5	4x green vacuum infiltration (SiO_2)	73.1	-11	-10

Table A.4: Density and linear shrinkage of green infiltrated parts after FS.

Green infiltration with an alumina suspension Parts 2 and 3 were green infiltrated with an alumina suspension. Part 2 was infiltrated once and part 3 twice. After infiltration and drying, part 2 had a density of 82.4% (table A.3). As depicted in table 6.5, green infiltration with an alumina suspension slightly increased the density after solid state sintering up to 80.2%. Green infiltration decreased the linear shrinkage to about -19% in the x/y direction and -14% in the z-direction.
In accordance with the same vacuum green infiltration experiments performed on the parts containing a PP binder (see section 6.5.1.1), green infiltration decreased the linear shrinkage. This phenomenon can be explained by assuming that the part shrinkage is generally larger for more porous parts: as infiltration reduced the porosity inside a part, the shrinkage after infiltration was less (see also section 4.6.2.5, section 5.6.3.4 and chapter 6).
In contrast to the same vacuum green infiltration experiments performed on the parts containing a PP binder (see section 6.5.1.1), the density after SSS was only increased a few percentages: from 77.2% up to only 80.2%. This can be explained by the higher green density obtained after SLS: due to the lower amount of porosity, it was more difficult for the same suspension to infiltrate the part.
Figure A.5a illustrated that part 2 contained a macrocrack after SSS. This crack, which probably led to the smaller shrinkage in the z-direction (table A.4), might be caused by:

- the formation of a shell (figure A.5b) after infiltration. This shell caused a nonuniform shrinkage during debinding and SSS, resulting in the crack.
- thermal stresses, causing improper powder deposition during SLS (see figure A.4a).

Infiltrating twice led to about the same result as infiltrating only once: the density after green infiltration (86.7%, table A.3) and SSS (80.5%, table A.4) was only slightly higher for part 3, compared to part 2. The shrinkage during debinding and SSS was also similar: about -19%.
Although no cracks could be observed in the 3D microscope image (figure A.5c), SEM investigations revealed a small horizontal crack (figure A.5d). Similar to green infiltration of the PP containing parts (figures 6.7b and 6.7e), an infiltrated zone, consisting of a porous zone and a dense shell was clearly visible (figure A.5e).

Green infiltration with a silica suspension Parts 4 and 5 were green infiltrated with a silica suspension. Part 4 was infiltrated once and part 5 was infiltrated 4 times. After green infiltrating part 4, the weight gain was measured. Since the

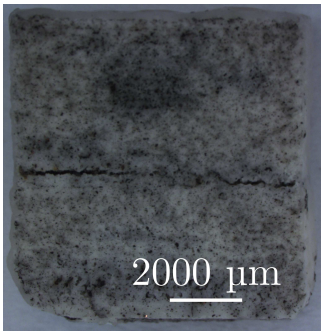

(a) part 2: 3D microscope

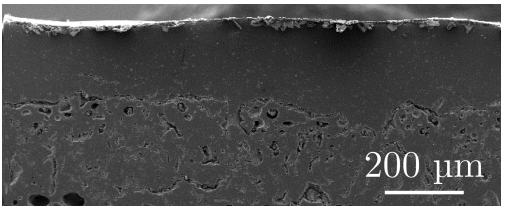

(b) part 2: SE-SEM

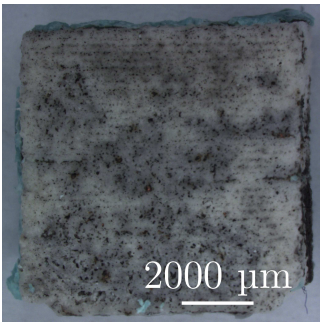

(c) part 3: 3D microscope

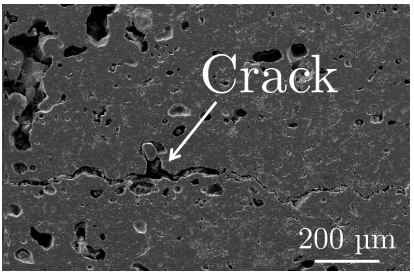

(d) part 3: SE-SEM

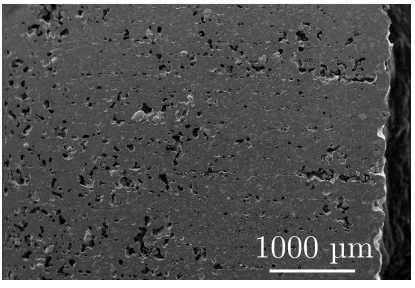

(e) part 3: SE-SEM

Figure A.5: 3D microscope and SEM images showing the microstructure of parts which were green infiltrated with an alumina suspension: part 2 (a,b; 1x infiltrated), part 3 (c,d,e; 2x infiltrated).

density of the part before infiltration and the density of the silica suspension was known, the density after infiltration and before drying could be calculated and was 93.2%. After drying, part 4 had a green density of 71.7% (table A.3). As depicted in table A.4, green infiltration with a silica suspension decreased the density after furnace sintering at 1600°C up to 65.1%. The linear shrinkage decreased to about -16% in the scan/cross scan x/y directions and -13% in the build z direction.
As depicted in figure A.6b, no macrocracks could be observed after furnace sintering. Similar to the green PP containing parts which were green infiltrated with silica (see section 6.5.1.1), a denser shell was visible at the edge of the part (figure A.6b). Although no EDX measurements were performed on the samples, two phases seemed to be present in the denser shell: a phase which consisted of SiO_2 filling the inter-agglomerate pores and a phase which consisted of alumina and SiO_2 (figure A.6c). The latter phase might be mullite (figure 6.14). The denser shell also contained microcracks, which probably arose due to tensile stresses during cooling. The porous zone did not contain the SiO_2 phase (figure A.6d).
The decrease in linear shrinkage during debinding and SSS could be explained by the decrease in porosity after infiltration. The decrease in density after furnace sintering could be explained by the occurrence of nonuniform shrinkage: since the dense shell shrunk less than the more porous core, the porosity of the core increased. The porosity of the shell also increased due to the formation of the microcracks.

When infiltrating four times (part 5) instead of only once (part 4), the green density after drying was increased up to 81.3% (table A.3). As a result, the linear shrinkage during debinding and SSS was less: about -10% instead of -13% to -16% (table A.4). Probably, as more silica particles entered part 5, the porosity and concomitant shrinkage decreased. Furthermore, when infiltrating four times instead of only once, the density after furnace sintering was increased: 73.1% (part 5) instead of 65.1% (part 4). However, the density after furnace sintering was still higher when no infiltration was applied: 77.2% (part 1). Infiltration seemed to influence the density after furnace sintering in two ways:

- increase of density: as the infiltrant material fills the pores.
- decrease of density: due to the shell formation and concomitant nonuniform shrinkage during debinding and SSS.

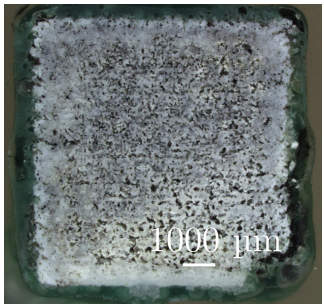

(a) part 4: 3D microscope

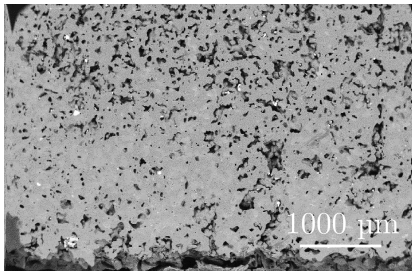

(b) part 4: BSE-SEM

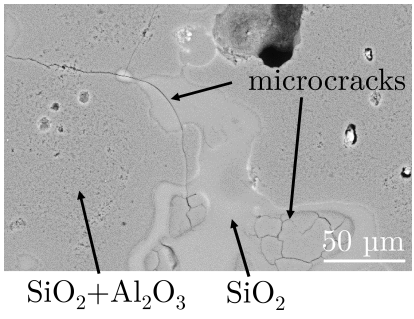

(c) part 4: BSE-SEM, edge

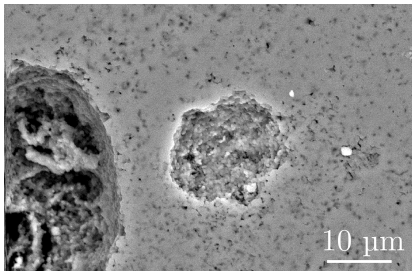

(d) part 4: BSE-SEM, core

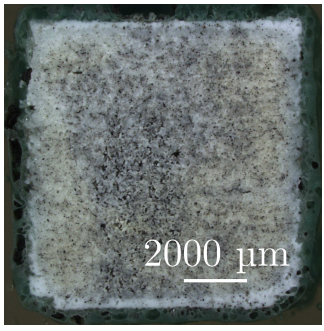

(e) part 5: 3D microscope

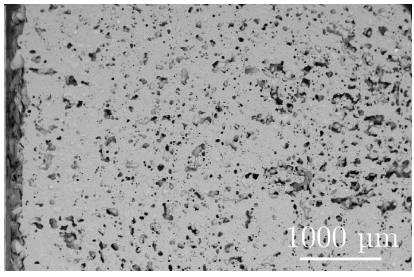

(f) part 5: BSE-SEM

Figure A.6: 3D microscope and BSE-SEM images showing the microstructure of parts which were green infiltrated with a silica suspension: part 4 (a,b,c,d; 1x infiltrated), part 5 (e,f; 4x infiltrated).

In summary:

- In accordance with the same vacuum green infiltration experiments performed on the parts obtained through SLS of PP containing composite agglomerates, the green infiltrated parts tend to shrink less during debinding and SSS. Also in accordance with the PP containing parts, green vacuum infiltration causes the formation of a dense shell.
- In contrast to the same vacuum infiltration experiments performed on the green parts obtained through SLS of PP containing composite agglomerates, the density after SSS was only increased a few percent (alumina suspension) or decreased (silica suspension). This can be explained by the higher green density obtained after SLS: due to the lower amount of porosity, it was more difficult for the same suspension to infiltrate the part. The resulting shell formation and concomitant nonuniform shrinkage during debinding and SSS, decreased the sintered density.

A.5.1.2 Infiltration after pre-sintering with an alumina or silica suspension

Parts 6, 7 and 8 were vacuum infiltrated after pre-sintering at 1050°C. Part 6 was infiltrated three times with the alumina suspension and parts 7 and 8 were infiltrated with the silica suspension. Part 7 was infiltrated only once and part 8 four times.
The results of these infiltration experiments were quite similar to the results of the green infiltration experiments:

- Infiltration with the alumina suspension (part 6) increased the density after furnace sintering only a few percent: from 77.2% up to 78.3% (table A.6).
- Infiltration with the silica suspension (part 7 and 8) decreased the density after furnace sintering: from 77.2% for part 1, to 76.1% for part 7 and 73.1% for part 8 (table A.6).
- Infiltrated parts tended to shrink less during SSS.
- The more silica entered the part during pre-sintering, the less shrinkage occurred during debinding and SSS. During infiltration, the weight of part 7 and 8 increased respectively +12.8% and +36.1% (table A.5). The resulting shrinkages were respectively -10% to -16% and -8% (table A.6).

Similar to the green infiltration experiments, these results could be explained by assuming that:

- Infiltration decreased the porosity of the parts. As a result, the parts shrunk less during SSS.
- Infiltration could increase the density of the parts by filling the pores, or decrease the density of the parts by the formation of a shell and concomitant nonuniform shrinkage.

In contrast to the results of the green infiltration experiments, the parts which were infiltrated after pre-sintering contained macrocracks (see figures A.7a, A.7c and A.7e). Similar to the macrocrack of part 2 (figure A.5a), the macrocracks could be caused by shell formation and concomitant nonuniform shrinkage or thermal stresses, causing improper powder deposition during SLS (figure A.4a).

As depicted in section 6.5.1.2, the final density of the furnace sintered parts, produced with the PP containing powder, increased by applying infiltration after pre-sintering. This is in contrast with the results of this section, which reported only a small increase or a decrease of the density. This can be explained by the higher green density obtained after SLS when using the carnauba wax binder: due to the lower amount of porosity, it was more difficult for the same suspension to infiltrate the part. The resulting shell formation and concomitant nonuniform shrinkage during debinding and SSS, could lead to a decrease of the sintered density.

In summary:

- Despite the formation of macrocracks, both infiltration after pre-sintering and infiltration after SLS led to about the same densification and shrinkage behavior.

Part nr	Additional densification steps (besides SLS, deb. and FS)	ρ_{SLS} [%]	Δweight [wt%]
1	None, only SLS	65.9	/
6	3x infiltration after pre-sintering (alumina)	63.0	+12.2
7	1x infiltration after pre-sintering (silica)	66.2	+12.8
8	4x infiltration after pre-sintering (silica)	64.2	+36.1

Table A.5: Density after SLS and weight increase during infiltration after pre-sintering.

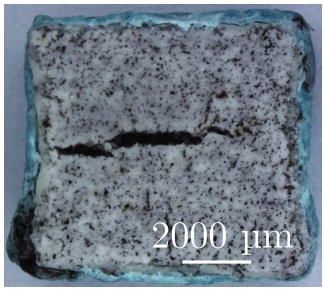

(a) part 6: 3D microscope

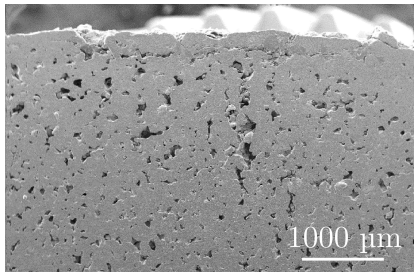

(b) part 6: SE-SEM

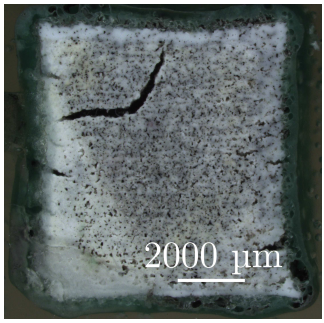

(c) part 7: 3D microscope

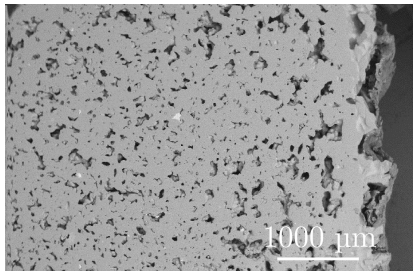

(d) part 7: BSE-SEM

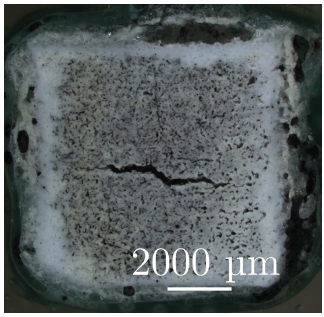

(e) part 8: 3D microscope

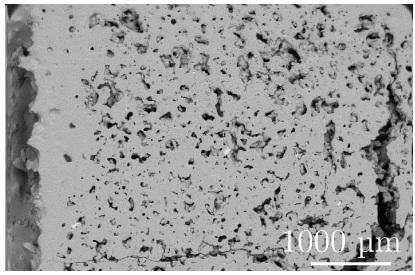

(f) part 8: BSE-SEM

Figure A.7: 3D microscope images (a,c,e) and SEM images (b,d,f) showing the microstructure of parts 6, 7 and 8 which were infiltrated after pre-sintering.

Part nr	Additional densification steps (besides SLS, deb. and FS)	ρ [%]	x-y [%]	z [%]
1	None, i.e. only deb. and FS	77.2	-21	-26
6	3x vac. infiltration after pre-sint. (Al_2O_3)	78.3	-19	-26
7	1x vac. infiltration after pre-sint. (SiO_2)	76.1	-16	-10
8	4x vac. infiltration after pre-sint. (SiO_2)	73.1	-8	-8

Table A.6: Density and linear shrinkage after FS of parts infiltrated after pre-sintering.

A.5.1.3 Green infiltration and infiltration after pre-sintering with an alumina or silica suspension

Similar to the vacuum infiltration experiments, described in section 6.5.1.3, the combination of green vacuum infiltration and vacuum infiltration after pre-sintering with the alumina/silica suspension, led to the following results:

- When infiltrating after SLS and after pre-sintering, a part was formed which had a dense shell and a porous core (figure A.8).
- After green infiltration, already filled inter-agglomerate pores and the dense shell (figure A.8) partially prohibited effective infiltration after pre-sintering. Since a green infiltration step was applied before infiltration after pre-sintering, the (dry) weight increase of the presintered part was only +3.8wt% for the alumina suspension and +27.1% for the silica suspension (cf. part 9 and part 10 in table A.7). As depicted in table A.5, the weight increase after drying was respectively +12.2wt% (alumina suspension) and +36.1wt% (silica suspension), when the green infiltation step was not applied before infiltration after pre-sintering.
- As infiltration lowers the porosity of the parts, the shrinkage during debinding and SSS was lower: compare the shrinkage of part 9 and 10 with the shrinkage of part 1 in table A.8.
- A macrocrack was present in part 10, which was infiltrated with the silica suspension (see figures A.8c and 6.15a). As the dense shell prohibited part 10 to shrink uniformly, cracks perpendicular to the z 'build' direction and along the inter-layer porosities arose.

In contrast to the vacuum infiltration experiments, described in section 6.5.1.3, infiltration decreased the density of the parts after furnace sintering. As described in sections A.5.1.1 and A.5.1.2, this can be explained by the higher

green density obtained after SLS when using the carnauba wax binder: due to the lower amount of porosity, it was more difficult for the same suspension to infiltrate the part. The resulting shell formation and concomitant nonuniform shrinkage during debinding and SSS, lead to a decrease of the sintered density.

In summary:

- In general, the combination of green vacuum infiltration and vacuum infiltration after pre-sintering with the alumina/silica suspensions lead to similar results for both the parts obtained through SLS of the carnauba wax containing powder (this section), as for the parts obtained through SLS of the PP containing powder (section 6.5.1.3). The only difference is that, due to the lower amount of porosity after SLS, it is more difficult for the same suspension to infiltrate the carnauba wax containing parts. As a result, shell formation and concomitant nonuniform shrinkage during debinding and SSS, led to a decrease of the density after furnace sintering.

Part nr	Additional densification steps (besides SLS, deb. and FS)	ρ_{SLS} [%]	$\rho_{gr.\ inf.}$ [%]	Δweight [wt%]
1	None, only SLS	65.9	/	/
9	1x gr. inf. & 3x inf. after pre-sint. (Al_2O_3)	63.4	76.0	+3.8
10	1x gr. inf. & 4x inf. after pre-sint. (SiO_2)	63.1	68.0	+27.1

Table A.7: Density after SLS, density after green infiltration and weight increase during infiltration after pre-sintering.

Part nr	Additional densification steps (besides SLS, deb. and FS)	ρ [%]	x-y [%]	z [%]
1	None, i.e. only deb. and FS	77.2	-21	-26
9	1x gr. vac. inf. & 3x vac. inf. after pre-sint. (Al_2O_3)	67.2	-14	-15
10	1x gr. vac. inf. & 4x vac. inf. after pre-sint. (SiO_2)	58.6	-3	-3

Table A.8: Density and linear shrinkage after FS of parts infiltrated after SLS and pre-sintering.

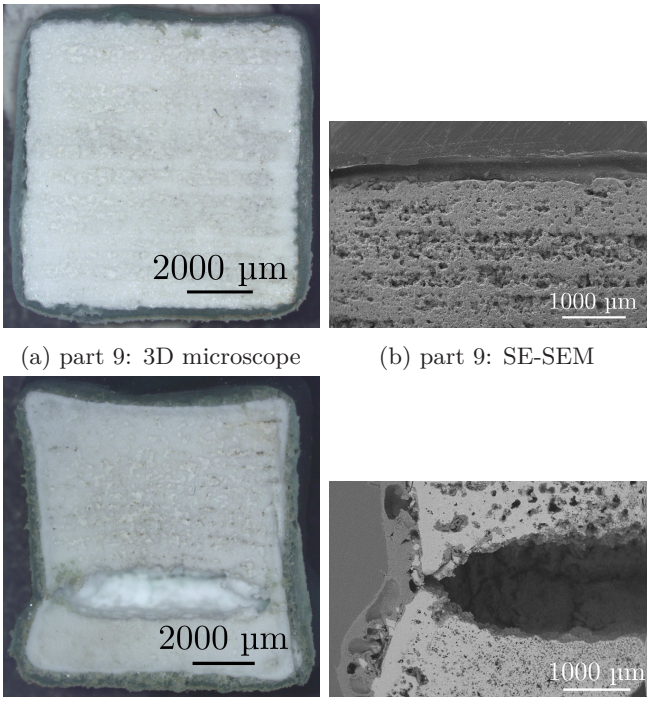

(a) part 9: 3D microscope (b) part 9: SE-SEM

(c) part 10: 3D microscope (d) part 10: SE-SEM

Figure A.8: 3D microscope image (a,c) and SEM images (b,d) showing the microstructure of part 9 (a,b) which was 1 time green infiltrated and 3 times infiltrated after pre-sintering with an alumina suspension, and part 10 (c,d) which was 1 time green infiltrated and 4 times infiltrated after pre-sintering with a silica suspension.

A.5.2 Warm isostatic pressing

WIPing was investigated, with or without infiltration after SLS and/or after pre-sintering. The infiltration experiments were performed with the stabilized 40vol% alumina - ethanol suspension. In order to obtain a good plastic deformation behaviour during WIPing, the samples were vacuum packed in bags of low density polyethylene (LDPE, i.e. the same material as one of the two binder components). All parts were WIPed for 15 minutes at a pressure between 48 and 56 MPa and a temperature of 60°C. After the WIPing step, the LDPE bags were manually removed from the WIPed part.

Only WIP Part 11 was only densified by WIP. As a result, the part shrunk uniformly about -15% (not depicted in a table) and the green density increased up to 89.9% (tableA.9). The WIPing step increased the density after SSS up to 82.2% (table A.10). WIPing also increased the linear shrinkage. The linear shrinkage of -30% in the z 'build' direction was larger compared to the linear shrinkage of -25% in the x/y 'scan'/'cross-scan' directions.
After furnace sintering, part 11 contained large cracks (figure A.9a). These cracks could be caused by the following phenomena (see also section 4.7):

- Inhomogeneous distribution of alumina, carnauba wax and LDPE concentrations in the composite starting powder, resulting in inhomogeneous shrinkage during debinding and SSS.
- Swelling of the components during debinding (see also figure 3.8): in this case, the gases formed during the thermal debinding step could not escape from the dense WIPed part.

Between the cracks, only closed pores in a fine grained (grain size $< 5\mu$m) alumina matrix seemed to be present (figure A.9b). This means that the WIPing process could break the composite agglomerates.

Green infiltration and WIP Part 12 was first green infiltrated with an alumina suspension and WIPed afterwards. Green infiltration increased the green density up to 80.6%. The subsequent WIPing step resulted in a uniform part shrinkage of about -4% (not depicted in a table) and an increase of the green density up to 89.3% (table A.9). After furnace sintering, the density of part 12 was increased up to 87.6% (table A.10). The part shrinkage was -21% in the scan/cross-scan x/y directions and -18% in the build z direction. From these results, it can be concluded that the green infiltration step before WIPing increased both the green and sintered density and reduced the amount

Part nr	Additional densification steps (besides SLS, deb. and SSS)	ρ_{SLS} [%]	$\rho_{gr.\,inf.}$ [%]	ρ_{WIP} [%]	Δweight [wt%]
1	None, only SLS	65.9	/	/	/
11	WIP, 60°C, 48 MPa, 15 minutes	60.7	/	89.9	/
12	gr. infiltration & WIP	65.8	80.6	89.3	/
13	WIP & 3x inf. after pre-sint.	67.5	/	88.8	+23.6
14	gr. inf., WIP, 3x inf. after pre-sint.	62.6	77.9	86.9	+2

Table A.9: Density after SLS, green infiltration and warm isostatic pressing and weight increase during infiltration after pre-sintering.

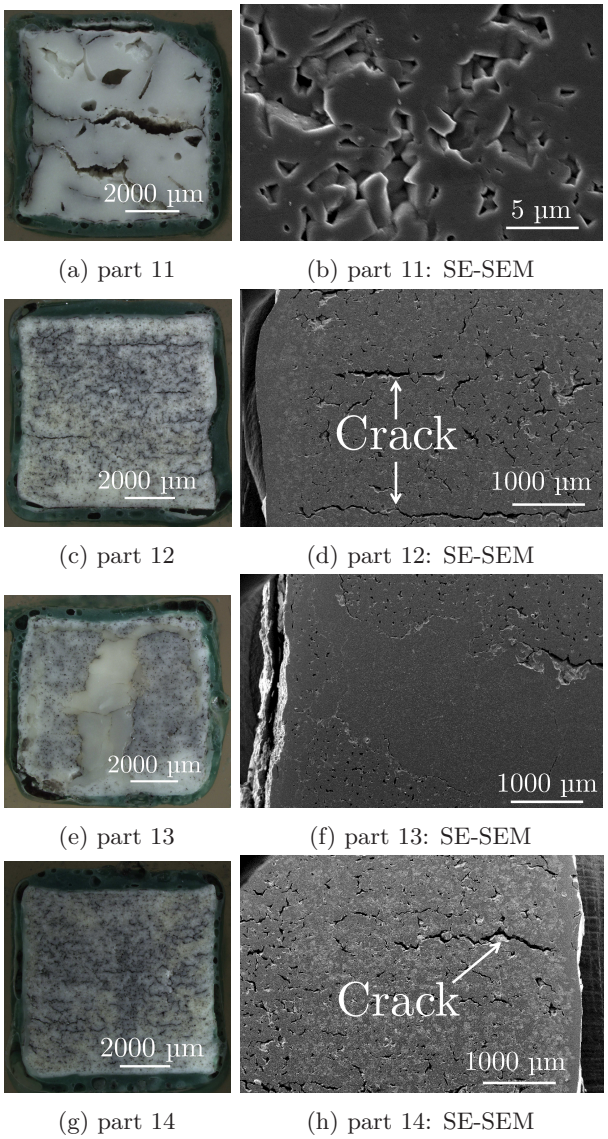

(a) part 11 (b) part 11: SE-SEM

(c) part 12 (d) part 12: SE-SEM

(e) part 13 (f) part 13: SE-SEM

(g) part 14 (h) part 14: SE-SEM

Figure A.9: 3D microscope images (a,c,e,g) and SE-SEM (b,d,f,h) images showing the microstructure after furnace sintering of parts 11 to 14, which were post-densified by green infiltration, WIP and/or infiltration after pre-sintering.

Part nr	Additional densification steps (besides SLS, deb. and SSS)	ρ [%]	x-y [%]	z [%]
1	None, i.e. only deb. and FS	77.2	-21	-26
11	WIP, 60°C, 48 MPa, 15 minutes	82.8	-25	-30
12	gr. vacuum infiltration (Al_2O_3) and WIP	87.6	-21	-18
13	WIP and 3x vac. inf. after pre-sint. (Al_2O_3)	89.0	-20	-27
14	gr. vac. inf., WIP, 3x vac. inf. after pre-sint. (Al_2O_3)	86.5	-19	-22

Table A.10: Density and linear shrinkage after SSS of parts: infiltrated after SLS, WIPed and/or infiltrated after pre-sintering.

of shrinkage both during WIPing and during debinding and SSS.
As depicted in figures A.9c and A.9d, part 12 contained some cracks after furnace sintering. These cracks were smaller compared to the large cracks, obtained without green infiltration (figure A.9a). This means that green infiltration seemed to improve the debinding step after WIPing. Furthermore, most (not all) composite agglomerates seemed to be broken during the WIPing step.

WIP after SLS and infiltration after pre-sintering Part 13 was WIPed after SLS and infiltrated with the alumina suspension after pre-sintering. After WIP, the green density was increased up to 88.8% (table A.9). Similar to part 11, part 13 cracked during debinding and SSS. Similar to part 18 of chapter 4, which was pressure infiltrated after pre-sintering without WIPing (figure 4.12), this crack was filled with alumina suspension during the infiltration step (figures A.9e and A.9f). This led to a weight increase +23.6wt% (table A.9) which was large, compared to the weight increase of +12.2% for part 6 (table A.5), which was not WIPed, but only infiltrated after pre-sintering.
After furnace sintering, part 13 had a density of 89.0% (table A.10). This was the highest density obtained for alumina parts produced through SLS of the alumina - carnauba wax - LDPE composite agglomerates.

Green infiltration, WIP and infiltration after pre-sintering Part 14 was infiltrated after SLS, WIPed before debinding and infiltrated with the alumina suspension after pre-sintering in a furnace. Infiltration after pre-sintering led to a weight increase of only +2wt% (table A.9). Probably, the infiltration after pre-sintering was impeded by the green infiltration step (i.e. the filling of the inter-agglomerate pores and the formation of a dense shell) and the WIPing process (i.e. the decrease of pore size). As infiltration after pre-sintering was

not effective, the obtained densities, shrinkages (tables A.9 and A.10) and microstructure (figures A.9g and A.9h) of part 14 were similar to part 12, which was also green infiltrated and WIPed, but not infiltrated after pre-sintering.

Discussion Similar to the results of section 6.5.2, WIPing with or without infiltration after SLS and/or after pre-sintering led to the following results:

- WIPing increased the green density, the density after SSS and the part shrinkage.
- WIPing at a sufficiently high temperature, led to breaking of the composite agglomerates at a pressure between 48 and 64 MPa.
- Green infiltration before WIPing was an effective method to increase the sintered density.
- Infiltration after pre-sintering was a non-effective densification step after WIPing. Since WIPing decreased the pore size after pre-sintering, the infiltrant could no longer flow inside the part.

In contrast to the results of section 6.5.2, the combination of WIPing and infiltration after pre-sintering led to a very high alumina density after furnace sintering: up to 89.0% (part 13, table A.10). This high density could be explained by the cracking of part 13 after WIPing, during the debinding and pre-sintering step. During infiltration after pre-sintering, this crack could be filled with alumina suspension. Part 16 of chapter 6 was also WIPed and infiltrated after pre-sintering. Since this part did not crack during debinding & pre-sintering and since WIPing decreased the pore size after pre-sintering, the infiltration after pre-sintering was not effective.

In summary:

- In general, WIPing with or without infiltration after SLS and/or after pre-sintering led to similar results for both the parts obtained through SLS of the carnauba wax containing powder (this section) and PP containing powder (section 6.5.2). The only difference is that the WIPed carnauba wax containing parts crack during debinding and furnace sintering when no green infiltration step is applied. During infiltration after pre-sintering, these cracks can be filled with infiltrant material, and as a result, an increased density can be obtained.

A.6 Conclusions

A powder metallurgy process was developed to produce alumina parts through SLS, starting from 78wt% alumina - 18wt% carnauba wax - 4wt% LDPE composite agglomerates synthesized by temperature induced phase separation (TIPS). The composite agglomerates were very difficult to SLS due to the occurrence of balling, thermal stresses (and resulting outer cracks) and dross formation. These phenomena were mainly a result of the low viscosity of carnauba wax at elevated temperatures. Anchoring the parts to a base plate improved the laser sintering of agglomerates, containing low viscosity binders. Cardboard seemed to be the best base plate material: it provided sufficient rigidity to anchor the parts during the SLS process and the parts could be easily removed from the base plate after SLS. The SLS process was also improved by preheating the composite agglomerates up to a temperature just below the melting onset temperature T_{om} (i.e. up to 75°C), and by lowering the particle size of the agglomerates.
After optimizing the SLS parameters, parts with a green density up to 66% could be produced. These parts contained inter-agglomerate porosity and some of the parts contained outer cracks. During debinding and SSS, the density of the parts SLSed with optimized parameters increased up to 77.2%. The linear shrinkage of these parts was about -21% (x/y direction) to -26% (z direction). Furthermore, the final parts contained inter-agglomerate pores and had a grain size $< 5\mu$m.

In order to eliminate the inter-agglomerate pores after furnace sintering, similar densification strategies as already described in section 6.5 were applied on parts of 10x10x10 mm^3, produced with the optimized parameters for SLS: vacuum infiltration, warm isostatic pressing (WIP) or a combination of both was applied (table A.11). Vacuum infiltration was performed on both SLSed samples (i.e. green infiltration) and/or samples which were pre-sintered at 1050°C. In contrast to section 6.5, only the 40vol% alumina - ethanol suspension and the a 40wt% silica - water suspension were used to infiltrate the parts.
Similar to the densification experiments applied in section 6.5, infiltration with the alumina and silica suspensions led to the following results:

- Infiltration filled the pores of the parts. As a result, the shrinkage during debinding and/or SSS decreased.
- Infiltration with the alumina and silica suspensions led to the formation a shell. This shell led to nonuniform shrinkage during debinding and SSS. As a result, cracks could be formed.

- Unless cracks were formed, infiltration after pre-sintering was a non-effective densification step when applied after a green infiltration and/or WIPing step. After green infiltration, already filled inter-agglomerate pores and the dense shell prohibited the infiltration after pre-sintering. Moreover, since WIPing decreased the pore size after pre-sintering, the infiltrant could not flow inside the part anymore.

- WIPing at a sufficient temperature and pressure, broke the initial composite agglomerates. However, during debinding and furnace sintering, macrocracks could arise. The size of the cracks could be reduced by infiltrating the SLSed part prior to WIPing. In this way, desities up to about 90% could be obtained after furnace solid state sintering.

Not all results of the densification experiments were in agreement with the results of section 6.5. During laser irradiation, the carnauba wax - LDPE binder, used in this chapter, had a lower viscosity than the PP binder, used in chapter 6. As a result, the green and final density of the parts produced with the carnauba wax - LDPE binder system (green density: about 66%, table A.3; final density: 77.2%, table A.2), was much higher than the green and final density of the parts produced with the PP binder system (green density: 50.7%, figure 6.3a; final density: about 39%, table 6.3). Due to the concomitant lower amount of porosity after SLS and pre-sintering, it was more difficult for the same suspension to infiltrate the part. The resulting shell formation and concomitant nonuniform shrinkage during debinding and SSS, led to a decrease (or only a small increase) of the furnace sintered density.
Furthermore, in contrast to the WIPing experiments applied in chapter 6, the WIPed parts contained large cracks after furnace sintering if green vacuum infiltration was not applied. During infiltration after pre-sintering, these cracks could be filled with infiltrant material, and as a result, an increased density after furnace sintering could be obtained.

Part nr	Additional densification steps (besides SLS, deb. and FS)	ρ [%]	x-y [%]	z [%]
1	None, i.e. only deb. and FS	77.2	-21	-26
2	1x green vacuum infiltration (Al_2O_3)	80.2	-19	-14
3	2x green vacuum infiltration (Al_2O_3)	80.5	-19	-19
4	1x green vacuum infiltration (SiO_2)	65.1	-16	-13
5	4x green vacuum infiltration (SiO_2)	73.1	-11	-10
6	3x vac. infiltration after pre-sint. (Al_2O_3)	78.3	-19	-26
7	1x vac. infiltration after pre-sint. (SiO_2)	76.1	-16	-10
8	4x vac. infiltration after pre-sint. (SiO_2)	73.1	-8	-8
9	1x gr. vac. inf. & 3x vac. inf. after pre-sint. (Al_2O_3)	67.2	-14	-15
10	1x gr. vac. inf. & 4x vac. inf. after pre-sint. (SiO_2)	58.6	-3	-3
11	WIP, 60°C, 48 MPa, 15 minutes	82.8	-25	-30
12	gr. vacuum infiltration (Al_2O_3) and WIP	87.6	-21	-18
13	WIP and 3x vac. inf. after pre-sint. (Al_2O_3)	89.0	-20	-27
14	gr. vac. inf., WIP, 3x vac. inf. after pre-sint. (Al_2O_3)	86.5	-19	-22

Table A.11: Sintered densities and linear shrinkages of the cubic (10x10x10 mm^3) alumina parts after additional densification steps. The dimensional shrinkages of the table indicate the geometrical changes that appear after the SLS process, i.e. the geometry after SLS is the reference geometry. The vacuum infiltration (vac. inf.) experiments were performed using 40 vol% Al_2O_3 - ethanol and 40 wt% SiO_2 - water suspensions.

Appendix B

Selective laser melting of metals

During my dissertation period, I also performed research on Selective Laser Melting (SLM) of metals. This research mainly focused on the influence of laser remelting (i.e. laser scanning powder layers two or more times) on the properties of Ti-6Al-4V parts produced by SLM and the investigation of residual stresses. The results of this research can be found in the following publications:

IT (Articles in internationally reviewed academic journals)

Kruth, J., Deckers, J., Yasa, E., Wauthlé, R. (2012). Assessing and comparing influencing factors of residual stresses in Selective Laser Melting using a novel analysis method. Proceedings of the Institution of Mechanical Engineers B, Journal of Engineering Manufacture, 226 (6), 980-991. [113]

Yasa, E., Deckers, J., Kruth, J. (2011). The investigation of the influence of laser re-melting on density, surface quality and microstructure of selective laser melting parts. Rapid Prototyping Journal, 17 (5), 312-327. [233]

Yasa, E., Kruth, J., Deckers, J. (2011). Manufacturing by combining Selective Laser Melting and Selective Laser Erosion/laser re-melting. CIRP Annals. Manufacturing Technology, 60 (1), 263-266. [237]

Yasa, E., Deckers, J., Kruth, J., Rombouts, M., Luyten, J. (2010). Charpy impact testing of metallic selective laser melting parts. Virtual and Physical Prototyping, 5 (2), 89-98. [235]

IC (Papers at international scientific conferences and symposia, published in full in proceedings)

Kruth, J., Badrossamay, M., Yasa, E., Deckers, J., Thijs, L., Van Humbeeck, J. (2010). Part and material properties in selective laser melting of metals. Proceedings of the 16th International Symposium on Electromachining. 16th International Symposium on Electromachining (ISEM XVI). Shanghai-China, 19-23 April 2010. [116]

Yasa, E., Deckers, J., Kruth, J., Rombouts, M., Luyten, J. (2010). Investigation of sectoral scanning in Selective Laser Melting. Proceedings of 10th Biennial ASME Conference on Engineering Systems, Design and Analysis. ASME Conference on Engineering Systems, Design and Analysis. Istanbul, Turkey, 12-14. [236]

Kruth, J., Deckers, J., Yasa, E., Wauthlé, R. (2010). Assessing Influencing Factors of Residual Stresses in SLM using a Novel Analysis Method. Proceedings of the 16th International Symposium on Electromachining. 16th International Symposium on Electromachining (ISEM XVI). Shanghai, China, 19-23 April 2010 (pp. 531-537). [118]

Yasa, E., Deckers, J., Craeghs, T., Badrossamay, M., Kruth, J. (2009). Investigation on occurrence of elevated edges in Selective Laser Melting. Twentieth Annual International Solid Freeform Fabrication Symposium. SFF Symposium. Austin, Texas, USA, 3-5 August, 2009. [232]

Kruth, J., Yasa, E., Deckers, J. (2009). Experimental investigation of laser surface re-melting for the improvement of selective laser melting process. European Forum on Rapid Prototyping. Paris, France, 24-25 June 2009. [115]

Yasa, E., Deckers, J., Kruth, J., Rombouts, M., Luyten, J. (2009). Experimental Investigation of Charpy Impact Tests on Metallic SLM parts. Innovative Developments in Design and Manufacturing Advanced Research in Virtual and Rapid Prototyping. The International Conference on Advanced Research in Virtual and Rapid Prototyping. Leiria, Portugal, 6-10 October 2009 (pp. 207-214). [234]

Kruth, J., Yasa, E., Deckers, J. (2008). Roughness Improvement in selective laser melting. Proceedings of the 3rd International Conference on Polymers and Moulds Innovations. International Conference on Polymers and Moulds Innovations. Gent, Sep 17-19, 2008 (pp. 170-183). [120]

Kruth, J., Deckers, J., Yasa, E. (2008). Experimental investigation of laser surface remelting for the improvement of selective laser melting process. Proceedings of the 19th Solid Freeform Fabrication Symposium. 19th Solid Freeform Fabrication Symposium. Austin, USA, Aug 4-6, 2008. [117]

Bibliography

[1] Gettysburg national military park commission: annual reports of the secretary of war. Washington, DC: National Archives and Records Administration, July 1.

[2] http://3dceram.com.

[3] http://www.baikowski.com/products.php.

[4] http://www.ceramic3dprinting.com.

[5] http://www.ceramics.nist.gov/srd/summary/scdaos.htm.

[6] http://www.ivoclarvivadent.com.

[7] http://www.lithoz.com.

[8] http://www.reportlinker.com.

[9] http://www.sirris.be.

[10] http://www.tuwien.ac.at.

[11] Website of Laserinstitut der Hochschule Mittweida (LHM) : Lasermikros-intern - Mikrowerkzeuge und Mikrobauteile aus Metall und Keramik, 2012.

[12] Production specification: Ludox TM-40 colloidal silica. Tech. rep., Sigma Aldrich, 2013.

[13] 3D Systems. *DTM: the sinterstation system 2000 user's guide.*

[14] Agarwala, M., Klosterman, D., Osborne, N., and Lightman, A. Hard metal tooling via SFF of ceramics and powder metallurgy. In *Proceedings of the SFF Symposium* (1999).

[15] Anné, G., Neirinck, B., Vanmeensel, K., der Biest, O. V., and Vleugels, J. Origin of the potential drop over the deposit during electrophoretic deposition. *Journal of the American Ceramic Society 89* (2006), 823–828.

[16] Badev, A., Abouliatim, Y., Chartier, T., Lecamp, L., Lebaudy, P., Chaput, C., and Delage, C. Photopolymerization kinetics of a polyether acrylate in the presence of ceramic fillers used in stereolithography. *Journal of Photochemistry and Photobiology A: Chemistry 222* (2011), 117–122.

[17] Bae, C., and Halloran, J. Influence of residual monomer on cracking in ceramics fabricated by stereolithography. *Int. J. Appl. Ceram. Technol. 8*, 6 (2011), 1289–1295.

[18] Bae, C., and Halloran, J. Integrally cored ceramic mold fabricated by ceramic stereolithography. *Int. J. Appl. Ceram. Technol. 8*, 6 (2011), 1255–1262.

[19] Bai, P., Cheng, J., and Liu, B. Selective Laser Sintering of polymer-coated Al_2O_3/ZrO_2/TiC ceramic powder. *Trans. Nonferrous Met. Soc. China 15*, 2 (2005), 261–265.

[20] Balla, V., Bose, S., and Bandyopadhyay, A. Processing of bulk alumina ceramics using Laser Engineered Net Shaping. *Int. J. Appl. Ceram. Technol. 5*, 3 (2008), 234–242.

[21] Barlow, J. W., and Vail, N. K. International patent WO 93/19019: Producing high-temperature parts by low-temperature sintering, 1993.

[22] Beaman, J., Barlow, J., Bourell, D., Crawford, R., Marcus, H., and McAlea, K. *Solid Freeform Fabrication: a new direction in manufacturing*. Kluwer academic, 1997.

[23] Beinhocker, E. *The origin of wealth: evolution, complexity and the radical remaking of economics*. Havard Business School Press, 2006.

[24] Bertrand, P., Bayle, F., Combe, C., Goeuriot, P., and Smurov, I. Ceramic components manufacturing by Selective Laser Sintering. *Applied Surface Science 254* (2007), 989–992.

[25] Bertrand, P., Yadroitsev, I., and Smurov, I. Prototypage rapide et fabrication directe par laser d'objets multimatériaux multifonctionnels. In *Dixième assisses Europ. de Prototypage Rapide* (2004).

[26] Bertsch, A., Jiguel, S., Hofmann, H., and Renaud, P. Ceramic microcomponents by microstereolithography. *IEEE* (2004), 725–728.

[27] Bertsch, A., Jiguet, S., and Renaud, P. Microfabrication of ceramic components by microstereolithography. *J. Micromech. Microeng. 14* (2004), 197–203.

[28] Berzins, M., Childs, T., and Ryder, G. The Selective Laser Sintering of polycarbonate. *Annals of the CIRP 45*, 1 (1996), 187–190.

[29] Birmingham, B., and Marcus, H. Solid Freeform Fabrication of silicon nitride shapes by Selective Laser Reaction Sintering (SLRS). In *Proceedings of the SFF conference* (1995).

[30] Bocanegra-Bernal, M., and Matovic, B. Dense and near-net-shape fabrication of Si_3N_4 ceramics. *Materials Science and Engineering A 500* (2009), 130–149.

[31] Brooks, H., and Aitchison, D. A review of state-of-the-art large-size foam cutting rapid prototyping and manufacturing technologies. *Rapid Prototyping Journal 16*, 5 (2010), 318–327.

[32] Cai, K., Roman-Manso, B., Smay, J., Zhou, J., Osendi, M., Belmonte, M., and Miranzo, P. Geometrically complex silicon carbide structures fabricated by Robocasting. *J. Am. Ceram. Soc. 95*, 8 (2012), 2660–2666.

[33] Cardon, L., Deckers, J., Verberckmoes, A., Ragaert, K., Delva, L., Shahzad, K., Vleugels, J., and Kruth, J. Polystyrene-coated alumina powder via dispersion polymerization for indirect selective laser sintering applications. *Journal of Applied Polymer Science 128*, 3 (2013), 2121–2128.

[34] Carter, C. B., and Norton, M. G. *Ceramic Materials - Science and Engineering*. Springer, 2007.

[35] Cawley, J. Solid Freeform Fabrication of ceramics. *Current opinion in Solid State and Materials Science 4* (1999), 483–489.

[36] Cevolinni, F., Davis, S., and Rinland, S. New rapid casting techniques for competitive motor sports. In *Proceedings of the SFF Symposium* (2008), pp. 558–569.

[37] Chakravarthy, K. M., and Bourell, D. L. Binder development for indirect SLS of non metallics. In *Proceedings of the SFF Symposium* (2010).

[38] Chartier, T., Badev, A., Abouliatim, Y., Lebaudy, P., and Lecamp, L. Stereolithography process: influence of the rheology of silica

suspensions and of the medium on polymerization kinetics – cured depth and width. *Journal of Photochemistry and Photobiology A: Chemistry 32* (2012), 1625–1634.

[39] Chartier, T., Chaput, C., Doreau, F., and Loiseau, M. Stereolithography of structural complex ceramic parts. *Journal of Materials Science 37* (2002), 3141–3147.

[40] Cheah, C., Chua, C., Lee, C., Feng, C., and Totong, K. Rapid prototyping and tooling techniques: a review of applications for rapid investment casting. *Int. J. Adv. Manuf. Technol. 25* (2005), 308–320.

[41] Clarinval, A. Production of metallic and ceramic parts with the Optoform process. Tech. rep., CRIF, 2006.

[42] Clarinval, A., Carrus, R., and Dormal, T. European patent 1.434.089A1: Photo-polymerisable paste compositions, 2004.

[43] Cormier, D., Taylor, J., Unnanon, K., Kulkarni, P., and West, H. Experiments in layered electro-photographic printing. In *Proceedings of the SFF Symposium* (2000), pp. 267–274.

[44] Cuypers, M. Selectief laser sinteren van polypropyleen-gecoat aluminapoeder en toepassingen. Master's thesis, KU Leuven, 2012.

[45] Darwin, C. *The Origin of Species*, vol. 11. The Harvard Classics - New York, 1909-14.

[46] Das, S., Beaman, J., Wohlert, M., and Bourell, D. Direct laser freeform fabrication of high performance metal components. *Rapid Prototyping Journal 4*, 3 (1998), 112–117.

[47] Das, S., Beaman, J., Wohlert, M., and Bourell, D. L. Producing metal parts by Selective Laser Sintering/Hot Isostatic Pressing. *JOM 50*, 12 (1998), 17–20.

[48] Das, S., Wohlert, M., Beaman, J., and Bourell, D. Processing of Titanium Net Sapes by SLS/HIP. In *Proceedings of the SFF Symposium* (1998), pp. 469–478.

[49] Das, S., Wohlert, M., Beaman, J., and Bourell, D. Processing of titanium net shapes by SLS/HIP. *Materials and design 20* (1999), 115–121.

[50] de Hazan, Y., Heinecke, J., Weber, A., and Graule, T. High solids loading ceramic colloidal dispersions in UV curable media via comb-polyelectrolyte surfactants. *Journal of Colloid and Interface Science 337* (2009), 66–74.

[51] de Hazan, Y., Thänert, M., Trunec, M., and Misak, J. Robotic deposition of 3D nanocomposite and ceramic fiber architectures via UV curable colloidal inks. *Journal of the European Ceramic Society 32* (2012), 1187–1198.

[52] de Smit, B., and Broeck, H. Analysing the cutting process of a heated flexible blade in extruded polystyrene foam. In *Proceedings of the SFF Symposium* (2004), pp. 591–601.

[53] de Witte, P. V., Dijkstra, P., den Berg, J. V., and Feijen, J. Review: Phase separation processes in polymer solutions in relation to membrane formation. *Journal of Membrane Science 117* (1996), 1–31.

[54] Deckers, J., Cardon, L., Shahzad, K., Vleugels, J., and Kruth, J. Production of alumina parts through indirect selective laser sintering of alumina-polystyrene composite powder. In *Proceedings of PMI 2012, 5th International Conference on Polymers and Moulds Innovations* (2012), pp. 178–183.

[55] Deckers, J., Denhouwe, A. V., (as contr.), B. L., and (as contr.), K. M. Complexe keramiekvormen opbouwen via SLS van composietpoederagglomeraten, 2012.

[56] Deckers, J., Kruth, J., Cardon, L., Shahzad, K., and Vleugels, J. Densification and geometrical assessments of alumina parts produced through indirect Selective Laser Sintering of alumina-polystyrene composite powder. *Strojniški vestnik - Journal of Mechanical Engineering 59*, 11 (2013), 646–661.

[57] Deckers, J., Kruth, J., Shahzad, K., and Vleugels, J. Density improvement of alumina parts produced through selective laser sintering of alumina-polyamide composite powder. *Annals of the CIRP, Manufacturing Technology 61*, 1 (2012), 211–214.

[58] Deckers, J., Shahzad, K., Vleugels, J., and Kruth, J. Isostatic pressing assisted indirect selective laser sintering of alumina components. *Rapid Prototyping Journal 18*, 5 (2012), 409–419.

[59] Deckers, J., Shahzad, K., Vleugels, J., Kruth, J., and Boury, S. Production of alumina parts through selective laser sintering of alumina-polyamide composite powder. In *Innovative Developments in Virtual and Physical Prototyping. The International Conference on Advanced Research in Virtual and Rapid Prototyping (VRAP)* (Leira, Portugal, September-October 2012), J. Bártolo, Ed., Taylor & Francis Group (London), pp. 319–327.

[60] Dewidar, M., Lim, J.-K., and Dalgarno, K. A comparison between direct and indirect Selective Laser Sintering of metals. *J. Mater. Sci. Technol. 24*, 2 (2008), 227–232.

[61] Dickerson, J., and Boccaccini, A., Eds. *Electrophoretic deposition of nanomaterials*. Springer, 2012.

[62] Dierkes, S., Faber, A., Wilkes, J., Welters, M., Meiners, W., and Wissembach, K. International patent WO2011/018463A1: Ceramic or glass-ceramic article and methods for producing such article, 2011.

[63] Dierkes, S., Faber, A., Wilkes, J., Welters, M., Meiners, W., and Wissemnbach, K. European patent EP2292357A1: Ceramic or glass-ceramic article and methods for producing such article, 2011.

[64] Doreau, F., Chaput, C., and Chartier, T. Stereolithography for manufacturing ceramic parts. *Advanced Engineering Materials 2*, 8 (2000), 493–496.

[65] Drummer, D., Rietzel, D., and Kühnleinet, F. Development of a charcterization approach for the sintering behavior of new thermoplastics for selective laser sintering. *Physics Procedia 5* (2010), 533–542.

[66] Du, Y., Shi, Y., and Wei, Q. Forming simulation and experimental verification of combined formation of Selective Laser Sintering and Cold Isostatic Pressing. *Journal of Materials Science Engineering and Performance* (2010).

[67] Ebert, J., Özkol, E., Zeichner, A., Uibel, K., Weiss, Ö., Koops, U., Telle, R., and Fischer, H. Direct Inkjet Printing of dental prostheses made of zirconia. *J. Dent. Res. 88*, 7 (2009), 673–676.

[68] Ebert, R., Exner, H., Hartwig, L., Keiper, B., Klötzer, S., and Regenfuss, P. International patent WO2004/076101 A2: Method and device for producing miniature bodies or microstructured bodies, 2004.

[69] Eklund, P., Beckers, M., Jansson, U., Högberg, H., and Hultman, L. The $M_{n+1}AX_n$ phases: Materials science and thin-film processing. *Thin Solid Films 518* (2010), 1851–1878.

[70] Evans. *Indirect rapid manufacturing of silicon carbide composites*. PhD thesis, The University of Texas Austin, 2005.

[71] Evans, R., Bourell, D., Beaman, J., and Campbell, M. Rapid manufacturing of silicon carbide composites. *Rapid Prototyping Journal 11* (2005), 37–40.

[72] Exner, H., Horn, M., Streek, A., Ullmann, F., Hartwig, L., Regenfuss, P., and Ebert, R. Laser Micro Sintering: a new method to generate metal and ceramic parts of high resolution with sub-micrometer powder. *Virtual and Physical Prototyping 3*, 1 (2008), 3–11.

[73] Exner, H., Regenfuss, P., and Ebert, R. Laser Micro Sintering - a versatile instrument for the generation of microparts. *Laser Technik Journal 1* (2007), 26–31.

[74] Exner, H., Regenfuss, P., Ebert, R., Hartwig, L., Streek, A., Klötzer, S., and Horn, M. Lasermikrosintern von keramischen Materialien. *RTejournal - Forum für Rapid Technologie 3* (2006), 1–18.

[75] Exner, H., Regenfuss, P., Hartwig, L., Klötzer, S., and Ebert, R. Selective laser micro sintering with a novel process. In *Proceedings of the 4th International Symposium on Laser Precision Microfabrication* (2003), pp. 145–151.

[76] Fischer, K., Moszner, N., Rheinberger, V., Wachter, W., Homa, J., and Längle, W. Patent nr. 20120010066: Light-curing ceramic slips for the stereolithographic preparation of high-strength ceramics, 2012.

[77] Frederickx, I., Deckers, J., Craeghs, T., and Stevens, R. Wetenschap in stroomversnelling: van inkt naar keramiek in de printer. *Campuskrant 23*, 10 (2012), 6.

[78] Frischholz, P. Verband der Keramischen Industrie e.V.: Breviary of Technical Ceramics.

[79] Frost, H., and Ahsby, M. F. *Deformation-mechanism maps: the platicity and creep of metals and ceramics*. Pergamon Press, 1982.

[80] Gahler, A., and Heinrich, J. Direct Laser Sintering of Al_2O_3-SiO_2 dental ceramic components by layer-wise slurry deposition. *J. Am. Ceram. Soc. 89*, 10 (2006), 3076–3080.

[81] Galusek, D., Sedlacek, J., and Riedel, R. Al_2O_3-SiC composites prepared by warm pressing and sintering of an organosilicon polymer coated alumina powder. *Journal of European Ceramic Society 27* (2007), 2385–2392.

[82] German, R. *Sintering theory and practice*. Wiley, 1996.

[83] Gill, T., and Hon, K. Experimental investigations into the selective laser sintering of silicon carbide polyamide compositesand. *proc. IMechE, Part B: Journal of Engineering Manufacture 218*, 10 (2004), 1249–1256.

[84] Gomes, C., Oliveira, A., Hotza, D., Travitzky, N., and Greil, P. LZSA glass-ceramic laminates: fabrication and mechanical properties. *Journal of Materials Processing Technology 206* (2008), 194–201.

[85] Goodridge, R. D., Wood, D. J., Ohtsuki, C., and Dalgarno, K. W. Biological evaluation of an apatite-mullite glass-ceramic produced via Selective Laser Sintering. *Acta Biomaterialia 3* (2007), 221–231.

[86] Grida, I., and Evans, J. Extrusion freeforming of ceramics through fine nozzles. *Journal of the European Ceramic Society 23* (2003), 629–635.

[87] Gu, D., and Shen, Y. Direct Laser Sintered WC-10Co/Cu nanocomposites. *Applied Surface Science 254* (2008), 3971–3978.

[88] Gupta, S., and Barsoum, M. On the tribology of the MAX phases and their composites during dry sliding: A review. *Wear 271* (2011), 1878–1894.

[89] Gupta, S., Filiminov, D., Palanisamy, T., and Barsoum, M. Tribological behavior of select MAX phases against Al_2O_3 at elevated temperatures. *Wear 265* (2008), 560–565.

[90] Hagedorn, Y. Event: High-end applications for additive manufacturing: Selective laser melting of net-shaped oxide ceramics. Tech. rep., Fraunhofer-ILT, 2013.

[91] Hagedorn, Y.-C., Balachandran, N., Meiners, W., Wissembach, K., and Poprawe, R. SLM of net-shaped high strength ceramics: new opportunities for producing dental restaurations. In *Proceedings of the SFF Symposium* (2011).

[92] Hagedorn, Y.-C., Wilkes, J., Meiners, W., Wissembach, K., and Poprawe, R. Additive Manufacturing of Al_2O_3-ZrO_2-ceramic parts by Selective Laser Melting. In *Proceedings of the 5th International Conference on Additive Manufacturing.* (2010), Loughborough University.

[93] Hagedorn, Y.-C., Wilkes, J., Meiners, W., Wissembach, K., and Poprawe, R. Net shaped high performance oxide ceramic parts by Selective Laser Melting. *Physics procedia 5* (2010), 587–594.

[94] Halloran, J., Griffith, M., and Chu, T. United States patent 6.117.612: Stereolithography resin for rapid prototyping of ceramics and metals, 2000.

[95] Halloran, J., Tomeckova, V., Gentry, S., Das, S., Cilino, P., Yuan, D., Guo, R., Rudraraju, A., Shao, P., Wu, T., Alabi, T., Baker, W., Legdzina, D., Wolski, D., Zimbeck, W., and Long, D. Photopolymerization of powder suspensions for shaping ceramics. *Journal of European Ceramic Society 31* (2011), 2613–2619.

[96] Heinrich, J. LSD-based Selective Laser Sintering. Tech. Rep. 10, TU Clausthal, 2009.

[97] Heinrich, J., Gahler, A., Günster, J., Schmücker, M., Zhang, J., Jiang, D., and Ruan, M. Microstructural evolution during direct Laser Sintering in the Al_2O_3-SiO_2 system. *J. Mater. Sci. 42* (2007), 5307–5311.

[98] Hernaez, M., Matias, I., Corres, J., Goicoechea, J., Bravo, J., and Arregui, F. Study of superhydrophilic nanoparticle-based ultra-thin films towards the development of optical fiber humidity sensors. *International journal on smart sensing and intelligent systems 2*, 1 (2009), 63–74.

[99] Hertoghs, J., Deckers, J., Lambaerts, M., and Mertens, M. 3D-printing: een nieuwe industriële revolutie? *HUMO*, 3716/47 (2011), 44–49.

[100] Hon, K., Li, L., and Hutchings, I. Direct writing technology - advantages and developments. *CIRP Annals - Manufacturing Technology 57* (2008), 601–620.

[101] Hongjun, L., Zitian, F., Naiyu, H., and Xuanpu, D. A note on rapid manufacturing process of metallic parts based on SLS plastic prototype. *Journal of Meterials Processing Technology 142* (2003), 710–713.

[102] Howell, P., Davy, K., and Boyde, A. Mean atomic number and backscattered electron coefficient calculations for some materials with low mean atomic number. *Scanning 20* (1998), 35–40.

[103] Ion, J. *Laser processing of engineering materials.* Elsevier, 2005.

[104] Jacobs, P. *Rapid prototyping & manufacturing - fundamentals of stereolithography.* Society of Manufacturing Engineers, 1992.

[105] Janssen, R., Scheppokat, S., and Claussen, N. Tailor-made ceramic-based components - advantages by reactive processing and advanced shaping techniques. *Journal of the European Ceramic Society 28* (2008), 1369–1379.

[106] Khoshnevis, B., Asiabanpour, B., Mojdeh, M., Koraishy, B., Palmer, K., and Deng, Z. SIS - a new SFF method based on powder sintering. *Rapid Prototyping Journal 9*, 1 (2003), 30–36.

[107] King, B., Dimos, D., Yang, P., and Morissette, S. Direct-write fabrication of integrated, multilayer ceramic components. *Journal of Electroceramics 3*, 2 (1999), 173–178.

[108] Kingery, W., Bowen, H., and Uhlmann, D. *Introduction to Ceramics*, 2nd ed. Wiley, New York, 1976.

[109] Kinsella, M., Lilly, B., Carpenter, B., and Cooper, K. Ejection forces and friction coefficients from injection molding experiments using rapid tooled inserts. In *Proceedings of the SFF Sympsium* (2004), pp. 669–680.

[110] Klocke, F., Derichs, C., Ader, C., and Demmer, A. Investigations on Laser Sintering of ceramic slurries. *Prod. Eng. Res. Devel. 1* (2007), 279–284.

[111] Klocke, F., and Wirtz, H. Selective Laser Sintering of ceramics. In *Laser Assisted Net Shape Engineering 2, Proceedings of the LANE'97* (1997).

[112] Kolosov, S., Vansteenkiste, G., Boudeau, N., Gelin, J., and Boillat, E. Homogeneity aspects in selective laser sintering (SLS). *Journal of Materials Processing Technology 177* (2006), 348 – 351.

[113] Kruth, J., Deckers, J., Yasa, E., and Wauthlé, R. Assessing and comparing influencing factors of residual stresses in Selective Laser Melting using a novel analysis method. *Proceedings of the Institution of Mechanical Engineers B, Journal of Engineering Manufacture 226*, 6 (2012), 980–991.

[114] Kruth, J., Levy, G., Schindel, R., Craeghs, T., and Yasa, E. Consolidation of polymer powders by selective laser sintering. In *Proceedings of the 3rd International Conference on Polymers and Moulds Innovations* (2008), pp. 15–30.

[115] Kruth, J., Yasa, E., and Deckers, J. Experimental investigation of laser surface re-melting for the improvement of selective laser melting process. In *Proceedings of the European forum on rapid prototyping* (June 2009).

[116] Kruth, J.-P., Badrossamay, M., Yasa, E., Deckers, J., Thijs, L., and Humbeeck, J. V. Part and material properties in selective laser

melting of metals. In *Proceedings of the 16th International Symposium on Electromachining (ISEM XVI)* (April 2010).

[117] Kruth, J.-P., Deckers, J., and Yasa, E. Experimental investigation of laser surface remelting for the improvement of Selective Laser Melting process. In *Proceedings of the 19th Solid Freeform Fabrication Symposium* (Aug 2008).

[118] Kruth, J.-P., Deckers, J., Yasa, E., and Wauthlé, R. Assessing influencing factors of residual stresses in SLM using a novel analysis method. In *Proceedings of the 16th International Symposium on Electromachining (ISEM XVI)* (April 2010), pp. 531–537.

[119] Kruth, J.-P., Levy, G., Klocke, F., and Childs, T. Consolidation phenomena in laser and powder-bed based layered manufacturing. *Annals of the CIRP 56*, 2 (2007), 730–759.

[120] Kruth, J.-P., Yasa, E., and Deckers, J. Roughness improvement in Selective Laser Melting. In *Proceedings of the 3rd International Conference on Polymers and Moulds Innovations* (Sep 2008), pp. 170–183.

[121] Ku, C., Gibson, I., and Cheung, W. Selective Laser Sintered CastForm Polystyrene with controlled porosity and its infiltration characteristics by red wax. In *Proceedings of the SFF Symposium* (2002), pp. 107–114.

[122] Lee, I. Rapid full densification of alumina-glass composites fabricated by a Selective Laser Sintering process. *Journal of Materials Science Letters 17* (1998), 1907–1911.

[123] Lee, I. Influence of heat treatment upon SLS processed composites fabricated with alumina and monoclinic HBO_2. *Journal of Materials Science Letters 21* (2002), 209–212.

[124] Lenk, R. Hot moulding – an interesting forming process. *Ceramic forum international: CFI. Berichte der Deutschen Keramischen Gesellschaft. 72*, 10 (1995), 636–642.

[125] Leu, M., Pattnaik, S., and Hilmas, G. E. Investigation of Laser Sintering for freeform fabrication of zirconium diboride parts. *Journal of Virtual and Physical Prototyping 7*, 1 (2012), 25–36.

[126] Levy, G., Schindel, R., and Kruth, J. Rapid manufacturing and rapid tooling with layer manufacturing (LM) technologies, state of the art and future perspectives. *Annals of the CIRP 52*, 2 (2003), 589–609.

[127] Lewis, J. Binder removal from ceramics. *Annu. Rev. Mater. Sci. 27* (1997), 147–173.

[128] Li, J., Habibovic, P., van den Doel, M., Wilson, C., de Wijn, J., van Blitterswijk, C., and de Groot, K. Bone ingrowth in porous titanium implants produced by 3D fiber deposition. *Biomaterials 28* (2007), 2810–2820.

[129] Lithoz GmbH. Additive manufacturing for high-performance ceramics. Flyer at Euromold 2012 (Frankfurt), 2012.

[130] Liu, B., Wildman, R., Tuck, C., Ashcroft, I., and Hague, R. Investigation of the effect of particle size distribution on processing parameters optimisation in selective laser melting process. In *Proceedings of the 22th Solid Freeform Fabrication Symposium* (2011), pp. 227–238.

[131] Liu, D.-M., and Tseng, W. Influence of debinding rate, solid loading and binder formulation on the green microstructure and sintering behaviour of Ceramic Injection Mouldings. *Ceramics International 24* (1998), 471–481.

[132] Liu, F. Manufacturing porous multi-channel ceramic by Laser Gelling. *Ceramics International 37* (2011), 2789–2794.

[133] Liu, F., and Liao, Y. Fabrication of inner complex ceramic parts by Selective Laser Gelling. *Journal of European Ceramic Society 30* (2010), 3283–3289.

[134] Liu, H., Li, Y., Hao, Y., Dong, X., and Huang, N. Study of rapid casting process based on SLS prototypes. *Advances in Abrasive Technology 8* (2005), 593–596.

[135] Liu, J., Shi, Y., Lu, Z., and Huang, S. Manufacturing near dense metal parts via indirect selective laser sintering combined with isostatic pressing. *Appl. Phys. A 89* (2007), 743–748.

[136] Liu, J., Zhang, B., Yan, C., and Shi, Y. The effect of processing parameters on characteristics of Selective Laser Sintering dental glass-ceramic powder. *Rapid Prototyping Journal 16*, 2 (2010), 138–145.

[137] Liu, X.-Q., Li, Y.-M., Yue, J.-L., and Luo, F.-H. Deformation behavior and strength evolution of MIM compacts during thermal debinding. *Trans. Nonferrous Met. Soc. China 18* (2008), 278–284.

[138] Liu, Z., Ko, T., Best, J., Cawley, J., and Heuer, A. CAM-LEM processing: materials flexibility. In *Proceedings of the SFF Symposium* (1997).

[139] Liu, Z. H., Nolte, J. J., Packard, J. I., Hilmas, G., Dogan, F., and Leu, M. C. Selective Laser Sintering of high density alumina ceramic parts. In *Proceedings of the 35th international MATADOR conference* (2007), pp. 351–354.

[140] Lorrison, J. C., Dalgarno, K. W., and Wood, D. J. Processing of an apatite-mullite glass-ceramic and an hydroxyapatite/phosphate glass composite by Selective Laser Sintering. *Journal of Materials Science: Saterials in Medicine 16* (2005), 775–781.

[141] Lu, G. Evolution of the pore structure of a ceramic powder compact during sintering. *Journal of Materials Processing Technology 59* (1996), 297–302.

[142] Lu, Z., Shi, Y., Liu, J., Chen, Y., and Huang, S. Manufacturing AISI304 metal parts by indirect selective laser sintering combined with isostatic pressing. *Int. J. Adv. Manuf. Technol. 39* (2008), 1157–1163.

[143] Maalderink, H. Event: High-end applications for additive manufacturing: SLA processing of highly filled resins. Tech. rep., TNO Delft, 2013.

[144] Mahale, T., Taylor, J., and Cormier, D. Five-axis freeform fabrication of the thermoplastic parts via SWIFT. In *Proceedings of the SFF Symposium* (2000), pp. 289–297.

[145] Mahale, T. H. *Electron Beam Melting of advanced materials and structures*. PhD thesis, North Carolina State University, 2009.

[146] Medvedovski, E., and Peltsman, M. Low pressure injection moulding mass production technology of complex shape advanced ceramic components. *Advances in Applied Ceramics 111*, 5-6 (2012), 333–344.

[147] Megias-Alguacil, D., and Gauckler, L. J. Capillary and van der Waals forces between uncharged colloidal particles linked by a liquid bridge. *Colloid. Polym. Sci. 288* (2010), 133–139.

[148] Meijer, J., Du, K., Gillner, A., Hoffmann, D., Kovalenko, V., Masuzawa, T., Ostendorf, A., Poprawe, R., and Schulz, W. Laser machining by short and ultrashort pulses, state of the art and new opportunities in the age of photons. *CIRP Annals - Manufacturing Technology 51*, 2 (2002), 531–550.

[149] Melville, H. *The Whale*. Richard Bentley (Brittain); Harper & Brothers (U.S.), 1851.

[150] Miranda, P., Siaz, E., Gryn, K., and Tomsia, A. Sintering and Robocasting of beta-tricalcium phosphate scaffolds for orthopaedic applications. *Acta Biomaterialia 2* (2006), 457–466.

[151] Modest, M. *LIA handbook of laser materials processing*. Laser institute of Amerika, 2001.

[152] Moszner, N., Wachter, W., Christoph, A., Rheinberger, V., Liska, R., Stampfl, J., and Patzer, J. United States patent 7.927.538B2: Licht-curing slips for the stereolithographic preparation of dental ceramics, 2011.

[153] Mousah, A. *Effects of filler content and coupling agents on the mechancial properties and geometrical accuracy of selective laser sintered parts in glass bead-filled polyamide 12 composites*. PhD thesis, Cardiff University, 2011.

[154] Munro, R. G. Evaluated material properties for a sintered alpha-Al_2O_3. *Journal of the American Ceramic Society 80* (1997), 1919–1928.

[155] Niino, T., and Yamada, H. Full densification of SLS parts by re-melting. In *Proceedings of the SFF Symposium* (2004), pp. 400–407.

[156] Nogueira, R., Bezerra, A., dos Santos, F., de Sousa, M., and Acchar, W. Low pressure injection molding of alumina ceramics using a carnauba based binder: preliminary results. *Key Engineering Materials 189-191* (2001), 67–72.

[157] Nold, A., Zeiner, J., Assion, T., and Clasen, R. Electrophoretic deposition as Rapid Prototyping method. *Journal of European Ceramic Society 30* (2010), 1163–1170.

[158] Novak, S., and König, K. Fabrication of alumina parts by electrophoretic deposition from ethanol and aqueous suspensions. *Ceramics International 35* (2009), 2823–2829.

[159] Oetzel, C., and Clasen, R. Preparation of zirconia dental crowns via electrophoretical deposition. *J. Mater. Sci. 41* (2006), 8130–8137.

[160] Olakanmi, E. Effect of mixing time on the bed density, and microstructure of selective laser sintered (SLS) aluminum powders. *Materials Research 15* (2012), 167–176.

[161] Olevsky, E., Ma, J., LaSalvia, J., and Meyers, M. Densification of porous bodies in a granular pressure-transmitting medium. *Acta Materialia 55* (2007), 1351–1366.

[162] Özkol, E., Wätjen, A., Bermejo, R., Deluca, M., Ebert, J., Danzer, R., and Telle, R. Mechanical characterisation of miniaturised direct inkjet printed 3Y-TZP specimens for microelectronic applications. *Journal of the European Ceramic Society 30* (2010), 3145–3152.

[163] Paglia, G. *Determination of the structure of γ-alumina using empirical and first principles calculations combined with supporting experiments*. PhD thesis, Curtin University of Technology, 2004.

[164] Petsch, T., Regenfuss, P., Ebert, R., Hartwig, L., Klötzer, S., Brabant, T., and Exner, H. Industrial Laser Micro Sintering. In *Proceedings of the 23rd international congress on applications of lasers and electro-optics 2004* (2004).

[165] Pfeifer, R., Wang, L., and Eyerer, P. Rapid tooling of ceramic parts and molds using high pressure slip casting of Si_3Ni_4. In *Proceedings of the SFF Symposium* (1999), pp. 615–622.

[166] Popma, R. L. W. *Sintering characteristics of nano-ceramic coatings*. PhD thesis, Rijksuniversiteit Groningen, 2002.

[167] Provin, C., Monneret, S., Gall, H. L., and Corbel, S. Three-dimensional ceramic microcomponents made using microstereolithography. *Adv. Mater. 15*, 12 (2003), 994–997.

[168] Radovic, M., and Barsoum, M. MAX phases: Bridging the gap between metals and ceramics. *American Ceramic Society Bulletin 2013* (92), 20–27.

[169] Rahaman, M. *Ceramic processing and sintering*, second ed. Marcel Dekker, Inc., 2003.

[170] Regenfuss, P., Hartwig, L., Klötzer, S., and Ebert, R. Industrial freeform generation of microtools by Laser Micro Sintering. *Rapid Prototyping Journal 11*, 1 (2005), 18–25.

[171] Regenfuss, P., Streek, A., Hartwig, L., Horn, M., Klötzer, S., Ebert, R., and Exner, H. Freeform fabrication of dental inlays by Laser Micro-Sintering. *The laser user magazine 52* (2008), 36–38.

[172] Regenfuss, P., Streek, A., Hartwig, L., Klötzer, S., Brabant, T., Horn, M., Ebert, R., and Exner, H. Principles of Laser Micro Sintering. In *The proceedings of the 17th annual SFF symposium 2006* (2006), D. Bourell, Ed., pp. 740–753.

[173] Regenfuss, P., Streek, A., Hartwig, L., Klötzer, S., Brabant, T., Horn, M., Ullmann, F., Ebert, R., and Exner, H. Material depending mechanisms in Laser Micro Sintering. In *Proceedings of the 5th LANE 2007* (2007), M. Geiger, A. Otto, and M. Schmidt, Eds., pp. 403–418.

[174] Regenfuss, P., Streek, A., Ullmann, F., Hartwig, L., Horn, M., Kühn, C., Ebert, R., and Exner, H. Laser Microsintering - reaction models and results. *cfi/Berichte DKG 85*, 13 (2008), 65–72.

[175] Regenfuss, P., Streek, A., Ullmann, F., Kühn, C., Hartwig, L., Horn, M., Ebert, R., and Exner, H. Laser Micro Sintering of ceramic materials, part 2. *Interceram 57* (2008), 6–9.

[176] Rethfeld, B., Sokolowski-Tinten, K., Von Der Linde, D., and Anisimov, S. Timescales in the response of materials to femtosecond laser excitation. *Appl. Phys. A 79* (2004), 767–769.

[177] Rödel, J., Kounga, A. B. N., Weissenberg-Eibl, M., Koch, D., Bierwisch, A., Rossner, W., Hoffmann, M. J., Danzer, R., and Schneider, G. Development of a roadmap for advanced ceramics: 2010-2025. *Journal of European Ceramic Society 29* (2009), 1549–1560.

[178] Rombouts, M., Deckers, J., Thijs, I., Deckx, J., and Kruth, J.-P. Wax based binder for indirect selective laser sintering of alumina. In *Proceedings of the 5th International PMI Conference* (2012), pp. 184–188.

[179] Sachs, E., Haggerty, J., Cima, M., and Williams, P. United States patent 5.204.055: Three-dimensional printing techniques, 1993.

[180] Schwarz, M., Schäfer, M., Wessler, B., and Gia, K. P. International patent WO2007/063014: Verfahren zum herstellen keramischer Gusswerkzeuge (Method for producing ceramic casting tools), 2007.

[181] Sercombe, T., and Hopkinson, N. Process shrinkage and accuracy during indirect laser sintering of aluminum. *Advanced Engineering Materials 8*, 4 (2006), 260–264.

[182] Shahzad, K., Deckers, J., Boury, S., Neirinck, B., Kruth, J., and Vleugels, J. Preparation and indirect selective laser sintering of alumina/PA microspheres. *Ceramics International 38* (2012), 1241–1247.

[183] Shahzad, K., Deckers, J., Boury, S., Neirinck, B., Kruth, J.-P., and Vleugels, J. Powder preparation and indirect selective laser sintering of alumina. In *ECerS XII: Conference of the European Ceramic Society* (June 2011).

[184] Shahzad, K., Deckers, J., Cuypers, M., Kruth, J.-P., and Vleugels, J. Fabrication of high density alumina parts by indirect selective laser sintering. In *2nd international symposium on materials processing science with lasers as energy sources* (April 2012).

[185] Shahzad, K., Deckers, J., Kruth, J.-P., and Vleugels, J. Additive manufacturing of alumina parts by indirect selective laser sintering and post processing. *Journal of Materials Processing Technology 213*, 9 (2013), 1484–1494.

[186] Shahzad, K., Deckers, J., Zhang, Z., Kruth, J.-P., and Vleugels, J. Additive manufacturing of zirconia parts by indirect selective laser sintering. *Journal of the European Ceramic Society 34*, 1 (2014), 81–89.

[187] Shishkovsky, I., Yadroitsev, I., Bertrand, P., and Smurov, I. Alumina-zirconium ceramics synthesis by Selective Laser Sintering/Melting. *Applied Surface Science 254* (2007), 966–970.

[188] Sirringhaus, H., and Shimoda, T. Inkjet Printing of functional materials. *Materials Research Society Bulletin: Inkjet Printing of functional materials 28*, 11 (2003), 802–806.

[189] Souriou, D., Goeuriot, P., Bennefoy, O., Thomas, G., and Dore, F. Influence of the formulation of an alumina powder on compaction. *Powders and Technology 190* (2009), 152–159.

[190] Stevinson, B., Bourell, D., and Beaman, J. Dimensional stability during post-processing of Selective Laser Sintered ceramic preforms. *Virtual and Physical Prototyping 1*, 4 (2006), 209–216.

[191] Stevinson, B. Y., Bourell, D. L., and Beaman, J. J. Support-free infiltration of Selective Laser Sintered (SLS) silicon carbide preforms. In *Proceedings of the SFF conference* (2006).

[192] Streek, A., Regenfuss, P., Ebert, R., and Exner, H. Laser Micro Sintering - upgrade of the technology. In *Proceedings of the ICALEO conference* (2009).

[193] Streek, A., Regenfuss, P., Ullmann, F., Hartwig, L., Ebert, R., and Exner, H. Processing of silicon carbide by Laser Micro Sintering. In *Proceedings of the 17 Solid Freeform Fabrication symposium* (2006), pp. 349–358.

[194] Subramanian, K., Vail, N., Barlow, J., and Marcus, H. Selective Laser Sintering of alumina with polymer binders. *Rapid Prototyping Journal 1*, 2 (1995), 24–35.

[195] Sugijoka, K., Meunier, M., and Piqué, A., Eds. *Laser Precision Microfabrication*. Springer, 2010.

[196] Sukeshini, M., Meisenkothen, F., Gardner, P., and Reitz, T. Aerosol Jet Printing of functionally graded SOFC anode interlayer and microstructural investigation by low voltage Scanning Electron Microscopy. *Journal of Power Sources 224* (2013), 295–303.

[197] Tang, H. Ceramic Laser Sintering – optimization of ceramic Rapid Prototyping. Tech. rep., National Taipei University of Technology of Taiwan.

[198] Tang, H. Direct Laser Fusion to form ceramic parts. *Rapid Prototyping Journal 8*, 5 (2002), 284–289.

[199] Tang, H., and Liu, F. Ceramic Laser Gelling. *Journal of European Ceramic Society 25* (2006), 627–632.

[200] Tang, H., Yen, H., and Lin, W. On ceramic parts fabricated Rapid Prototyping machine based on Ceramic Laser Fusion. In *Proceedings of the SFF Symposium* (2003).

[201] Tang, H., Yen, H., Su, S., and Lin, Z. Prospect of making ceramic shell mold by ceramic laser fusion. In *Proceedings of the SFF Symposium* (2004).

[202] Tang, H.-H. Building ultra-thin layers by Ceramic Laser Sintering. *Materials Transactions 47*, 3 (2006), 889–897.

[203] Tang, H.-H., Chiu, M.-L., and Yen, H.-C. Slurry-based Selective Laser Sintering of polymer-coated ceramic powders to fabricate high strength alumina parts. *Journal of the European Ceramic Society 31* (2011), 1383–1388.

[204] Tesavibul, P., Felzmann, R., Gruber, S., Liska, R., Thompson, I., Boccaccini, A., and Stampfl, J. Processing of 45S5 Bioglass by lithography-based Additive Manufacturing. *Materials Letters 74* (2012), 81–84.

[205] Tian, X., Günster, J., Melcher, J., Li, D., and Heinrich, J. Process parameters analysis of direct Laser Sintering and post treatment of porcelain components using Taguchi's method. *Journal of European Ceramic Society 29* (2009), 1903–1915.

[206] Tian, X., Li, D., and Heinrich, J. Rapid Prototyping of porcelain products by Layer-wise Slurry Deposition (LSD) and direct Laser Sintering. *Rapid Prototyping Journal 18* (2012), 362–373.

[207] Tian, X., Sun, B., Heinrich, J., and Li, D. Stress relief mechanism in layer-wise laser directly sintered porcelain ceramics. *Materials Science and Engineering A 527* (2010), 1695–1703.

[208] Tolochko, N., Laoui, T., Khlophkov, Y., Mozzharov, S., Titov, V., and Ignatiev, M. Absorptance of powder materials suitable for Laser Sintering. *Rapid Prototyping Journal 6*, 3 (2000), 155–160.

[209] Tomeckova, V., and Halloran, J. Critical energy for photopolymerization of ceramic suspensions in acrylate monomers. *Journal of European Ceramic Society 30* (2010), 3273–3282.

[210] Tomeckova, V., and Halloran, J. Cure depth for photopolymerization of ceramic suspensions. *Journal of European Ceramic Society 30* (2010), 3023–3033.

[211] Tomeckova, V., and Halloran, J. Predictive models for the photopolymerization of ceramic suspensions. *Journal of the Europenan Ceramic Society 30* (2010), 2833–2840.

[212] Tu, W., and Lange, F. Liquid precursor infiltration processing of powder compacts: kinetic studies and microstructure development. *Journal of the American Ceramic Society 78*, 12 (1995), 3277–3288.

[213] van der Eijk, C., Mugaas, T., Karlsen, R., Asebo, O., Kolnes, O., and Skjevdal, R. Metal printing process - development of a new Rapid Prototyping process for metal parts. In *Proceedings of the World PM conference held in Vienna* (2004).

[214] Venkataraman, N., Rangarajan, S., Matthewson, M., Harper, B., Safari, A., Danforth, S., Wu, G., Langrana, N., Guceri, S., and Yardimci, A. Feedstock material property - process relationships in Fused Deposition of Ceramics (FDC). *Rapid Prototyping Journal 6*, 4 (2000), 244–253.

[215] Vleugels, J. KU Leuven course B-KUL-H00D5B: Ceramics and Powder Metallurgy.

[216] Vorst, G. V. D. *Modelling and numerical simulation of viscous sintering*. PhD thesis, Technische Universiteit Eindhoven, 1994.

[217] Wang, F., Mei, J., Jiang, H., and Wu, X. Laser fabrication of Ti6Al4V/TiC composites using simultaneous powder and wire feed. *Materials Science and Engineering A 445* (2007), 461–466.

[218] Wang, H.-R., Cima, M., Kernan, B., and Sachs, E. Alumina-doped silica gradient-index (GRIN) lenses by Slurry-based Three-dimensional Printing (S-3DP). *Journal of Non-crystalline Solids 349* (2004), 360–367.

[219] Wang, J.-C. A novel fabrication method of high strength alumina ceramic parts based on solvent-based slurry stereolithography and sintering. *International Journal of Precision Engineering and Manufacturing 14*, 3 (2013), 485–491.

[220] Wang, Y. United States patent 2003/0180665 A1: Ionization radiation imageable photopolymer compositions, 2003.

[221] Wilkes, J. Fraunhofer ILT Annual Report: Manufacturing of ceramic components by Selective Laser Melting. Tech. rep., Fraunhofer ILT, 2006.

[222] Wilkes, J. *Selektives laserschmelzen zur generativen herstellung von Bauteilen aus hochfester Oxidkeramik*. PhD thesis, Fraunhofer ILT, 2009.

[223] Wilkes, J., and Wissembach, K. Rapid Manufacturing of ceramic components for medical and technical applications via Selective Laser Melting. In *Proceedings of the Euro-uRapid conference* (2006).

[224] Williams, C. *Design and development of a layer-based Additive Manufacturing process for the realization of metal parts of designed mesostructure*. PhD thesis, Georgia institute of technology, 2008.

[225] Williams, C., Mistree, F., and Rosen, D. A functional classification framework for the conceptual design of Additive Manufacturing technologies. *Journal of Mechanical Design 133* (2011), 121002–1 Ű 121002–11.

[226] Wohlert, M., Das, S., Beaman, J. J., and Bourell, D. L. Direct laser fabrication of high performance metal components via SLS/HIP. In *Solid Freeform Fabrication Symposium Proceedings* (1999).

[227] Wu, Y., Du, J., Choy, K.-L., and Hench, L. Laser densification of alumina powder beds generated using aerosol assisted spray deposition. *Journal of European Ceramic Society 27* (2007), 4727–4735.

[228] Xiong, Y., and J.E. Smugeresky, L. Ajdelsztajn, J. S. Fabrication of WC-Co cermets by Laser Engineered Net Shaping. *Materials Science and Engineering A 493* (2008), 261–266.

[229] Yang, H., Lee, J., and Kim, K. Ruber isostatic pressing of metal powder under warm temperatures. *Powder Technology 134* (2004), 249–251.

[230] Yang, J., Shi, Y., Shen, Q., and Yan, C. Selective laser sintering of HIPS and investment casting technology. *Journal of Materials Processing Technology 209* (2009), 1901–1908.

[231] Yardimci, M., and Güçeri, S. Conceptual framework for the thermal process modelling of fused deposition. *Rapid Prototyping Journal 2*, 2 (1996), 26–31.

[232] Yasa, E., Deckers, J., Craeghs, T., Badrossamay, M., and Kruth, J.-P. Investigation on occurrence of elevated edges in Selective Laser Melting. In *Twentieth Annual International Solid Freeform Fabrication Symposium (SFF Symposium)* (August 2009).

[233] Yasa, E., Deckers, J., and Kruth, J.-P. The investigation of the influence of laser re-melting on density, surface quality and microstructure of selective laser melting parts. *Rapid Prototyping Journal 17*, 5 (2011), 312–327.

[234] Yasa, E., Deckers, J., Kruth, J.-P., Rombouts, M., and Luyten, J. Experimental investigation of charpy impact tests on metallic SLM parts. In *Innovative Developments in Design and Manufacturing Advanced Research in Virtual and Rapid Prototyping* (October 2009), pp. 207–214.

[235] Yasa, E., Deckers, J., Kruth, J.-P., Rombouts, M., and Luyten, J. Charpy impact testing of metallic selective laser melting parts. *Virtual and Physical Prototyping 5*, 2 (2010), 89–98.

[236] Yasa, E., Deckers, J., Kruth, J.-P., Rombouts, M., and Luyten, J. Investigation of sectoral scanning in Selective Laser Melting. In *Proceedings of 10th Biennial ASME Conference on Engineering Systems, Design and Analysis* (2010).

[237] Yasa, E., Kruth, J.-P., and Deckers, J. Manufacturing by combining Selective Laser Melting and Selective Laser Erosion / laser re-melting. *CIRP Annals. Manufacturing Technology 60*, 1 (2011), 263–266.

[238] Yen, H., and Tang, H. Study on direct fabrication of ceramic shell mold with slurry-based Ceramic Laser Fusion and Ceramic Laser Sintering. *Int. J. Adv. Manuf. Technol. 60* (2012), 1009–1015.

[239] Yen, H.-C. A new slurry-based shaping process for fabricating ceramic green part by selective laser scanning the gelled layer. *Journal of the European Ceramic Society 32* (2012), 3123–3128.

[240] Yen, H.-C., Chiu, M.-L., and Tang, H.-H. Laser scanning parameters on fabrication of ceramic parts by liquid phase sintering. *Journal of the European Ceramic Society 29* (2009), 1331–1336.

[241] Yen, H.-C., and Tang, H.-H. Developing a paving system for fabricating ultra-thin layers in ceramic laser rapid prototyping. *Int. J. Adv. Manuf. Technol. 36* (2008), 280–287.

[242] Yen, H.-C., Tang, H.-H., and Wu, C.-H. Improving staircase effect in the process of Ceramic Laser Gelling. *Advanced Materials Research 284-286* (2011), 43–47.

[243] Yoo, J., Cima, M., Khanuja, S., and Sachs, E. Structural ceramic components by 3D Printing. In *Proceedings of the SFF Symposium* (1993).

[244] Yuan, Q., and Williams, R. Large scale manufacture of magnetic polymer particles using membranes and microfluidic devices. *China Particuology 5*, 1-2 (2007), 26–42.

[245] Zhang, L., Kanjarla, A., Vleugels, J., and der Biest, O. V. Textured α-alumina through electrophoretic deposition and templated grain growth. *Key Engineering Materials 412* (2009), 261–266.

[246] Zheng, H., Zhang, J., Lu, S., Wang, G., and Xy, Z. Effect of core-shell composite particles on the sintering behavior and properties of nano-Al_2O_3/polystyrene composite prepared by SLS. *Materials Letters 60*, 9-10 (2006), 1219–1223.

[247] Zhou, W., Li, D., and Wang, H. A novel aqueous ceramic suspension for ceramic stereolithography. *Rapid Prototyping Journal 16*, 1 (2010), 29–35.

Curriculum

Contact: deckersjan@gmail.com

PhD in Engineering Science
Katholieke Universiteit Leuven
2008-2013

Master of Science in Engineering, Biomechanics
Katholieke Universiteit Leuven
2002-2007

Postgraduate, Fundamentals in Management
Leuven School of Business and Economics
2012-2013

German
CLT language center: level 2
2011-2012

Spanish
CLT language center: level 1
2010-2011

Languages:
Dutch, English, French, German, Spanish

Publications

IT (Articles in internationally reviewed academic journals)

Shahzad, K., Deckers, J., Zhongying Z., Kruth, J., Vleugels, J. (2014). Additive manufacturing of zirconia parts by indirect selective laser sintering. Journal of the European Ceramic Society, 34 (1), 81-89. [186]

Cardon, L., Deckers, J., Verberckmoes, A., Ragaert, K., Delva, L., Shahzad, K., Vleugels, J., Kruth, J. (2013). Polystyrene-coated alumina powder via dispersion polymerization for indirect selective laser sintering applications. Journal of Applied Polymer Science, 128 (3), 2121-2128. [33]

Deckers, J., Kruth, J., Cardon, L., Shahzad, K., Vleugels, J. (2013). Densification and geometrical assessments of alumina parts produced through indirect Selective Laser Sintering of alumina-polystyrene composite powder. Strojniški Vestnik - Journal of Mechanical Engineering, 59 (11), 646-661. [56]

Shahzad, K., Deckers, J., Kruth, J., Vleugels, J. (2013). Additive manufacturing of alumina parts by indirect selective laser sintering and post processing. Journal of Materials Processing Technology, 213 (1), 1484-1494. [185]

Shahzad, K., Deckers, J., Boury, S., Neirinck, B., Kruth, J., Vleugels, J. (2012). Preparation and indirect selective laser sintering of alumina/PA microspheres. Ceramics International, 38 (2), 1241-1247. [182]

Deckers, J., Shahzad, K., Vleugels, J., Kruth, J. (2012). Isostatic pressing assisted indirect selective laser sintering of alumina components. Rapid Prototyping Journal, 18 (5), 409-419. [58]

Deckers, J., Kruth, J., Shahzad, K., Vleugels, J. (2012). Density improvement of alumina parts produced through selective laser sintering of alumina-polyamide composite powder. CIRP Annals. Manufacturing Technology, 61 (1), 211-214. [57]

Kruth, J., Deckers, J., Yasa, E., Wauthlé, R. (2012). Assessing and comparing influencing factors of residual stresses in Selective Laser Melting using a novel analysis method. Proceedings of the Institution of Mechanical Engineers B, Journal of Engineering Manufacture, 226 (6), 980-991. [113]

Yasa, E., Deckers, J., Kruth, J. (2011). The investigation of the influence of laser re-melting on density, surface quality and microstructure of selective laser melting parts. Rapid Prototyping Journal, 17 (5), 312-327. [233]

Yasa, E., Kruth, J., Deckers, J. (2011). Manufacturing by combining Selective Laser Melting and Selective Laser Erosion/laser re-melting. CIRP Annals. Manufacturing Technology, 60 (1), 263-266. [237]

Yasa, E., Deckers, J., Kruth, J., Rombouts, M., Luyten, J. (2010). Charpy impact testing of metallic selective laser melting parts. Virtual and Physical Prototyping, 5 (2), 89-98. [235]

IC (Papers at international scientific conferences and symposia, published in full in proceedings)

Rombouts, M., Deckers, J., Thijs, I., Deckx, J., Kruth, J. (2012). Wax based binder for indirect selective laser sintering of alumina. Proceedings of the 5th International PMI Conference. PMI conference. Ghent, 12-14 September 2012 (art.nr. 29) (pp. 184-188). [178]

Deckers, J., Shahzad, K., Vleugels, J., Kruth, J., Boury, S. (2012). Production of alumina parts through Selective Laser Sintering of alumina-polyamide composite powder. In Bártolo, J. (Ed.), Innovative Developments in Virtual and Physical Prototyping. The International Conference on Advanced Research in Virtual and Rapid Prototyping (VRAP). Leira (Portugal), September 28 - October 1 (pp. 319-327). London: Taylor & Francis Group. [59]

Deckers, J., Cardon, L., Shahzad, K., Vleugels, J., Kruth, J. (2012). Production of alumina parts through indirect Selective Laser Sintering of alumina-polystyrene composite powder. Proceedings of PMI 2012, 5th International Conference on Polymers and Moulds Innovations. PMI. Ghent, Belgium, 12-14 September 2012 (art.nr. 28) (pp. 178-183). [54]

Kruth, J., Badrossamay, M., Yasa, E., Deckers, J., Thijs, L., Van Humbeeck, J. (2010). Part and material properties in selective laser melting of metals. Proceedings of the 16th International Symposium on Electromachining. 16th International Symposium on Electromachining (ISEM XVI). Shanghai-China, 19-23 April 2010. [116]

Yasa, E., Deckers, J., Kruth, J., Rombouts, M., Luyten, J. (2010). Investigation of sectoral scanning in Selective Laser Melting. Proceedings of 10th Biennial

ASME Conference on Engineering Systems, Design and Analysis. ASME Conference on Engineering Systems, Design and Analysis. Istanbul, Turkey, 12-14. [236]

Kruth, J., Deckers, J., Yasa, E., Wauthlé, R. (2010). Assessing Influencing Factors of Residual Stresses in SLM using a Novel Analysis Method. Proceedings of the 16th International Symposium on Electromachining. 16th International Symposium on Electromachining (ISEM XVI). Shanghai, China, 19-23 April 2010 (pp. 531-537). [118]

Yasa, E., Deckers, J., Craeghs, T., Badrossamay, M., Kruth, J. (2009). Investigation on occurrence of elevated edges in Selective Laser Melting. Twentieth Annual International Solid Freeform Fabrication Symposium. SFF Symposium. Austin, Texas, USA, 3-5 August, 2009. [232]

Kruth, J., Yasa, E., Deckers, J. (2009). Experimental investigation of laser surface re-melting for the improvement of selective laser melting process. European Forum on Rapid Prototyping. Paris, France, 24-25 June 2009. [115]

Yasa, E., Deckers, J., Kruth, J., Rombouts, M., Luyten, J. (2009). Experimental Investigation of Charpy Impact Tests on Metallic SLM parts. Innovative Developments in Design and Manufacturing Advanced Research in Virtual and Rapid Prototyping. The International Conference on Advanced Research in Virtual and Rapid Prototyping. Leiria, Portugal, 6-10 October 2009 (pp. 207-214). [234]

Kruth, J., Yasa, E., Deckers, J. (2008). Roughness Improvement in selective laser melting. Proceedings of the 3rd International Conference on Polymers and Moulds Innovations. International Conference on Polymers and Moulds Innovations. Gent, Sep 17-19, 2008 (pp. 170-183). [120]

Kruth, J., Deckers, J., Yasa, E. (2008). Experimental investigation of laser surface remelting for the improvement of selective laser melting process. Proceedings of the 19th Solid Freeform Fabrication Symposium. 19th Solid Freeform Fabrication Symposium. Austin, USA, Aug 4-6, 2008. [117]

IMa (Meeting abstracts, presented at international scientific conferences and symposia, published or not published in proceedings or journals)

Shahzad, K., Deckers, J., Cuypers, M., Kruth, J., Vleugels, J. (2012). Fabrication of high density alumina parts by indirect selective laser sintering. 2nd International Symposium on Materials Processing Science with Lasers as Energy Sources. Clausthal-Zellerfeld, Germany, 24-25 April 2012. [184]

Shahzad, K., Deckers, J., Boury, S., Neirinck, B., Kruth, J., Vleugels, J. (2011).

Powder preparation and indirect selective laser sintering of alumina. ECerS XII, Conference of the European Ceramic Society. Stockholm, Sweden, 19-23 June 2011. [183]

WP (Science popularisation)

Frederickx, I. Deckers, J. (as contr.), Craeghs, T. (as contr.), Stevens, R. (as contr.) (2012). Wetenschap in stroomversnelling: van inkt naar keramiek in de printer. Campuskrant, 23 (10), 6. [77]

Deckers, J., Van Denhouwe, A. Lauwers, B. (as contr.), Mielnik, K. (as contr.) (2012). Complexe keramiekvormen opbouwen via SLS van composietpoederagglomeraten. [55]

Hertoghs, J. Deckers, J. (as contr.), Lambaerts, M. (as contr.), Mertens, M. (as contr.) (2011). 3D-printing: een nieuwe industriële revolutie? HUMO (3716/47), 44-49. [99]

FACULTY OF ENGINEERING SCIENCE
DEPARTMENT OF MECHANICAL ENGINEERING
PRODUCTION ENGINEERING, MACHINE DESIGN AND AUTOMATION (PMA)
Celestijnenlaan 300B - box 2420
B-3001 Heverlee, Belgium
jan.deckers@mech.kuleuven.be
http://www.mech.kuleuven.be